Electron transfer across covalent and hydrogen bonded interfaces

Oliver Glenister

A thesis submitted to the university of Huddersfield in partial fulfilment of the qualification of PhD.

2020

Acknowledgements

First and foremost, I would like to thank Dr Nathan Patmore for his support throughout my masters and my PhD. I would also like to thank him for constantly challenging me to be better both practically and theoretically and humouring my self-confessed stupid theories some of which worked. To Paul Scattergood for his wealth of knowledge in all thing's chemistry. To Lee for teaching me the fundamentals of air sensitive chemistry and continued support and friendship. Working with Lee was one of the most enjoyable and productive periods of my PhD, I wish him all the best in the future. The final two years of my PhD were the most difficult and I would like to thank Andrew, Becky, Rayhaan and Jen for their support during this difficult period. A special thank you goes to Dr Luke Wilkinson for his enthusiasm and support, I have never met someone who gets so excited by chemistry and his passion is truly contagious. In no particular order, Gage, Heidi, Rob, Chris, Jasmine, Daisy, Becky and Ryan for providing such an amazing work environment.

I would like to thank Dr Chris Wedge for teaching me the fundamentals of electron paramagnetic resonance spectroscopy and more importantly how to simulate them. I would also like to thank Chris for facilitating collaborations and introducing me to Old Peculiar, I look forward to having another pint with him in the future. To Professor Rice and the Rice group for all their help with everything related to XRD, I appreciate Craig for taking the time to run crystals for me and for teaching me the basics of solving crystal structures. To Neil McLay for anything NMR related as well as the constant supply of liquid nitrogen. I would like to thank Anthony Meijer for the DFT that helped to rationalise many aspects of this project.

Finally, I would like to thank my parents for their constant support and listening to me talking about chemistry despite it 'all sounding Greek to them'.

Contents

Introduction to Metal-Metal Quadruple Bonds and Electron Self-Exchange Reactions

1.1 Metal-Metal Bonding

The recognition of the first metal-metal bonded species in 1957 originated alongside the development of X-ray crystallography.[1,2] The study presented the first real evidence of a metal-metal bond between transition metals, these bonds were found in the complexes $Mn_2(CO)_{10}$ and $Re_2(CO)_{10}$. In 1964 Cotton *et al.* recognised the first metal-metal quadruple bond in the complex $K_2[Re_2Cl_8]\cdot 2H_2O$, this complex had previously been reported but the structure was incorrectly rationalised.[3–5] It was found that upon the reduction of ReO_4^- in aqueous hydrochloric acid or hydrobromic acid, a very short Re-Re bond that did not incorporate any halogen bridges was formed. The eclipsed conformation (Figure 1.1), and the very short and strong bond was explained to be due to the formation of a δ bond which unlike the σ bond imposes a restriction on the rotation about the Re-Re axis. The π bonds are also sensitive to rotation about the Re-Re axis but there is no net loss of orbital overlap upon rotation unlike the δ bond. It was surmised that a quadruple bond must exist between the two rhenium centres and it was calculated that the stabilisation offered by the δ bond was in the region of 6 kcal mol^{-1}, about 10 % of the overall bond strength.[4]

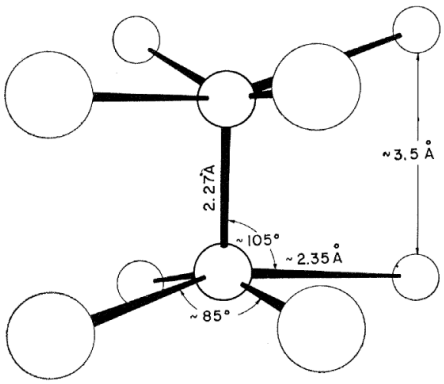

Figure 1.1:The crystal structure of $[Re_2Cl_8]^{2-}$, Reported by Cotton et al. in 1964.[3,4] From F. A. Cotton, N. F. Curtis, C. B. Harris, B. F. G. Johnson, S. J. Lippard, J. T. Mague, W. R. Robinson and J. S. Wood, Science, 1964, 145, 1305–1307. Reprinted with permission from AAAS.

Following the formal recognition of the quadruple bond, several previously reported complexes which were incorrectly formulated were subsequently found to contain a quadruple bond.[6] In one such case the yellow product resulting from the reflux of molybdenum hexacarbonyl and benzoic acid at temperatures exceeding 150 °C, was originally believed to be a polymeric chain consisting of $Mo(O_2CC_6H_5)_2$ units.[6] Although the report is from 1959, the complex was thought to be a structure where the arene is bound to the molybdenum by a sandwich type bond and the free carbonyl would then coordinate to a second molybdenum creating a polymeric chain. The actual complex was determined to be $Mo_2(O_2CC_6H_5)_4$, the four benzoate ligands bridge the dimetal core in a paddlewheel arrangement.[1]

A metal-metal paddlewheel complex consists of a dinuclear core typically surrounded by four equatorial bridging μ_2-ligands. As shown in Figure 1.2, dimetal complexes with monodentate ligands can form the square parallel pipped structure, found in $Re_2Cl_8^{2-}$, and related complexes such as $Tc_2Cl_8^{2-}$.[7] The dimetal core can have formal bond orders ranging from 0.5 to 4 depending on the metal and its oxidation state.[1] At the same time Cotton reported a quadruple bond between technetium in the complex $[Tc_2Cl_8]^{3-}$ which had an analogous structure as shown in Figure 1.2.

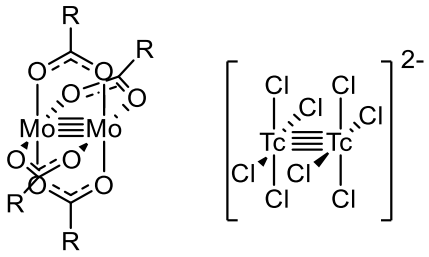

Figure 1.2: The structure of the species reported by both Cotton and Mason in 1965.[7,8]

1.1.1 *Electronic Structure of the Quadruple Bond*

Carbon-carbon bonds have a maximum bond order of three (alkyne), firstly a σ-bond generated by the constructive overlap of the sp mixed-orbitals. A π bond is generated by the in-phase overlap of both lobes of the p-orbitals. A second π bond can be generated by the in-phase overlap of a secondary p orbital perpendicular to the first. A triple bond in an organic compound therefore contains one σ and two π molecular orbitals with an electron configuration of $\sigma^2\pi^4$.

Transition metals have access to higher bond orders as the d-orbitals (Figure 1.3) are involved in the metal-metal bonding. When two metals come together, bonds can be formed from the corresponding orbitals overlapping.

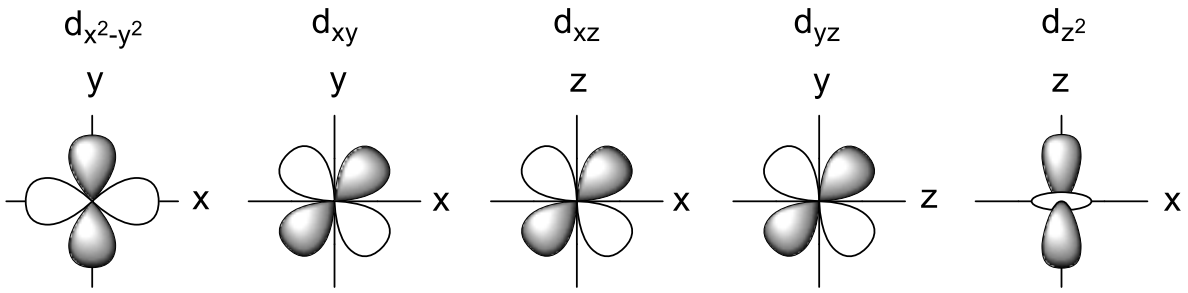

Figure 1.3: The five d orbitals.

A quadruple bond is formed between two d^4 metal fragments of similar energy. Figure 1.4 shows the molecular orbital diagram of a quadruple bond; each metal fragment is of D_{4h} symmetry and the atomic orbitals are those of a square planar complex. As the two complexes come together the σ bond is formed as a result of the direct overlap of the d_{z^2} along the z axis. As there is a high degree of orbital overlap, this will form the strongest component. The two π components are formed due to the overlap of the d_{xz} and d_{yz} orbitals. Finally the δ component is formed due to the face-on overlap of the d_{xy}, as the overlap is poor the δ components is typically the weakest of the four bonds, it is predicted to only contribute 10 % of the overall bond strength.[1] The $d_{x^2-y^2}$ orbital is typically too high in energy to be involved in metal-metal bonding and are primarily involved in metal-ligand bonding, although the

energy of the orbital can be decreased by removing ligands and careful ligand choice so that a quintuple bond can be synthesised.[9]

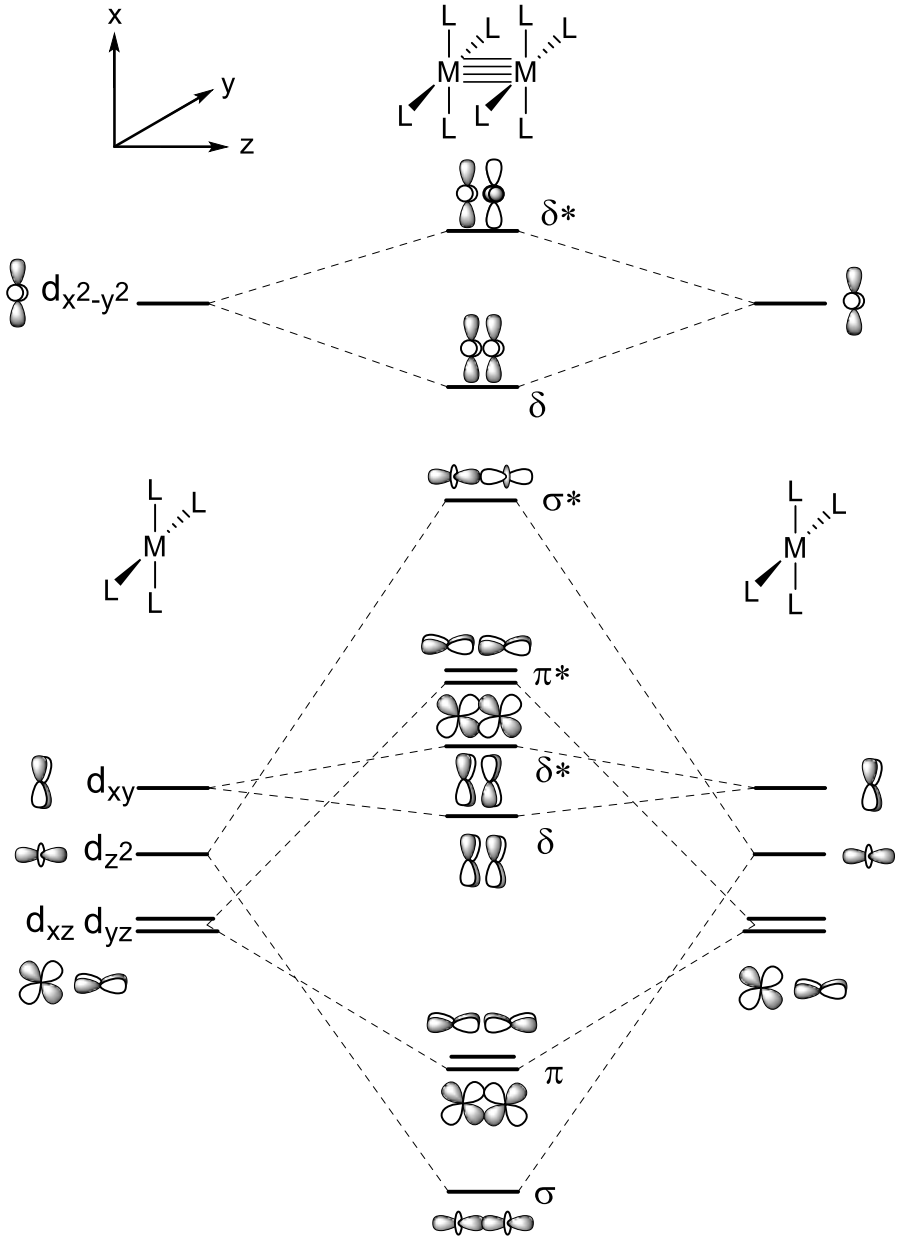

Figure 1.4: The Molecular orbital diagram for a quadruply bonded complex.

The quadruple bond has two main characteristics, firstly a short MM bond length, and secondly an eclipsed ligand conformation. Taking $[Re_2Cl_8]^{2-}$ as an example, the ligands are in an eclipsed

conformation and the bond length is 2.27 Å, which is shorter than the Re-Re bond length in its metallic form which is 2.75 Å.[1]

The propensity for the eclipsed conformation to be taken by quadruple bonds can be inferred qualitatively from the molecular orbital diagram. The quadruple bond can exist as two extremes, eclipsed or staggered, the eclipsed conformation would result in the maximum orbital overlap of the d orbitals, while the staggered conformation would lead to the minimum orbital overlap. Therefore, any rotation away from being eclipsed would result in a decrease in the δ bond energy. The additional stabilisation provided by the δ bond overcomes the steric interaction of the ligands, but they can account for rotations of up to 10 °.[1] The quadruply bonded complex $Mo_2Br_2(arphos)_2$ (where arphos = 1-diphenylphosphino-2-dipehnylarsinoethane) has been reported with a rotation of 30 °. This resulted in the δ bond strength halving due to the decreased orbital overlap, resulting in the lengthening of the Mo-Mo bond length by ca. 0.03 Å. Any rotation past 30 ° results in a much greater decrease in δ-bond strength with the δ-bond strength becoming 0 when the torsion angle becomes 45 °.[10] The σ and π molecular orbitals in the quadruple bond remain unaffected by the rotation about the z-axis, as there is no net loss in the orbital overlap.

1.2 Paddlewheel complexes as redox centres

Quadruple bonds have been observed for Cr (II), W (II), Re (III), Tc(III) and Mo (II).[1] The majority of known quadruple bonds being homobimetalic, although heterobimetallic quadruple bonds are known, for instance Mo-W.[11] These complexes generally take the paddlewheel architecture as seen in Figure 1.5. Variation of the metal core or the bridging and axial ligands makes these complexes highly versatile and tuneable redox centres with unique spectroscopic properties. Although typically the bridging ligands (E_2CR) are π-donors, the R group can be varied resulting in a great deal of structural diversity.

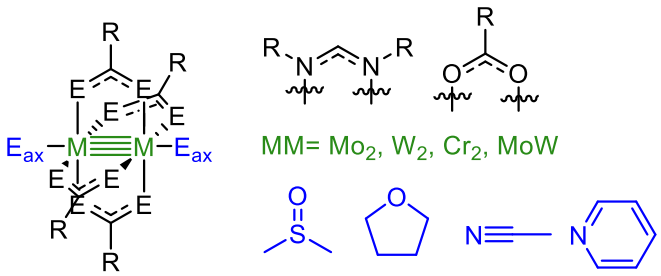

Figure 1.5: Examples of the versatility as a result of structural modifications of paddlewheel complexes.

The versatility of these paddlewheel complexes is complimented by their well-defined geometry, the structurally rigid motif can be used in synthesising larger systems with repeating paddlewheel units, such as dimers,[12] squares,[13] triangles[14] and metal organic frameworks.[15] Dimolybdenum paddlewheel complexes also have redox active cores, with the electron configuration of $\sigma^2\pi^4\delta^2$ which becomes $\sigma^2\pi^4\delta^1$ upon oxidation. The oxidative processes of dimolybdenum paddlewheels are often reversible and can produce stable products following a one electron oxidation.[1] The reversibility of the redox processes in electrochemical techniques coupled with the high tunability of the electronics of the quadruple bond, make these complexes prime redox centres for studying electron transfer which will be discussed hereafter.

1.3 Mixed Valency

Electron transfer (ET) and the important role it plays in chemistry and biology cannot be overstated. ET is a fundamental aspect required for life, for instance photosystem II employs an active site with mixed valent states to catalyse the light driven oxidation of water to evolve oxygen.[16,17] Photosystem II employs the use of Mn_4CaO_5 cluster to evolve oxygen, it is believed that the Mn ions go through five valence states during this process but for much of the process the valence state of the Mn in the Mn_4CaO_5 cluster remains unknown.[18] Understanding ET process at a fundamental level could allow for the production of biomimetrics,[19–24] molecular electronics[25–27] and electrochromic devices.[28] To study ET in complicated systems such as photosystem II, smaller simpler mixed valence compounds (MV) are used as models. In its simplest form, a MV compound can be described as having two or more identical redox centres that are in different oxidation states. Depending on the species ET can occur between these active sites in a self-exchange reaction. The redox centres are generally bonded by π conjugated systems which are referred to as bridges, these systems can then be simplified and represented as an electron donor-bridge-acceptor as shown in Figure 1.6.

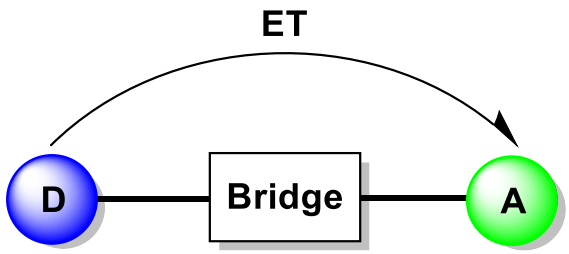

Figure 1.6: Schematic of a general mixed valence compound. D is an Electron donor and A is an Electron acceptor.

MV compounds can be used experimentally to calculate aspects of ET that would otherwise be extremely difficult to calculate, such as, energy barriers and rate constants which would otherwise be hard to elucidate for complex systems.[29,30] As simple MV compounds can be used to model larger systems, research into MV compounds is now common place in literature.[31] These small, readily synthesised, models for probing ET allow for large variations in bridging ligands, steric effects and

electronic effects which have all been shown to effect ET, allowing for us to understand the processes involved at a fundamental level.

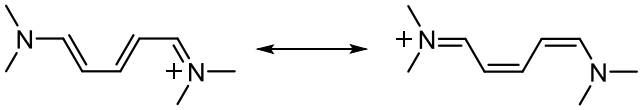

Figure 1.7: The resonance structures of the pentamethinium ion.

Resonance is a well-documented phenomenon in chemistry. Compounds that are stabilised by resonance structures have markedly different properties expected from compounds that show no stabilisation. Take the pentamethinium ion for example, This species requires multiple structures to describe its ground state, two of which are shown in Figure 1.7. If this compound only existed as a statistical mixture of both structures with no resonance occurring, it would be assumed to be colourless like 1,3,5-hexatriene.[32] Due to the resonance the nitrogen atoms assume two equivalent valences, which results in the deep green colour. Resonance is a well understood phenomenon for organic compounds but for complexes this phenomenon is less well understood and observed the notable exception is MV complexes. This leads to an interesting observation if resonance structures have such a pronounced effect on organic molecules, it can be expected that unusual properties will be observed in inorganic MV complexes.

Inorganic MV complexes have existed since at least the 18th century, with arguably the first MV complex being Prussian blue, a complex containing iron in two different oxidation states. Prussian blue is of note because it was the first stable and lightfast blue pigment to be synthesised. The complex has a formula of $Fe_4[Fe(CN)_6]_3 \cdot xH_2O$ (x = 14-16), four of iron atoms are Fe^{III} and the remaining three are Fe^{II}. The complex assumes a cubic structure with alternating Fe(II) and Fe(III) ions in the solid state. The deep blue colour is a result of the ET from the Fe^{II} to Fe^{III} as a result of absorbing orange to red light in the range of 680 nm.[33]

In 1967 Alan and Hush prepared multiple examples of MV systems and showed that in every case the absorption spectra were a mixture of the fully reduced and fully oxidised species, with a new transition in the visible to the IR region. This new transition was termed the intervalence charge transfer band (IVCT).[34] The following year Hush proposed a model for understanding inner-sphere electron transfer by building on Marcus theory.[35]

1.3.1 *Robin- Day classification*

Robin and Day published a method of classification of MV species in 1968.[32] The method reported three distinct classes of MV species, by relating the degree of electron delocalisation to the similarity of the crystallographic sites and the spectroscopic properties. A plot of the potential energy surfaces (PES) against the reaction coordinate can be used to explain the differences between the classes. The two-state model will be employed to describe the differences in the Robin-Day classification.

1.3.1.1 Class I: Valence trapped

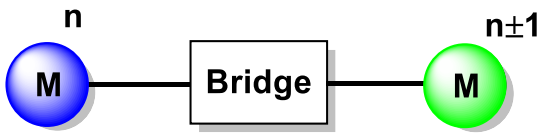

Figure 1.8: M-B-M model for class I MV compounds.

Robin-Day class I compounds have little to no communication between the redox centres and upon oxidation/reduction the charge becomes isolated on a single redox centre and is referred to as valence trapped (Figure 1.8). Due to the redox centres occupying different oxidation states they consequently occupy inequivalent ligand fields and can be distinguished crystallographically through changes in the associated bond lengths and angles.

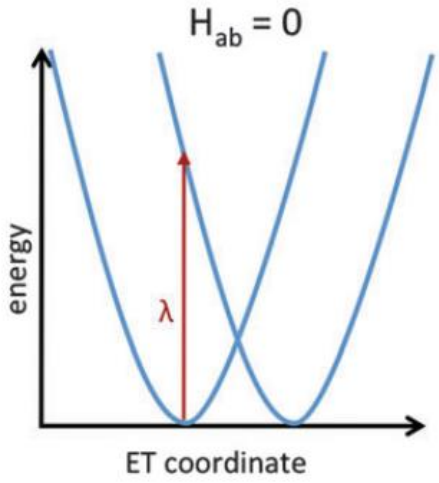

Figure 1.9: The potential energy diagram for a Robin-Day class I system. The left PES can be attributed to M+-B-M and the right PES can be attributed to M-B-M+. The PES are described as diabatic. Figures adapted from reference with permission of the RSC.[36,37]

The potential energy diagram of the reactants M^{+}-B-M and M-B-M^{+} has two diabatic PES, as they are non-interacting there can be no interconversion between the two redox centres (Figure 1.9). As a result, both the electrochemical and spectroscopic properties are those of the constituent redox centres. An example of a class I compound would be lead tetroxide (2 PbO · PbO_2) as it contains a mixture of both Pb^{II} and Pb^{IV}.[38]

1.3.1.2 Class II: Moderately coupled

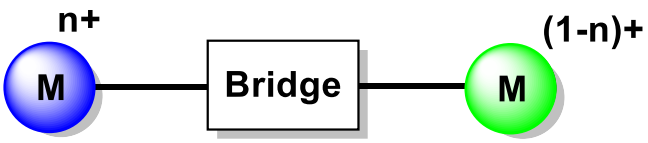

Figure 1.10: M-B-M model for class II MV compounds.

Class II compounds have weakly coupled redox centres such that there is partial delocalisation of the electron. As a result of the weak coupling there is an energy barrier to ET which results in the electron localisation being greater on one redox centre as shown in Figure 1.10 (where 0.5 < n < 1). The two

redox centres are crystallographically similar but potentially distinguishable due to minor changes in bond lengths and angles.

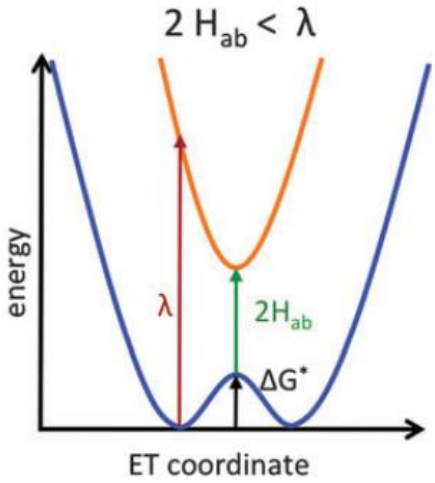

Figure 1.11: The potential energy diagram for a Robin-Day class II system. The solid blue lines represent the adiabatic energy levels, λ is the reorganisational energy and H_{ab} is the electronic coupling matrix. Figures adapted from reference with permission of the RSC.[36,37]

The potential energy diagram for class II compounds is a double-well minima potential energy diagram (Figure 1.11). The ET coordinates correspond to the reactants M^+-B-M and M-B-M^+. Unlike class I compounds we now see mixing of the wavefunctions which results in two adiabatic PES. The two minima on the ground state PES represents where the electron can reside in the compound. The energy barrier to ET can be overcome by thermal excitation (ΔG^*) in the ground state (following the PES of the ground state). Immediate thermal ET is forbidden as the Frank-Cordon principle states that nuclear motion (10^{-13} s) is orders of magnitude slower than electron transfer (10^{-15} s).[39] For the electron to thermally transfer there has to be both inner-sphere (λ_i) and outer sphere (λ_o) reorganisation which gives rise to the energy barrier to ET.[35] The second PES is a optically accessible excited state between which interconversion between the reactants can occur through photoexcitation. The energy difference between the ground state and excited state at the minima of the excited state is twice the electronic coupling parameter (H_{ab}) which is a direct measure of donor and acceptor wavefunction overlap. For class II compounds the sum of the reorganisation energies is greater than $2H_{ab}$. Optical

excitation results in a broad, low intensity Gaussian shaped transition in the near infrared (NIR), termed an intervalence charge transfer band (IVCT). As a result of the net dipole induced in class II compounds, IVCT transitions shows solvent dependence and are solvatochromic in nature.[40]

1.3.1.3 Class III: Fully delocalised

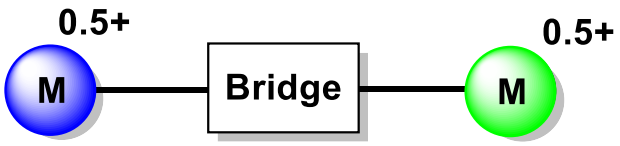

Figure 1.12: M-B-M model for class III MV compounds.

Class III compounds have strong electronic coupling between the two redox centres, which results in the electron being equally delocalised across both redox centres (Figure 1.12). As the electron is now fully delocalised, the redox centres are symmetric and are indistinguishable crystallographically. This delocalisation gives rise to adiabatic PES surfaces that have a merged single-well ground state and an optically accessible excited state (Figure 1.13). As the two sites are crystallographically identical there is no energy barrier to thermal ET ($\Delta G^{*} = 0$).

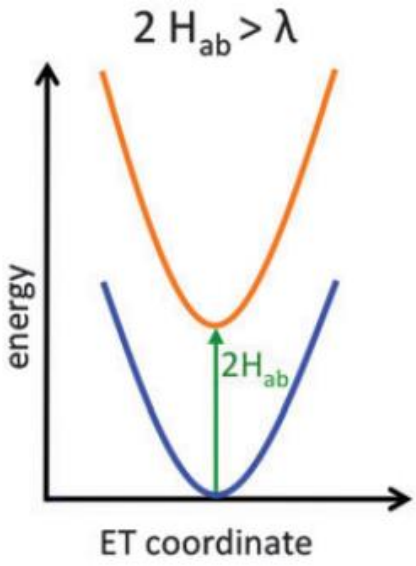

Figure 1.13: The potential energy diagram for a Robin-Day class III system. the solid blue line represents the adiabatic PES for $M^{0.5+}$-B - $M^{0.5+}$. λ is the reorganisation energy and H is the electronic coupling matrix. Figures adapted from reference with permission of the RSC. [36,37]

The transition from the ground to excited state PES can be observed in the NIR, the transition is now an intense band that often shows low energy cut off. This transition is referred to as a charge resonance band as opposed to an IVCT transition. As class III compounds have no net dipole, the charge resonance band shows no solvent dependence. Krejcik *et al.* reported the complex t*rans*, *mer*-$[(PPr^i_3)_2(CO)_3Mo(\mu\text{-}pz)Mo(CO)_3(PPr^i_3)_2]^+$ (pz = pyrazine) which was determined to be delocalised (class III) by using EPR spectroscopy and vibrational absorption spectroscopy.[41]

1.3.1.4 Beyond the Robin-Day classification

As more examples of MV compounds were reported, exceptions to the Robin-Day classification began to arise. In 1969 the first deliberately designed MV complex was synthesised by Creutz during her PhD under the guidance of Taube. This model complex uses two $Ru(NH_3)_5$ fragments as the redox centres and a pyrazine as the bridging ligand as shown in Figure 1.14. The complex has a formal charge of 5+ with one Ru^{II} and one Ru^{III}. The Creutz-Taube ion has become the most studied MV compound within

the field due to the difficulty in assigning a class using the Robin-Day method.[42,43] Numerous physical and computational techniques have been employed in an attempt to categorise the MV complex.[37]

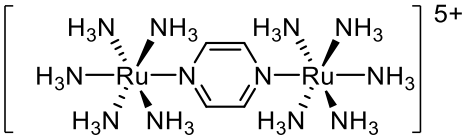

Figure 1.14:The Creutz-Taube ion.

The Creutz-Taube ion has now been classed as Class II-III borderline, a class II-III borderline compound has electronic localisation as discussed above but solvent delocalisation meaning there is no outer sphere energy of reorganisation, the Creutz-Taube ion was the first compound to be assigned as this class but many more complexes followed.[31] The analysis of the Creutz-Taube ion will be discussed in section 1.4.

Lear and Chisholm while exploring oxalate bridged complexes $[(^{t}BuCO_2)_3MM]_2(\mu_2\text{-}O_2CCO_2)$ (where MM = Mo_2, MoW, and W_2) proposed a new class of MV compound a subsection of class III called class IV.[44] They stated that if a class III compound showed no solvent dependence of both the charge resonance band and the metal to ligand charge transition (MLCT), and did not exhibit any vibronic progression that they were class IV.

1.3.2 *Techniques for studying mixed valency*

Robin and Day based their classes by looking at both the spectroscopic properties and the molecular structure and, as such, several techniques can be used to study mixed valency. One of the original and most important methods was X-ray crystallography. X-ray crystallography can easily distinguish between class I and class III by comparing the bond lengths and angles between the two redox centres. Although, this technique has limitations, class II compounds can be very difficult to assign by crystallography alone and it also requires single crystals which are potentially very difficult to grow or isolate as well as the long time frame required to acquire the structures. Robin and Day also based

their classification on electronic absorption spectroscopy in the UV-Vis-NIR region where analysis of the shape and intensity of the IVCT transition can be used to determine both the classification and strength of electronic coupling (H_{ab}). Several other techniques have been used to probe ET such as, X-ray photoelectron spectroscopy, Mössbauer spectroscopy, Raman spectroscopy and Stark effect spectroscopy.[30,45–47] This section will focus on the techniques employed in this thesis; electronic absorption spectroscopy, IR spectroscopy, electronic paramagnetic spectroscopy and voltammetry.

1.3.2.1 Electronic absorption spectroscopy

Electronic absorption spectroscopy is a well understood and powerful technique for characterising MV compounds. Each of the three classes has a distinct action in the UV to NIR region of the absorption spectra. Typically, Class I systems display the transitions associated with their constituent ions with no new transitions as the H_{ab} is 0 and there are no adiabatic PES.[32] Class II spectra differ as they include an intervalence charge transfer (IVCT) band in the NIR region. As previously discussed for class II systems the IVCT band is approximately equal in energy to the reorganisational energy (λ) between the ground state and excited state. The electronic coupling parameter (H_{ab}) can be calculated from the IVCT transition using Hush theory, as shown in Equation 1.1**,** where ν_{max} (cm^{-1}) is the is the absorption energy, ε_{max} ($M^{-1}\ cm^{-1}$) is the extinction coefficient, $\Delta\nu_{1/2}$ (cm^{-1}) is the peak width at half height and r_{ab} (Å) is electron transfer distance**.**[32,35] IVCT bands are typically weak ($\varepsilon_{max} \leq 1000\ M^{-1}\ cm^{-1}$) and Gaussian in shape. The transition is also solvent dependent.[40]

$$H_{ab} = \frac{0.026 \text{ x } (\upsilon_{max}\, \varepsilon_{max}\, \Delta\upsilon_{1/2})^{1/2}}{r_{ab}}$$

Equation 1.1: Equation for calculating H_{ab} for a class II compound.

As the electronic coupling parameter increases, the reorganisational energy tends towards zero. When the two redox centres are strongly coupled (class III) $2H_{ab}$ is equal to that of the transition such that the electronic coupling parameter can be calculated using Equation 1.2.

$$H_{ab} = \frac{1}{2}v_{max}$$

Equation 1.2: Equation for calculating H_{ab} for a class III compound.

Where v_{max} (cm^{-1}) is the peak maximum of the charge resonance band. The charge resonance band typically observed in the NIR is expected to be more intense (ε_{max} ≥1000 M^{-1} cm^{-1}) with a sharper profile ($\Delta v_{1/2} \leq 2000$ cm^{-1}) and no solvent dependance.[40]

$$\Delta v_{1/2}° = (2310 \times v_{max})^{\frac{1}{2}}$$

Equation 1.3: Calculation of theoretical band width at half height.

The shapes of the IVCT and charge resonance bands can be used to determine the class of the compound. With class II transitions being Gaussian, broad and have a low intensity and class III transitions being considerably sharper and often displaying low energy cut off. Using Equation 1.3 the theoretical band width at half height ($\Delta v_{1/2}°$) for the ET transition can be calculated.

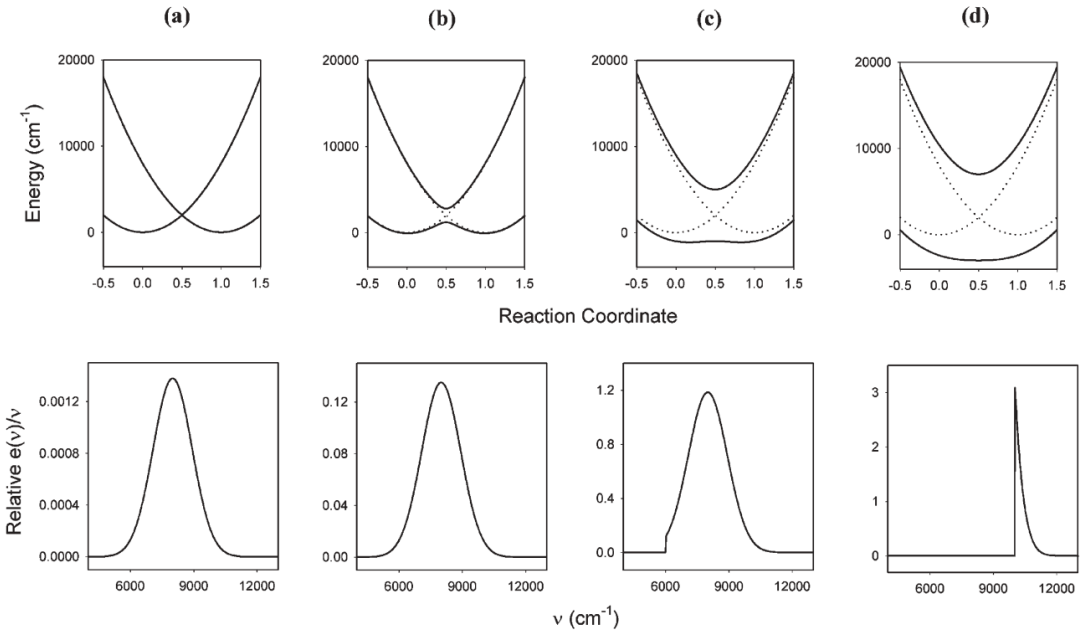

Figure 1.15: Potential energy surfaces and band predications. Top: energy Vs. Reaction coordinate bottom: ε/ν vs. ν. The values of H_{ab} are a: 80 cm^{-1} b: 800 cm^{-1} c: 3000 cm^{-1} and d: 5000 cm^{-1}. *Figure reproduced from reference with permission from the RSC.*

The calculated band shapes for symmetrical di-nuclear compounds as the H_{ab} increases are shown in Figure 1.15, with the assumption that there is a Boltzmann distribution over the energy levels of the ground state.[40] Going from A to D in Figure 1.15 shows a steady increase in H_{ab}. The IVCT transition in A is Gaussian in nature, as the H_{ab} increases the band begins to exhibit an increasing degree of low energy cut off until only the high energy side of the transition remains. It should be noted that low energy cut off is temperature dependent and that the band exhibiting low energy cut off will once again become Gaussian at lower temperatures .[31,45] As the coupling increases so does the intensity and energy of the transition.

1.3.2.2 Infrared Spectroscopy

The time scale for IR spectroscopy is relatively fast at ~10^{-11} s, and can be used to determine the electron transfer rate (k_{et}) if it has a similar value.[47,48] If an IR handle such as a carbonyl, nitrile or alkyne are present, when there is no coupling the MV species will be a combination of the neutral and doubly oxidised species. However, for Class II systems, the associated peaks in the IR begin to coalesce

due to the partial charge on each redox centre. Using a method developed by Kubiak and Ito the rate of ET can be estimated if it is between 10^{10}-10^{13} s^{-1}, which they termed IR spectroelectrochemistry coalescence (IRSEC).[49] Kubiak employed oxo centred triruthenium clusters with a carbonyl IR handle bridged by a pyrazine ligand (Figure 1.16 A). The *v*(CO) is strongly dependent on the oxidation state of the metal, and is therefore a good IR handle as its sensitive to charge distribution.[49,50] The *v*(CO) of the neutral and doubly reduced species shows a shift in wavenumber, due the change in oxidation state of both redox centres. Interestingly, the MV compound that is generated following a one electron reduction, shows coalescence of the $[Ru_3O]^0$ and $[Ru_3O]^{1-}$ *v*(CO), this single peak is a hybrid of both the neutral and doubly oxidised species. The coalescence of the peaks indicate that ET occurs on faster time scale than IR spectroscopy at room temperature and can be used to calculate the ET rate constant in the MV state.[49]

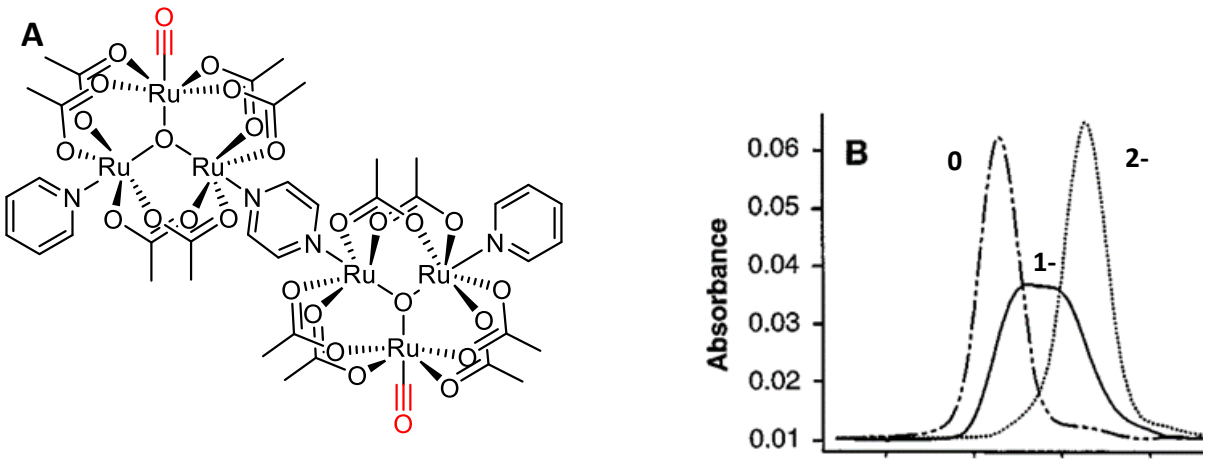

Figure 1.16: (A) The structure of Kubiaks Tri-oxoruthenium cluster bridged by a pyrazine ligand the carbonyl IR handle is highlighted in red. (B) The IR spectra focusing on the CO stretch of the neutral, reduced (1-) and doubly reduced (2-). Reproduced From reference Reprinted with permission from AAAS.[49]

1.3.2.3 Electron paramagnetic resonance spectroscopy

Electron paramagnetic resonance (EPR) spectroscopy also known as electron spin resonance (ESR) spectroscopy is a technique used to study unpaired electrons in molecules. The technique works in a similar fashion to nuclear magnetic resonance (NMR) spectroscopy, but instead of measuring nuclear

transitions EPR measures the transitions of unpaired electrons. By placing the compound in an applied magnetic field, the electron(s) align themselves to be either parallel (-1/2) or anti-parallel (+1/2). These two orientations have their own energy levels and excitation from the lower energy level to the higher energy level can be achieved using microwave radiation (1 – 100 GHz) (ΔE), as the magnetic field increases so does the splitting between the parallel and antiparallel energy levels (Figure 1.17).

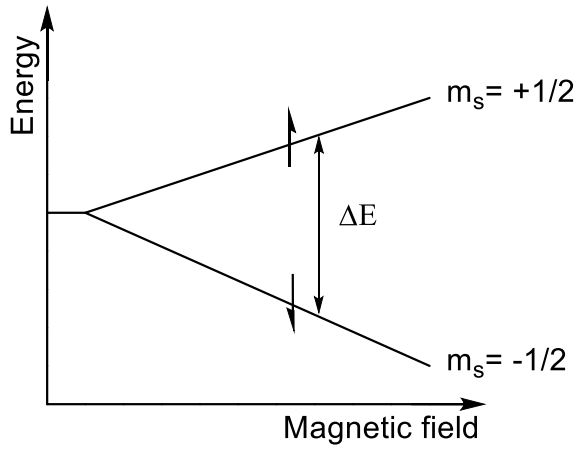

Figure 1.17: The influence of the applied magnetic field strength on ΔE.

The strength of the magnetic field can also be altered by the surrounding nuclei of the compound, this results in a change in g-factor and therefore a change in ΔE. The surrounding nuclei can also split the observed signals, these are referred to as hyperfine splitting. The hyperfine splitting can be calculated using the 2NI+1 rule, often employed in NMR spectroscopy. N is the number of equivalent nuclei, and I is the nuclear spin. The magnitude of the isotropic hyperfine splitting can be used to determine localisation of the electron.[51] Variable temperature EPR has been employed to determine ET barriers in organic MV systems, although this has proven to be more difficult for transition metal complexes due to the difficulties in calculating the hyperfine constants.[52,53]

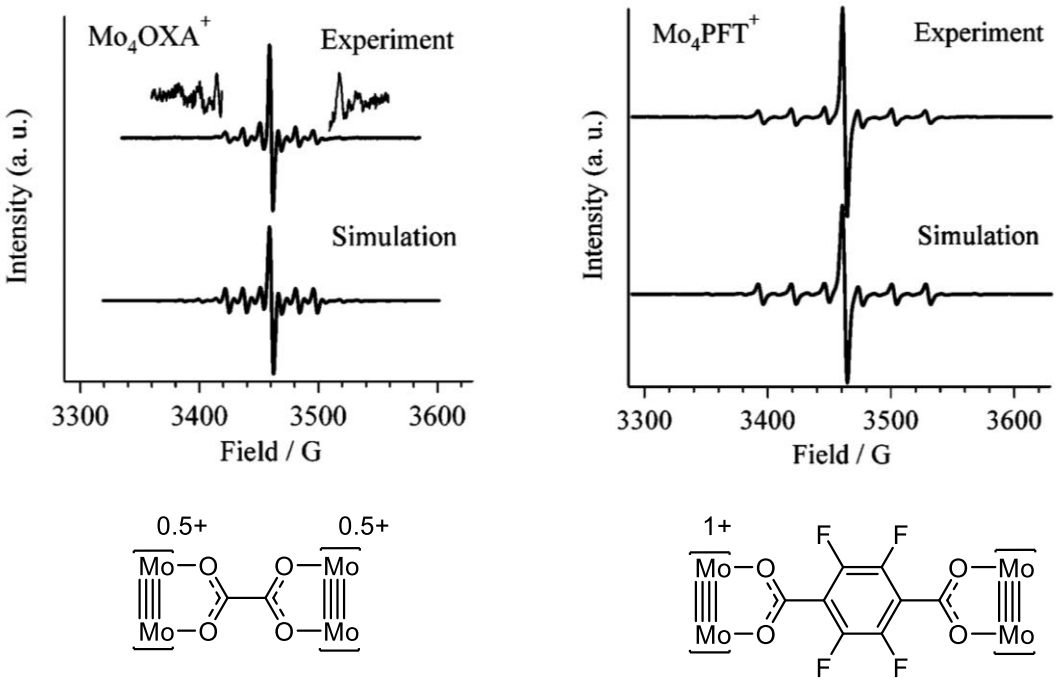

Figure 1.18: Top: X -band EPR spectra and simulations of $[Mo_2(Piv)_3]_2(\mu_2\text{-oxalate})^+$ and $[Mo_2(Piv)_3]_2(\mu_2\text{-PFT})^+$ in 2:1 THF/CH_2Cl_2 at 210 K, the bridges are shown below (left); oxalate (right); perfluoroterephthalate. Figure Reproduced by permission of The Royal Society of Chemistry.[54]

Molybdenum has two spin active isotopes of I = 5/2 (^{95}Mo and ^{97}Mo) with a combined natural abundance of 25 %, the remaining 75 % of isotopes are I = 0. Therefore, the spectra of a molybdenum species would show a single symmetric peak (I = 0) and a sextet of lower intensity peaks (I = 5/2). For a dimolybdenum paddlewheel complex of formula $[Mo_2(O_2CR)_4]^+$ the peaks are centred at a g-factor of around ~1.93 as the unpaired electron is predominantly in the Mo_2-δ orbital.[55] The magnitude of the hyperfine coupling for a dimolybdenum paddlewheel is around 2.8 mT as the electron is delocalised over two molybdenum atoms.[56] For a strongly coupled bridged species of formula $[Mo_4(O_2CR)_6(\mu_2\text{-bridge})]^+$ a similarly shaped spectra is expected, but the magnitude of the hyperfine coupling constant halves and is now around 1.4 mT, reflecting the delocalisation of the odd electron over four molybdenum atoms.[56] This is demonstrated in Figure 1.18, where $[Mo_2(Piv)_3]_2(\mu_2\text{-oxalate})^+$ (left) is class III and shows a hyperfine coupling of 1.48 mT as the electron is delocalised across both

Mo_2 centres. Whereas, when the bridge is changed to perfluoroterephthalate (right) the hyperfine coupling is 2.72 mT indicating the electron is localised on one Mo_2 centre.[54] As a result EPR spectroscopy is a powerful tool in determining the electron delocalisation within a complex.

1.3.2.4 Electrochemistry

Electrochemical techniques can be used to generate the MV compound following a one electron oxidation/reduction. Typically, cyclic voltammetry (CV) and differential pulse voltammetry (DPV) are used to study the redox behaviour of the analyte by measuring the current response as the potential is swept cyclically between two potentials. In an ideal situation these redox events should be symmetrical and fully reversible.[57] These techniques are very useful in screening potential MV compounds.[58]

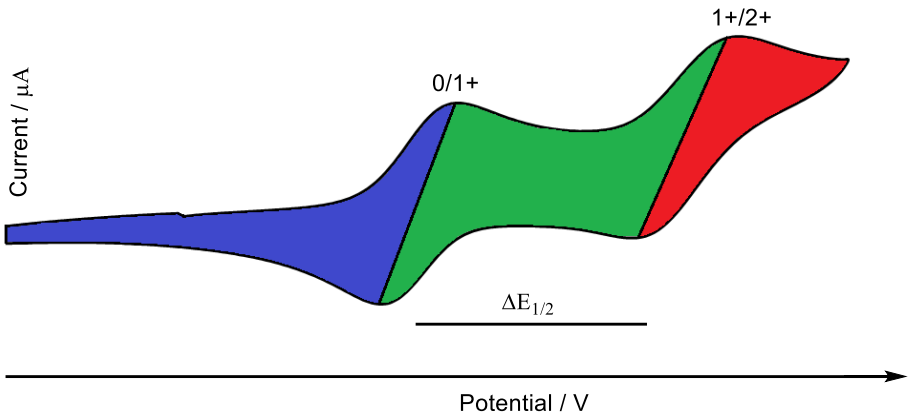

Figure 1.19: An Idealised cyclic voltammogram of a class II or above mixed valence compound, with two reversible redox events separated by $\Delta E_{1/2}$.

For a complex of formula [M-B-M] the voltammogram will be dependent upon the electronic communication between the two redox centres. In the absence of electronic coupling the oxidation of both redox centres will happen at the same potential and will be indistinguishable from each other (Class I), resulting in a single two electron redox process. If there is coupling (class II and class III), then two one electron redox processes will be observed, as when the first redox centre is oxidised there is

a change in charge density which is communicated across the bridge making the second redox centre more difficult to oxidise (Figure 1.19).[59,60] The potential of each redox event is termed the half wave potential ($E_{1/2}$), and the difference between the two redox events is the $\Delta E_{1/2}$. The magnitude of $\Delta E_{1/2}$ is proportional to the thermodynamic stability of the MV state [M^+-B-M] in comparison to the doubly oxidised species [M^+-B-M^+] and the neutral species [M-B-M]. This can be expressed as the comproportionation constant (K_c) as shown in Equation 1.4.1 and Equation 1.4.2.

$$[Mo_2^{4+} - Mo_2^{4+}] + [Mo_2^{5+} - Mo_2^{5+}] \rightleftharpoons^{K_c} 2[Mo_2^{4+} - Mo_2^{5+}] \quad (1)$$

$$K_c = exp^{(\frac{\Delta E_{1/2} F n_1 n_2}{RT})} = exp^{(\frac{\Delta E_{1/2}}{25.69})} \quad (2)$$

$$\Delta G_c = -RTlnK_c \quad (3)$$

$$\Delta G_c = \Delta G_s + \Delta G_e + \Delta G_i + \Delta G_r \quad (4)$$

Equation 1.4: Equations to calculate the thermodynamic stability of the MV state.

The K_c can be calculated electrochemically from the $\Delta E_{1/2}$ as shown in Equation 1.4.2 where $\Delta E_{1/2}$ is the difference between the two redox processes (mV), F is the Faraday constant, R is the gas constant, T is the absolute temperature (K) and n_1n_2 are the number of electrons involved in each redox event. This can be simplified if the number of electrons involved in each redox process is 1 and the temperature is 298 K.[40,61] The K_c can be used to determine the free energy of comproportionation (ΔG_c) which is a direct measure of the thermodynamic stability of the MV complex using Equation 1.4.3.[58] The thermodynamic stability of the mixed valence state is the culmination of several different factors as shown in Equation 1.4.4.[62,63] Four terms contribute to the magnitude of ΔG_c, the electrostatic effect (ΔG_e) which reflects the repulsion between the charged redox centres, the electronic resonance effect (ΔG_r) which accounts for the energy change of the resonance exchange, the statistical contribution (ΔG_s) which is the statistical distribution of the comproportionation

equilibrium and an inductive factor which deals with the stabilisation of the MV state by electron polarisation by means such as back bonding (ΔG_i).[58,64] Two more terms have been proposed, the magnetic stabilisation of the doubly oxidised species (ΔG_{st}) and the ion pairing effects (ΔG_{ip}) which takes into account the medium and electrolyte.[62,65] The value of K_c and ΔG_c have often been used to assess the magnitude of electronic coupling in MV complexes, however, as K_c and ΔG_c are a measure of the thermodynamic stability of the MV state they cannot be used determine the Robin-Day class.[34,36,56,59,66,67]

1.4 Mixed Valency through covalent bridges

1.4.1 *Mononuclear redox centres*

The Creutz-Taube ion, $[(NH_3)_5Ru\text{-}py\text{-}Ru(NH_3)_5]^{5+}$ was the first deliberately designed MV compound, which has been studied more than any other MV compound (Figure 1.14). There has been considerable controversy in assigning the Creutz-Taube ion and some of the contradictory studies are discussed below. The MV spectra of $[(NH_3)_5Ru\text{-}py\text{-}Ru(NH_3)_5]^{5+}$in D_2O have a narrow and solvent independent absorption band at 6410 cm^{-1}.[42] A number of further techniques also suggested electron delocalisation, the EPR data showed delocalisation of the electron along the $[Ru^{2.5+}\text{-}py\text{-}Ru^{2.5+}]$ axis.[68] IR spectroscopy showed that the vibrations of the MV compound are an average of those from $[Ru^{II}\text{-}py\text{-}Ru^{II}]$ and $[Ru^{III}\text{-}py\text{-}Ru^{III}]$ once again indicating the electron is delocalised.[69] Density functional theory (DFT) has also suggested that the complex is class III.[70] But, the crystal structure of [Ru-py-Ru] 5OTs showed the two Ru centres have differences in their coordination geometries, which could only happen if there was a degree of localisation of the electron.[71] The difficulty in assigning the complex was because it doesn't conform to the conventional Robin-Day classification being a class II/III borderline complex, where the electron is localised but the solvent is delocalised.[31]

ET is a diverse and difficult field with numerous unanswered questions, and this is exemplified by the difficulty in assigning a Robin-Day class to the Creutz-Taube ion. The effect of changing the redox centre, the ancillary ligands, the bridge and solvent have been some of the many avenues of research

being explored. As the Creutz-Taube ion serves as a template, the complexes that followed often retained the general structure while one aspect was varied. For instance the osmium analogue of the Creutz-Taube Ion $[(NH_3)_5Os\text{-}pz\text{-}Os(NH_3)_5]]^{5+}$ has a comproportionation constant that is a factor of 10 greater than the Ru analogue.[72] It has been classified as class III due to absence of the expected spin orbit couplings for Os^{III} in the electronic absorption spectra. The symmetric stretches of the pyrazine ligand in the IR are indicative of a delocalised system and the charge resonance band that is visible upon a one electron oxidation of the complex is very intense and characteristic for a class III compound.

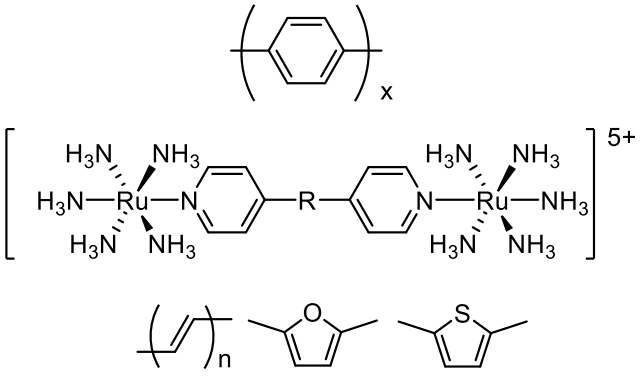

Figure 1.20: Variations of the bridge in the Creutz-Taube ion (where n=1-4 and x=1-2).

Equation 1.1 tells us that as the internuclear separation between the two redox centres (r_{ab}) increases the smaller the electronic coupling constant (H_{ab}). Using a series or related bringing ligands such as polyphenylene or polyene dipyridyls this has been demonstrated and in each case as the value of n increased the coupling decreased (Figure 1.20).[73–75] Furthermore, it was demonstrated that when there was a lack on conjugation in the bridge there was no electronic coupling.[74] When the bridge was dipyridylthiophene and dipyridylfuran a greater degree of coupling was observed compared to the polyene, 4,4'-bipyridine and 1,4-bis(4-pyridyl)benzene.[75] The authors suggested that the increase in electronic coupling when R was a heterocycle was because the linker was more rigid which kept the bridge coplanar increasing the orbital overlap. Although 4,4'-bipyridine and 1,4-bis(4-pyridyl)benzene also form rigid bridges but the dipyridylthiophene and dipyridylfuran linkers were suggested to have

greater coupling as the phenylene is strongly aromatic and for conjugative interactions with the pyridine to occur it would have to lose its aromaticity decreasing the coupling. The dipyridylthiophene and dipyridylfuran linkers are less aromatic and can more readily facilitate electron transfer.

When considering the bridge, it can facilitate electron transfer or prevent it entirely by controlling the distance, orientation as well as the intercomponent electron transfer process. The ET process can occur indirectly through space which is mediated by the bridge, or a through bond mechanism, although, typically a mix of both mechanisms can occur.[40] Superexchange theory provides an approach which takes the bridge into account in the ET process. By considering the overlap of the frontier orbitals between the metals and those of the bridge and their relative energies, two through bond ET mechanisms can be envisaged.[61]

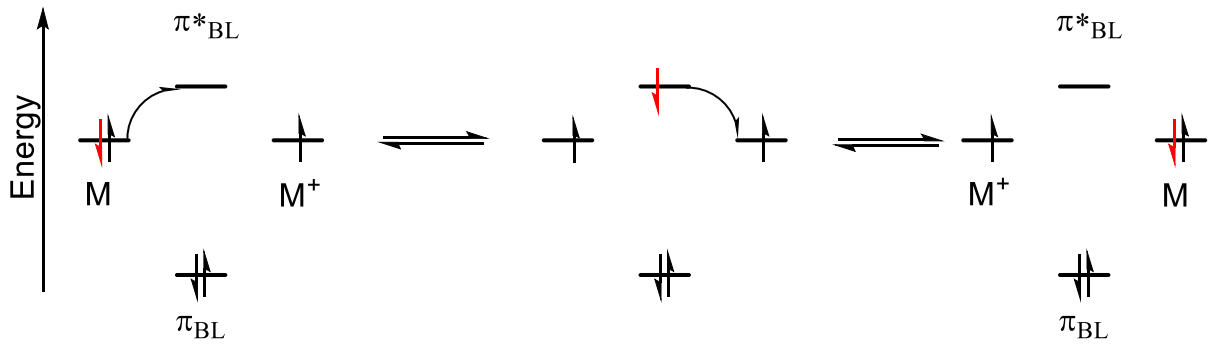

Figure 1.21: A stepwise diagram depicting the electron hopping mechanism.

The first mechanism uses the Highest Occupied Molecular Orbital (HOMO) and the Singly Oxidised Molecular Orbital (SOMO) of the metals and the Lowest Unoccupied Molecular Orbital (LUMO) of the bridge this is termed electron hopping mechanism (Figure 1.21). The electron from HOMO travels through the π* orbital of the ligand and into the SOMO, the ligand π orbital is uninvolved due to the greater difference in energy. ET in the Creutz-Taube Ion proceeds through an electron hopping mechanism.[76]

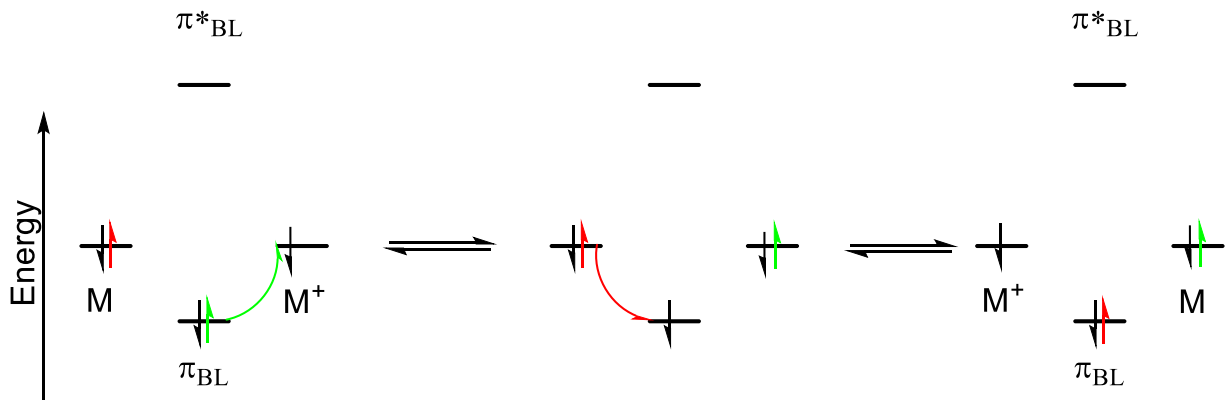

Figure 1.22: A stepwise diagram depicting the hole hopping mechanism.

When the ligand π orbital is closer to the HOMO of the metal then the ET proceeds through a hole hopping mechanism. An electron from the ligand π hops into the SOMO, and an electron from the donor metal then hops into the hole in the ligand-π orbital (Figure 1.22). When the bridge in the Creutz-Taube ion is changed to 1,4-dicyanamidobenzene dianion the ET transfer occurs through a hole hopping mechanism.[62] The ET process typically incorporates both mechanisms although one dominates.

Meyer *et al.* looked at the effect of changing the ancillary ligand in the Creutz-Taube ion, they synthesised the analogous compound $[(bpy)_2ClRu\text{-}pz\text{-}RuCl(bpy)_2]^{3+}$ (bpy = 2,2'-bipyridine).[77] The result of substituting the amines resulted in the coupling decreasing and becoming class II. The IVCT transition was broad and Gaussian in nature and showed solvent dependence consistent with a class II compound. The absorption spectra of the MV compound showed an amalgamation of the monomeric ruthenium complexes $[(bpy)_2ClRu\text{-}pz]^{1+}$ and $[(bpy)_2ClRu\text{-}pz]^{2+}$. The explanation for this decrease in coupling was because the 2,2'-bipyridine ligands competitively back bonded to the ruthenium decreasing the available electron density for delocalisation of the electron across the bridge.

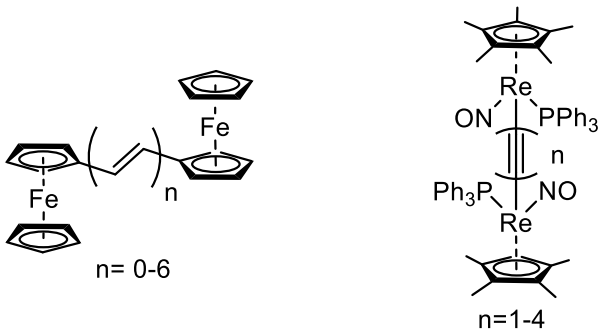

Figure 1.23: Examples of MV complexes containing a monometallic redox centre reported by Gladysz et al. and Meyer et al.

Since the report of the Creutz-Taube ion, many other redox fragments both organic and inorganic that can form MV compounds have been reported. Ruthenium and iron based redox centres are by far the most studied, although others have been reported, examples are shown in Figure 1.23 but a further discussion is outside of the scope of this thesis.[53,78,79]

1.4.2 *Polynuclear redox sites*

The redox fragments in the previous section primarily employed the use of monometallic redox centres, although several compounds that employ redox centres consisting of two or more metals have been reported. Kubiak *et al.* employed oxo-centred triruthenium clusters as seen in Figure 1.16. These clusters consist of a Ru_3O redox centre, with the oxidation state of $Ru^{(III, III, II)}$ in the neutral complex. When two Ru_3O redox centres are linked by an appropriate bridge the MV state can be generated following a one electron reduction to generate M-B-M^{-}. The effect of the ancillary ligands and bridges on the extent of delocalisation have been extensively probed.[66]

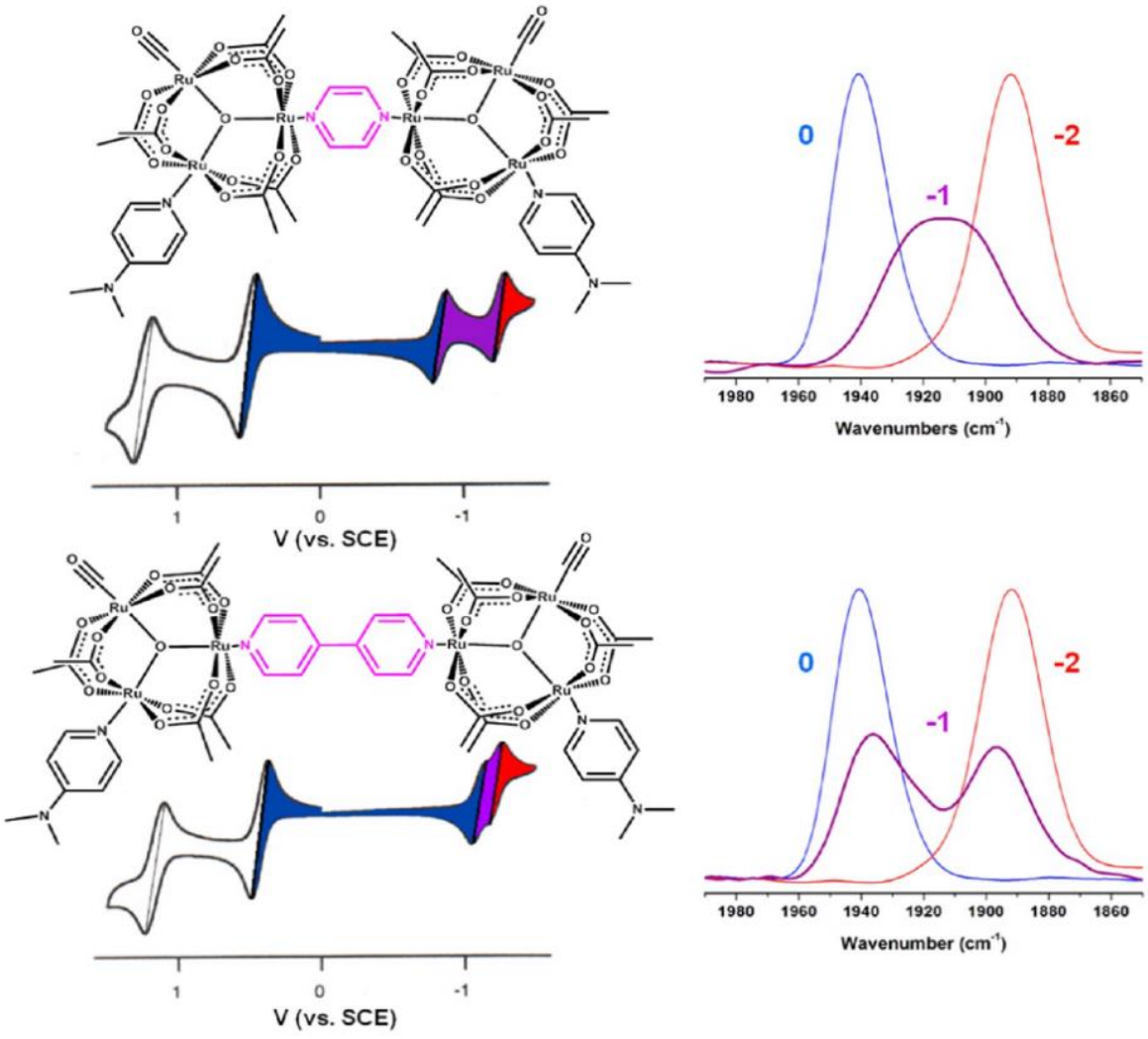

Figure 1.24: $[Ru_3O(OAc)_6(CO)(dmap)]_2$(B) B = pyrazine (top) and 4,4'-bpy (bottom) together with their corresponding CV's (left) and the spectroelectrochemical IR spectra (right). Reprinted with permission from reference. Copyright (2013) American Chemical Society.[66]

By comparing the complexes $[Ru_3O(OAc)_6(CO)(dmap)]_2$(B) where B is pyrazine (pz) or 4,4'-bipyridine (4,4'-bpy) the effect of distance on the MV state was explored (Figure 1.24). When probing these complexes using CV it was found that both complexes exhibited two sequential one electron reductive processes. When the bridging ligand was pyrazine the $\Delta E_{1/2}$ was 435 mV and when the bridge was 4,4'-bipyridine the $\Delta E_{1/2}$ decreased substantially to 120 mV. The decrease in the $\Delta E_{1/2}$ indicates that when the bridge is extended the stability of the MV state drops sharply. When IRSEC is used to compare *v*(CO), for the pyrazine bridged complex coalescence of the *v*(CO) bands is observed indicating a k_{et} *of*

~1.5 x 10^{12} s^{-1}. Whereas, no coalescence of the *v*(CO) band is observed when the bridge is changed to 4-4'-bipyridine indicating electron localisation on the IR timescale.

The rate of ET was found to be heavily influenced by electronic structural effects, which was achieved by varying the ancillary ligand (L) in the complex $[Ru_3O(OAc)_6(CO)(L)]_2(pz)$, where L is changed from 4-dimethylaminopyridine (DMAP) to pyridine (py) to 4-cyanopyridine (cpy) (Figure 1.25). As L was varied for progressively stronger electron donors, the *v*(CO) stretch of the MV compound shows greater coalescence, indicating stronger coupling with an increased rate of ET. The ET occurs through an electron hopping mechanism and by looking at the relative energies of the Ru-dπ and the ligand π* orbitals the change in delocalisation can be rationalised.[80] As L was substituted for stronger donor ligands, the Ru_3-dπ manifold raises in energy, closer to that of the bridging ligand, leading to a greater delocalisation of the electron. This model also accounts for the decrease in delocalisation seen when the bridging ligand is changed from pyrazine to 4,4'-bipyridine as the ligand π* is much higher energy in the 4,4'-bipyridine then compared to the pyrazine.

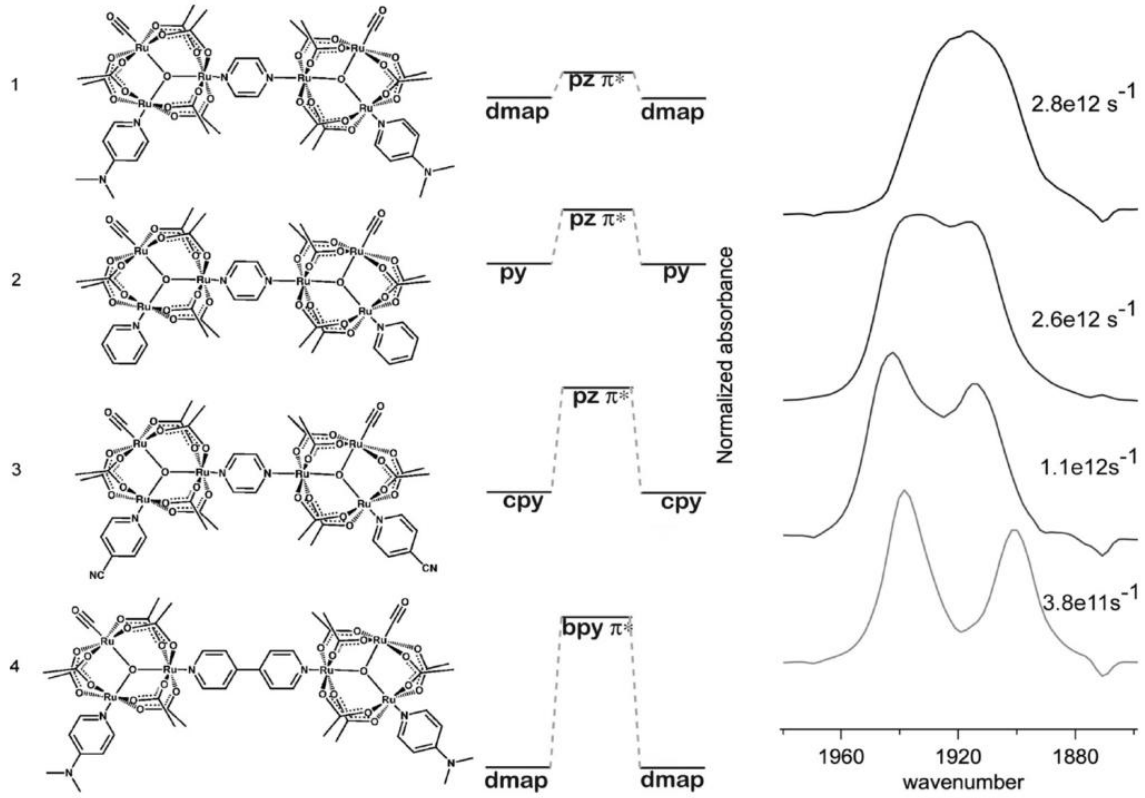

Figure 1.25: Left: $[Ru_3O(OAc)_6(CO)(L)]_2(pz)$ complexes where L = 1. DMAP 2. Py 3. And complex 4. $[Ru_3O(OAc)_6(CO)(DMAP)]_2(bpy)$ Centre: Frontier molecular orbital energies for 1 – 4. Right: The observed ν(CO) bands of the MV complex. Reprinted with permission from reference. Copyright (2013) American Chemical Society.[66]

1.4.3 *Mixed valency in molybdenum and tungsten Paddlewheel complexes*

Dimolybdenum and ditungsten paddlewheel complexes have also been extensively studied in the literature as a result of their tunability and electrochemical reversibility.[56,81] Paddlewheel complexes are well suited for studying mixed valency due to the simplicity of the MV spectra when compared to monometallic redox centres. In MV paddlewheel complexes a single IVCT transition is observed as the Mo_2-δ orbital is higher in energy. Whereas, multiple charge resonance or IVCT transitions can be observed in mono-metallic species as a result of Kramers doublets.[40] Further to this EPR spectroscopy is a powerful tool in examining the degree of delocalisation observed in dimolybdenum paddlewheel complexes. The magnitude of the isotropic hyperfine splitting (A_{iso}) can be used to unambiguously determine whether the electron is localised or delocalised on the EPR timescale (~10^{-9} s).

The use of dimolybdenum paddlewheel complexes as redox centres to study various aspects of mixed valency is the focus of our research group. These complexes exhibit several interesting transitions that are exploitable spectroscopically and informative on the MV state. A plethora of complexes with the formula M_2-B-M_2 have been reported but a small number of these have been selected to exemplify the unique spectroscopic properties.[44,56,81] Complexes that conform to the general formula of M_2-B-M_2 are typically referred to as a "dimer of dimers".

The most common bridge for dimolybdenum paddlewheel complexes are dicarboxylates, the simplest of which is oxalate ($O_2CCO_2^{2-}$). Chisholm *et al.* reported the complex [$(Piv)_3Mo_2$-O_2CCO_2-$Mo_2(Piv)_3$] (where Piv is 2,2-dimethylpropanoate), that, following a one electron oxidation forms a MV complex.[82,83] The electrochemistry indicated a stable mixed valent state with a K_c of 5.4 x 10^4, and the spectroelectrochemistry showed a strongly coupled species (class III) with a H_{ab} of 2000 cm^{-1}. The strong electron coupling is a result of extensive mixing between the M_2-δ orbital and the ligand π* (Figure 1.26 and Figure 1.27).

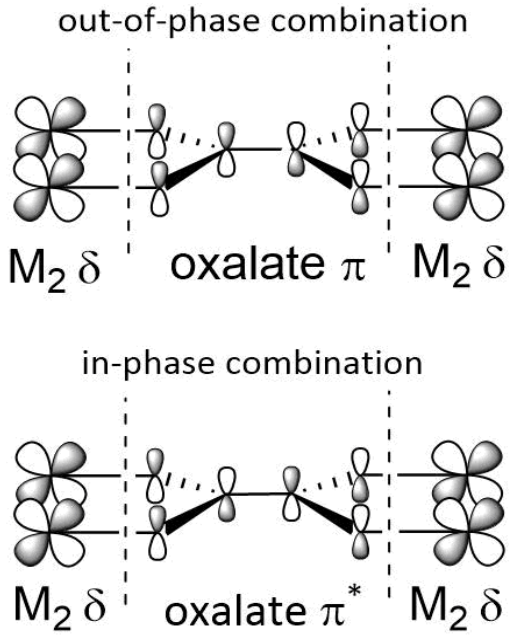

Figure 1.26: The orbital interactions between the M_2 δ and ligand π and π Figure reproduced with permission from the CJC.*[84]

As the oxalate-π orbital is much lower in energy than the M_2-δ there is little mixing between the two and the resulting orbital (HOMO) is nearly non-bonding in character. The π* of the oxalate is closer in energy to the M_2-δ, the combination of these generates the HOMO -1 which is predominantly M_2-δ in character and the LUMO which is ligand π* in character. The complex retains a planar structure (D_{2h}) due to the M_2-δ back bonding into the ligand π* which stabilises the complex by 16 kJ mol^{-1} relative to the twisted (D_{2d}) conformer. In Figure 1.27 the excitation of the electron from the HOMO-1 to the SOMO depicted in red is the charge resonance band corresponding to the electron transfer from donor to acceptor in the MV complex.

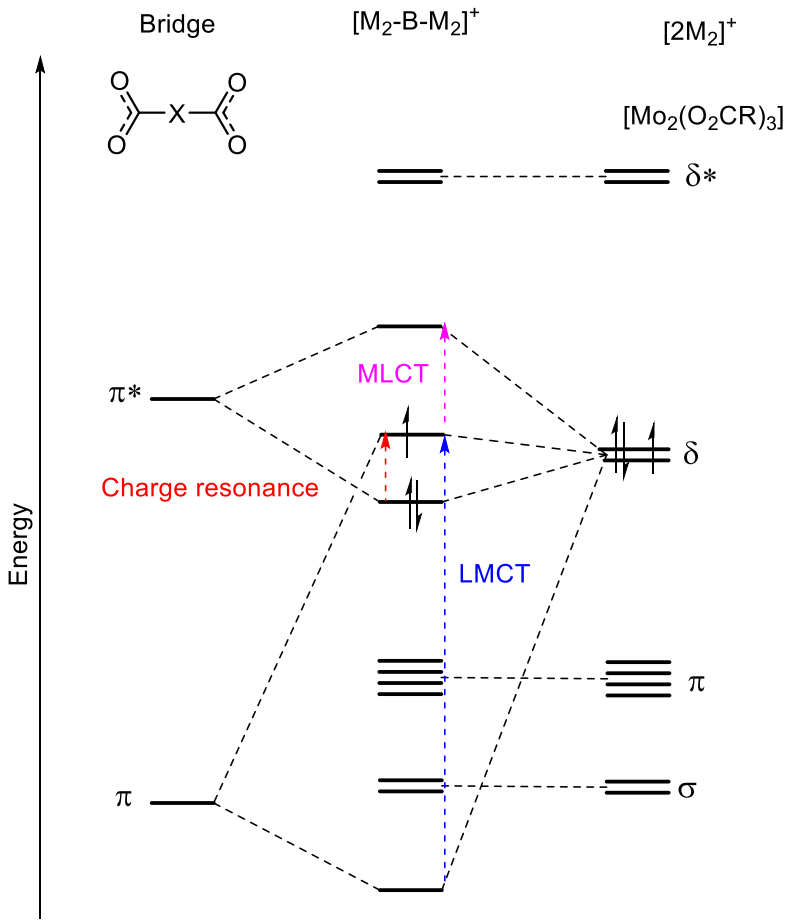

Figure 1.27: frontier molecular orbital diagram for $[(Piv)_3M_2\text{-}O_2CCO_2\text{-}M_2(Piv)_3]^+$. All-important electronic transitions are labelled.[84]

Tungsten paddlewheel complexes allow for an interesting comparison to their molybdenum counterparts, as tungsten is of a similar size to molybdenum due to the lanthanide contraction, and therefore will have similar same solvation effects and reorganizational energies. They differ in the energy of the valence orbitals which as a result strongly affects the electronic coupling. Figure 1.28 shows the charge resonance bands for $[(Piv)_3M_2\text{-}O_2CCO_2\text{-}M_2(Piv)_3]$ (where M_2 = Mo_2, MoW and W_2), as more molybdenum's are substituted for tungsten, the electronic coupling increases as shown by the observed blue shift in the charge resonance bands. This is because the energy levels of the W δ are closer in energy to the ligand π* allowing for better mixing of the orbitals. The origins of other commonly observed electronic transitions are shown on Figure 1.27.

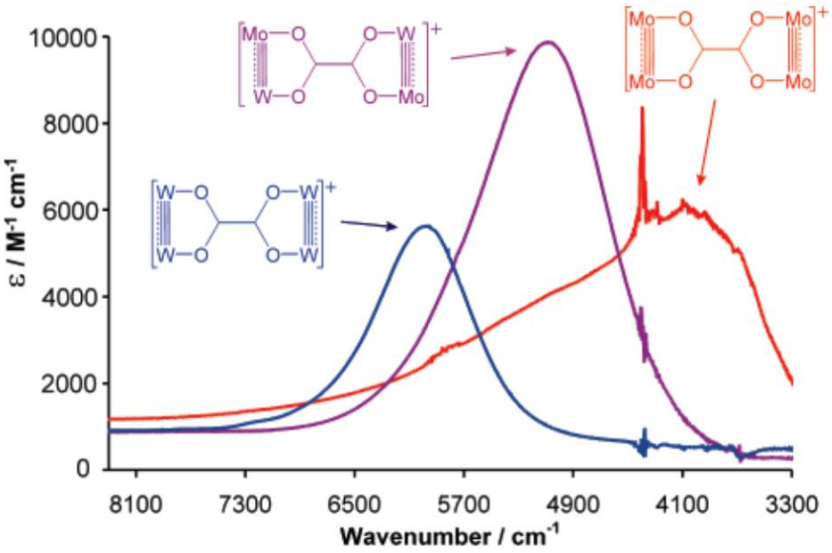

Figure 1.28: The change in the charge resonance bands as molybdenum is substituted for tungsten. Reprinted with permission from the American Chemical Society.[56]

Cotton *et al.* reported an analogous oxalate bridged species where the ancillary carboxylates were substituted for N,N'-di(p-anisyl)- formamidinate (DAniF). The electronic absorption spectra show both an IVCT and two transitions resulting from ligand π to metal δ charge transfer (LMCT). The ET occurs through a hole hopping mechanism as indicated by the appearance of an LMCT, whereas when the ancillary ligand is changed to pivlate the ET occurs through the electron hopping mechanism which is

indicated by the absence of an LMCT transition. The complex has a reported H_{ab} of 2376 cm^{-1} and is classified as class II/III borderline due to being solvent dependent.[14,85]

Building on the work of Cotton, Liu *et al.* explored the effect of the coordinating atom of the bridge on the $[Mo_2(DAniF)_3]$ redox centre by changing the oxalate bridge [OO-OO] to 1,2-dithioxalate [OS-OS] then to tetrathiooxalate [SS-SS].[85] The use of short bridge prevents issues such as bridge localisation and the effect of the plane on ET. The extent of delocalisation of the electron in the mixed valence state increases with the increasing number of sulphur atoms in the bridge, as it shows the transition from class II/III to class III.

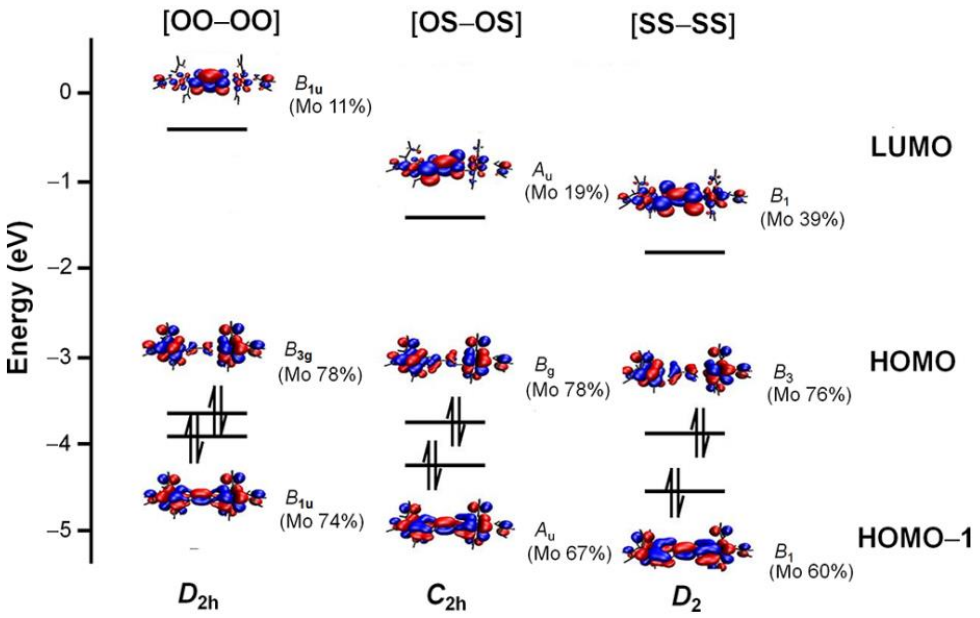

Figure 1.29: MO diagram showing the energy of the LUMO, HOMO and HOMO-1 for the complexes [OO-OO], [OS-OS] and [SS-SS]. Reprinted with permission from the American Chemical Society.[85]

The substitution from O to S coordinating atoms results in a decrease in energy of the ligand π* resulting in a decrease in energy between the HOMO Mo_2-δ and LUMO ligand π* (Figure 1.29). This is consistent with papers from Liu *et al.* and Patmore *et al.* where the substitution of the coordinating atom from N to O to S shows a similar trend.[86,87] The change in substituent coordinating atoms results

in an increase in electronic coupling as evidenced by an increase in K_c. The change in the energy gap between the HOMO and LUMO can be observed in the absorption spectra as a redshifted MLCT transition as more S coordinating atoms are added. The absorption spectra of $[OS\text{-}OS]^+$ and $[SS\text{-}SS]^+$ show no change in the MLCT transition, as previously stated $[OO\text{-}OO]^+$ shows the appearance of an LMCT consistent with a class II/III system.

The charge resonance transitions of the mixed valent state are shown in Figure 1.30, the bands increase In energy from 4077 cm^{-1}, 4149 cm^{-1} to 4926 cm^{-1} for $[OO\text{-}OO]^+$, $[OS\text{-}OS]^+$ and $[SS\text{-}SS]^+$ respectively. The H_{ab} was shown to increase from 2376 cm^{-1} to 2726 cm^{-1} to 2950 cm^{-1} for $[OO\text{-}OO]^+$, $[OS\text{-}OS]^+$ and $[SS\text{-}SS]^+$ respectively. The charge resonance transitions were recorded in more polar solvents in order to determine the solvent dependence of the transitions. For the complex $[OO\text{-}OO]^+$ the transition shows solvent dependence with the charge resonance band only being present in dichloromethane and as the polarity of the solvent increased the band became broad and weak showing typical class II behaviour. In contrast the $[OS\text{-}OS]^+$ and $[SS\text{-}SS]^+$ show solvent independence in the IVCT transition with no change in the transition energy and bandwidth, although the intensity is reduced in polar solvents. The solvent dependence shows that $[OO\text{-}OO]^+$ exhibits is indicative of a large solvent reorganisation energy, thus the solvent can control the charge localisation, from class II/III in less polar solvent to weakly class II in polar solvents. The $[SS\text{-}SS]^+$ complex has been proposed to be class IV and is reaching the extremes of electronic coupling.

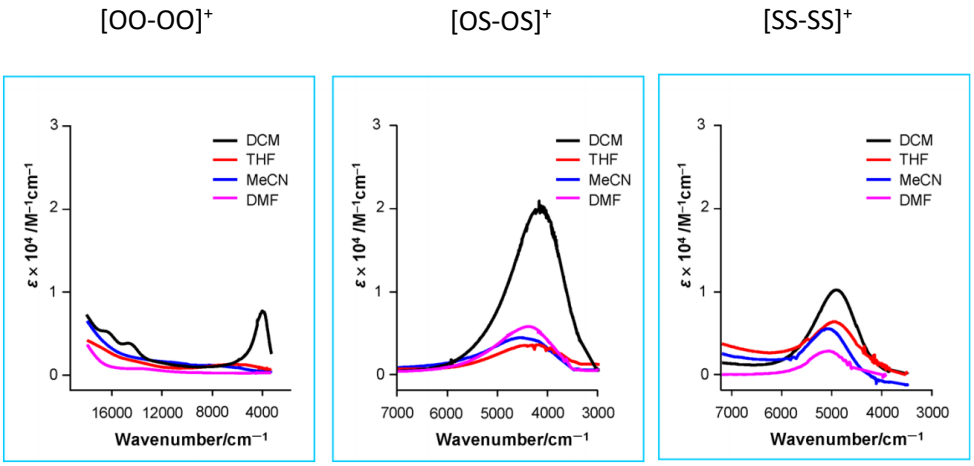

Figure 1.30: NIR spectra of [OO-OO]+, [OS-OS]+ and [SS-SS]+ in increasingly polar solvents. Reprinted with permission from the American Chemical Society.[85]

A plethora of dimolybdenum bridged systems have been reported with huge variations in structure, although most commonly the bridging ligand is changed. Some examples have been discussed in detail above, other examples have been reported where the dimolybdenum redox centres have been bridged by halides,[88] hydrides,[89] cyclic polyamidato anions,[90] terephthalate,[56] carborane dicarboxylate[14] and even metals such as ferrocenedicarboxylate[14] and $M(OMe)_4$ groups (M=Zn or Co).[91]

1.5 Proton coupled electron transfer

Proton coupled electron transfer (PCET) describes a reaction in which both an electron and a proton are transferred. The term was originally coined in 1981 to describe the comproportionation reaction between $[Ru^{IV}(bpy)_2(py)(O)_2]^{2+}$ and $[Ru^{II}(bpy)_2(py)(OH_2)]^{2+}$ to form $[Ru^{III}(bpy)_2(py)(OH)_2]^{2+}$.[92] Figure 1.31 shows the potential mechanisms of PCET, stepwise PT followed by ET or ET followed by PT or a concerted mechanism.

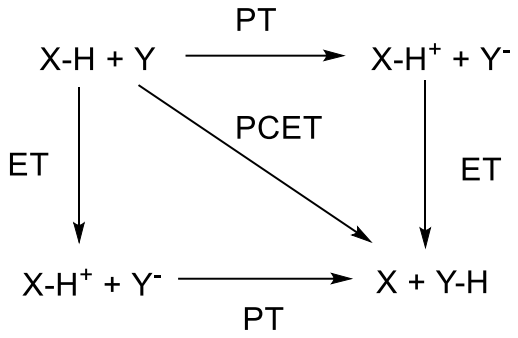

Figure 1.31: The potential mechanisms for PCET.

The rate of PCET is typically slower than ET, Meyer *et al.* demonstrated that the comproportionation reaction between $[Fe^{II}(H_2bim)_2(Hbim)]^{2+}$ and $[Fe^{III}(H_2bim)_3]^{2+}$ (H_2bim = 2,2'-biimidazoline) had a k_{PCET} = (5.8 ± 0.6) X 10^3 M^{-1} s^{-1} at 298 K. The addition of the two complexes resulted in the broadening of the ^1H NMR resonances which was used to calculate the rate of PCET. It was found that the rate of PCET was around three times slower than the ET between to $[Fe^{II}(H_2bim)_3]^{2+}$ and $[Fe^{III}(H_2bim)_3]^{3+}$ which was found to be k_{et} = 1.7 ± 0.2 × 10^4 M^{-1} s^{-1} at 298 K.

The crystallisation of the $[Ru^{III}(Hbim)_3]^-$ produces a hydrogen bonded coordination polymer which has been shown to act as a semiconductor.[93] The complex forms a MV polymer stabilised by proton-coupled electron transfer following a one electron oxidation, this was the first reported case of PCET in the solid state. Tadokoro *et al.* reported that the complex acts as a semiconductor in the solid state. The polymeric structure adopts a honeycomb sheet which following a one electron oxidation adopts alternating Ru^{II} and Ru^{III} units as shown in Figure 1.32.

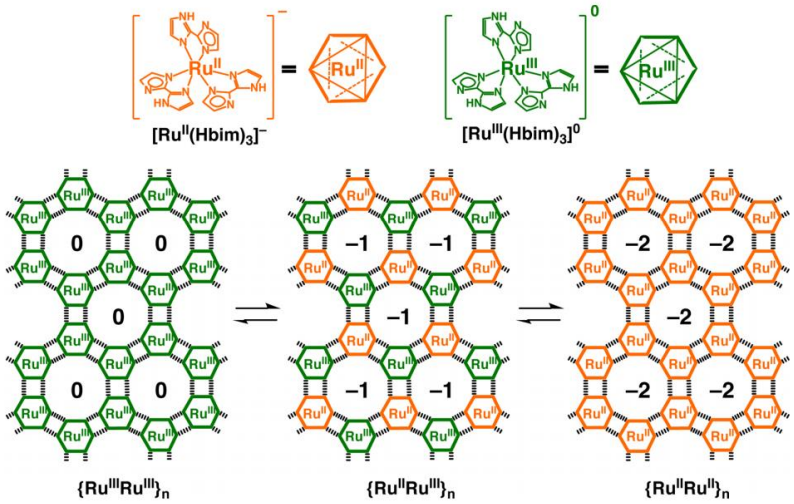

Figure 1.32: The honeycomb lattice adopted in the solid state of the polymeric $[Ru^{III}(Hbim)_3]^-$ reported by Tadokoro et al. . Reprinted with permission from the American Chemical Society.[93]

1.6 Mixed valency across hydrogen bonded complexes

The vast majority of MV complexes studied to date employ redox-active moieties linked by conjugated π systems, but as discussed above electron self-exchange through hydrogen bonds has also been extensively studied in the form of PCET.[63,68] Although recently research has reported the mixed valence compounds that employ self-complementary hydrogen bonds as bridges, as there is no proton hole the MV state is stabilised by a different mechanism. The mechanism of stabilisation is not well understood but there are potentially three mechanisms of stabilisation (Figure 1.33). ET can occur between the donor and acceptor if there is strong overlap between the donor, bridge and acceptor orbitals. If this were the case the hydrogen bonded complexes would be similar to a covalently bridged dimer and exhibit an IVCT in the NIR. Alternatively, a proton could transfer from the donor to acceptor. Finally, both proton transfer and electron transfer can occur, where ET is dependent upon the proton coordinate, this is called proton coupled mixed valency (PCMV).

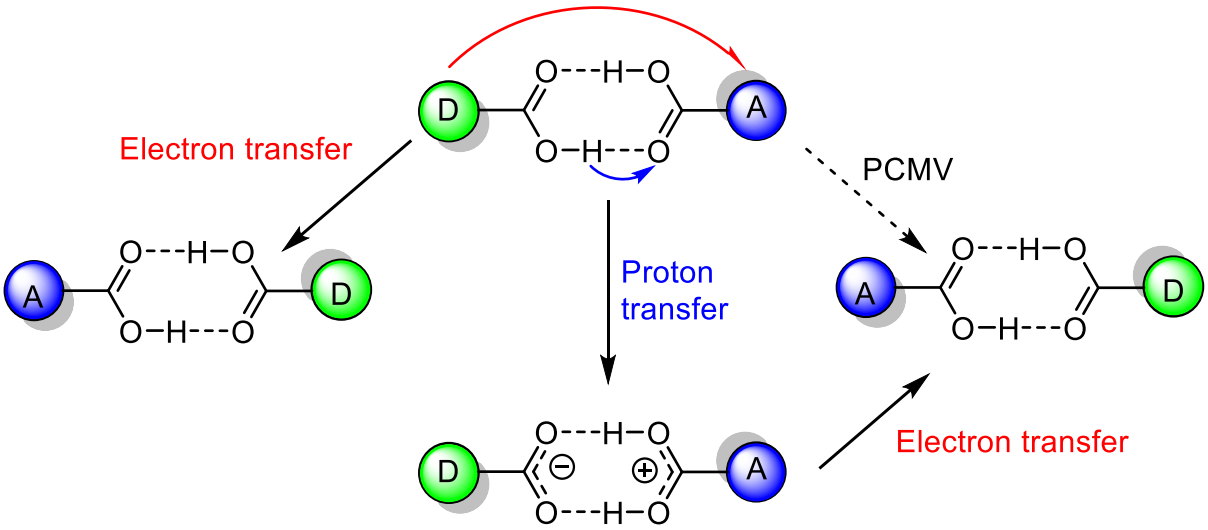

Figure 1.33: Potential mechanisms for the stabilisation of the MV state in hydrogen bonded dimer, electron transfer, proton transfer and proton coupled mixed valency (PCMV).

Kaifer *et al.* reported the first MV compound stabilised over a self-complimentary hydrogen bond, employing a ureidopyrimidine based bridging ligand bonded to a ferrocene redox centre (Figure 1.34).[94] ^{1}H NMR spectroscopy was used to show the complex dimerises in chloroform at concentrations as low as 10 µM indicating a high equilibrium constant ($K_{dim} > 10^{6}$ M^{-1}).

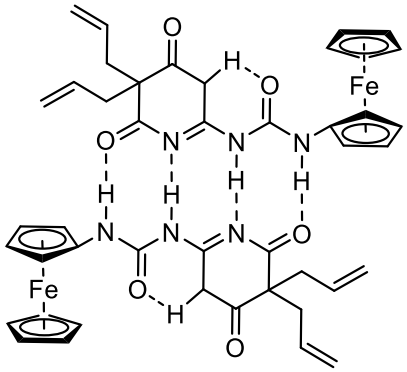

Figure 1.34: The ferrocence ureidopyrimidine complex reported by Kaifer et al.

The electrochemistry of the dimer in CH_2Cl_2 shows two successive one electron oxidations with a $\Delta E_{1/2}$ of 390 mV (k_c 3.9 x10^6). When run in acetonitrile only one oxidation with twice the current response is observed indicating only a monomer was observed in coordinating solvents. This reinforces the importance of the self-complementary hydrogen bond in the stabilisation of the MV state. Biferrocene has a $\Delta E_{1/2}$ of 350 mV in the same medium but $[Fc]_2$ has a greater $\Delta E_{1/2}$ despite the internuclear separation being much greater at close to 1 nm.[95] The observed IVCT transition for $[Fc]_2^+$ was observed in the NIR at 8368 cm^{-1}, with a half-height peak width of 560 cm^{-1} which is much smaller than the calculated bandwidth of 4397 cm^{-1}. The overestimation of the half height bandwidth is consistent with the large K_c and therefore a strongly coupled system. The observation of an IVCT transition indicates that there is sufficient orbital overlap over the hydrogen bond for ET transfer to occur.

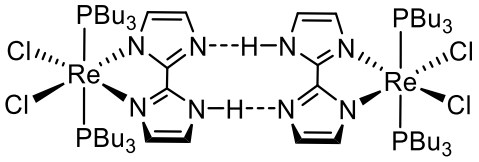

Figure 1.35: The structure of the $[Re^{III}Cl_2(PBu_3)_2(Hbim)_2]_2$ complex reported by Tadokoro et. al.

Tadokoro *et al.* reported a rhenium dimer that employed biimidazole as its bridge, $[Re^{III}Cl_2(PBu_3)_2(Hbim)_2]_2$ [Re] (Figure 1.35).[96] Dimerization was confirmed using ^1H NMR which showed the complex had an association constant of k=1.4 x 10^4 M^{-1} in CD_2Cl_2 at -80 °C. The crystal structure shows that the complex dimerises in the solid state. The cyclic voltammogram of $[Re]_2$ in dichloromethane shows two successive oxidative redox events corresponding to the $Re^{III/IV}$ redox couple and two successive redox events corresponding to the $Re^{II/III}$ redox couple. Cyclic voltammetry of [Re] shows only a single oxidation and reduction. The complex was found to form two separate MV states that correspond to $Re^{III/IV}$ and $Re^{II/III}$ with a $\Delta E_{1/2}$ of 0.28 V and 0.24 V respectively. Although no IVCT band was observed for either MV state as there is insufficient orbital overlap between the redox centres. The authors proposed the proton transfer stabilised the MV state.

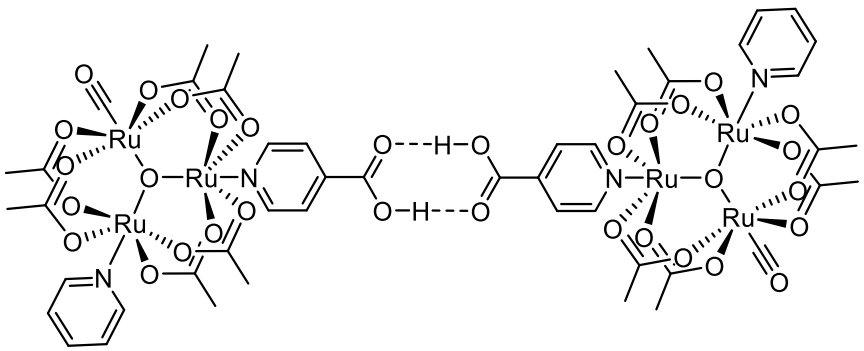

Figure 1.36: The structure of the $[Ru_3O(OAc)_6(CO)(py)B]_2$ (where B is isonicitinic acid) complex reported by Kubiak et al.

Kubiak *et al.* reported a variation of their oxo-centred triruthenium clusters [Ru_3] where isonicotinic acid was employed as the bridging ligand (Figure 1.36).[97] In its neutral state the complex is reported to be a monomer but following a one electron reduction the complex dimerises to generate a MV state. The reduction waves have a smaller splitting than the corresponding re-oxidation waves due to the formation of the dimer, when the CV was run in DMSO only a single redox process was observed. The K_c in dichloromethane was reported to be ≈ 10^7 when calculated from the re-oxidation half waves. The use of diffusion ordered spectroscopy (DOSY) NMR confirms the presence of neutral monomer [Ru_3] and the reduced dimer $[Ru_3]^-_2$.

Like in the previous examples of the oxo-centred triruthenium clusters the use of (IRSEC) shows that the MV *ν*(CO) stretch is a combination of [Ru_3O] and $[Ru_3O]_2^{2-}$ indicating a localised MV state and an electron transfer rate of ca. 10^{10} s^{-1}. The UV-Vis NIR SEC of $[Ru_3O]_2^-$ is not a combination of the neutral and doubly reduced species like in the IRSEC. Two NIR transitions are observed at 11000 cm^{-1} and 8500 cm^{-1} and are both attributed to being IVCT transitions as predicted by the three-state model where the bridge is considered. The transition at 8500 cm^{-1} is a metal to metal charge transfer and the absorption at 11000 cm^{-1} attributed to metal to bridge charge transfer from the metal donor to acceptor bridge.[76,98] When the bridging ligand was changed from isonicotinic to pyrimidinone the coupling increased resulting in a change from localised (class II) to delocalised (class III).[99] An increase in the rate of electron transfer was also observed with a calculated k_{et} of 3.8 x 10^{11} s^{-1}. The IR spectra

of the MV state showed an increase in intensity of the *v*(NH) band. This band was absent in the neutral and doubly reduced species indicating strong vibrionic coupling between the ruthenium oxo clusters and bridge wavefunctions which is attributed to promoting ET. As an IVCT is observed for these complexes the stabilisation method is therefore due to electron transfer.

Patmore *et al.* reported a series of dimolybdenum paddlewheel complexes bearing pendant lactam bridges; $[Mo_2(TiPB)_3(HDON)]$ and $[Mo_2(TiPB)_3(HDOP)]$ as shown in Figure 1.37 (where TiPB is triisopropyl benzoate, H_2DON is 2,7-dihdroxy-1,8-naphthyridine and H_2DOP = 3,6-dihydroxypyridazine).[100,101] These complexes have been shown to generate self-complimentary hydrogen bonds in solution using ^1H NMR and DOSY where the hydrodynamic volume halves when DMSO is added to a dichloromethane solution of the dimers.

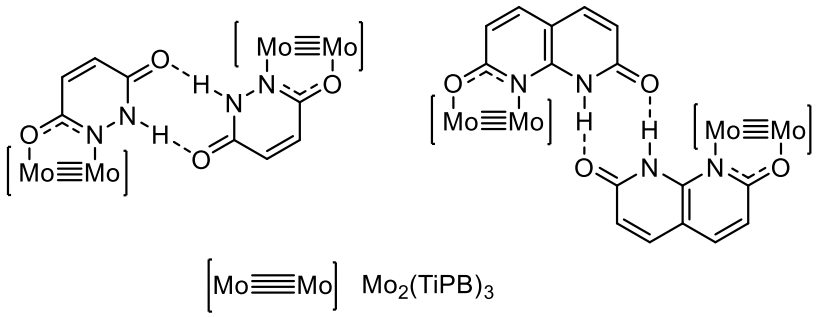

Figure 1.37: The structures of the $[Mo(TiPB)_3Bridge]_2$ (where TiPB is 2,4,6-triisopropyl benzoate, (Right) H_2DON is 2,7-dihydroxy-1,8-naphthyridine and (Left) H_2Dop = 3,6-dihydroxypyridazine.

Cyclic voltammetry indicates stabilisation of the MV state over the hydrogen bond, as in solutions of dichloromethane two successive one electron oxidations were observed. The addition of DMSO results in the disruption of the hydrogen bond and only a single oxidative event being observed. When the bridge is HDON the K_c was found to be 233 but when the bridge was HDOP the K_c was found to be 487. Although both complexes stabilise the MV state HDOP has a greater K_c despite the having a greater internuclear separation between the redox centres (HDOP: 8.38 Å, HDON: 7.29 Å). The

stabilisation of the MV state must occur over the hydrogen bond, analysis of $[Mo_2(TiPB)_3HDOP]_2^+$ in the UV-VIS NIR and IR shows the absence of an IVCT transition and no presence of PT. IRSEC showed no spectral coalescence of the *v*(CO) and *v*(NH) stretches indicating the ET rate was slower than 10^{10} s^{-1}. As PCET self-exchange reactions are between the EPR and electrochemical timescales EPR spectroscopy was conducted. EPR analysis showed a central peak at ~1.94 with two hyperfine splitting of 25.3 G and 32.8 G indicating localisation of the electron on one Mo_2 unit. Two sets of hyperfine splitting are observed due to the polarisation of the molybdenum-molybdenum bond as one Mo is co-ordinated to N and the other O on the HDOP ligand indicating that ET is slower than 10^9 s^{-1}.

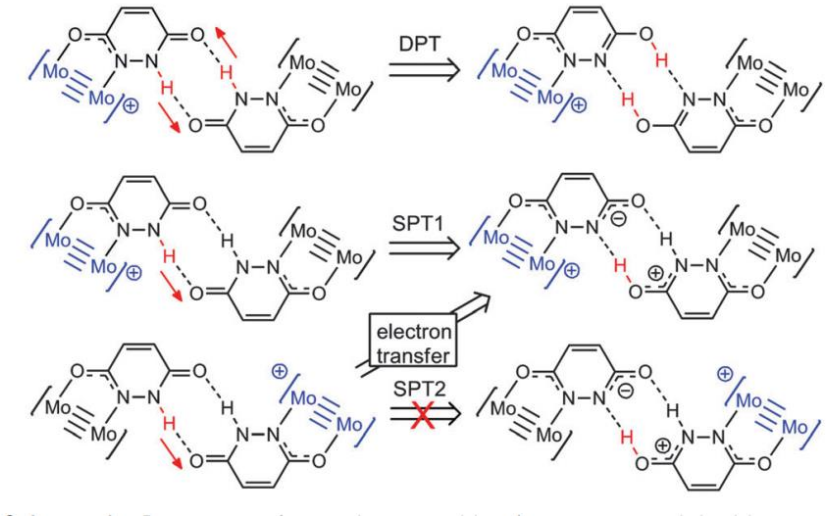

Figure 1.38: The proposed stabalisation mechanisms for $Mo_2(TiPB)_3HDop$ reported by Patmore et al. Where the proton transfer prodcuts from a concerted double proton transfer (DPT) and single proton transfer (STP 1 and STP 2) are shown. Figure Reproduced by permission of The Royal Society of Chemistry.[102]

To determine how the MV state is stabilised DFT calculations were employed to model asymmetric PT (SPT1/SPT2) and double proton transfer (DPT) (Figure 1.38).[102] Using the complex $[(HCO_2)_3Mo_2(HDOP)]_2^+$ to decrease calculation time, geometry optimisation shows the electron is localised on one Mo_2 unit and that the HDOP ligand is the NH tautomer. Calculations were done by constraining the NH proton at certain intervals. It was found that the energy barrier to DPT was 10

kcal mol^{-1} and that the product was 4 kcal mol^{-1} higher in energy. STP1 has a lower energy barrier but the product is 6.8 kcal mol^{-1} higher in energy than the ground state indicating that standard PT is unlikely. In STP2 as the proton moves from the donor to acceptor a dipole builds up that induces electron transfer and it is unlikely the proton fully transfers indicating a concerted process. This stabilisation mechanism is dependent on the position of the proton and as the proton does not transfer and there is no proton hole it is distinctly different from PCET, this new mechanism has been termed proton coupled mixed valency (PCMV).

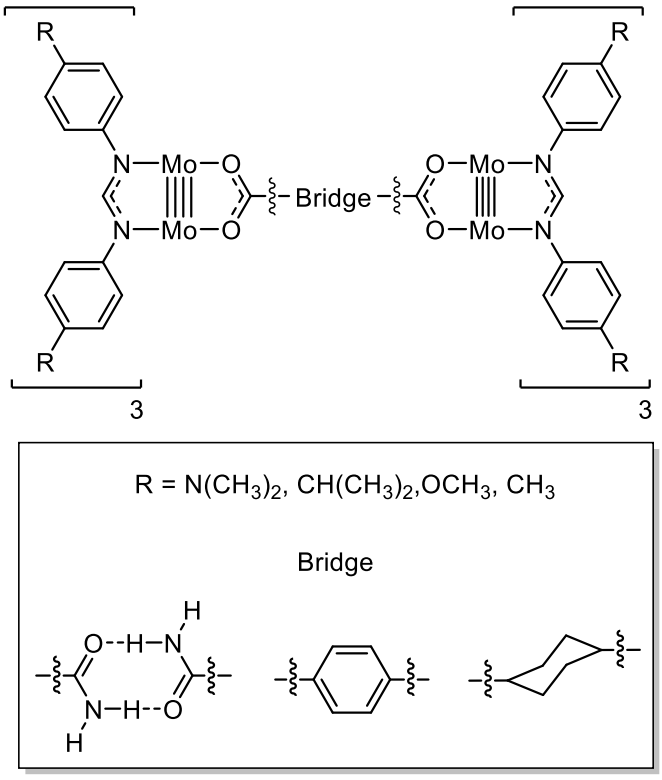

Figure 1.39: The structure of the [Mo_2(L)$_3$Oxamic]$_2$ (where L is DarF = N,N'- diarylformamidinate where the para substituent is N(CH_3)$_2$, CH(CH_3)$_2$, OCH_3 or CH_3) reported by Liu et al.

Liu *et al.* report several quadruply bonded dimolybdenum species bridged by either oxamic acid, terephthalate or 1,4-cyclohexanedicarboxalate (Figure 1.39).[103] Cyclic voltammetry in dichloromethane shows $\Delta E_{1/2}$ values of between 100-140 mV depending on the ancillary ligand, although in every case the oxamide had the largest $\Delta E_{1/2}$. Following chemical one electron oxidation

the complex $[Mo_2(DArF)_3(oxamide)]_2^+$ exhibits a Gaussian IVCT in the NIR which was shown to be dependent upon the ancillary ligand (Figure 1.40).

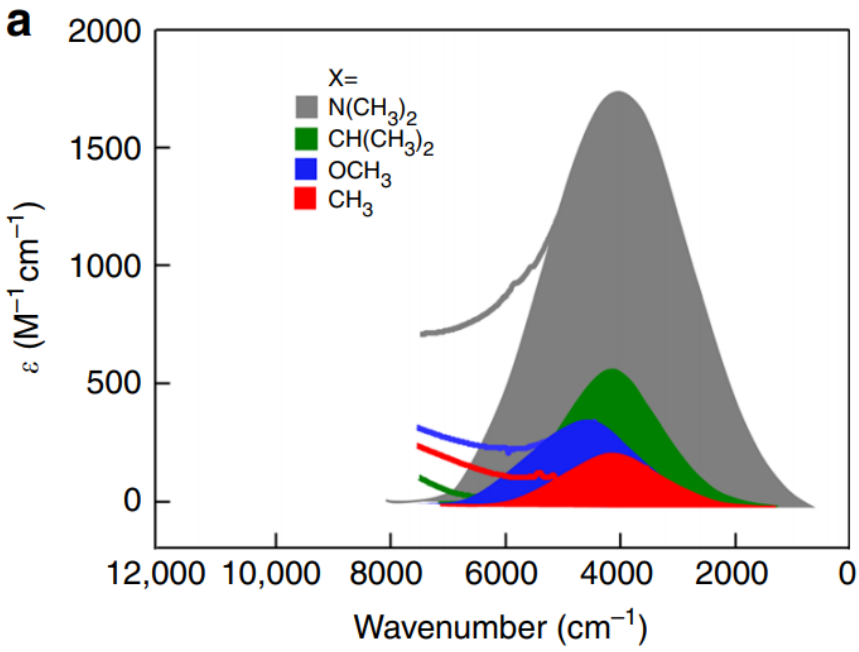

Figure 1.40: A spectra of the MV complexes showing the vibronic charge transfer bands for the hydrogen bridged complexes reported by Liu et al.[103]

The electronic coupling parameter (H_{ab}) was 410 cm^{-1} when R is $N(CH_3)_2$ but decreases to 190 to 130 cm^{-1} as R becomes less electron donating. These complexes have all been assigned as class II in nature. Whilst the presence of an IVCT demonstrates electronic coupling through overlap of the donor-bridge-acceptor orbitals, termed proton uncoupled electron (PUET) by the authors, additional stabilisation of the MV state was proposed to arise from a PCMV mechanism. By changing the electronic nature of the ligand, the ratio of PCMV and PUET changed, resulting in rates of electron transfer (k_{et}) ranging from 6 X 10^{10} s^{-1} when R = $N(CH_3)_2$ which has the most contribution from PUET to 2 X 10^{10} s^{-1} when R = $CH(CH_3)_2$ which has more PCMV. Remarkably, the authors demonstrated that ET transfer across the hydrogen bonded oxamide bridge was as efficient as it was across the covalently bound terephthalate bridge.

1.7 Conclusions and statement of purpose

Although MV complexes have been studied since the 1960s, the field is still flourishing 60 years later due to the insight MV complexes provide into nature, functional materials, solar energy conversion and molecular electronics. It is clear that ET is a complicated subject which requires multiple techniques to study. This is further complicated as trends in one series of MV complexes are not necessarily observed or obeyed in other MV series. These complexes are then subjected to a number of external factors which require consideration prior to the analysis of the IVCT transition such as the solvent, electrolyte and temperature. One major avenue of research is probing the transition between the localised and delocalised regimes to develop theoretical models because the two-state model is only accurate for fully localised or delocalised systems.

In comparison to covalent MV complexes there are comparatively few MV complexes employing a hydrogen bonded bridges and there is a plethora of unanswered questions. These include electron transfer distance, the effect of the ancillary ligand, solvation effects and how to dictate the mechanism of stabilisation. There are still many questions surrounding electron transfer across both covalent and hydrogen bonded interfaces, the following chapters employ the use of dimolybdenum paddlewheel complexes in an attempt to provide an answer to some of these questions. The complexes were studied using electrochemical, spectroscopic and theoretical techniques to understand ET in these systems.

Chapter 2 explores the effect of bridge asymmetry on the degree of electronic coupling in the strongly coupled complex $[Mo_2(Piv)_3]_2(\mu_2$-4,5-R,R'-Dop), the asymmetry is induced by the introduction of electron-donating and withdrawing substituents in the on the 4,5-positions of the bridging Dop^{2-} ligand.

Chapter 3 examines electron localisation in both the localised and delocalised regimes using structures analogous to $[Mo_2(Piv)_3]_2(\mu_2$-Dop). By using ligands analogous to Dop^{2-} the through space $Mo_2\cdots Mo_2$ separation and therefore the degree of through space communication can be modulated resulting in localisation of an electron within the redox active unit as well as between the redox units.

Chapter 4 employs complexes with the general structure $[Mo_2(Piv)_3]_2(\mu_2\text{-L})$, where L utilises a 2,3-dihydroxy or 2,3-dithiopyridazine core. The bridging ligands employed in this chapter are structural isomers of the bridges employed in chapter 3. The bridges employed in these complexes allow for electron transfer to occur across a linear bridge and are unexpected to facilitate through space electron transfer as a result of the increased $Mo_2\cdots Mo_2$ separation.

In chapter 5 the effect changing the ancillary ligand has on MV complexes stabilised by proton coupled mixed valency is discussed. This is the second systematic study on the effect of the ancillary ligand on MV complexes containing a self-complementary hydrogen bond. This will be achieved by substituting the ligand *trans* to the HDop ligand in the complex $[Mo_2(TiPB)_3(HDOP)]_2$.

Six new complexes are reported in chapter six; the complexes employ the use of functionalised imidazole bridging ligands to increase the degree of electronic coupling over a hydrogen bond by decreasing the effective electron transfer distance. This chapter also provides the first systematic study of dimolybdenum complexes employing functionalised imidazole ligands.

1.8 References

1 F. A. Cotton, C. A. Murillo and R. A. Walton, *Multiple Bonds Between Metal Atoms*, Springer, 3 rd., 2005.

2 L. F. Dahl, E. Ishishi and R. E. Rundle, *J. Chem. Phys.*, 1957, **26**, 1750–1751.

3 F. A. Cotton, N. F. Curtis, C. B. Harris, B. F. G. Johnson, S. J. Lippard, J. T. Mague, W. R. Robinson and J. S. Wood, *Science*, 1964, **145**, 1305–1307.

4 F. A. Cotton and C. B. Harris, *Inorg. Chem.*, 1965, **4**, 330–333.

5 A. S. Kotel'nikov and V. G. Tronev, *J. Inorg. Chem. USSR (English trans.)*, 1958, **3**, 1008.

6 E. W. Abel, A. Singh and G. Wilkinson, *J. Chem. Soc. Chem. Commun.*, 1959, 3097–3099.

7 F. A. Cotton and B. W. K. Cotton F A, *J. Am. Chem. Soc.*, 1965, **87**, 921–922.

8 D. Lawton and R. Mason, *J. Am. Chem. Soc.*, 1965, **87**, 921–922.

9 T. Nguyen, A. D. Sutton, M. Brynda, J. C. Fettinger, G. J. Long and P. P. Power, *Science*, 2005, **310**, 844–847.

10 F. A. Cotton, P. E. Fanwick, J. W. Fitch, H. D. Glicksman and R. A. Walton, *J. Am. Chem. Soc.*, 1979, **101**, 1752–1757.

11 F. A. Cotton and B. E. Hanson, *Inorg. Chem.*, 1978, **17**, 3237–3240.

12 F. A. Cotton, C. Lin and C. A. Murillo, *Inorg. Chem.*, 2001, **40**, 472–477.

13 F. A. Cotton, L. M. Daniels, C. Lin and C. A. Murillo, *J. Am. Chem. Soc.*, 1999, **121**, 4538–4539.

14 F. A. Cotton, J. P. Donahue, C. Lin and C. a Murillo, *Inorg. Chem.*, 2001, **40**, 1234–44.

15 M. Köberl, M. Cokoja, W. A. Herrmann and F. E. Kühn, *Dalt. Trans.*, 2011, **40**, 6834–6859.

16 P. E. M. Siegbahn, *Acc. Chem. Res.*, 2009, **42**, 1871–1880.

17 S. Schinzel, J. Schraut, A. V. Arbuznikov, P. E. M. Siegbahn and M. Kaupp, *Chem. - A Eur. J.*, 2010, **16**, 10424–10438.

18 W. He and H. J. M. Hou, in *Contemporary Problems of Photosynthesis*, 2015, pp. 381–405.

19 C. Hsiao, I. C. Chou, C. D. Okafor, J. C. Bowman, E. B. O'neill, S. S. Athavale, A. S. Petrov, N. V. Hud, R. M. Wartell, S. C. Harvey and L. D. Williams, *Nat. Chem.*, 2013, **5**, 525–528.

20 Y. Li, T. Liu, H. Liu, M. Z. Tian and Y. Li, *Acc. Chem. Res.*, 2014, **47**, 1186–1198.

21 T. M. Powers and T. A. Betley, *J. Am. Chem. Soc.*, 2013, **135**, 12289–12296.

22 M. D. K. Ark, *Acc. Chem. Res.*, 2014, **47**, 100–111.

23 S. Ghosh, S. Rana, N. Hollingsworth, M. G. Richmond, S. E. Kabir and G. Hogarth, *Inorganics*, , DOI:10.3390/inorganics6040122.

24 S. Ghosh, A. Rahaman, G. Orton, G. Gregori, M. Bernat, U. Kulsume, N. Hollingsworth, K. B. Holt, S. E. Kabir and G. Hogarth, *Eur. J. Inorg. Chem.*, 2019, **2019**, 4506–4515.

25 P. J. Low, *Dalt. Trans.*, 2005, 2821–2824.

26 S. Rigaut, *Dalt. Trans.*, 2013, **42**, 15859–15863.

27 R. Sakamoto, S. Katagiri, H. Maeda and H. Nishihara, *Coord. Chem. Rev.*, 2013, **257**, 1493–1506.

28 R. Sakamoto, S. Kume and H. Nishihara, *Chem. - A Eur. J.*, 2008, **14**, 6978–6986.

29 N. S. Hush, *Chem. Phys.*, 1975, **10**, 361–366.

30 P. H. Citrin and A. P. Ginsberg, *J. Am. Chem. Soc.*, 1981, **103**, 3673–3679.

31 K. D. Demadis, C. M. Hartshorn and T. J. Meyer, *Chem. Rev.*, 2001, **101**, 2655–2685.

32 M. B. Robin and P. Day, *Adv. Inorg. Chem. Radiochem.*, 1968, **10**, 247–422.

33 R. Dunbar, Kim and A. Heintz, Robert, *Chemistry of Transition Metal Cyanide Compounds :*

Modern Perspectives, 1997, vol. 45.

34 N. S. Hush and G. C. Allen, *Prog. Inorg. Chem.*, 1967, **8**, 357–390.

35 N. S. Hush, *Electrochim. Acta*, 1968, **13**, 1005–1023.

36 S. F. Nelsen, *Chem. Eur. J.*, 2000, **6**, 581.

37 M. Parthey and M. Kaupp, *Chem. Soc. Rev.*, 2014, **43**, 5067–5088.

38 C. N. R. Rao and J. Gopalakrishnan, *New Direction in Solid State Chemistry*, Cambridge Univeristy Press, 2nd edn., 1997.

39 W. F. Libby, *J. Phys. Chem.*, 1952, 863–868.

40 D. M. D'Alessandro and F. R. Keene, *Chem. Soc. Rev.*, 2006, **35**, 424–440.

41 W. Bruns, K. Eberhard and M. Krejikb, *J. Chem. Soc. Chem. Commun.*, 1993, **12**, 1868–1869.

42 C. H. Creutz and H. Taube, *J. Am. Chem. Soc.*, 1969, **91**, 3988–3989.

43 C. H. Creutz and H. Taube, *J. Am. Chem. Soc.*, 1973, **320**, 1086–109.

44 B. J. Lear and M. H. Chisholm, *Inorg. Chem.*, 2009, **48**, 10954–10971.

45 B. S. Brunschwig and N. Sutin, *Coord. Chem. Rev.*, 1999, **187**, 233–254.

46 S. Iijima, F. Mizutani, O. Niwa, N. Matsumoto, Y. Sunatsuki and M. Kojima, *Hyperfine Interact.*, 2005, **166**, 397–402.

47 J. T. Hupp and R. D. Williams, *Acc. Chem. Res.*, 2001, **34**, 808–817.

48 W. Kaim and A. Klein, Eds., *Spectroelectrochemistry*, RSC publishing, Cambridge, 2008.

49 T. Ito, T. Hamaguchi, H. Nagino, T. Yamaguchi, J. Washington and C. P. Kubiak, *Science*, 1997, **277**, 660.

50 F. Coat, M. A. Guillevic, L. Toupet, F. Paul and C. Lapinte, *Organometallics*, 1997, **16**, 5988–5998.

51 E. C. Fitzgerald, N. J. Brown, R. Edge, M. Helliwell, H. N. Roberts, F. Tuna, A. Beeby, D. Collison, P. J. Low and M. W. Whiteley, *Organometallics*, 2012, **31**, 157–169.

52 K. Lancaster, S. A. Odom, S. C. Jones, S. Thayumanavan, S. R. Marder, J. L. Brédas, V. Coropceanu and S. Barlow, *J. Am. Chem. Soc.*, 2009, **131**, 1717–1723.

53 M. Brady, W. Weng, Y. Zhou, J. W. Seyler, A. J. Amoroso, A. M. Arif, M. Böhme, G. Frenking and J. A. Gladysz, *J. Am. Chem. Soc.*, 1997, **119**, 775–788.

54 M. H. Chisholm, B. D. Pate, P. J. Wilson and J. M. Zaleski, *Chem. Commun.*, 2002, **2**, 1084–1085.

55 F. A. Cotton, L. M. Daniels, E. A. Hillard and C. A. Murillo, *Inorg. Chem.*, 2002, **41**, 1639–1644.

56 M. H. Chisholm and N. J. Patmore, *Acc. Chem. Res.*, 2007, **40**, 19–27.

57 P. Zanello, *Inorganic Electrochemistry: Theory, Practice and Application*, The Royal Society of Chemistry, London, 2003.

58 D. E. Richardson and H. Taube, *Inorg. Chem.*, 1981, **20**, 1278–1285.

59 M. D. Ward, *Chem. Soc. Rev.*, 1995, **24**, 121–134.

60 S. Byungho and H. M. Goff, *Inorganica Chim. Acta*, 1994, **226**, 231–235.

61 G. Giuffrida and S. Campagna, *Coord. Chem. Rev.*, 1994, **135**–**136**, 517–531.

62 C. E. B. Evans, M. L. Naklicki, A. R. Rezvani, C. A. White, V. V. Kondratiev and R. J. Crutchley, *J. Am. Chem. Soc.*, 1998, **120**, 13096–13103.

63 R. J. Crutchley, in *Advances in Inorganic Chemistry*, 1994, pp. 273–325.

64 C. Lapinte, *J. Organomet. Chem.*, 2008, **693**, 793–801.

65 F. Barrière, N. Camire, W. E. Geiger, U. T. Mueller-Westerhoff and R. Sanders, *J. Am. Chem. Soc.*, 2002, **124**, 7262–7263.

66 C. P. Kubiak, *Inorg. Chem.*, 2013, **52**, 5663–5676.

67 D. M. D'Alessandro and F. R. Keene, *Dalt. Trans.*, 2004, 3950–3954.

68 A. Stebler, J. H. Ammeter, U. FÜRholz and A. Ludil, *Inorg. Chem.*, 1984, **23**, 2764–2767.

69 J. K. Beattie, N. S. Hush and P. R. Taylor, *Inorg. Chem.*, 1976, **15**, 992–993.

70 A. Bencini, I. Ciofini, C. A. Daul and A. Ferretti, *J. Am. Chem. Soc.*, 1999, **121**, 11418–11424.

71 S. Joss, H. B. Bürgi and A. Ludi, *Inorg. Chem.*, 1985, **24**, 949–954.

72 P. A. Lay, R. H. Magnuson and H. Taube, *Inorg. Chem.*, 1988, **27**, 2364–2371.

73 Y. Kim and C. M. Lieber, *Inorg. Chem.*, 1989, **28**, 3990–3992.

74 J. E. Sutton and H. Taube, *Inorg. Chem.*, 1981, **20**, 3125–3134.

75 A. C. Ribou, J. P. Launay, K. Takahashi, T. Nihira, S. Tarutani and C. W. Spangler, *Inorg. Chem.*, 1994, **33**, 1325–1329.

76 B. S. Brunschwig, C. Creutz and N. Sutin, *Chem. Soc. Rev.*, 2002, **31**, 168–184.

77 R. W. Callahan, F. R. Keene, T. J. Meyer and D. J. Salmon, *J. Am. Chem. Soc.*, 1977, **99**, 1064–1073.

78 J. W. Seyler, W. Weng, Y. Zhou and J. A. Gladysz, *Organometallics*, 1993, **12**, 3802–3804.

79 A. C. Ribou, J. P. Launay, M. L. Sachtleben, H. Li and C. W. Spangler, *Inorg. Chem.*, 1996, **35**, 3735–3740.

80 J. C. Salsman, S. Ronco, C. H. Londergan and C. P. Kubiak, *Inorg. Chem.*, 2006, **45**, 547–554.

81 M. H. Chisholm, *Philos. Trans. R. Soc. A Math. Phys. Eng. Sci.*, 2008, **366**, 101–112.

82 B. E. Bursten, M. H. Chisholm, R. J. H. Clark, S. Firth, C. M. Hadad, A. M. Macintosh, P. J. Wilson, P. M. Woodward and J. M. Zaleski, *J. Am. Chem. Soc.*, 2002, **124**, 3050–3063.

83 M. H. Chisholm, *Coord. Chem. Rev.*, 2013, **257**, 1576–1583.

84 M. H. Chisholm and N. J. Patmore, *Can. J. Chem.*, 2009, **87**, 88–94.

85 Y. N. Tan, T. Cheng, M. Meng, Y. Y. Zhang, C. Y. Liu, M. F. Sun, Y. Zheng and P. J. Low, *J. Phys. Chem. C*, 2017, **121**, 27860–27873.

86 J. Hicks, S. P. Ring and N. J. Patmore, *Dalt. Trans.*, 2012, **41**, 6641.

87 Y. Yang Wu, M. Meng, G. Yi Wang, P. Feng and C. Y. Liu, *Chem. Commun.*, 2017, **53**, 3030–3033.

88 F. A. LeCottoni, C. Y. Liu, C. A. Murillo and X. Wang, *Chem. Commun.*, 2003, **3**, 2190–2191.

89 F. A. Cotton, C. A. Murillo and Q. Zhao, *Inorg. Chem.*, 2007, **46**, 6858–6863.

90 F. A. Cotton, J. P. Donahue, C. A. Murillo, L. M. Pérez and R. Yu, *J. Am. Chem. Soc.*, 2003, **125**, 8900–8910.

91 F. A. Cotton, N. S. Dalal, C. Y. Liu, C. A. Murillo, J. M. North and X. Wang, *J. Am. Chem. Soc.*, 2003, **125**, 12945–12952.

92 J. M. Mayer, *Annu. Rev. Phys. Chem.*, 2004, **55**, 363–390.

93 M. Tadokoro, H. Hosoda, T. Inoue, A. Murayama, K. Noguchi, A. Iioka, R. Nishimura, M. Itoh, T. Sugaya, H. Kamebuchi and M. A. Haga, *Inorg. Chem.*, 2017, **56**, 8513–8526.

94 H. Sun, J. Steeb and A. E. Kaifer, *J. Am. Chem. Soc.*, 2006, **128**, 2820–2821.

95 C. LeVanda, K. Bechgaard, D. O. Cowan and M. D. Rausch, *J. Am. Chem. Soc.*, 1977, **99**, 2964–2968.

96 M. Tadokoro, T. Inoue, S. Tamaki, K. Fujii, K. Isogai, H. Nakazawa, S. Takeda, K. Isobe, N. Koga, A. Ichimura and K. Nakasuji, *Angew. Chemie - Int. Ed.*, 2007, **46**, 5938–5942.

97 J. C. Goeltz and C. P. Kubiak, *J. Am. Chem. Soc.*, 2010, **132**, 17390–17392.

98 G. Canzi, J. C. Goeltz, J. S. Henderson, R. E. Park, C. Maruggi and C. P. Kubiak, *J. Am. Chem. Soc.*, 2014, **136**, 1710–1713.

99 T. M. Porter, G. P. Heim and C. P. Kubiak, *J. Am. Chem. Soc.*, 2018, **140**, 12756–12759.

100 L. A. Wilkinson, L. McNeill, P. A. Scattergood and N. J. Patmore, *Inorg. Chem.*, 2013, **52**, 9683–9691.

101 L. A. Wilkinson, L. McNeill, A. J. H. M. Meijer and N. J. Patmore, *J. Am. Chem. Soc.*, 2013, **135**, 1723–1726.

102 L. A. Wilkinson, K. B. Vincent, A. J. H. M. Meijer and N. J. Patmore, *Chem. Commun.*, 2016, **52**, 100–103.

103 T. Cheng, D. X. Shen, M. Meng, S. Mallick, L. Cao, N. J. Patmore, H. L. Zhang, S. F. Zou, H. W. Chen, Y. Qin, Y. Y. Wu and C. Y. Liu, *Nat. Commun.*, 2019, **10**, 1–10.

Electron localisation in fully delocalised asymmetric MV complexes

2.1 Abstract

A series of symmetric and asymmetric dimolybdenum dimers bridged by substituted 3,6-dihydroxypyridazines, $[Mo_2(Piv)_3]_2(\mu_2$-4,5-R,R'-Dop) (Piv = trimethylacetate), where R, R' = Cl, H [**1**], Br, H [**2**], H, H [**3**], Me, H [**4**], Me, Me [**5**] have been synthesised. The complexes were characterised by ^{1}H NMR spectroscopy and the crystal structure of **5** is reported. The stability of the mixed valent (MV) state generated following a one electron oxidation has been probed by cyclic voltammetry, with the symmetric compounds displaying ΔE_{pc} of 0.444 V (**3**) and 0.412 V (**5**), and the asymmetric systems having ΔE_{pc} values of 0.435 V (**1**), 0.415 V (**2**) and 0.461 V (**4**). The UV-Vis-NIR spectra of the MV species exhibit a relatively intense, non-Gaussian, charge resonance band in the NIR region with a low energy cut off, consistent with full delocalisation of the electron between the dimetal units (Class III). The symmetric complexes have a cross coupling matrix parameter (H_{ab}) of 1390 cm^{-1} for **3**$^+$ and 1360 cm^{-1} for **5**$^+$. The introduction of asymmetry into the complexes results in a decrease in H_{ab} to 927, 971 and 1242 cm^{-1} for **1**$^+$, **2**$^+$ and **4**$^+$ respectively. Electron paramagnetic resonance spectroscopy of the MV species indicate the electron predominantly resides in a Mo_2-δ orbital with a g-factor of 1.93-1.94. Complexes **3**$^+$ and **5**$^+$ have two hyperfine couplings of between 1.09 mT and 1.45 mT indicating the electron is fully delocalised over all four Mo atoms despite polarisation of the dimolybdenum bond. The asymmetric complexes have four hyperfine couplings that could not be resolved, but the magnitude of the hyperfine splittings indicate that the electron is delocalised to different extents across the system. The EPR spectra have allowed localisation within fully delocalised symmetric and asymmetric MV complexes to be probed for the first time.

2.2 Asymmetric Mixed valence systems

Mixed valence compounds typically consist of two identical redox active fragments (M), bridged by a conjugated organic ligand (B). Following a one electron redox process of a symmetric M-B-M system, one redox centre becomes an electron donor (D) and the other the accepter (A). When these sites are identical ET occurs with no change in the free energy (ΔG°=0) of the system. Chapter 1 focussed on previous reports associated with symmetric mixed valence compounds, as these encompass the majority of the reported MV compounds in literature.[1–4] In this chapter asymmetric mixed valence compounds will be examined.

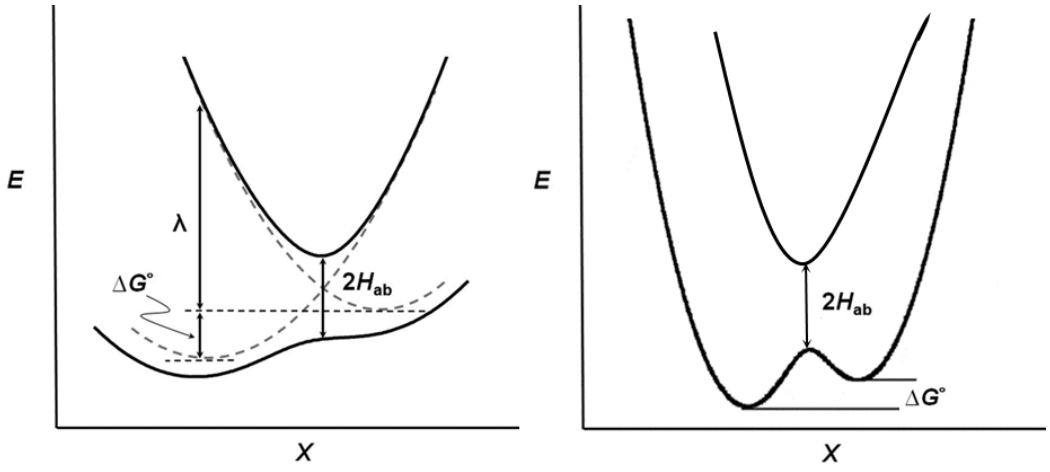

Figure 2.1: The potential energy surfaces of asymmetric (left) class III and (right) class II mixed valence systems. left: Figures reproduced from reference with permission of the RSC.[5] *Right: Figure adapted from reference with permission from John Wiley & Sons.*[6]

Asymmetry can be structurally induced into a MV system in two main ways: by altering one redox centre, by either changing the metal[2] or the ancillary ligands,[6–8] or by employing an asymmetric bridge.[9] By introducing asymmetry into the MV compound, a difference in energy is observed in the diabatic PES of the reactants such that ΔG°≠ 0. The adiabatic PES of a strongly coupled asymmetric (class III) system is shown in Figure 2.1, one energy minimum is formed on the lower PES with the minima skewed towards one reactant as a result of the change in ΔG°. By comparison to symmetric MV compounds, only a few examples of asymmetric MV complexes have been reported. This is in part

because if ΔG° is too large, the system becomes valence trapped.[7] The PES of a class II system is also shown in Figure 2.1, which contains two minima with differing ground state energies as a result of the change in ΔG°.

The use of asymmetric redox centres has a direct effect on the electrochemistry of the complexes, as the change in the coordination environment of the two redox centres results in different redox potentials. As a result of this, $\Delta E_{1/2}$ incorporates the intrinsic internal potential difference (ΔE_{ip}) between the two redox centres as well as the electronic interaction between both redox centres.[10]

The electronic coupling matrix H_{ab} for a strongly coupled system cannot be calculated in the same way as for a symmetric system, as $2H_{ab}$ is no longer equivalent to ν_{max}. Typically, the charge resonance bands for strongly coupled asymmetric systems are symmetrical, unlike symmetric systems where the charge resonance band exhibits low energy cut off. The symmetric charge resonance band is a result of the thermal Boltzmann distribution of the ground state.[10,11] For a strongly coupled asymmetric system (class III) the values of ΔG° and λ are experimentally inaccessible, but for weakly coupled (Class II) asymmetric system these can be calculated from the equation $\nu_{max} = \Delta G° + \lambda$.[12,5] As the number of systems that have strongly coupled asymmetric redox centres are limited, challenges remain in understanding the chemistry. Some prominent examples from literature are discussed herein.

Kubiak *et al.* have reported three oxo-centred triruthenium clusters where the ancillary ligand was varied to induce asymmetry, as seen in Figure 2.2.[6] Electrochemistry showed that the magnitude of the splitting between the first and second reduction was dependent on the nature of the ancillary ligand, with the $\Delta E_{1/2}$ of 410 mV, 310 mV and 350 mV for complexes **A, B** and **C** respectively. The separation was greater than the intrinsic reduction potentials indicating stabilisation of a mixed valent state, despite the significant ΔE_{ip} values of 100 mV, 130 mV and 230 mV for complexes **A, B** and **C** respectively. When the MV states were examined spectroscopically it was found that all three complexes displayed intense intervalence charge transfer bands. Employing IRSEC and isotopically labelling one redox centre with $C^{13}O^{18}$, the overlapping *v*(CO) bands for each species could be

deconvoluted (Figure 2.3). The top and bottom spectra represent the doubly reduced and the neutral species, with the bands at lower wavenumber corresponding to $\nu(C^{13}O^{18})$. The ν(CO) bands of the mixed valent species show two broad bands, all of which have a distinct shoulder indicating the presence of two charge transfer isomers. A charge transfer isomer is described as "identifiable chemical entities that exist in dynamic equilibrium determined by electron transfer".[13] The broadening of the band indicates that the ET occurs on the IR timescale resulting in interconversion of the isomers.

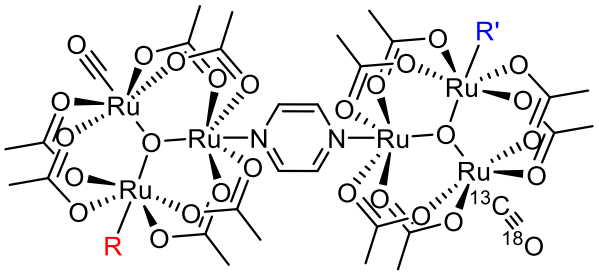

A= R = dmap R' = py
B= R = py R' =cpy
C = R = dmap R' = cpy

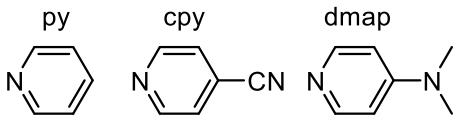

Figure 2.2: Asymmetric [R-Ru$_3$O-py-Ru$_3$O-R'] complexes reported by Kubiak et al.

IRSEC analysis of the IR bands found the equilibrium constant for the conversion between the isomers, the free energy difference between the diabatic redox centres and the rate of electron transfer from the lowest energy species to the higher energy species. Interestingly the equilibrium constant showed little temperature dependence (-40 °C - 7 °C). The IRSEC found that large magnitudes of H_{ab}, that are sufficient to nearly equalise the population of both the high energy and low energy isomer, are not sufficient to delocalise the systems to a state with a single energy minima.

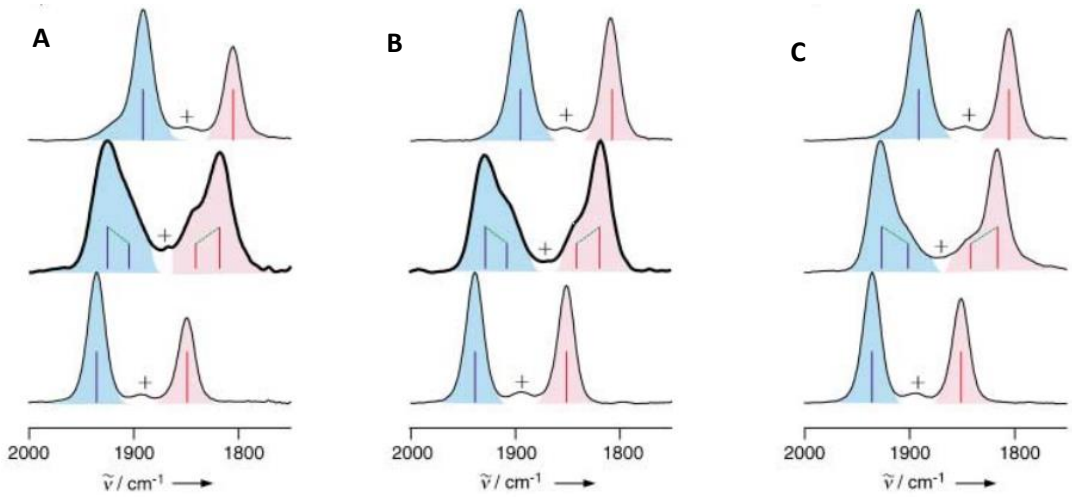

Figure 2.3: IRSEC analysis of Kubiack et al. oxo-centred triruthenium clusters peaks with + are $C^{13}O^{16}$ impurities. Figure reproduced from reference with permission from John Wiley & Sons.[6]

Liu *et al.* report three asymmetrical dimolybdenum dimers, $[Mo_2(DAniF)_3]_2(\mu_2$-bridge) (DAniF = *N,N'*-di(*p*-anisyl)-formamidinate) where the bridges were O_2CCOS [OO-OS], S_2CCO_2 [SS-OO] and S_2CCOS [SS-OS] (Figure 2.4).[5] The electrochemistry of the complexes showed significant redox asymmetry when compared to the symmetric analogous complexes [OO-OO], [OS-OS] and [SS-SS]. The substitution of oxygen for sulphur in bridges between dimolybdenum units typically increases the electronic coupling. However, in the case of [OO-OS] the introduction of the sulphur results in diminished coupling when compared to the [OO-OO] derivative as a result of the redox asymmetry, this result was also observed by the addition of a single oxygen to the [SS-SS] species.

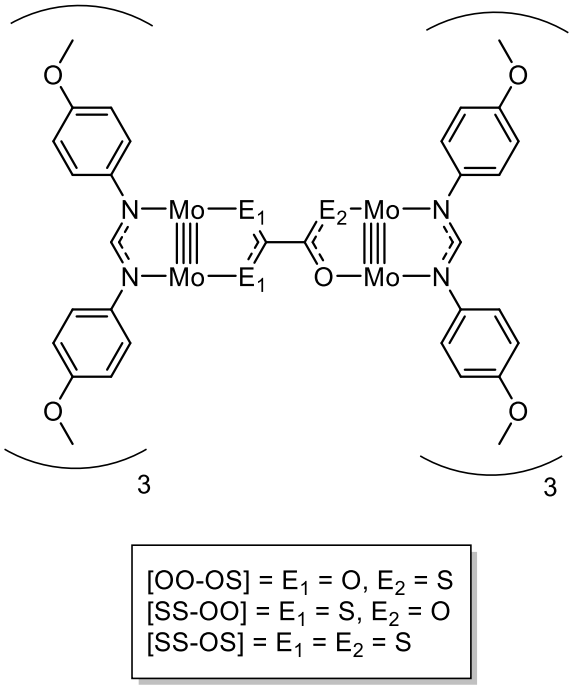

Figure 2.4: E_1E_1C-C-E_2O bridged $[Mo_2(DAniF)_3]$ complexes reported by Liu. [5]

When the oxidised species were analysed spectroscopically, the asymmetric complexes exhibited more complicated spectra than their symmetric counterparts. All complexes exhibited a symmetric IVCT transition as well as $Mo_2\delta \rightarrow$ L-π* (MLCT) and L-π $\rightarrow Mo_2\delta^*$ (LMCT) transitions. The LMCT transitions were not present in the symmetric species, which indicates that one redox centre primarily acts as a donor and one as the acceptor and that the thermal electron transfer process is energetically unfavourable. The electronic coupling matrix (H_{ab}) was found to be much smaller than the corresponding symmetric complexes with $[OO\text{-}OS]^+$ and $[SS\text{-}SO]^+$ showing the largest decrease in coupling. It should be noted that for each of the asymmetric systems, the calculated H_{ab} was less than ν_{max} / 2 due to the unbalanced PES.

The introduction of electron withdrawing and donating groups to the bridge have been shown to have a pronounced effect on the stabilisation of the MV state. Through the modulation of the bridge π/π* energy levels, the extent of electronic coupling can be directly affected. Chisholm *et al.* reported two symmetric and one asymmetric ditungsten dimers, $[W_2(Piv)_3]_2(\mu_2\text{-}O_2C\text{-}Ar\text{-}CO_2]$ (Where Ar = 1,4-

terephthalic acid, 2,3,5,6-tetrafluoro-1,4-terephthalic acid or 2-fluoro-1,4-terepthalic acid). The addition of the electron withdrawing groups to the bridge resulted in an increase in the H_{ab} from 1610 cm^{-1} in terephthalic acid to 1785 cm^{-1} in tetrafluoroterepthalic acid.[14] When the bridge was changed to 2-fluoro-1,4-terepthalic acid, the reported H_{ab} was 1726 cm^{-1}, indicating the increase in electronic coupling which resulted from the addition of an electron withdrawing group was retained despite inducing asymmetry in the complex.

2.3 Aims

The number of studies on strongly coupled asymmetric systems is limited, as are the number of studies that induce asymmetry through the addition of electron donating/withdrawing groups to the bridge backbone. As the modification of the bridging ligand π-system has been shown to have a large impact on the extent of electronic communication, a series of strongly coupled complexes, employing asymmetric ligands of form $[Mo_2(Piv)_3]_2(\mu_2$-4,5-R,R'-Dop) will be synthesised. The asymmetry is induced by the introduction of electron donating and withdrawing groups on the 4,5-positions of the bridging Dop^{2-} ligand.

Electronic coupling between the dimetal units will be evaluated through electrochemical and spectroelectrochemical studies. Based on previous studies, differences in the electronic coupling would be evidenced by changes in the $\Delta E_{1/2}$ values obtained by cyclic voltammetry and the IVCT transition expected in the NIR region. This series of compounds will also provide a rare opportunity to compare electronic coupling in symmetric and asymmetric MV complexes.

2.4 Results and discussion

2.4.1 *Synthesis*

Synthesis of the bridged species first requires the synthesis of homoleptic start material $Mo_2(Piv)_4$ (HPiv= 2,2-dimethylpropanoic acid) shown in Scheme 2.1.

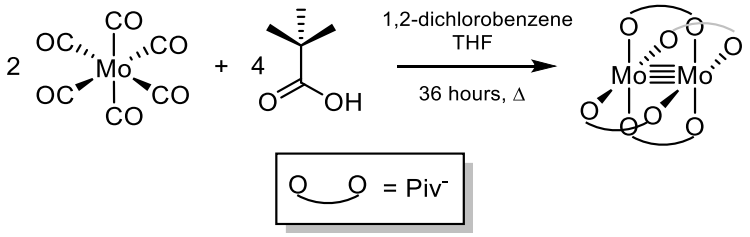

Scheme 2.1: Synthesis of $Mo_2(Piv)_4$

$Mo_2(Piv)_4$ was synthesised by refluxing $Mo(CO)_6$ and 2,2-dimethylpropanoic acid (Piv) in a 4:1 mixture of 1,2-dichlorobenzene and THF (Scheme 2.1). The reaction proceeds through the thermolysis of $Mo(CO)_6$, elevated temperatures are required to break the strong Mo-CO bonds which are a result of the strong back bonding from the Mo d_π-orbitals into the CO π^*-orbitals. The high reaction temperature therefore requires the use of a solvent with a high boiling point, in this case 1,2-dichlorobenzene. Constant sublimation of the $Mo(CO)_6$ is problematic and can potentially result in a blocked condenser, hence the addition of a small amount of THF into the reaction to wash any sublimed material back into the reaction vessel. The synthetic route reported in literature uses diglyme as the solvent, which meets the high temperature requirements of the reaction but does not prevent or minimise the sublimation of $Mo(CO)_6$.[15] To prevent excessive sublimation the sublimed $Mo(CO)_6$ is manually "pushed back" into the reaction vessel, potentially exposing the reaction mixture to the atmosphere resulting in a decreased yield (< 65 %). The product in our modified preparation is isolated in excellent yield (> 85 %) and offers superior yields to those reported in the literature.[15,16]

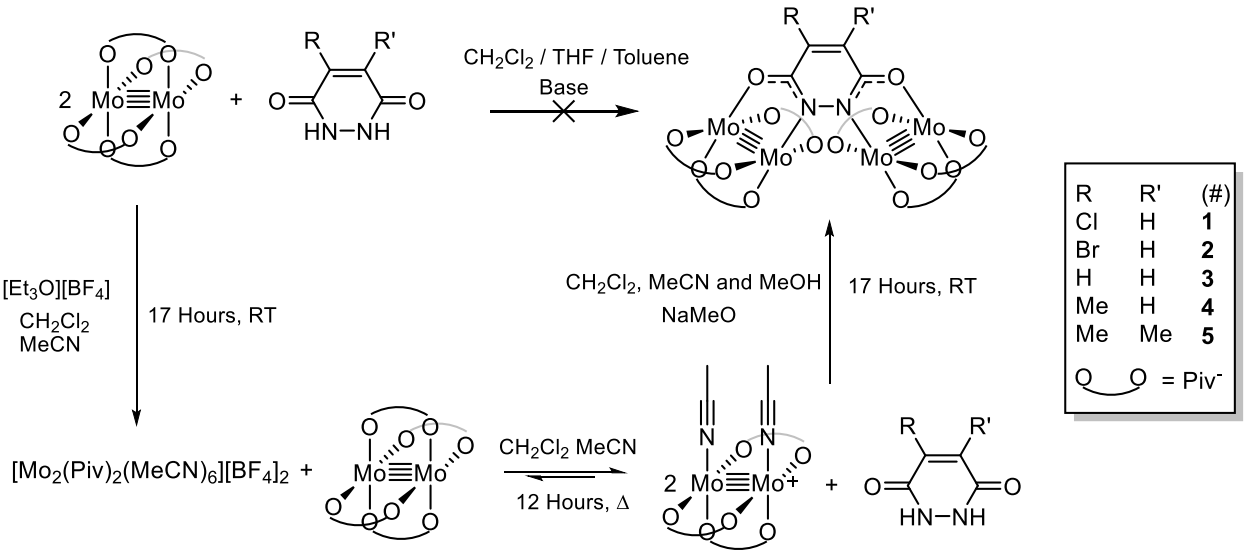

*Scheme 2.2: The synthetic route to $[Mo_2(Piv)_3]_2(\mu_2$-ClDop) (**1**), $[Mo_2(Piv)_3]_2(\mu_2$-BrDop) (**2**), $[Mo_2(Piv)_3]_2(\mu_2$-Dop) (**3**), $[Mo_2(Piv)_3]_2(\mu_2$-MeDop) (**4**) and $[Mo_2(Piv)_3]_2(\mu_2$-Me_2Dop) (**5**).*

Initial attempts to generate complexes **1 – 5** were made by reaction of the homoleptic complex $Mo_2(Piv)_4$ and the substituted 3,6-dihydroxypyridazines (R,R'-H_2Dop where R,R' = Cl, H [**1**], Br, H [**2**], H, H [**3**], H, Me [**4**], Me, Me [**5**]) in the presence of base (See Scheme 2.2). However, despite varying the solvent (DCM, THF, toluene), temperature (reflux), base (eg. NEt_3, K^tBuO and NaMeO) and reaction time (17 hours – 2 weeks), the reactions did not go to completion. The dimetal complexes isolated from the reaction were examined by ^{1}H NMR spectroscopy and were found to be the starting material $Mo_2(Piv)_4$, and the mono-substituted complex $Mo_2(Piv)_3(HL)$.[17] The coordination of the second dimetal unit to the bridging ligand was likely sterically hindered preventing the formation and isolation of the desired complex despite using elevated temperatures. We attempted the direct synthesis of the target complexes from the homoleptic starting materials to minimise the number of reaction steps and maximise yields. However, the synthesis of complex **3** has been previously been reported by Chisholm *et al*. from a multistep reaction, via a cationic intermediate.[18]

The dicationic complex $[Mo_2(Piv)_2(MeCN)_6][BF_4]_2$ can be synthesised following a literature preparation by treating $Mo_2(Piv)_4$ with excess triethyloxonium tetrafluoroborate in acetonitrile.[19] The mononcationic complex $[Mo_2(Piv)_3(MeCN)_2][BF_4]$ is then best prepared by a comproportionation

reaction between $Mo_2(Piv)_4$ and $[Mo_2(Piv)_2(MeCN)_4][BF_4]_2$ in a refluxing mixture of MeCN and CH_2Cl_2 for 12 hours (Scheme 2.2). The monocation undergoes disproportionation to the $Mo_2(Piv)_4$ and $[Mo_2(Piv)_2(MeCN)_4][BF_4]_2$ if left to stand in solution, so it was reacted immediately with the sodium 3,6-dioxypyridazines.

Reaction of monocationic intermediate $[Mo_2(Piv)_3(MeCN)_2][BF_4]$ with R,R'-Na_2Dop in methanol, resulted in an immediate colour change (**1** and **2** = purple, **3** = red, **4** and **5** = orange), and the reaction was stirred for 17 hours to ensure completion (Scheme 2.2). The solvent was removed *in vacuo*, and the ^{1}H NMR spectra indicated several impurities such as $Mo_2(Piv)_4$, $Mo_2(Piv)_3$(HDop), *cis*- and *trans*-$Mo_2(Piv)_2$(R,R'Dop)$_2$ as well as coordination isomers resulting from the use of asymmetric ligands. The number of impurities necessitated the use of air sensitive column chromatography as a means of purification. To the best of our knowledge, the use of column chromatography to purify air-sensitive dimolybdenum paddlewheel complexes has not been reported. They are surprisingly stable on the silica column but decompose when dry loading the thin layer chromatography (TLC) plate. The difficulty in running TLC on the complexes resulted in the use of gradient elution to isolate different fractions. The product was the second band eluted from the column in all cases using dichloromethane/hexane (50:50 (v/v)) → dichloromethane → THF/ dichloromethane (2:98 (v/v)) for complexes **1 – 4** and dichloromethane/hexane (50:50 (v/v)) → dichloromethane for complex **5.** The pure products were isolated with yields ranging from 16 % (**4**) to 50 % (**1**) when based on the amount of $Mo_2(Piv)_4$ used. The modest yields are a reflection of a multistep reaction that generates a number of by-products, and the need to isolate the relatively air-sensitive product by column chromatography. The complexes are readily soluble in coordinating solvents such as THF and DMSO; **5** is readily soluble in CH_2Cl_2 whereas complexes **1 – 4** are sparingly soluble. The compounds were found to be pure by elemental analysis.

Complexes **1 – 5** have all been characterised by ^{1}H NMR, MALDI-TOF mass spectrometry, and the crystal structure for complex **5** was obtained, *vide infra*.

2.4.2 *Mass spectrometry*

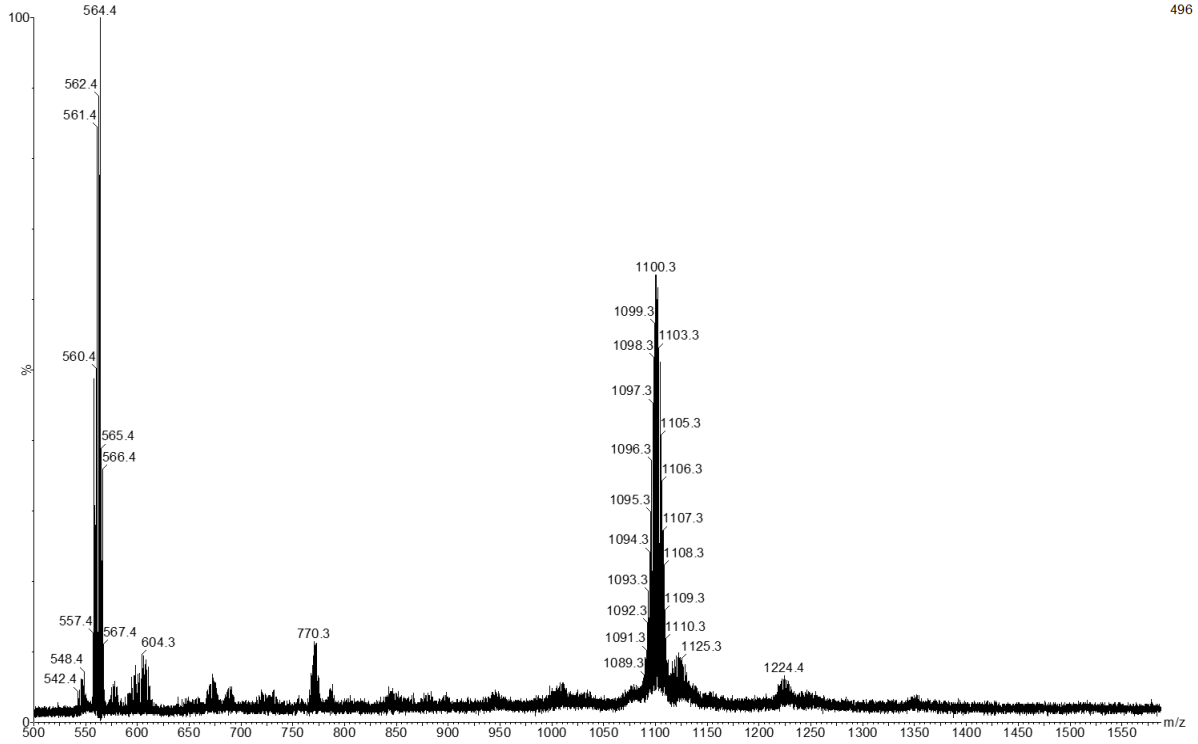

*Figure 2.5: The MALDI-TOF spectrum of **3**.*

Complexes **1 – 5** were all analysed using MALDI-TOF (matrix assisted laser desorption / ionisation – time of flight) mass spectrometry. The complexes all generated a signal at the expected m/z value for M^+, with an isotropic distribution pattern consistent with four molybdenums, an example spectrum of **3** is shown in Figure 2.5. The peak at an m/z of 564.4 is present in all spectra and is an unidentified analyte. Dimolybdenum paddlewheel complexes require a soft ionisation technique to observe the molecular ion (M^+) and prevent fragmentation, attempts to observe the complexes using a harsher ionisation technique such as electrospray ionisation were unsuccessful in all cases.

*Table 2.1: Selected bond lengths (Å), bond angles (°) and torsion angles (°) for complex **5**.*

Mo1-Mo2	2.1096(13)
Mo3-Mo4	2.1105(14)
Mo2···Mo3	3.7541(13)
Mo1-O1	2.081(6)
Mo2-N1	2.160(6)
Mo4-O2	2.093(5)
N1-N2	1.412(9)
C1-C2	1.452(11)
Mo3-N2	2.151(6)
C2-C3	1.337(11)
O1-C1	1.299(10)
C1-N1	1.333(9)
Mo1-O1-C1	119.9(4)
Mo2-N1-N2	123.2(4)
O1-C1-N1	118.4(7)
Mo2-N1-C1	117.5(5)
Mo2-N1-N2-Mo3	-3.583(7)
Mo1-Mo2-Mo3-Mo4	-7.806(8)

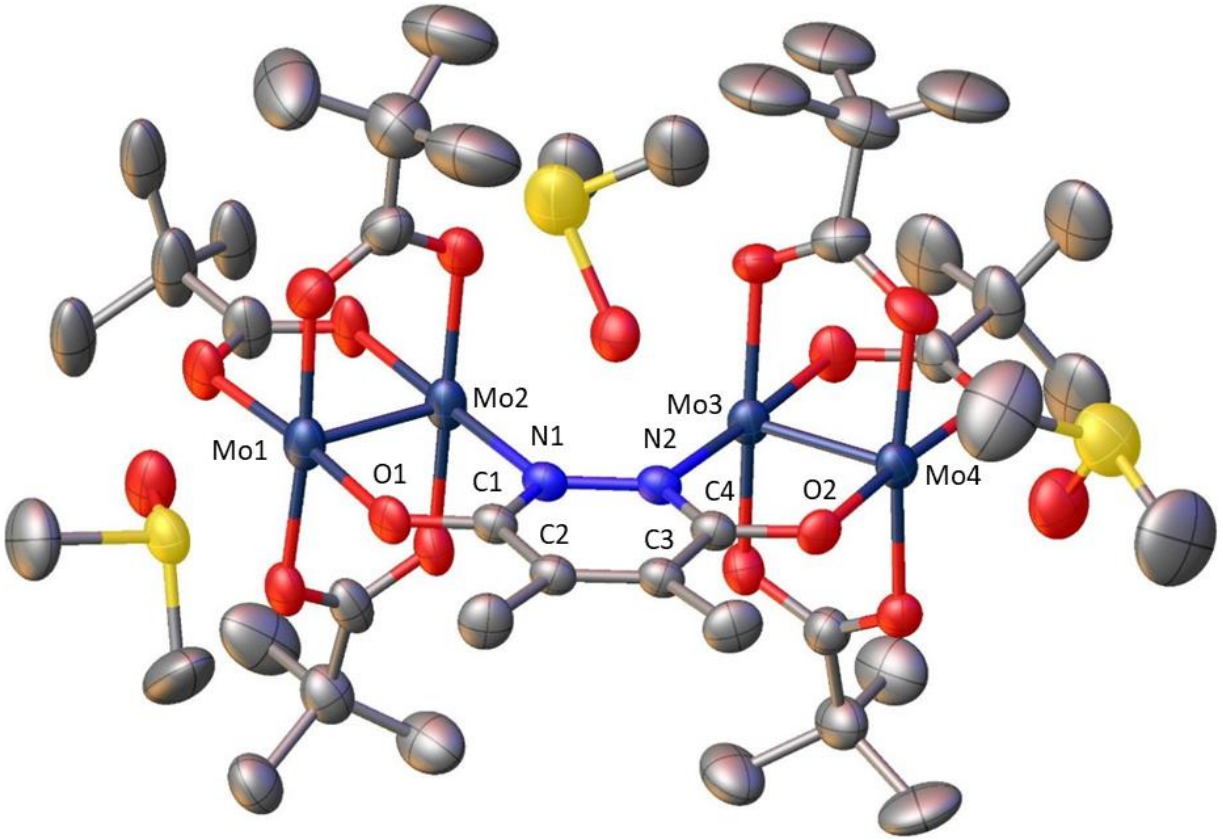

*Figure 2.6: Solid-state structure of $[Mo_2(Piv)_3]_2(\mu_2\text{-}Me_2Dop)(DMSO)_3$ (**5**) as determined by single-crystal XRD. Anisotropic displacement parameters are shown at 50 % probability. Hydrogen atoms are omitted for clarity.*

Although more than fifty $[Mo_2(O_2CR)_3]_2(\mu_2\text{-Bridge})$ complexes have been prepared, only a handful of crystal structures have been reported due to the difficulty in associated with generating large enough crystals. Despite numerous attempts suitable crystals for X-ray diffraction of complexes **1 – 4** could not be obtained, although the structures are all expected to be co-planar. However, crystals of **5**$(DMSO)_3$ were grown by the slow diffusion of water into a DMSO solution of **5** at room temperature. The structure was determined by single X-ray diffraction, and is shown in Figure 2.6 with selected bond lengths and angles given in Table 2.1, the cell parameters and refinement results are given in chapter 8. The unit cell was found to be triclinic and solved in the space group $P\bar{1}$. Both Mo_2 centres show the expected paddlewheel arrangement of the ligands around the dimetal core. The two dimetal units are bridged by the Me_2Dop ligand with three axially coordinated DMSO molecules. The MoMo quadruple bonds have similar relatively short bond lengths (Mo1-Mo2 and Mo3-Mo4 = 2.1096(13) and 2.1105(14) Å), and are comparable to related dimolybdenum species.[20] The through space separation between the quadruple bonds (Mo2···Mo3) is 3.7541(13) Å . The two Mo_2^{4+} units are essentially coplanar, with a Mo2-N1-N2-Mo3 torsion angle of 3.583(7) °; the coplanar nature of the quadruple bonds and bridging ligand will give rise to good overlap of the Mo_2-δ / Me_2Dop-π orbitals and maximise electronic communication**.** The Me_2Dop bond lengths indicate the species is aromatic and are consistent with the H_2Dop bond lengths found in the analogous compound $[W_2(Piv)_3(PPh_3)]_2(\mu_2\text{-Dop})\cdot$toluene.[21]

2.4.4 *^{1}H NMR spectroscopy*

The ^{1}H NMR spectra of $Mo_2(Piv)_4$ and $[Mo_2(Piv)_2(MeCN)_6][BF_4]_2$ are consistent with the literature.[16,17] The ^{1}H NMR spectra of complexes **1 – 5** in d_6-DMSO are shown in Figure 2.7. The ^{1}H NMR spectrum of **3** exhibits the expected 2:1 Piv resonances between 1.25 – 1.35 ppm and a singlet at 7.19 ppm indicative of a symmetrically substituted Dop ligand. The experimental spectra of **3** is consistent with literature.[18] The ^{1}H NMR spectrum of **5** has the expected 2:1 Piv resonances that arise from the carboxylates that are cis and trans to the bridging ligand. The methyl groups of the bridging ligand are obscured by the protio impurities contained within the d_6-DMSO solvent. The spectra of **1, 2** and **4** have inequivalent dimolybdenum paddlewheels as a result of the asymmetry of the bridging ligand

resulting in inequivalent carboxylate ligands. The spectrum of **1** exhibit 1:1:1 Piv resonances between 1.25 -1.35 ppm and a singlet at 7.54 ppm consistent with two asymmetrically bound dimolybdenum units. Complex **2** has a similar spectrum to **1**, with 1:1:1 Piv resonances between 1.25 -1.35 ppm and an aromatic singlet observed at 7.69 ppm, and shows signs of facile ligand scrambling commonly observed when using DMSO as the solvent, the MALDI-TOF, electrochemistry and elemental analysis confirm the purity of the complex.[22] Complex **4** has a 2:2:1:1 integral pattern of the Piv resonances, a doublet at 7.13 ppm which is coupled to the Me group and a Me group which is obscured by the protio impurities contained within the d_6-DMSO. All complexes have two axially coordinated THF molecules at 3.56 and 1.72 ppm these are shifted upfield from free THF.[23] The coordinated THF can be removed by placing the compounds under high vacuum for 48 hours, this was performed prior to the submission of the elemental analysis. The ^{1}H NMR spectra of **4** and **5** in d_8-THF shows the previously obscured Me group resonances, confirming isolation of the desired complexes.

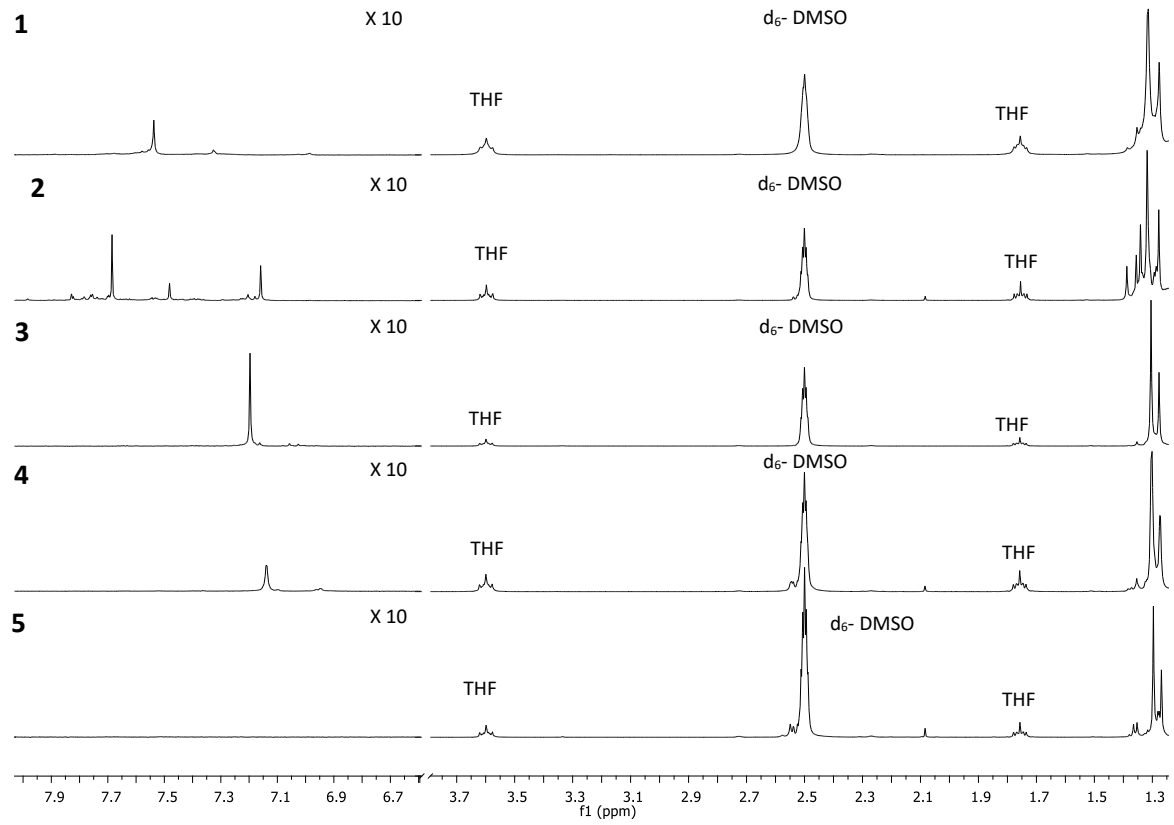

*Figure 2.7: ^{1}H NMR spectra of complexes **1 – 5** in d_6-DMSO Left: A magnified portion of the aromatic region showing bridging ligand resonances.*

2.4.5 *Electrochemistry*

The cyclic voltammograms and differential pulse voltammograms for complexes **1** – **5** in 0.1 M NBu_4PF_6 / THF solutions are shown in Figure 2.8, and the data is summarised in Table 2.2. All complexes show two successive one electron oxidation processes due to removal of electrons from the Mo_2-δ orbitals. The separation of the two redox processes is indicative of the thermodynamic stability of the mixed valence state. The first oxidation for complexes **1** – **5** is reversible, although the second oxidation process becomes more irreversible as electron withdrawing groups are added to the ligand backbone. Cationic dimolybdenum complexes are often unstable, and the electron withdrawing groups on the ligand reduce the electron density on the Mo_2^{5+} units making them more susceptible to attack by the donor solvent.[24]

$$K_c = e^{\frac{\Delta E_{1/2} F n_1 n_2}{RT}}$$

Equation 2.1: The determination of K_c from electrochemical parameters.

The comproportionation constant, K_c, can be determined by measuring the separation between successive oxidation processes ($\Delta E_{1/2}$). Due to the quasi-reversible second oxidation, the $\Delta E_{1/2}$ values for complexes **1 – 5** were estimated from the $E_{pc}(2) - E_{pc}(1)$ separation. The corresponding K_c values have been determined using Equation 2.1 (where n_1 and n_2 are the number of electrons involved in each redox couple, F is the Faraday constant, R is the gas constant and T is the temperature)and included in Table 2.2 for comparison. However, it is important to note that the rigorous determination of K_c relies on reversible oxidation processes, so the $\Delta E_{1/2}$ will be compared in the discussion. A full discussion of theory underpinning the electrochemical discussion can be found in chapter 1.

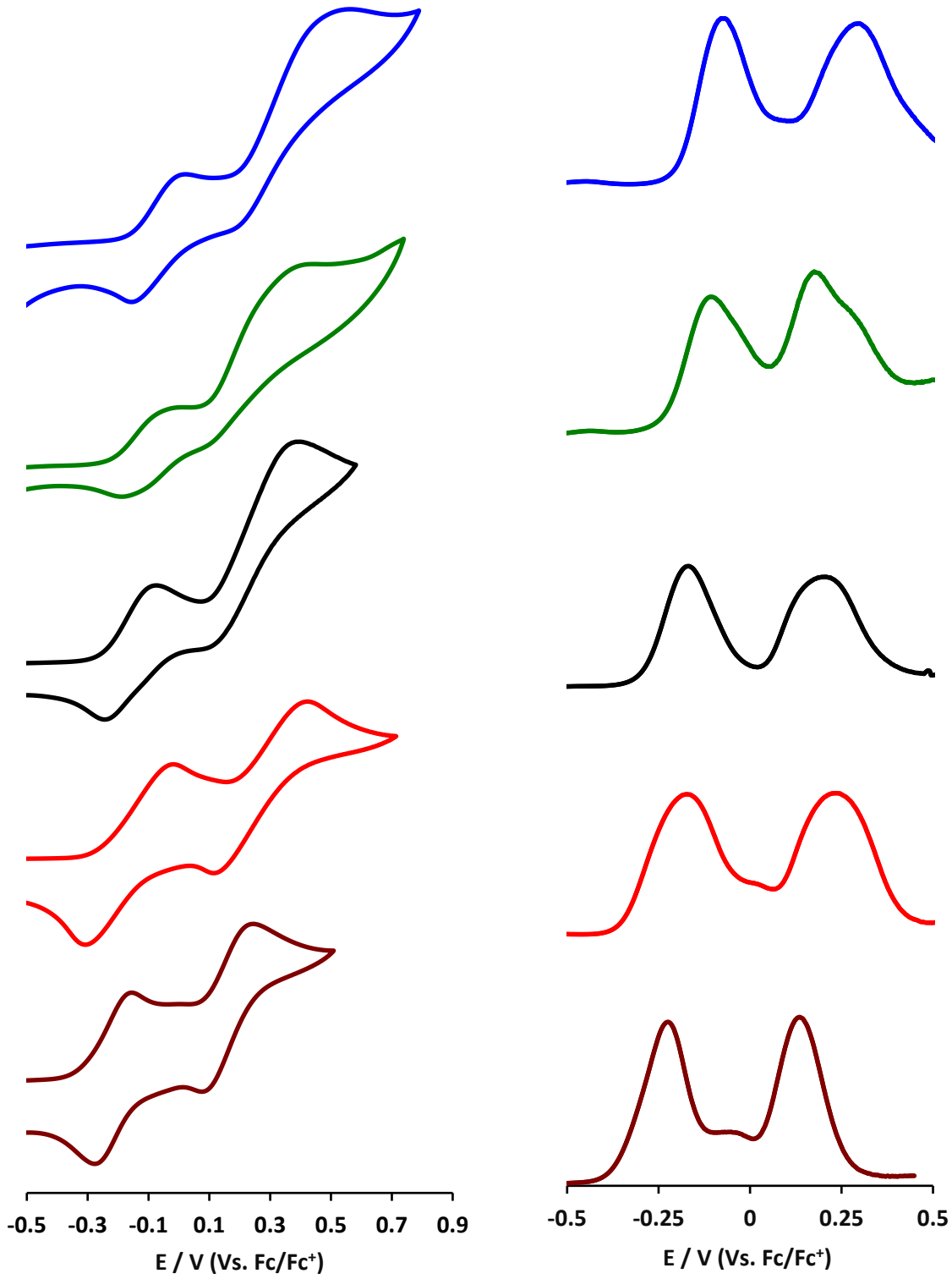

*Figure 2.8: CV (left, 100 mVs^{-1}) and DPV (right, 10 mVs^{-1}) of complexes **1** (blue), **2** (green) **3** (black), **4** (red) and **5** (brown) in 0.1 M NBu_4PF_6 / THF solution at a concentration of 5 mM, and referenced against the Fc/Fc^+ couple (0.00 V).*

The first oxidation potential ($E_{1/2}$ (1)) is anodically shifted as electron withdrawing groups are added to the ligand backbone with **1** (-0.078 V) being the most difficult to oxidise and **5** (-0.223 V) being the easiest.[25,26,27] The Cl and Br groups decrease the electron density on the dimolybdenum cores making them more difficult to oxidise, and as the Cl is a better electron withdrawing group than Br complex **1** exhibits a greater anodic shift compared to **2** (-0.115 V). The Me groups in **4** (-0.176 V) and **5** (-0.223 V) increase electron density on the dimolybdenum core resulting in them becoming more easily oxidised.

*Table 2.2: Cyclic voltammetry data for complexes **1 – 5** in 0.1 M NBu_4PF_6 / THF solution at a concentration of 5 mM, and referenced against the Fc/Fc^+ couple (0.00 V).*

Complex	$E_{1/2}$ (1) / V	E_{pc}(1) / V	E_{pc}(2) / V	ΔE_{pc}/ V	K_c (x 10^6)
1	-0.078	0.059	0.494	0.435	22.2
2	-0.115	-0.036	0.379	0.415	10.2
3	-0.165	-0.133	0.311	0.444	32.1
4	-0.176	-0.137	0.324	0.461	62.1
5	-0.223	-0.216	0.196	0.412	9.2

The $\Delta E_{1/2}$ and therefore the K_c are often purportedly related to the extent of electronic coupling in a MV system, but as the $\Delta E_{1/2}$ and the K_c are a thermodynamic properties the absolute values need to be discussed with care.[28,29] For covalent bridged dimolybdenum systems a K_c of ~10^4 is typically indicative of strong electronic coupling (Class III behaviour). This is smaller than the K_c of ~10^6 thought to be indicative of potential Class III behaviour in monometallic systems, and is because the charge is delocalised over two molybdenum atoms, and is therefore more diffuse.[19,30,31] Complexes **1 – 5** have a ΔE_{pc} of between 0.412 V and 0.461 V with no discernible trend based on the electronic donating or withdrawing nature of the ligand but in all cases the magnitude of the ΔE_{pc} potentially indicates strong coupling. The values of ΔE_{pc} are all comparable but complexes **1, 2** and **4** are expected to show redox

asymmetry due to the asymmetric nature of the bridging ligand, although the extent of redox asymmetry cannot be determined for these systems, it typically increases the observed $\Delta E_{1/2}$.[32,33] $[Mo_2(Piv)_3]_2(\mu_2$-oxalate) shows a decrease in thermodynamic stability of the MV state with a $\Delta E_{1/2}$ of 280 mV when compared to complexes **1 – 5** despite having a significantly larger electronic coupling parameter.[19] This large increase in the $\Delta E_{1/2}$ is a result of an increase in columbic interactions and through space electron transfer between the two dimetal centres.

2.4.6 *UV-Vis Absorption spectroscopy*

The UV-Vis absorption spectra for complexes **1 – 5** in THF are displayed in Figure 2.9 and the data summarised in Table 2.3. The assignments were aided by TD-DFT due to the complexity of the spectra, the calculated spectra and their transitions for complexes **1' – 5'** are displayed *vide infra*.

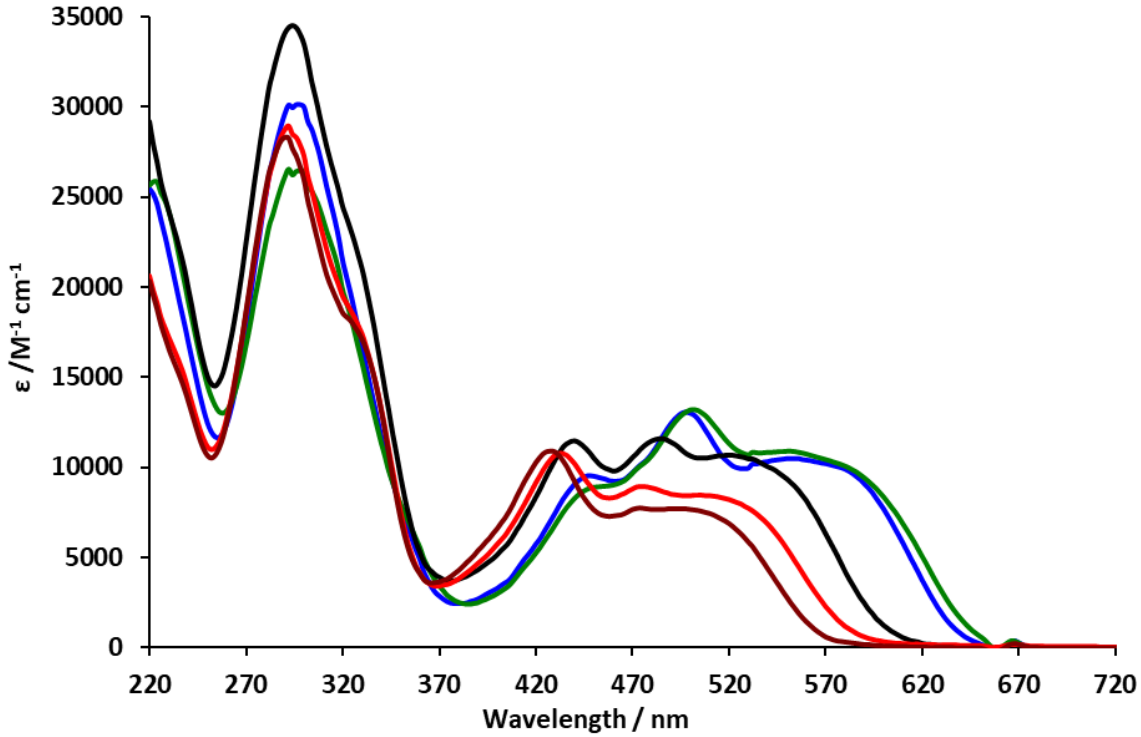

*Figure 2.9: The UV-Vis spectra of complexes **1** (blue), **2** (green) **3** (black), **4** (red) and **5** (brown) in THF.*

Complexes **1 – 5** have two absorbances between 290 – 330 nm associated with the pivalate-π → π* transitions. The two transitions are observed in a ~2:1 ratio which has been attributed to the cis and

trans pivalate ligands in related compounds.[18,19] The complexes all exhibit multiple transitions in the visible region that become increasingly blue shifted with the addition of electron donating groups. The lowest energy shoulder at ca. 530 nm for complexes **1 – 4** is assigned as the Mo_2-δ → pyridazine-π* (HOMO → LUMO) metal to ligand charge transfer (MLCT) as the transition is sufficiently removed in the TD-DFT *vide infra*. As the HOMO/LUMO gap increases from complex **1'** to **4'** the MLCT transition is blue shifted due to the increase in the electron donating character of the ligand. The Mo_2-δ → pyridazine π* (HOMO → LUMO+2) MLCT for complex **5** (472 nm) shows a large blue shift compared to **4** (514 nm). The transition from the HOMO/HOMO-1 to LUMO+1 for complexes **1 – 4** and the transitions from HOMO/HOMO-1 to LUMO/LUMO+1 for **5** are attributed to the Mo_2 -δ → Mo_2 -δ* transitions, although these are often too weak to be observed alongside the intense MLCT absorptions. Complexes **1 – 5** have several prominent transitions between 350 – 650 nm which include, Mo_2-δ → Mo_2-π* transitions and Mo_2-π → Mo_2 -δ*transitions, as well as transitions to or from hybridised orbitals such as the Mo_2-δ → Mo_2-δ/pyridazine-π* and Mo_2-δ/pyridazine-π → Mo_2-δ* transitions.

*Table 2.3: The UV-Vis data for complexes **1** – **5** in THF.*

Complex	*Cis* Piv π → Piv π* / nm (ε / M^{-1} cm^{-1})	Trans Piv π → Piv π* / nm (ε / M^{-1} cm^{-1})	Mo_2 δ (HOMO) → pyridazine π* / nm (ε / M^{-1} cm^{-1})
1	298 (30156)	326 (18732)	556 (9957)
2	296 (26500)	328 (16700)	554 (10880)
3	296 (34520)	326 (21800)	520 (10680)
4	296 (28963)	326 (18350)	514 (8377)
5	292 (28308)	328 (17528)	472 (7728)

2.4.7 *Density functional theory*

Theoretical calculations have been employed to help rationalise the observed spectroscopic behaviour of complexes **1** – **5** and were carried out by Dr Nathan Patmore and Dr Anthony Meijer (University of Sheffield). DFT calculations were performed on model complexes (**1'** - **5'**), in which the pivalate ligands have been replaced by formate groups to reduce computational time. The calculated frontier molecular orbital energy level diagrams for **1'** – **5'** are shown in Figure 2.10 and the Gaussview plots of selected orbitals of **3'** are shown in Figure 2.11. For complexes **1 – 5** the HOMO and the HOMO-1 are the Mo_2- δ orbitals. The HOMO results from the in-phase combination of the Mo_2-δ orbitals, which mixes with a pyridazine-π orbital, while the HOMO-1 is obtained from the out-of-phase combination of the Mo_2- δ orbitals which mixes with a pyridazine- π* orbital.[34]

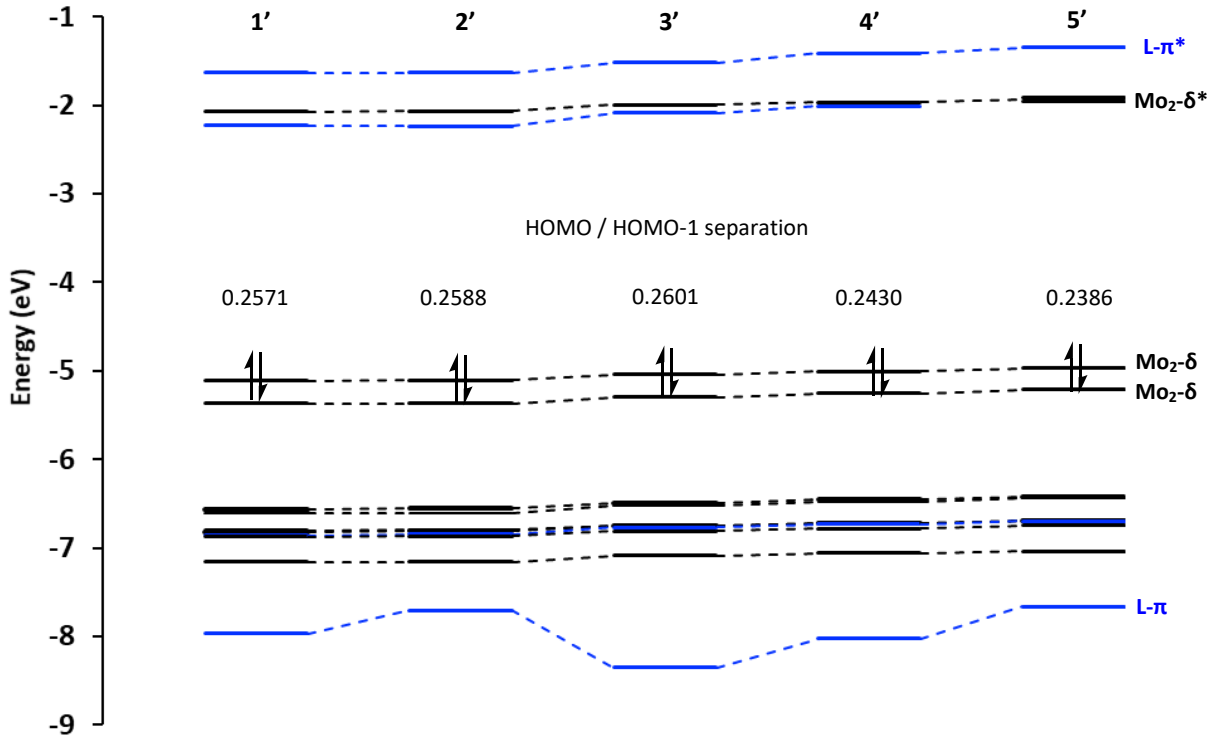

*Figure 2.10: The calculated frontier orbital energy level diagrams of model compounds **1'** - **5'**.*

The delta orbitals are non-degenerate due to the interactions of the metal and ligand, and the HOMO/HOMO-1 separation is therefore a measure of interaction between the Mo_2- δ orbitals and pyrazine-π orbitals, and hence the extent of coupling. Unlike previously reported asymmetric

dimolybdenum complexes very little change is observed in the HOMO/HOMO-1 separation.[5,32,33] The introduction of asymmetry increases the degeneracy between the two metal centres and can therefore effect the HOMO/HOMO-1 separation. The calculated HOMO/HOMO-1 separation varies by 0.022 eV between **3'** (0.2601 eV) and **5'** (0.2386 eV), this indicates that changing the asymmetry of the ligand has little to no effect on the HOMO/HOMO-1 separation in the reported examples, which is in agreement with the electrochemical analysis where no significant change in the ΔE_{pc} is observed. The complexes containing electron withdrawing groups (**1'** and **2'**) have marginally larger HOMO/HOMO-1 splittings than the complexes containing electron donating groups (**4'** and **5'**) which could indicate better coupling but could also be indicative of a greater redox asymmetry. When comparing the calculated HOMO/HOMO-1 separations with the reported separations for $[Mo_2(DAniF)_3]_2(\mu_2\text{-}OOCCOS)$ (DAniF = N,N'-di(*p*-anisyl) formamidinate) ([OO–OS]) (0.509 eV), $[Mo_2(DAniF)_3]_2(\mu_2\text{-}S_2CCO_2)$ ([SS–OO]) (0.749 eV), and $[Mo_2(DAniF)_3]_2(\mu_2\text{-}SSCCOS)$ ([SS–OS]) (0.759 eV) complexes **1 – 5** are expected to have decreased orbital overlap in comparison.[5]

For complexes **1' – 4'** the LUMO is the pyridazine π* orbitals and the LUMO+1 is one of the Mo_2-δ* orbitals. For complex **5'** the LUMO and LUMO+1 are both assigned as the Mo_2-δ* molecular orbitals and is a reflection of having electron donating groups on the ligand which raises the energy of pyridazine-π orbitals. The HOMO-9 is the pyridazine-π orbital that has the correct symmetry to interact with the in-phase Mo_2-δ orbital**.** Interestingly, the Mo_2-δ is situated evenly between the pyridazine-π and pyridazine-π* orbitals allowing for the complexes to potentially have access to both the electron hopping and hole hopping mechanisms if the bridge orbitals are involved in coupling. The energy of the HOMO and HOMO-1 groups increases in comparison to **3'** as more electron donation groups are added (**4'** and **5'**) and decreases in comparison to **3'** as better electron withdrawing groups are added (**1'** and **2'**). As more electron donating groups are added to the ligand the energy of the pyridazine-π* orbital increases to a greater extent than observed for the Mo_2-δ orbitals. Therefore, the Mo_2-δ – pyridazine-π* gap increases, matching the decrease in the absorption maxima of the Mo_2-δ → pyridazine-π* transitions observed by UV-Vis spectroscopy.

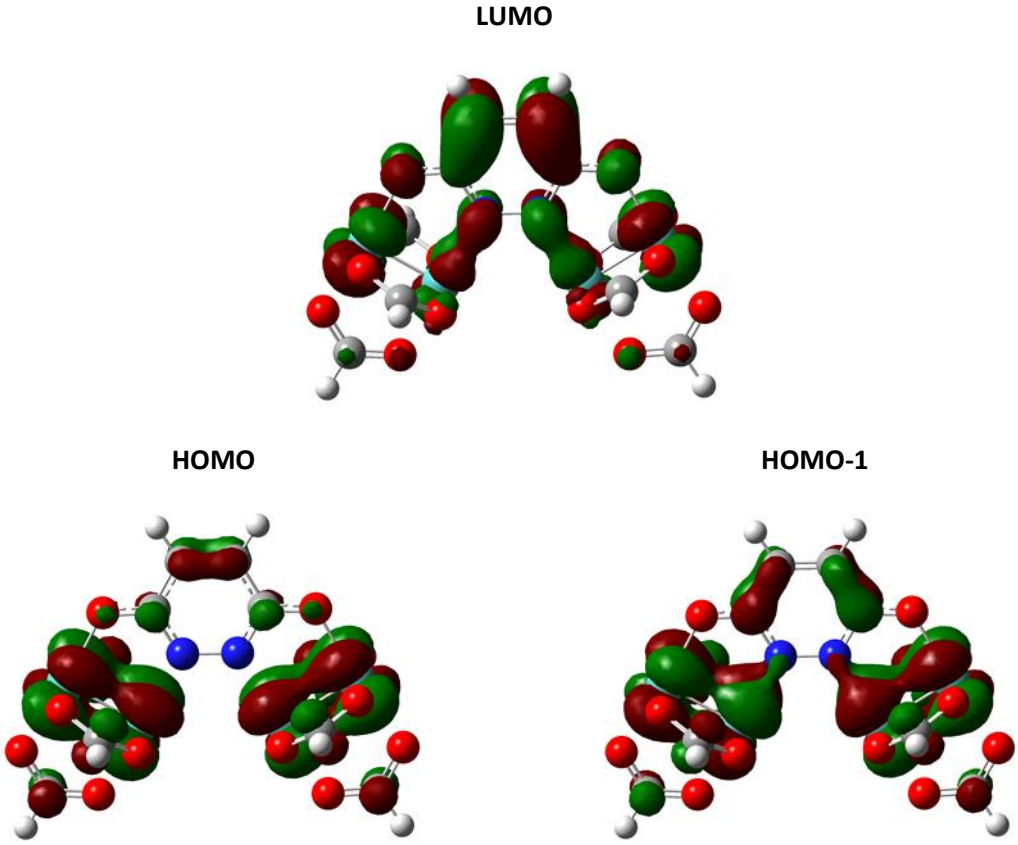

*Figure 2.11: Gausview plots (0.03 isosurface value) of selected orbitals for **3'**.*

2.4.7.1 TD-DFT calculations

The optical transitions for **1'** were calculated in THF, with the simulated spectra and the calculated transition energies compared in Figure 2.12 and summarised in Table 2.4.

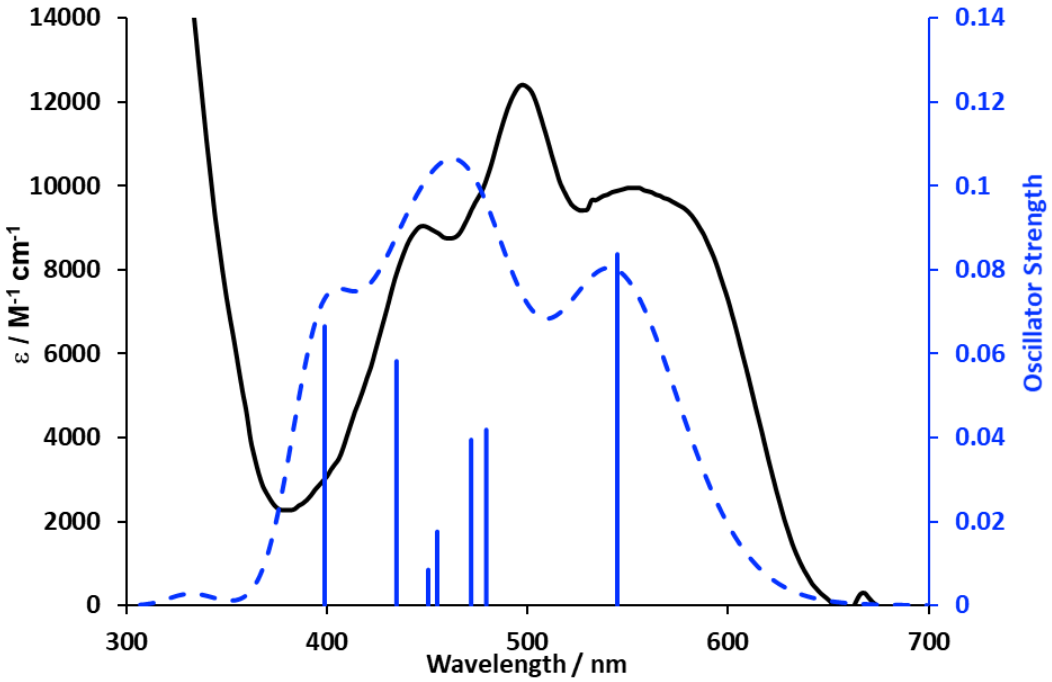

*Figure 2.12: The UV-Vis spectra of complexes **1** (black), the calculated spectra of **1'** (blue) and the calculated transitions with oscillator strengths of $f > 0.005$*

The experimental and calculated spectra are in good agreement in both energy and intensity. The calculated spectra of **1'** predicts the transitions at a slightly higher energy as a result of changing the ancillary ligands from Piv to formate groups, which decreases the energy of the HOMO and increases the energy of any transitions occurring from the Mo_2-δ orbitals. The lowest energy transition calculated for **1'** occur at 544 nm (0.0838 eV) and can be assigned as the Mo_2-δ → pyridazine-π* MLCT transition. The next peak observed experimentally at 450 nm is calculated to arise from a mixture of Mo_2-δ → Mo_2-δ*, Mo_2-δ → Mo_2-π* and Mo_2-δ → Mo_2-δ*/ pyridazine-π* transitions. The third feature at 400 nm corresponds to another Mo_2-δ → Mo_2-δ*/ pyridazine-π* mixed transition.

*Table 2.4: Calculated transitions for **1'** (f > 0.005) in THF, transitions are assigned on their most significant character.*

Energy / eV	λ_{max} / nm	*f*	Assignment
2.276	544	0.0838	Mo_2-δ → pyridazine-π*
2.586	479	0.0419	Mo_2-δ → Mo_2-δ*
2.627	471	0.0395	Mo_2-δ → pyridazine-π* / Mo_2-δ → Mo_2-δ *
2.724	455	0.0176	Mo_2-δ → Mo_2 -π*
2.751	450	0.0085	Mo_2-δ → Mo_2 -π*
2.851	434	0.0583	Mo_2-δ → Mo_2-δ*/ pyridazine-π*
3.106	399	0.0666	Mo_2-δ → Mo_2-δ*/ pyridazine-π*

The calculated spectra for **2' – 5'** are also in reasonable agreement with the experimental observations and are summarised in Table 2.5 - 2.8. The results demonstrate that the lowest energy transition is likely to be due to the Mo_2-δ → pyridazine-π* transition, with a mixture of Mo_2-δ → Mo_2-δ*, Mo_2-δ → Mo_2-π* and Mo_2-δ → Mo_2-δ*/ pyridazine-π* transitions responsible for the other features in the visible region.

*Table 2.7: Calculated transitions for **5'** (f > 0.005) in THF. Transitions are assigned on their most significant character.*

λ /eV	λ_{max} / nm	*f*	Assignment
2.359	525	0.035	Mo_2-δ → Mo_2-δ*
2.622	472	0.0256	Mo_2-δ → Mo_2-δ*
2.650	467	0.0101	Mo_2-δ → Mo_2-π* / Mo_2-δ → Mo_2-δ*
2.744	451	0.0075	Mo_2-δ → Mo_2-π*
2.746	451	0.0171	Mo_2-δ → Mo_2-δ* / Mo_2-δ → Mo_2-π*
2.981	415	0.1155	Mo_2-δ → pyridazine -π*
3.189	388	0.0056	Mo_2-π → Mo_2-δ*
3.242	382	0.0873	Mo_2-δ → pyridazine -π*

*Table 2.5: Calculated transitions for **4'** (f > 0.005) in THF. Transitions are assigned on their most significant character.*

λ /eV	λ_{max} / nm	*f*	Assignment
2.350	527	0.0439	Mo_2-δ → pyridazine -π*
2.618	473	0.0286	Mo_2-δ → Mo_2-δ*
2.656	466	0.0131	Mo_2-δ → Mo_2-π* / Mo_2-δ → pyridazine -π*
2.740	452	0.0114	Mo_2-δ → pyridazine -π*
2.754	450	0.0139	Mo_2-δ → Mo_2-π*
2.949	420	0.1067	Mo_2-δ→ Mo_2-δ*/ pyridazine -π*
3.219	385	0.0764	Mo_2-δ → Mo_2-δ*/ pyridazine -π*

Table 2.8: Calculated transitions for 3' (f > 0.005) in THF. Transitions are assigned on their most significant character.

λ /eV	λ_{max} / nm	*f*	Assignment
2.321	534	0.0644	Mo_2-δ → pyridazine -π*
2.622	472	0.0403	Mo_2-δ → Mo_2-δ*
2.645	468	0.0166	Mo_2-δ → pyridazine -π*
2.741	452	0.0202	Mo_2-δ → pyridazine -π*/ Mo_2-δ → Mo_2- π*
2.751	450	0.0072	Mo_2-δ → Mo_2- π*
2.884	429	0.0801	Mo_2-δ → Mo_2-δ*/ pyridazine -π*
3.160	392	0.0587	Mo_2-δ → Mo_2-δ*/ pyridazine -π*
3.180	389	0.008	Mo_2- π → Mo_2-δ*
3.181	389	0.0051	pyridazine -π → Mo_2-δ*

*Table 2.6: Calculated transitions for **2'** (f > 0.005) in THF. Transitions are assigned on their most significant character.*

λ /eV	λ_{max} / nm	*f*	Assignment
2.273	545	0.0873	Mo_2-δ → pyridazine -π*
2.589	478	0.0478	Mo_2-δ → Mo_2-δ*
2.619	473	0.0416	Mo_2-δ → pyridazine -π*
2.723	455	0.0182	Mo_2-δ → Mo_2-δ
2.752	450	0.0082	Mo_2-δ → Mo_2- π*
2.847	435	0.0556	Mo_2-δ → Mo_2-δ/ pyridazine -π*
3.097	400	0.0705	Mo_2-δ → Mo_2-δ/ pyridazine -π*

2.4.8 *Spectroelectrochemistry*

In order to understand the electronic properties of complexes **1 – 5** and their redox products, spectroelectrochemical studies have been carried out. The UV-Vis-NIR-IR spectra of complexes [**1 – 5**]^{n} (n= 0, 1, 2) were collected from 1 mM THF solutions in 0.1 M NBu_4PF_6 for the UV-Vis-NIR region, and in the IR from 10 mM THF solutions in 0.1 M NBu_4PF_6 in THF.

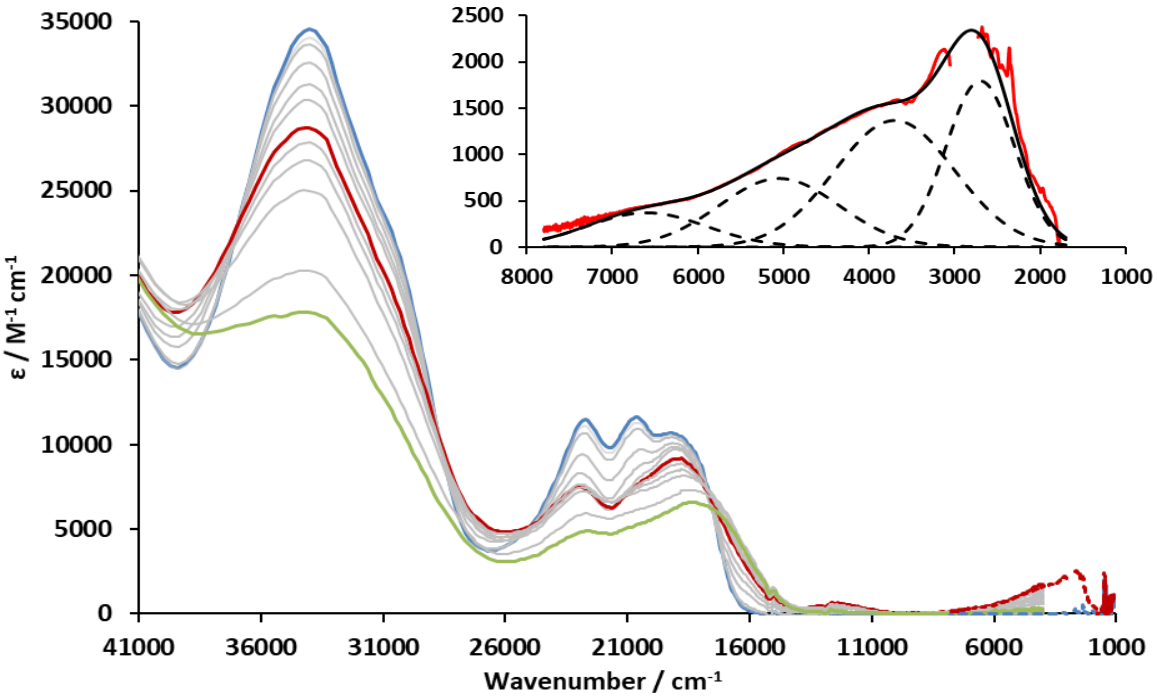

*Figure 2.13: The UV-Vis NIR SEC (solid line) and the IR SEC (Dashed line) of complex **3** in 0.1M NBu_4PF_6 /THF. **3** (blue), **3**$^{+}$ (red) and **3**$^{2+}$ (green). Top Right: A magnified portion of the IR spectra for **3**$^{+}$ showing the charge resonance transition (red), the Gaussian curves used to determine the integral (Black dashed lines), and the sum of the Gaussian curves (black solid line). The region around 3000 cm^{-1} is not shown due to strong THF CH vibrations.*

The UV-Vis-NIR-IR spectra of **3**, **3**$^{+}$ and **3**$^{2+}$ are displayed in Figure 2.13. The sequential formation of **3**$^{+}$ and **3**$^{2+}$ in the spectroelectrochemical studies is evidenced by the appearance of two separate isosbestic points in the **3** → **3**$^{+}$ and **3**$^{+}$ → **3**$^{2+}$ spectra at 17543 cm^{-1} (570 nm) and 17301 cm^{-1} (578 nm) respectively. Following a one electron oxidation a band grows in the NIR at 2780 cm^{-1} (3597 nm) which has been attributed to charge resonance band (class III) due to the relatively intense non-Gaussian transition that exhibits low energy cut off. This is confirmed as upon further oxidation (**3**$^{+}$ → **3**$^{2+}$) the band disappears. Due to the intense THF CH vibrations at 3000 cm^{-1}, the IR-SEC measurement for **3**

were repeated in d_8-THF to move the vibrations from the peak maxima and ensure the results were concurrent. A comparison of the charge resonance band observed for $\mathbf{3}^+$ in THF and d_8-THF is shown in Figure 2.14.The results from the spec-IR are in excellent agreement. An in-depth discussion of the charge resonance band can be found in section 2.4.9.

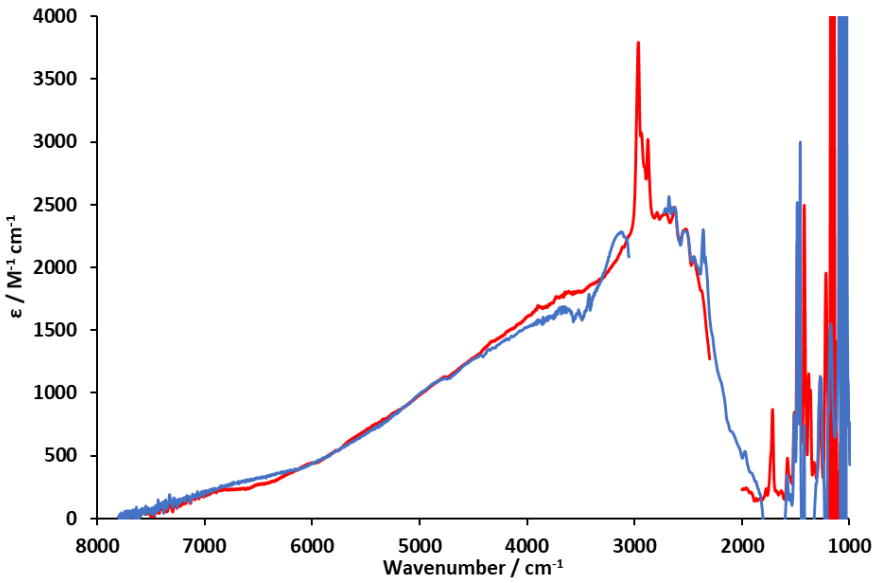

Figure 2.14: The IR spectra for $\mathbf{3}^+$ showing the charge resonance transition in THF (blue) and d_8-THF (red).

The MLCT for **3** is observed at 19230 cm^{-1} (520 nm), following the **3** → $\mathbf{3}^+$ oxidation the MLCT decreases in intensity and significantly broadens due to the appearance of a ligand to metal charge transfer (LMCT, Pyridazine-π → Mo_2-δ SOMO) as well as red shifting to 18868 cm^{-1} (530 nm). As the SOMO is evenly situated between the pyridazine-π (HOMO-9) and π* (LUMO) in **3'**, the complex is expected to undergo ET through both the electron hopping and hole hopping formalisms, resulting in both an MLCT and LMCT. As these are of similar energy the spectra will show a superposition of both the LMCT and MLCT. The peaks at 20661 cm^{-1} (484 nm) and 22727 cm^{-1} (440 nm) show a larger decrease in intensity following a one electron oxidation but no observable change in energy. Following the $\mathbf{3}^+$ → $\mathbf{3}^{2+}$ the MLCT is redshifted to 18181 cm^{-1} (550 nm), with a decrease in intensity and a further

broadening of the peak. The peaks observed at 20661 cm^{-1} (484 nm) and 22727 cm^{-1} (440 nm) show a further decrease in intensity. The spectra regained its original features following the reduction back to the neutral species but at ca. 60 % intensity as a result of the quasi-reversible second oxidation.

The UV-Vis spectroelectrochemical spectra for complexes **1, 2, 4** and **5** are shown in Figure 2.15, as all the spectra have similar features to **3** only the trends will be discussed. Upon oxidation ($\mathbf{M_4} \rightarrow \mathbf{M_4^+}$) all complexes exhibit a band resulting from ET in the NIR-IR, the bands are relatively intense, non-Gaussian and exhibit a low energy cut off, all of which indicate the complexes are class III. There is no change in the energy of the charge resonance transitions, although the intensity varies with $\mathbf{3^+}$ and $\mathbf{5^+}$ being the most intense, $\mathbf{4^+}$ showing a marginal decrease in intensity and $\mathbf{1^+}$ and $\mathbf{2^+}$ being the least intense transitions. An in-depth discussion and comparison of the charge resonance bands, and the determination of the electronic coupling parameter can be found in 2.4.9.

The effect of the substituent on the ligand backbone directly affects the changes observed in the spectra following the oxidation from $\mathbf{M_4} \rightarrow \mathbf{M_4^+}$**.** When compared to $\mathbf{3^+}$ the addition of electron donating groups ($\mathbf{4^+}$ and $\mathbf{5^+}$) results in a decrease in intensity of the transitions in the visible region, and an increased broadening of the MLCT transition as result of the LMCT (Pyridazine-π → Mo_2-δ SOMO) occurring at lower energy. Whereas the addition of electron withdrawing groups ($\mathbf{1^+}$ and $\mathbf{2^+}$) the transitions in the visible region are more intense and the MLCT does not broaden to the same degree as $\mathbf{3^+}$. Following the $\mathbf{M_4^+} \rightarrow \mathbf{M_4^{2+}}$ the transitions in the visible region continue to decrease in intensity following the same trend as above, the MLCT transitions broaden further and the peak moves to lower energy as a result, with the species containing the electron donating groups ($\mathbf{4^{2+}}$ and $\mathbf{5^{2+}}$) red shifting to a larger degree.

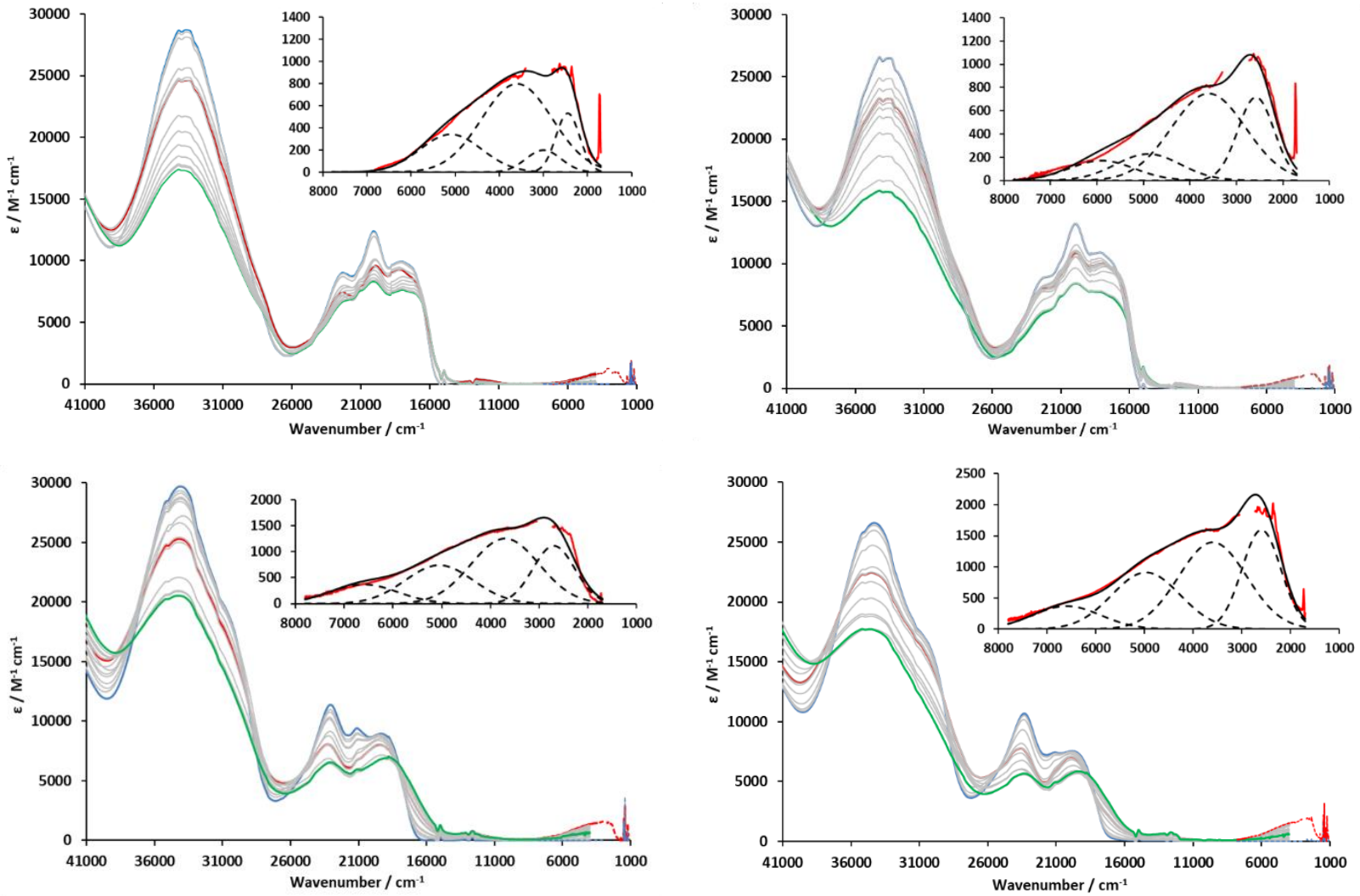

*Figure 2.15: The UV-Vis NIR SEC (solid line) and the IR SEC (Dashed line) of complexes **1** (top left), **2** (top right), **4** (bottom left) and **5** (bottom right) in 0.1M NBu_4PF_6 /THF. M_4 (blue), M_4^+ (red) and M_4^{2+} (green). Top Right: A magnified portion of the IR spectra for M_4^+ showing the charge resonance transition (red), the Gaussian curves used to determine the integral (Black dashed lines), and the sum of the Gaussian curves (black solid line). The region around 3000 cm^{-1} is not shown due to strong THF CH vibrations.*

2.4.9 *Calculation of the cross-coupling matrix parameter (H_{ab})*

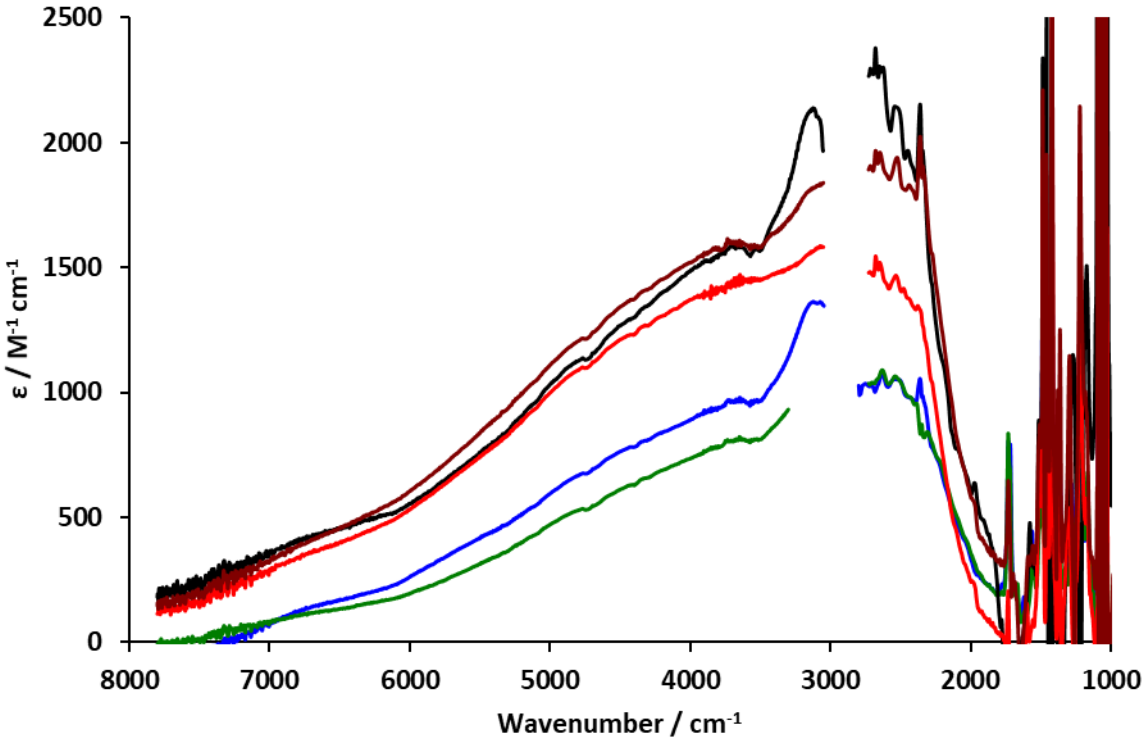

*Figure 2.16: The overlayed charge resonance transitions of **1**$^+$ (blue), **2**$^+$ (green) **3**$^+$ (black), **4**$^+$ (red) and **5**$^+$ (brown). The region around 3000 cm^{-1} is not shown due to strong THF CH vibrations.*

The charge resonance bands of **1**$^+$ **- 5**$^+$ are displayed in Figure 2.16, all complexes are classified as being class III as the charge resonance bands are relatively intense, non-Gaussian with a significant low energy cut off. All the ν_{max} values are between 2720 cm^{-1} (**5**$^+$) and 2780 cm^{-1} (**3**$^+$), and band shapes are similar for all complexes. The intensity does vary between the complexes, with the symmetric systems (**3**$^+$ and **5**$^+$) having greater intensity than the asymmetric systems. The predicted peak with at half height ($\Delta\nu_{1/2}$°) predicts the peak width for a Gaussian transition centred at the ν_{max} of the experimental transition and can be calculated using Equation 2.2. The $\Delta\nu_{1/2}$° predicted a peak width of between 2506 cm^{-1} (**5**$^+$) to 2534 cm^{-1} (**3**$^+$), the observed $\Delta\nu_{1/2}$ was much greater in all cases. The observed $\Delta\nu_{1/2}$ from the high energy side was calculated to be between 5194 cm^{-1} (**4**$^+$) and 4360 cm^{-1} (**2**$^+$) with no observable trend. The broadening was a result of vibronic progression, as excitation occurs from a single Mo_2-δ only one charge resonance transition is observed unlike the multiple transitions that can

be observed in mono-metallic species dimolybdenum species does not from Kramer's doublets.[10] Attempts were made to determine solvent dependence by changing the solvent to acetonitrile, but the complexes quickly decomposed upon oxidation.

$$\Delta v_{1/2}° = (2310 \times v_{max})^{\frac{1}{2}}$$

Equation 2.2: Calculation of the theoretical band maxima at half height of an IVCT transition.

The H_{ab} of a strongly coupled (Class III) MV complex is normally calculated using the equation $2H_{ab} = v_{max}$,[10,33] although this equation does not hold true for asymmetric systems as $2H_{ab} < v_{max}$. For asymmetric systems H_{ab} needs to be calculated using the generalised Muliken-Hush equation (Equation 2.3.1), where $|\mu_{ab}|$ is the transition dipole moment of the IVCT transition, e is the elementary charge of an electron and r_{ab} is the measure of distance between the donor and acceptor. This equation is a more rigorous quantum mechanical description of the coupling and makes no assumptions of the band shape and can be used for symmetric or asymmetric systems as well as class II and class III systems. $|\mu_{ab}|$ can be calculated from Equation 2.3.2 by integrating a plot of $\varepsilon(v)/v$ vs. v of the absorption band this is termed the reduced spectra.[9,11,12] The effective ET distance is often difficult to determine in strongly coupled systems as it is often a lot shorter than internuclear separation due to delocalisation onto the bridging ligand. For complexes **1 – 5** a crystallographic or computational estimate of the ET distance could be grossly inaccurate.[35,36] Stark absorption spectroscopy can be used to experimentally determine r_{ab}, but this is a specialised technique and not accessible in this study.

$$H_{ab} = \frac{|\mu_{ab}|}{e r_{ab}} \nu_{max} \quad (1)$$

$$|\mu_{ab}| = 0.0206 \left(\int \frac{\varepsilon}{\nu} dv\right)^{\frac{1}{2}} \quad (2)$$

Equation 2.3:The generalised Muliken-Hush equation.

The r_{ab} value was determined from analysis of the symmetric complexes $\mathbf{3}^{+}$ and $\mathbf{5}^{+}$. The equation $2H_{ab} = v_{max}$ can be used to calculate the electronic coupling matrix parameter (H_{ab}) and found to be 1390 cm^{-1} for $\mathbf{3}^{+}$ and 1360 cm^{-1} for $\mathbf{5}^{+}$. By taking the integral of the charge resonance transitions and using Equation 2.3.1 a value for r_{ab} was determined and found to be 1.706 Å for **3** and 1.720 Å for **5.** The experimentally determined r_{ab} values for **3** and **5** were in good agreement, therefore the average effective r_{ab} used is 1.713 Å. The crystal structure of **5** has a through space Mo2···Mo3 separation of 3.754 Å, and the significantly shorter effective ET distance is a result of delocalisation onto the bridging ligand. Although ligand asymmetry may alter r_{ab} slightly for complexes **1, 2** and **4**, it is a good approximation to use in the determination of H_{ab}.

Table 2.9: Summary of the NIR absorptions observed for $\mathbf{1}^{+}$ - $\mathbf{5}^{+}$.

Complex	ν_{max} / cm^{-1}	ε_{max} / M^{-1} cm^{-1}	$\lvert\mu_{ab}\rvert$ / eV	H_{ab} / cm^{-1}	$\Delta\nu_{1/2}$ / cm^{-1}	$\Delta\nu_{1/2}°$ / cm^{-1}
$\mathbf{1}^{+}$	2730	947	0.5841	927	4644	2511
$\mathbf{2}^{+}$	2778	971	0.6009	971	4360	2533
$\mathbf{3}^{+}$	2780	2311	0.8531	1390	4114	2534
$\mathbf{4}^{+}$	2740	1633	0.7798	1242	5194	2515
$\mathbf{5}^{+}$	2720	2162	0.8652	1360	4656	2506

The integrals of the reduced charge resonance bands for $\mathbf{1}^{+}$, $\mathbf{2}^{+}$ and $\mathbf{4}^{+}$ were used to calculate H_{ab} using Equation 2.3.2 and 2.3.1. Compounds $\mathbf{1}^{+}$, $\mathbf{2}^{+}$ and $\mathbf{4}^{+}$ show a lower degree of coupling with electronic couplings of 927, 971 and 1242 cm^{-1} consistent with the introduction of asymmetry into the system as the calculated H_{ab} are less than $v_{max}/2$ (Table 2.9). The introduction of the electron withdrawing groups (**1** and **2**) shows a greater effect on the coupling decreasing the H_{ab} by more than half. Whereas the addition of the electron donating group (**4**) decreased the electronic coupling by a third. The reduction

in the H_{ab} is consistent with the HOMO/HOMO-1 splitting which indicates that complex **1** and **2** have a greater redox asymmetry than **4.** Complexes **1 – 5** can be compared to [(Mo_2(Piv)$_3$)$_2$(μ_2-oxalate)], a similar complex with a H_{ab} of 2000 cm^{-1}, which has been assigned unequivocally as class III.[37] The absorption spectra of the MV complex shows a significant degree of low energy cut off like that observed for complexes **1 – 5.** The DFT shows that [(Mo_2(Piv)$_3$)$_2$(μ_2-oxalate)] has a HOMO/HOMO-1 separation of 0.63 eV indicating a greater degree of interaction between the Mo_2-δ and the bridge-π and π* orbitals than compounds **3** and **5** which have a HOMO/HOMO-1 separation of 0.2601 and 0.2386 eV respectively.

The calculation of the H_{ab} using the integral of the charge resonance band makes the assumption that the sample has been fully oxidised and the concentration of the MV state is equivalent to that of the neutral complex. This may not be the case if sample degradation has occurred or the thermodynamic stability of the MV ion is low resulting in a statistical mix of the M_4, M_4^+ and M_4^{2+}. Errors associated with degradation have been minimised in this study due to the extremely large thermodynamic stability of the MV ion and by running the SEC in duplicate where concurrent results were obtained for all complexes in both the UV and the IR.

2.4.10 *Electron Paramagnetic Resonance Spectroscopy*

For the EPR experiments, the MV complexes **1^+ - 5^+** were prepared by the *in-situ* chemical oxidation of the neutral complexes by the addition of one equivalent of silver hexafluorophosphate ($AgPF_6$) in THF and the resulting solutions immediately characterised by electron paramagnetic resonance spectroscopy at room temperature. Immediate measuring of the MV ion is imperative due to degradation which arises from facile ligand scrambling which was observed as new features appearing in the spectra during prolonged experiments.[38] The spectra and their simulations are shown in Figure 2.17 and the g factor and simulated hyperfine couplings reported in Table 2.10.

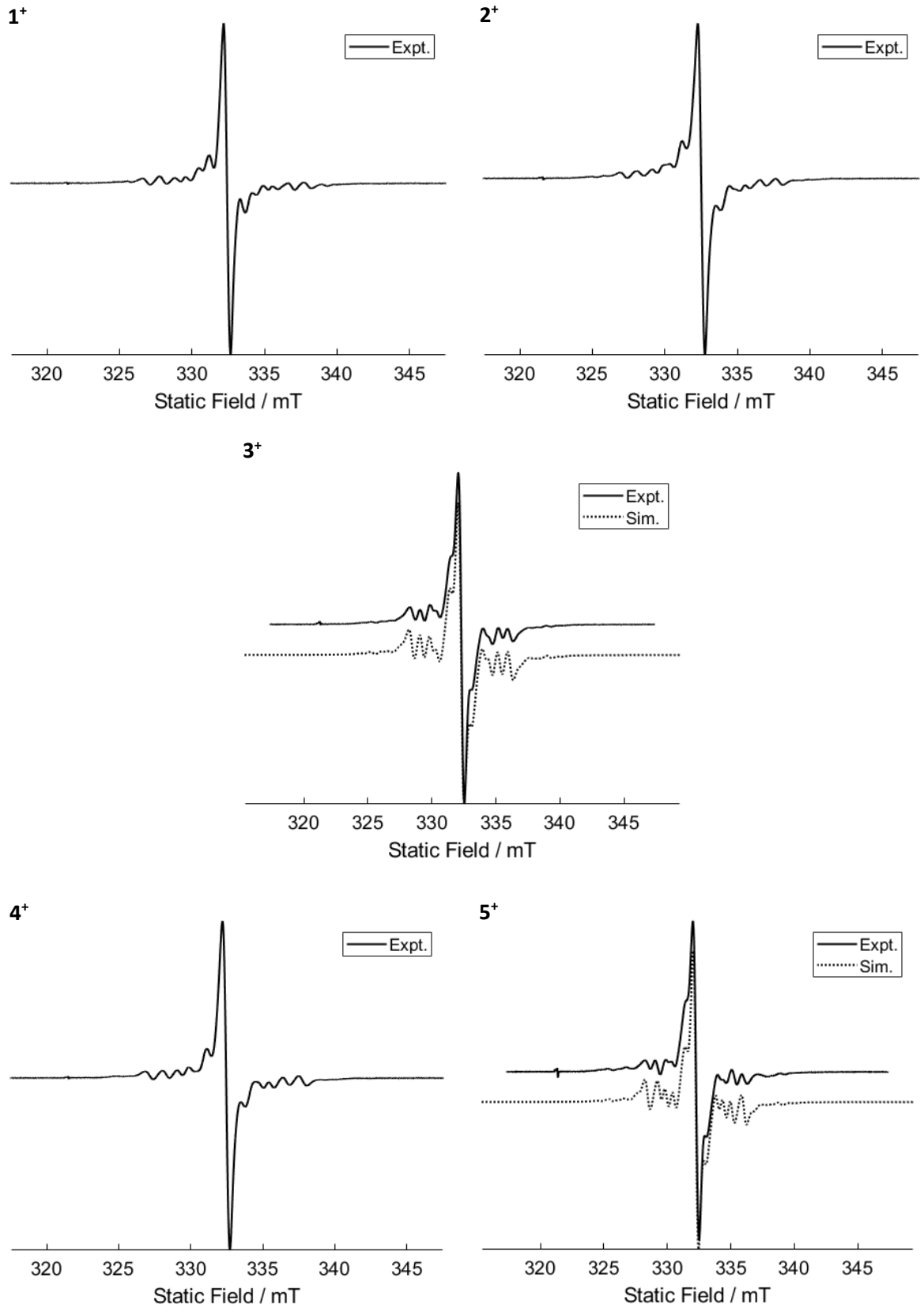

*Figure 2.17: Experimental (solid) and simulated (dashed) X-band EPR spectra **1**$^{+}$ - **5**$^{+}$ in THF. The abnormality at 321 mT is a quartz impurity.*

Table 2.10: Summary of the values determined from the simulated EPR spectra.

Complex	g-factor	A_{Iso} (1) / mT	A_{Iso} (2) / mT
1^+	1.932	-	-
2^+	1.936	-	-
3^+	1.933	1.447	1.161
4^+	1.931	-	-
5^+	1.933	1.154	1.093

In each spectra the complexes exhibit one central peak which is attributed to the ^{96}Mo (I=0, 75 % abundance) isotope, with hyperfine structures that arise from the ^{95,97}Mo (I=5/2, 25 % combined abundance) isotope. Each complex exhibits one main signal with g-factor in the range of 1.931-1.936, indicating that the unpaired electron resides primarily in a Mo_2-δ orbital.[34,39,40] The magnitude of the isotropic hyperfine splitting (A_{iso}) can be used to determine the localisation of the electron, if the electron is localised on the EPR timescale (~10^{-9} s) then the hyperfine coupling of the MV species would be around 2.8 mT. For example, Mo_2Piv_4 has a central peak at a g factor of 1.94 with an A_{iso} 2.7 mT.[2,41] For dimolybdenum 'dimer of dimers' the magnitude of the hyperfine is expected to be approximately half this value, 1.4 mT, if the electron is fully delocalised over four Mo atoms on the EPR timescale.[34] This is observed for $[(Mo_2(Piv)_3)_2(\mu_2\text{-oxalate})]^+$ which has the reported hyperfine of 1.4 mT consistent with full electron delocalisation.[34]

The EPR spectrum of **3^+** is shown in Figure 2.17 it displays a central peak at a g factor of 1.933 with a number of overlapping hyperfine splittings. The hyperfine splitting pattern can be well simulated using two equally weighted (A_{iso}(1)= 2Mo, A_{iso}(2)= 2Mo) independent hyperfine splittings of 1.447 mT and 1.161 mT, indicating that the electron is delocalised across four Mo redox centres, two separate hyperfines are observed due to the polarisation of the dimolybdenum bond. EPR analysis is a powerful tool in examining the polarization of the dimolybdenum bond, as the dimolybdenum redox centre is asymmetrically bound with one Mo coordinated to four O atoms whereas the other is coordinated to three O atoms and a N atom (Figure 2.18). As a result, the electron is drawn to one side of the dimolybdenum bond such that it is affected by each Mo differently. This is observed as a difference in

hyperfine couplings corresponding to the different chemical environments of the Mo. This can be directly observed when comparing the one hyperfine coupling observed for $[(Mo_2(Piv)_3)_2\text{-}\mu_2\text{-oxalate}]^+$ where all four Mo are in the same environment and the two hyperfine couplings observed for $\mathbf{3}^+$ where two Mo are in one environment and two are in a second enviroment.[2] The EPR spectrum of $\mathbf{5}^+$ is shown in Figure 2.17 it displays a central peak at a g factor of 1.933 with a number of overlapping hyperfine splittings. The hyperfine couplings of complex $\mathbf{5}^+$ can be well simulated using two equally weighted ($A_{iso}(1)$= 2Mo, $A_{iso}(2)$= 2Mo) independent hyperfine couplings of 1.154 mT and 1.093 mT. The magnitude of the hyperfine couplings indicate that the electron is delocalised over four Mo on the EPR timescale. The EPR analysis is consistent with the spectroelectrochemical measurements which all indicate $\mathbf{5}^+$ is a class III compound. The addition of electron donating groups results in a decrease in the polarisation of the dimolybdenum redox centre compared to $\mathbf{3}^+$ as seen by the convergence of the two hyperfine values.

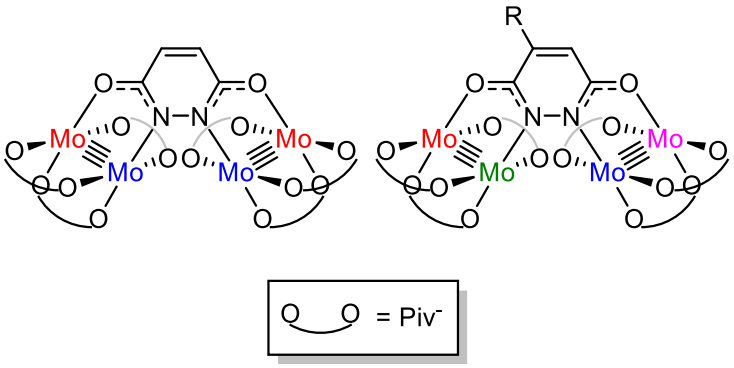

Figure 2.18: Highlighting the different coordination environments of (Left) ***3*** *and* ***5*** *(Right)* ***1, 2*** *and* ***5.***

$\mathbf{1}^+$, $\mathbf{2}^+$ and $\mathbf{5}^+$ have a central peak at a g factor of 1.932, 1.936 and 1.931 respectively, all the complexes exhibit complicated hyperfine couplings. These hyperfine couplings could not be confidently simulated using the continuous wave spectra obtained, due to the multiple overlapping hyperfine splittings. Complexes $\mathbf{1}^+$, $\mathbf{2}^+$ and $\mathbf{5}^+$ are expected to have at least four hyperfine couplings as a result of the asymmetry of the ligands as the addition of non-equivalent nuclei causing a multiplicative increase in the number of hyperfines in the system.[42] The asymmetric ligands are inducing differing degrees of

polarisation on each dimolybdenum redox centre resulting in each molybdenum atom being in a different environment and the local magnetic field affects the electron differently (Figure 2.18). This can be seen in the symmetric ligands, where changing from R = H, H to R = Me, Me results in an observable change in the hyperfine coupling. It should be noted that at least one of the hyperfine couplings in complexes $\mathbf{1}^{+}$, $\mathbf{2}^{+}$ and $\mathbf{5}^{+}$ must be in the magnitude of 2.4 mT to account for the increased hyperfine splitting with the final hyperfine being centred at 126.1 mT and I=0 peak centred at 133.3 mT such that A_{iso} ~2.4 mT. As the spectroelectrochemical results indicate the complexes are class III at least one hyperfine in the magnitude of 1.2 mT is also expected. As the asymmetric spectra all indicate localisation and delocalisation of the electron, it is believed that one side dimolybdenum redox centre primarily acts as the donor atom and the other dimolybdenum primarily acts as the acceptor despite the electron being fully delocalised. The symmetric compounds have equal charge distribution to both dimolybdenum redox centres, whereas the asymmetric complexes exhibit unequal charge distribution between the two dimolybdenum cores resulting in the polarisation of the complex similar to a strongly coupled but polarised $[Ru\text{-}Os]^{+}$ complex reported by Winter *et al.*[43] To determine whether this is the case and elucidate the exact hyperfine couplings, electron nuclear double resonance (ENDOR) spectroscopy could be used to deconvolute the spectra and determine the extent of delocalisation on each Mo atom.[42,44]

2.4.11 *The mechanism of ET*

The ET process can occur indirectly through space which is mediated by the bridge, or a through bond mechanism, although, typically a mix of both mechanisms can occur.[10] Both mechanisms are mediated by the bridge but for differing reasons: the through bond mechanism relies on the overlap of the frontier orbitals between the metals and those of the bridge and their relative energies. The ligand controls the distance and relative orientation of the metal centres which can facilitate through space electron transfer or prevent it entirely. In the case of the 3,6-dihydroxypyradazine ligand ET can occur through both mechanisms, as the frontier orbitals are of sufficient energy to allow for through bond

electron transfer and the ligand holds the redox centres in close proximity allowing for through space coupling (Figure 2.19).

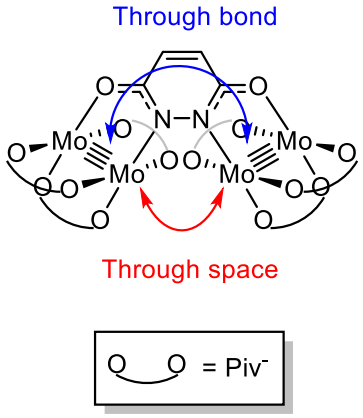

Figure 2.19: Highlighting the difference between through bond and through space electron transfer.

DFT calculations show substantial mixing of the metal and ligand orbitals, providing a suitable bridge for through bond electron transfer. The vibronic progression of the charge resonance band and appearance of an LMCT in the spectra of the MV ion is evidence that through bond electron transfer is occurring, but as little to no change in the v_{max} or spectral shape is observed despite the asymmetry of the complexes through space electron transfer must also be taking place.[10] The calculated through space $Mo_2 \cdots Mo_2$ separation is given in Table 2.11, the values are roughly 3.6 Å which is in agreement with the $Mo_2 \cdots Mo_2$ separation in **5** as determined by XRD. These distances might seem excessive for efficient through space ET, but through space ET between aromatic rings is known to occur at distances of upto 3.79 Å.[45,46]

Table 2.11: The calculated through space Mo ··· Mo separation

Complex	$Mo_2 \cdots Mo_2$ / Å	$Mo_2^{0.5+} \cdots Mo_2^{0.5+}$ / Å
1'	3.628	3.609
2'	3.626	3.593
3'	3.635	3.613
4'	3.639	3.602
5'	3.628	3.591

To determine if through space ET is occurring electrochemical analyses in differing mediums can be conducted. Geiger *et al.* have shown that changing the medium used for the electrochemical analyses can be used to determine if through space ET is helping stabilise the MV state. By using $[B(C_6H_3(3,5\text{-}CF_3)_2)_4]^-$ (Barf) a less coordinating electrolyte than $[PF_6]^-$ differences in the ion pairing can affect the $\Delta E_{1/2}$.[47–50] As in class III complexes through bond ET is largely solvent/electrolyte independent but through space ET is not, so using a less coordinating electrolyte will result in a decrease in the $\Delta E_{1/2}$ if through space ET is occurring. This cannot quantify the degree of through space coupling but can determine if through space electronic coupling stabilises the MV state.[51]

2.5 Conclusions

Two symmetric and three asymmetric dimolybdenum dimers of the general formula of $[Mo_2(Piv)_3]_2$ (μ_2-R,R'Dop) have been synthesised by stirring $[Mo_2(Piv)_3(MeCN)_2][BF_4]$ with Na_2R,R'Dop and characterised by ^{1}H NMR spectroscopy. As expected, the addition of electron donating and withdrawing groups results in significant changes to the UV-vis spectra, reflecting change to MO energies. The complicated absorption spectra are rationalised by DFT, which show a mixture of transitions in the visible region. Unexpectedly, the cyclic voltammetry and SEC UV-vis-NIR spectra for all compounds show similar features. The cyclic voltammogram for each complex displayed two successive one electron oxidations with little variation in the thermodynamic stability of the MV state and surprisingly little indication of redox asymmetry. The UV-Vis-IR spectra of the MV complexes all exhibited charge resonance transitions, with little change in the spectral shape and energy of the transitions despite variations in the electron donor/acceptor groups on the bridging Dop ligand between complexes. These surprising results may be a result of through space electron transfer dominating in these systems. However, it will be difficult to evaluate the exact mechanism.

2.6 Experimental

See chapter 8 for the methods and materials section.

2.6.1 *Synthesis of $Mo_2(Piv)_4$*

$Mo(CO)_6$ (20.000 g, 75.75 mmol) and pivalic acid (15.453 g, 151.50 mmol) were added to a Schlenk flask and suspended in a mixture of 1,2-dichlorobenzene (250 mL) and THF (100 mL). The suspension was refluxed for 36 hours to yield a dark yellow solution. The solvent was removed under reduced pressure and the resulting solid suspended in hexane (ca. 100 mL) resulting in a yellow solid and a black solution. The solid was isolated by filtration and washed with hexane until the filtrate ran clear. The solid was dried *in vacuo* to yield $Mo_2(Piv)_4$ as a bright yellow solid. Yield 20.594 g (91 %) ^{1}H NMR (400 MHz, $CDCl_3$,) δ 1.42 (s, 36H).

2.6.2 *Synthesis of $[Mo_2(Piv)_3]_2(\mu_2$-ClDop) (1)*

$Mo_2(Piv)_4$ (0.728 g, 1.22 mmol) and $[Mo_2(Piv)_2(MeCN)_6][BF_4]_2$ (1.000 g, 1.22 mmol) were added to a Schlenk flask and dissolved in a mixture of dichloromethane (20 mL) and MeCN (10 mL), the red solution was refluxed for 17 hours and cooled to room temperature. 4-Chloro-1,2-dihydro-3,6-pyridazinedione (0.170 g, 1.22 mmol) and NaOMe (0.132 g, 2.45 mmol) were suspended in MeOH (20 mL) and stirred at room temperature for 17 hours to yield a colourless solution, which was then added dropwise to the $[Mo_2(Piv)_3]^+$. This resulted in an immediate colour change to dark purple, and the resulting solution was stirred for a further 20 hours. The solvents were removed under reduced pressure and the products extracted into a mixture of hexane and dichloromethane (10 ml, 1:1) and purified by column chromatography (eluent dichloromethane/hexane (50:50 (v/v)) → dichloromethane → THF/ dichloromethane (2:98 (v/v)) collecting the first red band. The solvent was removed under reduced pressure and washed with hexane (3 x 10 ml) and dried to afford **1** as a dark purple solid. Yield 0.698 g (50 %) ^{1}H NMR (400 MHz, DMSO-d_6) δ 7.54 (s, 1H), 1.32 (s, 18H), 1.31 (s, 18H), 1.28 (s, 18H). MALDI-TOF-MS calcd. monoisotopic MW for $Mo_4C_{34}H_{55}O_{14}N_2Cl$, 1135.1, found *m/z*

1135.4 (M^+). Elemental Analysis calcd. For $Mo_4C_{34}H_{55}O_{14}N_2Cl$, C, 35.98; H, 4.88; N, 2.47; Found C, 36.26; H, 5.19; N, 2.58.

2.6.3 *Synthesis of $[Mo_2(Piv)_3]_2(\mu_2$-BrDop) (2)*

$Mo_2(Piv)_4$ (0.518 g, 0.87mmol) and $[Mo_2(Piv)_2(MeCN)_6][BF_4]_2$ (0.710 g, 0.87 mmol) were added to a Schlenk flask and dissolved in a mixture of dichloromethane (20 mL) and MeCN (10 mL), the red solution was refluxed for 17 hours and cooled to room temperature. 4-Bromo-1,2-dihydro-3,6-pyridazinedione (0.166 g, 0.87 mmol) and NaOMe (0.091 g, 1.75 mmol) were suspended in MeOH (20 mL) and stirred at room temperature for 17 hours to yield a colourless solution, which was then added dropwise to the $[Mo_2(Piv)_3]^+$. This resulted in an immediate colour change to dark purple, the resulting solution was stirred for a further 20 hours. The solvents were removed under reduced pressure and the products extracted into a mixture of hexane and dichloromethane (10 ml, 1:1) and purified by column chromatography (eluent dichloromethane /hexane (50:50 (v/v)) → dichloromethane → THF/ dichloromethane (2:98 (v/v)) collecting the first purple band. The solvent was removed under reduced pressure and washed with hexane (3 x 10 ml) and dried to afford **2** as a dark purple solid. Yield 0.477 g (46 %) ^{1}H NMR (400 MHz, DMSO-d_6) δ 7.69 (s, 1H), 1.32 (s, 18H), 1.32 (s, 18H), 1.28 (s, 18H). MALDI-TOF-MS calcd. monoisotopic MW for $Mo_4C_{34}H_{55}O_{14}N_2Br$, 1179.6, found *m/z* 1179.3 (M^+). Elemental Analysis calcd. For $Mo_4C_{34}H_{55}O_{14}N_2Br$, C, 34.62; H, 4.70; N, 2.37; Found C, 34.74; H, 4.81; N, 2.45.

2.6.4 *Synthesis of $[Mo_2(Piv)_3]_2(\mu_2$-Dop) (3)*

$Mo_2(Piv)_4$ (0.728 g, 1.22 mmol) and $[Mo_2(Piv)_2(MeCN)_6][BF_4]_2$ (1.000 g, 1.22 mmol) were added to a Schlenk flask and dissolved in a mixture of dichloromethane (20 mL) and MeCN (10 mL), the red solution was refluxed for 17 hours and cooled to room temperature. 1,2-Dihydro-3,6-pyridazinedione (0.136 g, 1.22 mmol) and NaOMe (0.132 g, 2.45 mmol) were suspended in MeOH (20 mL) and stirred at room temperature for 17 hours to yield a colourless solution, which was then added dropwise to the $[Mo_2(Piv)_3]^+$. This resulted in an immediate colour change to deep red, the resulting solution was stirred for a further 20 hours. The solvents were removed under reduced pressure and the products

extracted into a mixture of hexane and dichloromethane (10 ml, 1:1) and purified by column chromatography (eluent dichloromethane /hexane (50:50 (v/v)) → dichloromethane → THF/ dichloromethane (2:98 (v/v)) collecting the first red band. The solvent was removed under reduced pressure and washed with hexane (3 x 10 ml) and dried to afford **3** as a red solid. Yield 0.422 g (31 %) ^{1}H NMR (400 MHz, DMSO-d_6) δ 7.20 (s, 2H), 1.30 (s, 36H), 1.28 (s, 18H). MALDI-TOF-MS calcd. monoisotopic MW for $Mo_4C_{34}H_{56}O_{14}N_2$, 1100.6, found *m/z* 1100.3 (M^+). Elemental Analysis calcd. For $Mo_4C_{34}H_{56}O_{14}N_2$, C, 37.10; H, 5.13; N, 2.55; Found C, 36.95; H, 5.30; N, 2.61.

2.6.5 *Synthesis of $[Mo_2(Piv)_3]_2(\mu_2$-MeDop) (4)*

$Mo_2(Piv)_4$ (0.728 g, 1.22 mmol) and $[Mo_2(Piv)_2(MeCN)_6][BF_4]_2$ (1.000 g, 1.22 mmol) were added to a Schlenk flask and dissolved in a mixture of dichloromethane (20 mL) and MeCN (10 mL), the red solution was refluxed for 17 hours and cooled to room temperature. 4-Methyl-1,2-dihydro-3,6-pyridazinedione (0.154 g, 1.22 mmol) and NaOMe (0.132 g, 2.45 mmol) were suspended in MeOH (20 mL) and stirred at room temperature for 17 hours to yield a colourless solution, which was then added dropwise to the $[Mo_2(Piv)_3]^+$. This resulted in an immediate colour change to dark orange, the resulting solution was stirred for a further 20 hours. The solvents were removed under reduced pressure and the products extracted into a mixture of hexane and dichloromethane (10 ml, 1:1) and purified by column chromatography (eluent dichloromethane /hexane (50:50 (v/v)) → dichloromethane → THF/ dichloromethane (2:98 (v/v)) collecting the first orange band. The solvent was removed under reduced pressure and washed with hexane (3 x 10 ml) and dried to afford **4** as a red solid. Yield 0.210 g (16 %) ^{1}H NMR (400 MHz, THF-d_8) δ 7.00 (d, J = 1.0 Hz, 1H), 2.53 (s, 3H), 1.33 (s, 36H), 1.27 (s, 9H), 1.26 (s, 9H). MALDI-TOF-MS calcd. monoisotopic MW for $Mo_4C_{35}H_{58}O_{14}N_2$, 1114.7, found *m/z* 1114.4 (M^+). Elemental Analysis calcd. For $Mo_4C_{35}H_{58}O_{14}N_2$, C, 37.71; H, 5.24; N, 2.51; Found C, 37.83; H, 5.38; N, 2.56.

2.6.6 *Synthesis of $[Mo_2(Piv)_3]_2(\mu_2\text{-}Me_2Dop)$ (5)*

$Mo_2(Piv)_4$ (0.728 g, 1.22 mmol) and $[Mo_2(Piv)_2(MeCN)_6][BF_4]_2$ (1.000 g, 1.22 mmol) were added to a Schlenk flask and dissolved in a mixture of dichloromethane (20 mL) and MeCN (10 mL), the red solution was refluxed for 17 hours and cooled to room temperature. 4,5-Dimethyl-1,2-dihydro-3,6-pyridazinedione (0.170 g, 1.22 mmol) and NaOMe (0.132 g, 2.45 mmol) were suspended in MeOH (20 mL) and stirred at room temperature for 17 hours to yield a colourless solution, which was then added dropwise to the $[Mo_2(Piv)_3]^+$. This resulted in an immediate colour change to dark orange, the resulting solution was stirred for a further 20 hours. The solvents were removed under reduced pressure and the products extracted into a mixture of hexane and dichloromethane (10 ml, 1:1) and purified by column chromatography (eluent dichloromethane /hexane (50:50 (v/v)) → dichloromethane collecting the first orange band. The solvent was removed under reduced pressure and washed with hexane (3 x 10 ml) and dried to afford **5** as a dark orange solid. Yield 0.264 g (19 %) ^{1}H NMR (400 MHz, THF-d_8) δ 2.53 (s, 6H), 1.32 (s, 36H), 1.26 (s, 18H). MALDI-TOF-MS calcd. monoisotopic MW for $Mo_4C_{36}H_{60}O_{14}N_2$, 1128.7, found *m/z* 1128.4 (M^+). Elemental Analysis calcd. For $Mo_4C_{36}H_{60}O_{14}N_2$, C, 38.81; H, 5.36; N, 2.48; Found C, 38.65; H, 5.57; N, 2.58.

2.7 References

1 W. Kaim and B. Sarkar, *Coord. Chem. Rev.*, 2007, **251**, 584–594.

2 M. H. Chisholm, *Coord. Chem. Rev.*, 2013, **257**, 1576–1583.

3 P. Day, *Int. Rev. Phys. Chem.*, 1981, **1**, 149–193.

4 M. D. Ward, *Chem. Soc. Rev.*, 1995, **24**, 121–134.

5 S. Mallick, T. Cheng, L. Chen, M. Meng, Y. Y. Zhang and C. Y. Liu, *Dalt. Trans.*, 2017, **46**, 5711–5723.

6 T. Ito, N. Imai, T. Yamaguchi, T. Hamaguchi, C. H. Londergan and C. P. Kubiak, *Angew. Chemie - Int. Ed.*, 2004, **43**, 1376–1381.

7 J. C. Salsman, C. P. Kubiak and T. Ito, *J. Am. Chem. Soc.*, 2005, **127**, 2382–2383.

8 J. C. Salsman, S. Ronco, C. H. Londergan and C. P. Kubiak, *Inorg. Chem.*, 2006, **45**, 547–554.

9 M. H. Chou, C. Creutz and N. Sutin, *Inorg. Chem.*, 1992, **31**, 2318–2327.

10 D. M. D'Alessandro and F. R. Keene, *Chem. Soc. Rev.*, 2006, **35**, 424–440.

11 B. S. Brunschwig, C. Creutz and N. Sutin, *Chem. Soc. Rev.*, 2002, **31**, 168–184.

12 K. D. Demadis, C. M. Hartshorn and T. J. Meyer, *Chem. Rev.*, 2001, **101**, 2655–2685.

13 R. J. Crutchley, *Angew. Chemie - Int. Ed.*, 2005, **44**, 6452–6454.

14 M. H. Chisholm, F. Feil, C. M. Hadad and N. J. Patmore, *J. Am. Chem. Soc.*, 2005, **51**, 18150–18158.

15 A. B. Brignole, F. A. Cotton, Z. Dori and G. Wilkinson, in *Inorganic Syntheses*, Volume 13., 1972, pp. 81–89.

16 M. Jawiczuk, M. Górecki, A. Suszczyńska, M. Karchier, J. Jaźwiński and J. Frelek, *Inorg. Chem.*,

2013, **52**, 8250–8263.

17 R. H. Cayton, M. H. Chisholm, J. C. Huffman and E. B. Lobkovsky, *J. Am. Chem. Soc.*, 1991, **113**, 8709–8724.

18 R. H. Cayton, M. H. Chisholm, E. F. Putilina and K. Folting, *Polyhedron*, 1993, **12**, 2627–2633.

19 R. H. Cayton, M. H. Chisholm, J. C. Huffman and E. B. Lobkovsky, *J. Am. Chem. Soc.*, 1991, **113**, 8709.

20 F. A. Cotton, L. M. Daniels, E. A. Hillard and C. A. Murillo, *Inorg. Chem.*, 2002, **41**, 2466–2470.

21 M. H. Chisholm, R. J. H. Clark, J. Gallucci, C. M. Hadad and N. J. Patmore, *J. Am. Chem. Soc.*, 2004, **126**, 8303–8313.

22 J. M. Casas, R. H. Cayton and M. H. Chisholm, *Inorg. Chem.*, 1991, **30**, 358–360.

23 G. R. Fulmer, A. J. M. Miller, N. H. Sherden, H. E. Gottlieb, A. Nudelman, B. M. Stoltz, J. E. Bercaw and K. I. Goldberg, *Organometallics*, 2010, **29**, 2176–2179.

24 N. Elgrishi, K. J. Rountree, B. D. McCarthy, E. S. Rountree, T. T. Eisenhart and J. L. Dempsey, *J. Chem. Educ.*, 2018, **95**, 197–206.

25 B. S. Dolinar and J. F. Berry, *Dalt. Trans.*, 2014, **43**, 6165–6176.

26 C. Lin, J. D. Protasiewicz, E. T. Smith and T. Ren, *Inorg. Chem.*, 1996, **35**, 6422–6428.

27 M. B. Smith and J. March, *March's Advanced Organic Chemistry*, 2006.

28 D. M. D'Alessandro and F. R. Keene, *Dalt. Trans.*, 2004, 3950–3954.

29 R. F. Winter, *Organometallics*, 2014, **33**, 4517–4536.

30 M. H. Chisholm and N. J. Patmore, *Molecular Metal-Metal Bonds: Compounds, Synthesis, Properties*, Wiley, 1st edn., 2015.

31 M. H. Chisholm, B. J. Lear, A. Moscatelli and L. A. Peteanu, *Inorg. Chem.*, 2010, **49**, 3706–3713.

32 X. Xiao, C. Y. Liu, Q. He, M. J. Han, M. Meng, H. Lei and X. Lu, *Inorg. Chem.*, 2013, **52**, 12624–12633.

33 W. Y. Yu, M. Meng, H. Lei, X. D. He and C. Y. Liu, *J. Phys. Chem. C*, 2016, **120**, 12411–12422.

34 M. H. Chisholm and N. J. Patmore, *Acc. Chem. Res.*, 2007, **40**, 19–27.

35 G. Y. Zhu, M. Meng, Y. N. Tan, X. Xiao and C. Y. Liu, *Inorg. Chem.*, 2016, **55**, 6315–6322.

36 D. M. D'Alessandro, P. H. Dinolfo, J. T. Hupp, P. C. Junk and F. R. Keene, *Eur. J. Inorg. Chem.*, 2006, 772–783.

37 B. E. Bursten, M. H. Chisholm, R. J. H. Clark, S. Firth, C. M. Hadad, A. M. Macintosh, P. J. Wilson, P. M. Woodward and J. M. Zaleski, *J. Am. Chem. Soc.*, 2002, **124**, 3050–3063.

38 M. H. Chisholm and A. M. Macintosh, *J. Chem. Soc., Dalt. Trans.,* 1999, 1205–1208.

39 M. H. Chisholm, B. D. Pate, P. J. Wilson and J. M. Zaleski, *Chem. Commun.*, 2002, **2**, 1084–1085.

40 N. S. Dalal and C. A. Murillo, *Dalt. Trans.*, 2014, **43**, 8565–8576.

41 E. C. Fitzgerald, N. J. Brown, R. Edge, M. Helliwell, H. N. Roberts, F. Tuna, A. Beeby, D. Collison, P. J. Low and M. W. Whiteley, *Organometallics*, 2012, **31**, 157–169.

42 D. M. Murphy and R. D. Farley, *Chem. Soc. Rev.*, 2006, **35**, 249–268.

43 E. Wuttke, D. Fink, P. Anders, A. L. Maria Hoyt, W. Polit, M. Linseis and R. F. Winter, *J. Organomet. Chem.*, 2016, **821**, 4–18.

44 S. Van Doorslaer, I. Caretti, I. A. Fallis and D. M. Murphy, *Coord. Chem. Rev.*, 2009, **253**, 2116–2130.

45 B. Ding, C. Hua, C. J. Kepert and D. M. D'Alessandro, *Chem. Sci.*, 2019, **10**, 1392–1400.

46 D. L. Sun, S. V. Rosokha, S. V. Lindeman and J. K. Kochi, *J. Am. Chem. Soc.*, 2003, **125**, 15950–15963.

47 F. Barrière, N. Camire, W. E. Geiger, U. T. Mueller-Westerhoff and R. Sanders, *J. Am. Chem. Soc.*, 2002, **124**, 7262–7263.

48 F. Barrière and W. E. Geiger, *J. Am. Chem. Soc.*, 2006, **128**, 3980–3989.

49 A. Nafady, T. T. Chin and W. E. Geiger, *Organometallics*, 2006, **25**, 1654–1663.

50 W. E. Geiger and F. Barrière, *Acc. Chem. Res.*, 2010, **43**, 1030–1039.

51 A. K. Diallo, J. C. Daran, F. Varret, J. Ruiz and D. Astruc, *Angew. Chemie - Int. Ed.*, 2009, **48**, 3141–3145.

Electron localisation in symmetric localised and fully delocalised MV complexes

3.1 Abstract

A series of symmetric dimolybdenum dimers, $[Mo_2(Piv)_3]_2(\mu_2$-Dop) (**3,** H_2Dop = 3,6-dihydroxypyridazine, Piv = trimethylacetate), $[Mo_2(Piv)_3]_2(\mu_2$-Phthal) (**6,** H_2Phthal = 2,3-Dihydro-1,4-phthalazinedione) and $[Mo_2(Piv)_3]_2(\mu_2$-Pdt) (**7**, H_2Pdt = 3,6-Pyridazinedithiol) have been synthesised. The complexes were characterised by ^{1}H NMR spectroscopy and the crystal structure of **7** is reported. The stability of the mixed valent (MV) state generated following a one electron oxidation has been probed by cyclic voltammetry, with the compounds displaying ΔE_{pc} values of 0.444 V (**3**), 0.366 V (**6**) and 0.517 V (**7**). The UV-Vis-NIR spectra of $\mathbf{3}^+$ and $\mathbf{7}^+$ exhibit a relatively intense, non-Gaussian, charge resonance band in the NIR region with a low energy cut off, consistent with full delocalisation of the electron between the dimetal units (Class III). Complex **6** exhibits a low intensity Gaussian intervalence charge transfer band in the NIR consistent with localisation of the electron on one dimetal unit (class II). The complexes have a cross coupling matrix parameter (H_{ab}) of 1390 cm^{-1} ($\mathbf{3}^+$), 638 cm^{-1} ($\mathbf{6}^+$) and 1668 cm^{-1} for ($\mathbf{7}^+$). All complexes have a through space and through bond component attributed to the electron transfer event, with the change in the H_{ab} being attributed to the degree of through space electron transfer occurring which is dictated by the $Mo_2\cdots Mo_2$ separation. EPR spectroscopy of the MV species indicate the electron predominantly resides in a Mo_2-δ orbital with a g-factor of 1.93-1.94. Complex $\mathbf{3}^+$ has two hyperfine couplings of 1.447 and 1.161 mT indicating the electron is fully delocalised over all four Mo atoms. Complex $\mathbf{6}^+$ has two hyperfine couplings of 2.641 and 2.489 mT indicating the electron is localised on one dimetal unit. Complex $\mathbf{7}^+$ has one hyperfine coupling of 2.588 mT meaning the electron is delocalised between two molybdenums from different dimetal units. This is the first example of MV dimolybdenum species where localisation and delocalisation of the electron in a strongly coupled system can be observed and experimentally quantified and provides an example of how coupling can be further tuned.

3.2 Modulation of electronic coupling in mixed valence complexes

Chapter 2 explored the effect of introducing asymmetry into strongly coupled systems by the addition of electron donating and withdrawing groups onto the bridging ligand backbone. It was believed that each Mo atom had an unequal charge distribution between all four molybdenum atoms. This chapter is going to examine electron localisation in both the localised and delocalised regimes.

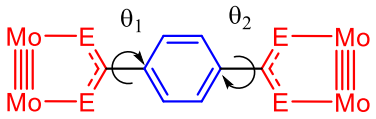

Figure 3.1: The major factors affecting electron transfer in dimolybdenum paddlewheel complexes (where E = O, S, {NH}) as described by Chisholm et al.

Chisholm *et al.* proposed two major factors which affect the electronic coupling in symmetric dimolybdenum mixed valent (MV) systems (Figure 3.1).[1] The first relates to the orbital overlap between the coordinating atoms of the bridge and the dimetal centre (highlighted in red). This term can be modified by changing the bridging ligand coordinating atoms where the substitution of N for O for S increases the degree of electronic coupling for dimolybdenum paddlewheels.[2,3] The increased coupling observed is a result of the more diffuse sulphur orbitals which allow for greater orbital overlap when compared to that observed for oxygen or nitrogen derivatives. Cotton *et al.* reported a number of complexes of the form $[Mo_2(DAniF)_3]_2(\mu_2$-EN-CC-NE) (DAniF = *N,N'*-di(*p*-anisyl)-formamidinate) and E = O or S) as shown in Figure 3.2.[4] Electrochemical measurements were conducted to determine the stability of the MV state, in both cases two successive one electron oxidations were observed, the magnitude of the separation between the two half wave potentials ($\Delta E_{1/2}$) is indicative of the thermodynamic stability of the MV state. When the bridge used was [ON-NO] the $\Delta E_{1/2}$ was 0.204 V, this increased to 0.407 V when [NS-NS] was used.

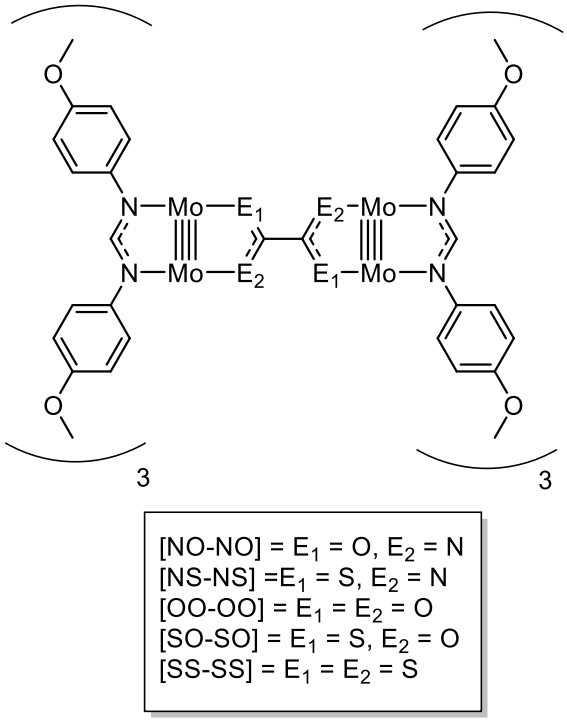

Figure 3.2: E_1E_2-CC-E_1E_2 bridged [Mo_2(DAniF)$_3$] complexes reported by Cotton et al and Liu et al.[3]

Liu *et al.* built on this work by reporting analogous complexes incorporating increasing numbers of sulphur atoms, [Mo_2(DAniF)$_3$]$_2$(μ_2-E_1E_2-CC-E_1E_2) where the bridge was oxalate [OO-OO] or the thiolated derivatives [OS-OS] and [SS-SS] (Figure 3.2).[3] Cyclic voltammetry showed that all complexes could stabilise the MV state with reported $\Delta E_{1/2}$ values of 0.260 V, 0.354 V and 0.393 V for [OO-OO], [OS-OS] and [SS-SS] respectively. Electronic coupling in the radical cations was determined by UV-Vis-NIR spectroscopy, and analysis of the charge resonance band showed that the cross-coupling matrix parameter (H_{ab}) increased from 2376 cm^{-1} [OO-OO] to 2726 cm^{-1} [OS-OS] and finally to 2950 cm^{-1} [SS-SS] as the sulphur content of the bridge was increased.[5] Sulphur atoms decrease the energy of the ligand-π* and increase the energy of the ligand-π allowing for greater degree of interactions between the Mo_2-δ orbitals and the ligand-π and π* orbitals compared to the oxygen and nitrogen containing complexes.

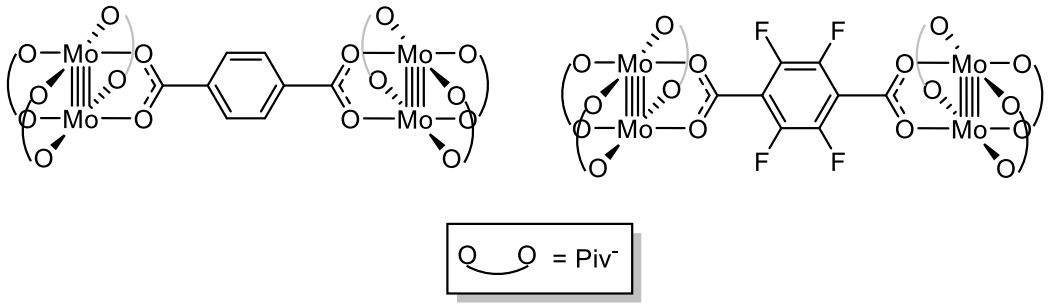

Figure 3.3: The $[Mo_2(Piv)_3]_2(\mu_2$-bridge) complexes (where the bridge = terephthalate ($O_2CC_6H_4CO_2$) or perfluoroterePhthalate ($O_2CC_6F_4CO_2$) reported by Chisholm et al.

The second factor that Cotton *et al.* identified consists of the interaction between the bridging atoms and the aromatic ring, in the case of Figure 3.1 this is the coupling between the CE_2 π-system and the Ar π-system (highlighted in blue). The degree of coupling between the two π-systems can be modulated by both the energy of the Ar π-system or by the dihedral angle (θ) between the CE_2 and the Ar ring. Chisholm *et al.* have reported the complexes $[Mo_2(Piv)_3]_2(\mu_2$-bridge) where the bridge was either terephthalate ($O_2CC_6H_4CO_2$) or perfluoroterePhthalate ($O_2CC_6F_4CO_2$) (Figure 3.3). When terephthalate was used as a bridge the complex showed no thermodynamic stabilisation of the MV state, whereas, when perfluoroterePhthalate was employed the complex showed weak stabilisation of the MV state with a $\Delta E_{1/2}$ of 0.065 V.[1,6] The increase in coupling is because CO_2-π* orbitals are lower in energy for the C_6F_4 system and are therefore closer in energy to the Mo_2-δ orbital resulting in stronger coupling.

The orbital overlap between the bridging atoms and the aromatic ring is also dependent upon the two dihedral angles between the CE_2 and the Ar ring. When θ1 = θ2 = 0 ° the complex is coplanar and has the maximum possible overlap between the CE_2 π-system and the Ar π-system but any deviation away from θ1 = θ2 = 0 ° results in a decrease in orbital overlap and therefore coupling. Through careful ligand design Chisholm *et al.* synthesised the complex $[Mo_2(Piv)_3]_2(\mu_2$-C_6H_2-2,5-$(OH)_2)$, the complex forms intramolecular hydrogen bonds, with the OH donating to the carboxylate oxygen resulting in a high energy barrier to rotation and therefore a coplanar complex (Figure 3.4). The planarity of the

complex has shown to be temperature and pH dependent; Chisholm *et al.* have shown that by using these external stimuli the complexes can act as a molecular switch.

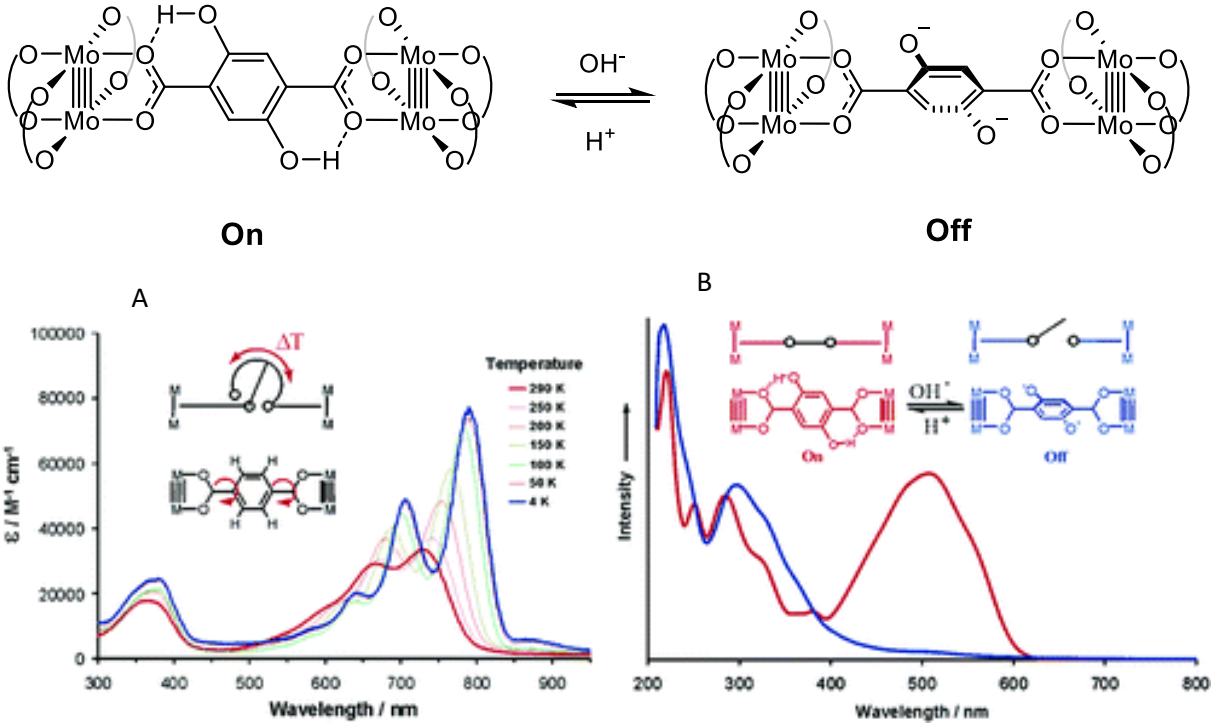

Figure 3.4: The molecular switch synthesised by Chisholm et al. with the absorption spectra showing (a) temperature dependence and (B) pH dependence of the dihedral angle. Reprinted with permission from reference. Copyright (2013) American Chemical Society.[1]

Electronic absorption spectroscopy can be used to determine whether the bridge and the redox centres are coplanar. If the complexes have an MLCT transition (Mo_2-δ → bridge-Ar-π*), there is sufficient Mo_2-δ → bridge-Ar-π conjugation as the complexes are planar, if the MLCT is unobserved the complexes are nonplanar. The temperature dependence of the dihedral angle was probed using the complex $[Mo_2(Piv)_3]_2(\mu_2\text{-}O_2CC_6H_4CO_2)$, at 4 K the MLCT was intense and low in energy but upon increasing the temperature to 298 K the intensity of the MLCT decreased and blue shifted as a result of the increased dihedral angle. The dihedral angle in $[Mo_2(Piv)_3]_2(\mu_2\text{-}C_6H_2\text{-}2,5\text{-}(OH)_2)$ is dependent on the pH of the solution with the complexes remaining planar in acidic conditions allowing for the observation of an MLCT and nonplanar in basic conditions. The deprotonation of the phenolic protons resulted in electrostatic repulsion between the phenolate and the carboxylate increasing the dihedral

angle such that the complex is no longer planar and the MLCT transition disappears (Figure 3.4.B). Electrochemical analysis showed that $[Mo_2(Piv)_3]_2(\mu_2\text{-}C_6H_2\text{-}2,5\text{-}(OH)_2)$ that the complexed had a thermodynamically stable MV state with a $\Delta E_{1/2}$ of 0.079 V. The UV-Vis-NIR spectra of the MV complex showed a low intensity Gaussian transition in the NIR, analysis of the IVCT transition showed the complex had a H_{ab} of 446 cm^{-1}. The loss of $Mo_2\text{-}\delta \rightarrow C_6H_2\text{-}2,5\text{-}(OH)_2\text{-}\pi$ conjugation upon deprotonation, would result in the H_{ab} decreasing substantially, which is why the complex was referred to as a molecular switch.

3.3 Aims

In the above examples it is shown that there are a number of factors affecting the degree of electronic communication between the two redox centres in MV complexes. In terms of electronic coupling we tend to think of the electron as either localised or delocalised between two redox centres. However, there could be further localisation of an electron within the redox active unit as well as between the redox units. The studies on complexes where the extent of electron localisation in both localised and delocalised systems are limited. Compounds that show localisation of the electron in a delocalised system could be used to probe intrinsic rectification. Research into intrinsic rectification is highly desirable as they have been challenging both theoretically and experimentally to design.

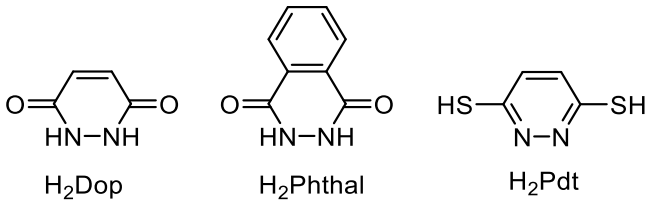

Figure 3.5: The structure of 3,6-pyridazinediol (H_2Dop), Phthalhydrazide (H_2Phthal) and 3,6-pyridazinedithiol (H_2Pdt) bridging ligands.

In this chapter the electronic coupling between the dimolybdenum redox centres bridged by the ligands 3,6-dihydroxypyridazine (H_2Dop), Phthalhydrazide (H_2Phthal) and 3,6-pyridazinedithiol (H_2Pdt) (Figure 3.5) will be evaluated. Electrochemical and spectroelectrochemical studies will be used to probe the delocalisation between the dimetal units. Based on previous studies, differences in the electronic coupling would be evidenced by changes in the $\Delta E_{1/2}$ values obtained by cyclic voltammetry and the cross-coupling matrix, H_{ab}, obtained by the analysis of the IVCT transition in the NIR region. The localisation of the electron will be probed using EPR spectroscopy and theoretical calculations. This series of compounds will provide a rare opportunity to compare electron localisation in the localised and delocalised regimes.

3.4 Results and discussion

3.4.1 *Synthesis*

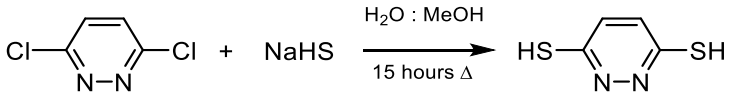

Scheme 3.1: Synthetic route to 3,6-Pyridazinedithiol (H_2Pdt).

3,6-Pyridazinedithiol (H_2Pdt) was synthesised through a nucleophilic aromatic substitution reaction, by refluxing 3,6-dichloropyradazine with sodium hydrogen sulphide in a 2:1 MeOH:H_2O mixture (Scheme 3.1). This new synthetic route offers a single step reaction to the desired compound, whereas the literature route synthesises the compound through a two-step reaction in identical yield (48 %).[7]

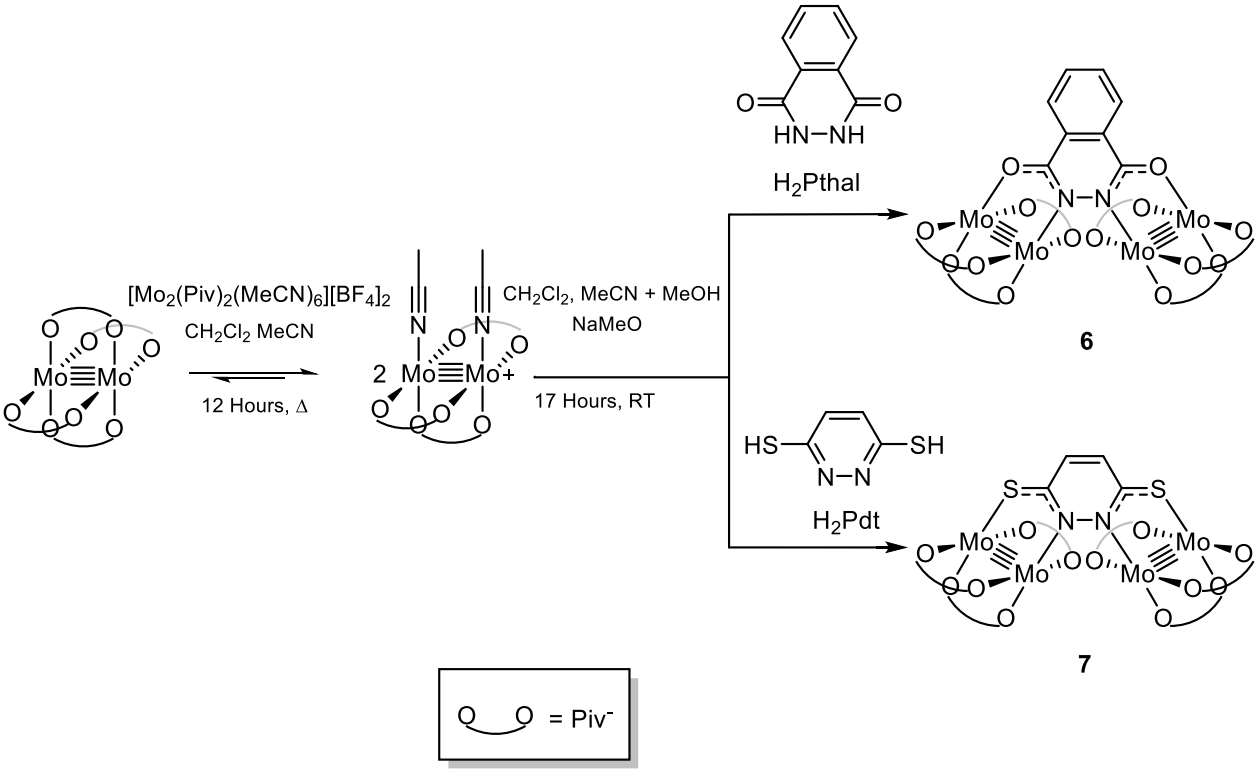

*Scheme 3.2: Synthesis of $[Mo_2(Piv)_3]_2(\mu_2$-Phthal) (**6**) and $[Mo_2(Piv)_3]_2(\mu_2$-Pdt) (**7**).*

$[Mo_2(Piv)_3]_2(\mu_2$-Phthal) (**6,** Phthal = 2,3-Dihydro-1,4-phthalazinedione) and $[Mo_2(Piv)_3]_2(\mu_2$-Pdt) (**7**) were synthesised by the reaction of the red monocationic intermediate $[Mo_2(Piv)_3(MeCN)_2][BF_4]$ with

Na_2Phthal and Na_2Pdt in methanol respectively. The reaction resulted in an immediate colour change (**6** = orange and **7** = green) and the reaction was stirred for 17 hours to ensure completion (Scheme 3.2). The solvent was removed *in vacuo,* and the ^{1}H NMR spectra indicated several impurities such as $Mo_2(Piv)_4$, $Mo_2(Piv)_3(L)$ and $Mo_2(Piv)_2(L)_2$. The products were purified using air sensitive column chromatography to isolate **6** as an orange solid (16 %) and **7** as a dark blue solid (14 %). The modest yields reflect the multistep reaction which generates numerous by-products as well as the difficulty in purifying the complexes. Complex **6** and **7** are soluble in THF, DMSO and CH_2Cl_2 and sparingly soluble in MeCN. The compounds were found to be pure by elemental analysis.

Complexes **6** and **7** have been characterised by ^{1}H NMR and IR spectroscopy, MALDI-TOF mass spectrometry, and the crystal structure for complex **7** was obtained, *vide infra*.

*Table 3.1: Selected bond lengths (Å), bond angles (°) and torsion angles (°) for complex **7**.*

Mo1-Mo2	2.1050(9)
Mo3-Mo4	2.1055(9)
Mo2-Mo3	3.3403(3)
Mo1-S1	2.4462(2)
Mo2-N1	2.1151(2)
Mo4-S2	2.439(2)
S1-C1	1.7148(2)
C1-N1	1.3369(1)
N1-N2	1.3998(1)
C1-C2	1.4309(1)
C2-C3	1.3548(1)
Mo3-N2	2.106(6)
Mo1-S1-C1	103.780(4)
Mo2-N1-C1	124.988(6)
Mo2-N1-N2	115.229(4)
S1-C1-N1	117.866(4)
Mo2-N1-N2-Mo3	24.637(2)
Mo1-Mo2-Mo3-Mo4	112.613(5)

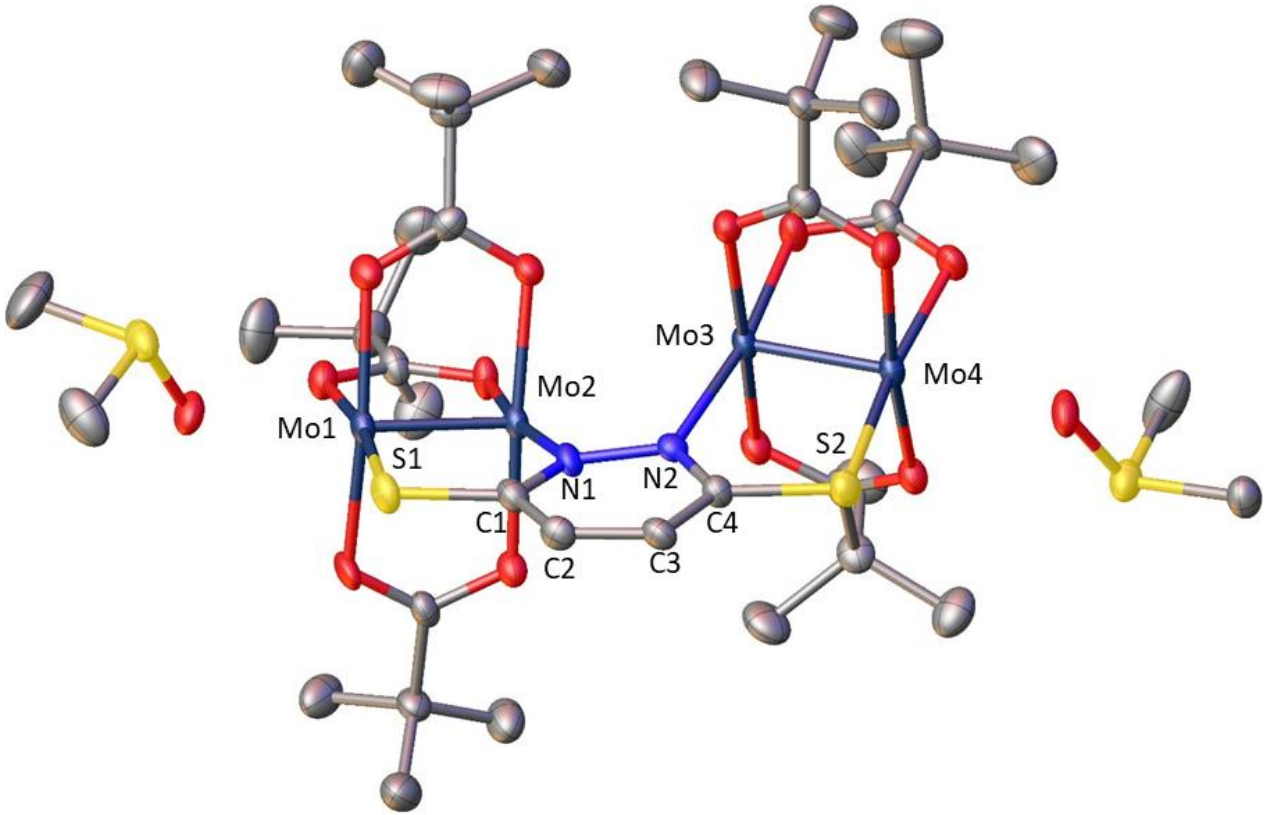

*Figure 3.6: Solid-state structure of $[Mo_2(Piv)_3]_2(\mu_2\text{-}Pdt)(DMSO)_2$ (**7**) as determined by single-crystal XRD. Anisotropic displacement parameters are shown at 50 % probability. Hydrogen atoms are omitted for clarity.*

A single crystal of **7**$(DMSO)_2$ was grown by the slow diffusion of water into a DMSO solution of **7** at room temperature. The structure was determined by single crystal X-ray diffraction, and is shown in Figure 3.6 with bond lengths and angles given in Table 3.1, the cell parameters and refinement results are summarised in chapter 8. The unit cell was found to be triclinic and solved in the space group $P\bar{1}$. The structure was founded to be twinned but could be solved using a twin law. Both Mo_2 centres show the expected paddlewheel arrangement of the ligands around the dimetal core, and the two dimetal units are bridged by the Pdt ligand with two axially coordinated DMSO molecules, the central DMSO is missing compared to **5**·3DMSO as coordination was sterically hindered. The MoMo bond lengths were (Mo1-Mo2 = 2.1050(9) Å and Mo3-Mo4 = 2.1055(9) Å) and show no variation within experimental error between **7**$(DMSO)_2$ which has a sulfur coordinating atoms and **5**$(DMSO)_3$ which has oxygen coordinating atoms (Mo1-Mo2 and Mo3-Mo4 = 2.1096(13) and 2.1105(14) Å, **5**$(DMSO)_3$).[8] For **7**$(DMSO)_2$, the two dimetal units are not coplanar, and they have a significant torsion angle of 24.637(2) °, increasing from 3.583(7) ° in **5**$(DMSO)_3$ as illustrated in Figure 3.7. The deviation away from coplanarity is a result of increased steric interactions between the dimetal units and the t-butyl groups in **7**$(DMSO)_2$. The increased steric interactions arise as a result of an increase in the C-S bonds and a decrease in the Mo-N bonds. The C-S bond lengths in **7**$(DMSO)_2$ (C1-S1 and C4-S2 =1.714(8) Å and 1.713(8) Å respectively) are significantly longer than the C-O bonds in **5**$(DMSO)_3$ (C1-O1 and C4-O2 = 1.299(10) Å and 1.307(9) Å).[4] The Mo-N bond lengths in **7**·2DMSO (Mo2-N1 = 2.1151(2) and Mo3-N2 = 2.106(6) Å) show a significant contraction when compared to the Mo-N bond lengths in **5**$(DMSO)_3$ (Mo2-N1 = 2.160(6) and Mo3-N2 = 2.151(6) Å). The through space separation between the quadruple bonds shows a significant decrease in **7**$(DMSO)_2$ where the Mo2···Mo3 separation is 3.3403(3) Å, compared to the Mo2···Mo3 separation in **5**$(DMSO)_3$ which is 3.7541(14) Å. The deviation away from being coplanar will decrease the overlap of the Mo_2-δ / Pdt-π orbitals resulting in a potential decrease in electronic communication. Despite numerous attempts suitable crystals for X-ray diffraction of complex **6** could not be obtained, although the structure is expected to be analogous to **5**$(DMSO)_3$.

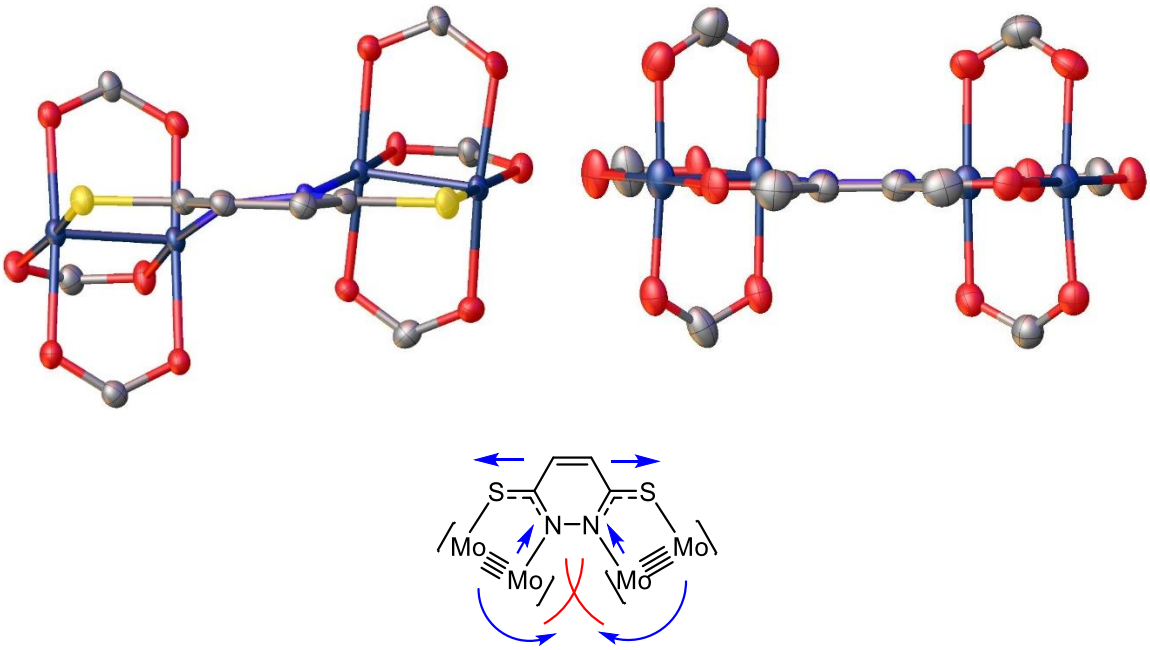

*Figure 3.7:The crystal structures of (left) **7**(DMSO)$_2$ and (right) **5**(DMSO)$_3$ as viewed along the plane of the bridge and (bottom) a schematic indicating the changes in bond lengths resulting in the deviation away from being coplanar.*

3.4.3 *^{1}H NMR spectroscopy*

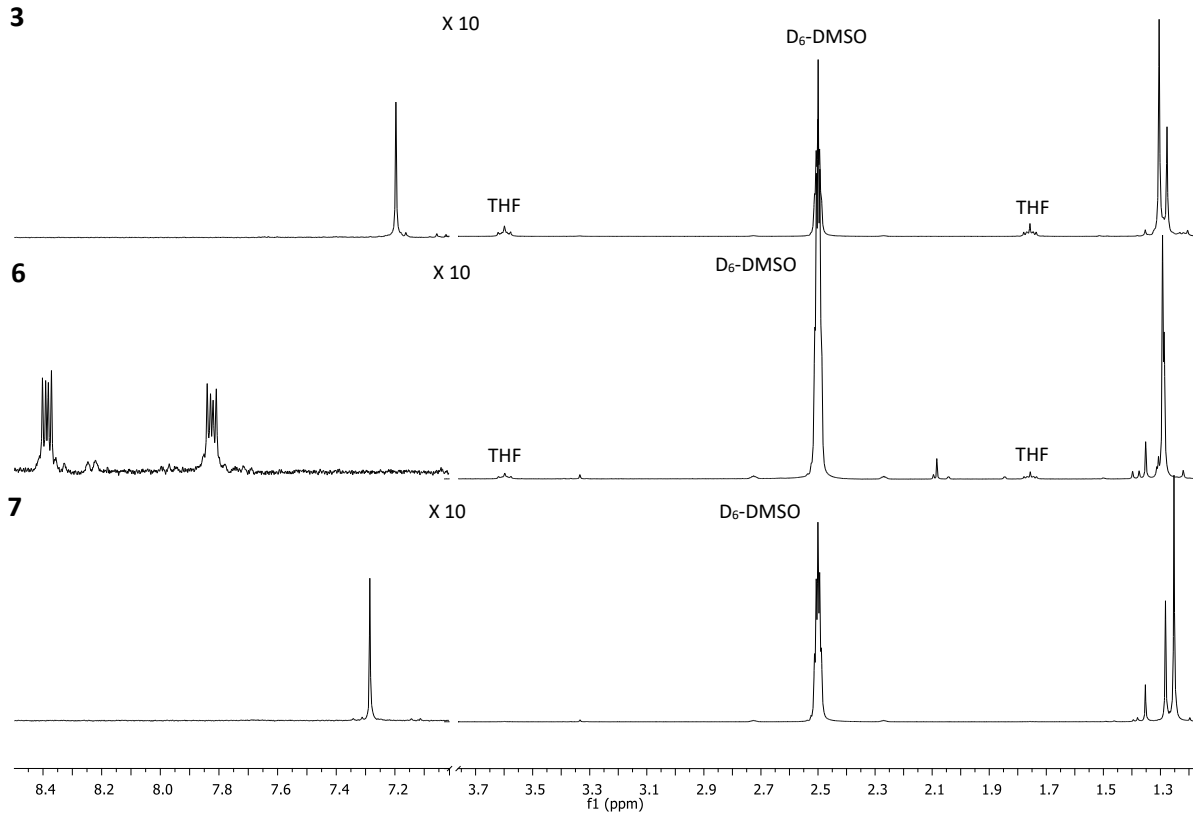

*Figure 3.8: ^{1}H NMR spectra of complexes **3, 6** and **7** in d_6-DMSO Left: A magnified portion of the aromatic region showing bridging ligand resonances.*

The ^{1}H NMR spectra of H_2Pdt was consistent with the literature.[7] The ^{1}H NMR spectra of complexes **3**, **6** and **7** in d_6-DMSO are shown in Figure 3.8. The spectra of **6** has the expected 2:1 Piv resonances at 1.29 ppm typical of a monosubstituted dimolybdenum unit. **6** also has two doublet of doublets (J = 6.1, 3.3 Hz) at 8.39 and 7.82 ppm corresponding to the aromatic backbone of the Phthal ligand. The ^{1}H NMR spectrum of **7** exhibits the expected 2:1 Piv resonances at 1.33 and 1.31 ppm and a singlet at 7.21 ppm corresponding to the Pdt backbone. All complexes have an impurity at 1.36 ppm which is a result of facile ligand scrambling in the presence of DMSO.[6,9] Complex **6** has two axially coordinated THF molecules, exposure to high vacuum for 48 hours removed the THF, this was done prior to submission for elemental analysis.

3.4.4 *Density functional theory*

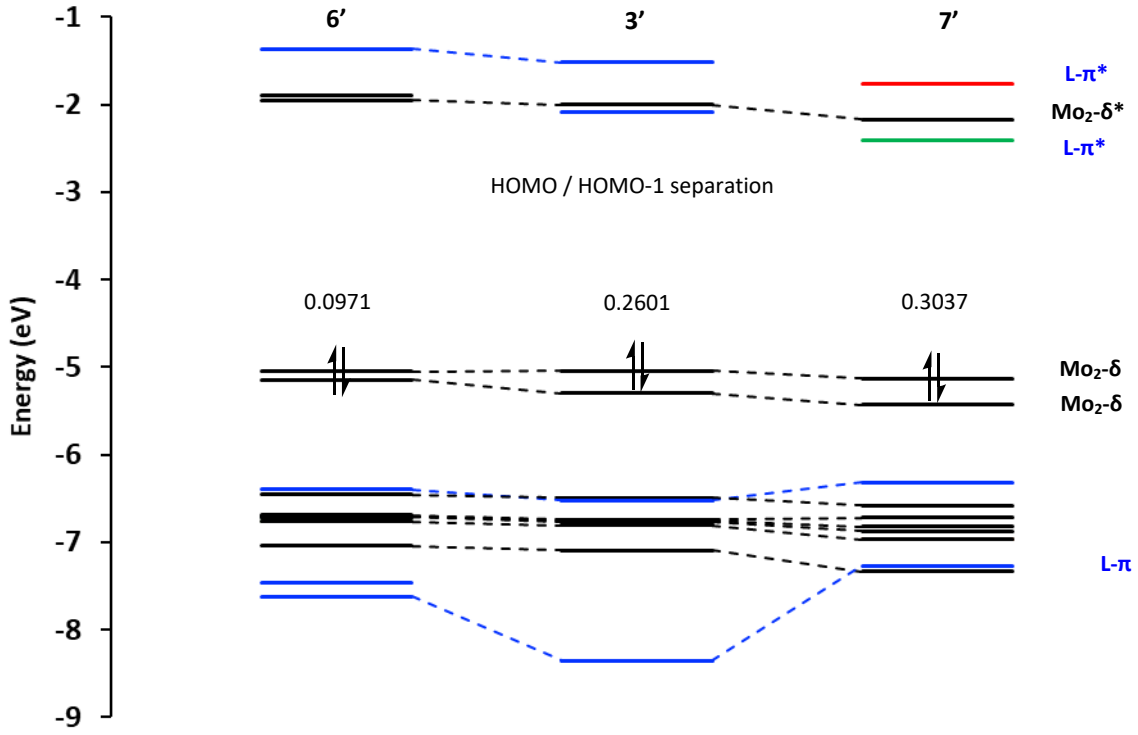

*Figure 3.9: The calculated frontier orbital energy level diagrams of model compounds **3', 6'** and **7'**.*

Theoretical calculations have been employed to help rationalise the observed spectroscopic behaviour of complexes **3, 6** and **7** and were carried out by Dr Nathan Patmore and Dr Anthony Meijer (University of Sheffield). DFT calculations were performed on model complexes (**3', 6'** and **7'**), in which the Pivalate ligands have been replaced by formate groups to reduce computational time. The calculated frontier molecular orbital energy level diagrams for **3', 6'** and **7'** are compared in Figure 3.9. For all complexes the HOMO and HOMO-1 orbitals are both Mo_2-δ orbitals and are different in energy as they mix with the pyridazine-π and -π*orbitals respectively. Therefore, the HOMO/HOMO-1 separation is a measure of interaction between the Mo_2- δ orbitals and pyrazine-π and π* orbitals, and hence the extent of coupling.[10,11] Therefore, the larger the HOMO/HOMO-1 gap and the smaller the HOMO/pyridazine π and π* gaps the greater the electronic coupling.[10]

For **6'** the HOMO/HOMO-1 are nearly degenerate with a splitting of 0.0971 eV indicating weaker electronic coupling compared to **3**' (0.2601 eV). The LUMO and LUMO+1 are both Mo_2-δ* orbitals, and the LUMO+2 is the pyridazine-π* orbital, this orbital has the correct symmetry to interact with the out-of-phase Mo_2-δ. The HOMO-10 is the pyridazine-π orbital and has the correct symmetry to interact with the in-Mo_2-δ. The HOMO/pyridazine-π* separation is 3.68 eV and the HOMO/pyridazine-π separation is 2.57 eV, due to the large variation through bond ET is predominantly expected to occur through the hole hopping formalism. In the previous chapter it was reported that complex **1 – 5** had significant through space stabilisation as a result of the redox centres being in close proximity to each other, as **6** and **7** employ a similar ligand architecture their $Mo_2 \cdots Mo_2$ separation are reported in Table 3.2. Analysis of the orbitals shows that for through bond coupling the electron transfer happens through the Mo_2-δ and the pyridazine-π and π* orbitals, whereas through space electron transfer is believed to happen through the Mo_2-π and σ orbitals.

The HOMO/HOMO-1 separation of **7'** is 0.3037 eV, larger than the calculated separation for **3**', as such complex **7** is expected to have greater coupling. The decrease in the energy of the HOMO between **3'** and **7'** is a result of the decreased π donation from the sulphur 3p orbital compared to that of the oxygen 2p orbital.[12] The complex shows a large degree of mixing and the LUMO is assigned as pyridazine-π*/Mo_2-δ* orbital and the LUMO+2 is assigned as the corresponding Mo_2-δ*/pyridazine-π* orbital. The HOMO-8 is the pyridazine-π orbital with the correct symmetry to interact with the Mo_2-δ orbital. Changing the chelating atom from O to S results in a decrease in energy of the pyridazine-π*/ Mo_2-δ* and increase in the pyridazine-π orbitals, as the Mo_2-δ is evenly situated between these orbitals the ET is expected to occur through both the electron hopping and hole hopping formalisms as well as through space. Complex **7** has the same bridge architecture as **3**, the complex takes a buckled arrangement, but the crystal structure shows that the $Mo_2 \cdots Mo_2$ separation decreases between **5** and **3**. This decrease in $Mo_2 \cdots Mo_2$ separation is shown in Table 3.2, and is expected to increase the through-space component in the ET mechanism.

Table 3.2: Calculated through space $Mo_2 \cdots Mo_2$ separation

Complex	$Mo_2 \cdots Mo_2$ / Å	$Mo_2^{0.5+} \cdots Mo_2^{0.5+}$ / Å
3'	3.635	3.613
6'	3.645	3.667
7'	3.353	3.348

3.4.4.1 Calculated absorption spectra

The optical transitions for **6'** and **7'** were calculated in THF, with the calculated transition energies summarised in Table 3.3 for **6'** and Table 3.4 for **7'**. The experimental spectra (*vide infra*) and calculated spectra are in good agreement in both energy and intensity. The calculated spectra predict the transitions at a slightly higher energy as a result of changing the ancillary ligands from Piv to formate groups, which decreases the energy of the HOMO and increases the energy of any transitions occurring from the Mo_2-δ orbitals. The spectra calculated for **6'** has a prominent transition at 379 attributed to the Mo2-δ → pyridazine-π* metal to ligand charge transfer band (MLCT), two more MLCT transitions are observed at 380 nm and 405 nm. The calculated spectra have a number of low-lying transitions attributed to a mixture of transitions consisting of Mo_2-δ → Mo_2-δ*, Mo_2-δ → Mo_2-π* and Mo_2-π → Mo_2-δ*.

*Table 3.3: Calculated transitions for **6'** ($f > 0.005$) in THF, transitions are assigned on their most significant character.*

Energy / eV	λ_{max} / nm	f	Transition	Assignment
2.403	515	0.0091	HOMO-1 → LUMO	Mo_2-δ → Mo_2-δ*
2.628	471	0.0141	HOMO → LUMO+1	Mo_2-δ → Mo_2-δ*
2.662	465	0.0132	HOMO-1 → LUMO+1	Mo_2-δ → Mo_2-δ*
2.758	449	0.0164	HOMO → LUMO+5	Mo_2-δ → Mo_2-π*
3.060	405	0.0969	HOMO → LUMO+2	Mo_2-δ → pyridazine-π*
3.199	387	0.0076	HOMO-5 → LUMO	Mo_2-π → Mo_2-δ*
3.262	380	0.0126	HOMO-1 → LUMO+3	Mo_2-δ → pyridazine-π*
3.264	379	0.2689	HOMO-1 → LUMO+2	Mo_2-δ → pyridazine-π*
3.271	378	0.0167	HOMO-7 → LUMO	Mo_2-π → Mo_2-δ*

Complex **7'** shows a greater degree of orbital mixing compared to **1' - 6'**, the most prominent transition is the Mo_2-δ → pyridazine-π* / Mo_2-δ* MLCT at 587 nm. Other transitions to hybridised orbitals include the Mo_2-δ → Mo_2-δ* / pyridazine-π* and the pyridazine-π → Mo_2-δ* / pyridazine-π* transitions. The O for S substitution results in the ligand to metal transitions (LMCT) red shifting with the pyridazine-π → Mo_2-δ* occurring at 358 nm.

*Table 3.4: Calculated transitions for **7'** (f > 0.005)in THF, transitions are assigned on their most significant character.*

Energy / eV	λ_{max} / nm	*f*	Transition	Assignment
2.109	587	0.0775	HOMO → LUMO	Mo_2-δ → pyridazine-π* / Mo_2-δ*
2.452	505	0.0159	HOMO-1 → LUMO	Mo_2-δ → pyridazine-π* / Mo_2-δ*
2.454	505	0.0111	HOMO → LUMO+3	Mo_2-δ → Mo_2-π*
2.572	481	0.0299	HOMO-1 → LUMO+1	Mo_2-δ → Mo_2-δ*
2.622	472	0.0054	HOMO-1 → LUMO+3	Mo_2-δ → Mo_2-π*
2.693	460	0.0123	HOMO → LUMO+5	Mo_2-δ → Mo_2-π*
2.763	448	0.0354	HOMO → LUMO+2	Mo_2-δ → Mo_2-δ* / pyridazine-π*
3.057	405	0.0137	HOMO-1 → LUMO+2	Mo_2-δ → Mo_2-δ* / pyridazine-π*
3.346	370	0.0196	HOMO-2 → LUMO	pyridazine-π → Mo_2-δ* / pyridazine-π*
3.459	358	0.0201	HOMO-2 → LUMO+1	pyridazine-π → Mo_2-δ*

3.4.5 *Electrochemistry*

The cyclic voltammograms and differential pulse voltammograms of **3**, **6** and **7** in 0.1 M NBu_4PF_6 / THF are displayed in Figure 3.10, and the data summarised in Table 3.5. All complexes show two successive one electron oxidations corresponding to the removal of electrons from the Mo_2-δ orbitals. As the complexes have a quasi-reversible second oxidation the $E_{1/2}(2)$ could not be determined and instead the potentials are reported as the cathodic peak potentials (E_{pc}), which in turn were used to estimate the values of $\Delta E_{1/2}$. As the K_c can only be strictly determined for reversible redox processes, the discussion will revolve around the ΔE_{pc}, although the K_c is included in Table 3.5 for comparison.

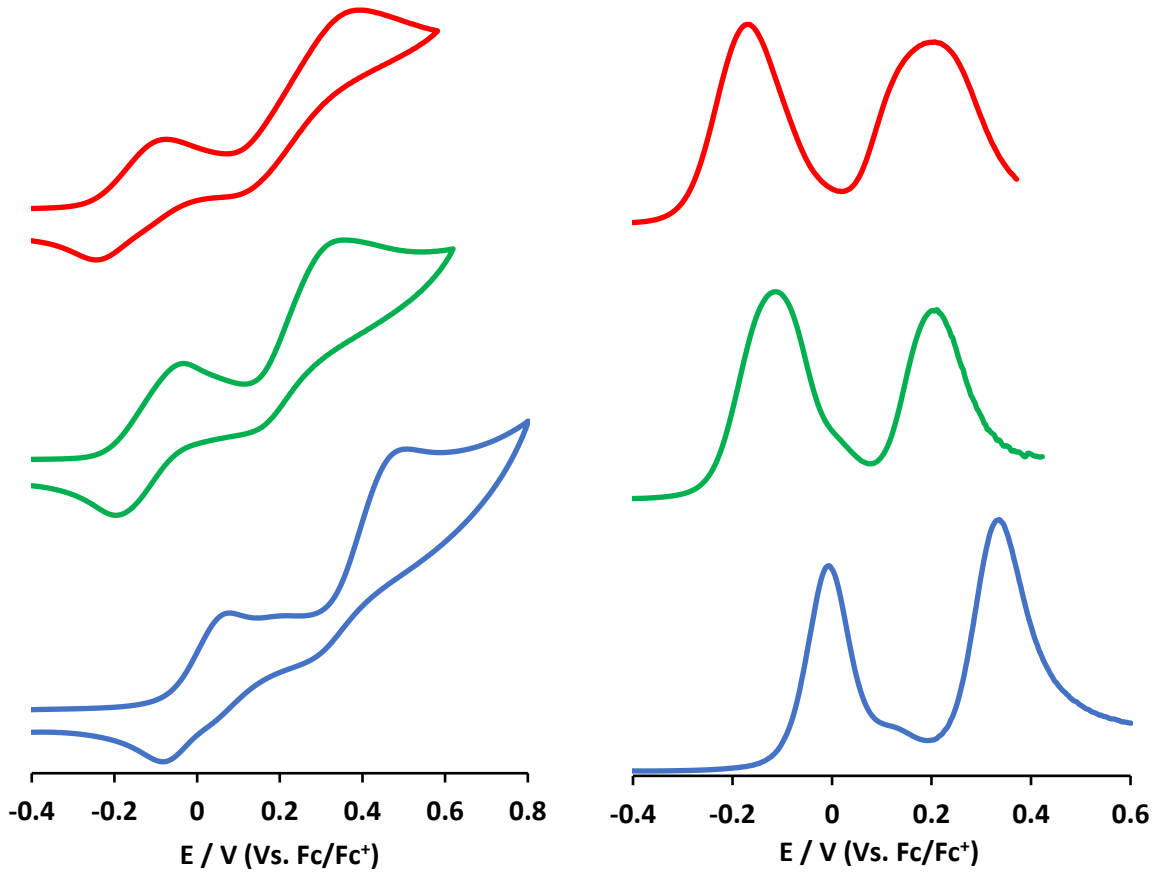

*Figure 3.10: CV (left, 100 mVs^{-1}) and DPV (right, 10 mVs^{-1}) of complexes **3** (red), **6** (green) and **7** (blue) in 0.1 M NBu_4PF_6/ THF solution at a concentration of 5 mM, and referenced against the Fc/Fc^+ couple (0.00 V).*

*Table 3.5: Cyclic voltammetry data for complexes **3**, **6** and **7** in 0.1 M NBu_4PF_6/ THF solution at a concentration of 5 mM, and referenced against the Fc/Fc^+ couple (0.00 V).*

Complex	$E_{1/2}(1)$ / V	$E_{pc}(1)$ / V	$E_{pc}(2)$ / V	ΔE_{pc}/ V	K_c (x 10^6)
3	-0.165	-0.133	0.311	0.444	321
6	-0.114	-0.041	0.325	0.366	1.54
7	-0.011	0.021	0.538	0.517	550

Four terms contribute to the magnitude of the free energy of comproportionation ΔG_c, (Equation 3.1) the electronic resonance effect (ΔG_r), the electrostatic effect (ΔG_e), the statistical contribution (ΔG_s) and an inductive factor (ΔG_i). The complexes are expected to have both a through space and through

bond component, where the though bond component is governed by ΔG_r and the through space component is governed by ΔG_e.[13–16] As each compound has a varying contribution from each factor only the overall thermodynamic stability of the MV state can be commented upon between these complexes.

$$\Delta G_c = \Delta G_s + \Delta G_e + \Delta G_i + \Delta G_r$$

Equation 3.1: factors contributing to the free energy of comproportionation (ΔG_c).

The first oxidation potentials $E_{1/2}(1)$ are -0.165 V, -0.114 V and -0.011 V for complexes **3, 6** and **7** respectively. The oxidation potentials of **6** and **7** are anodically shifted in compared to **3**, this is a result of π back bonding into the extended π system of the ligand in complex **6.**[17,18] The large anodic shift when changing the donor atom from O (**3**) to S (**7**) is consistent with literature due the increase in basicity of the bridging ligand.[2,4,5,10–12,19–21] The oxidation potentials are consistent with the absolute energy of the HOMO orbitals where **3** is the highest in energy and the easiest to oxidise and **7** is the lowest in energy and therefore more difficult to oxidise.[22]

The ΔE_{pc} for **3**, **6** and **7** are 0.444 V, 0.325 V and 0.550 V respectively, the magnitude of the ΔE_{pc} values for all complexes show considerable thermodynamic stabilisation of the MV state. The large ΔE_{pc} in all cases is indicative of a strongly coupled system, as a K_c of ~10^4 is typical for strong coupling in dimolybdenum dimers, although the ΔE_{pc} of **6** shows a decrease in thermodynamic stability when compared to **3**.[6] The magnitude of the ΔE_{pc} observed for **7** indicates an increase in coupling compared to complex **3**, as S is more diffuse than O it allows for better orbital overlap between the metal and the bridge resulting in better coupling. The through space component must also increase thermodynamic stability of the MV complex as a result of the decreased separation of the redox centres.

3.4.6 *UV-Vis Absorption spectroscopy*

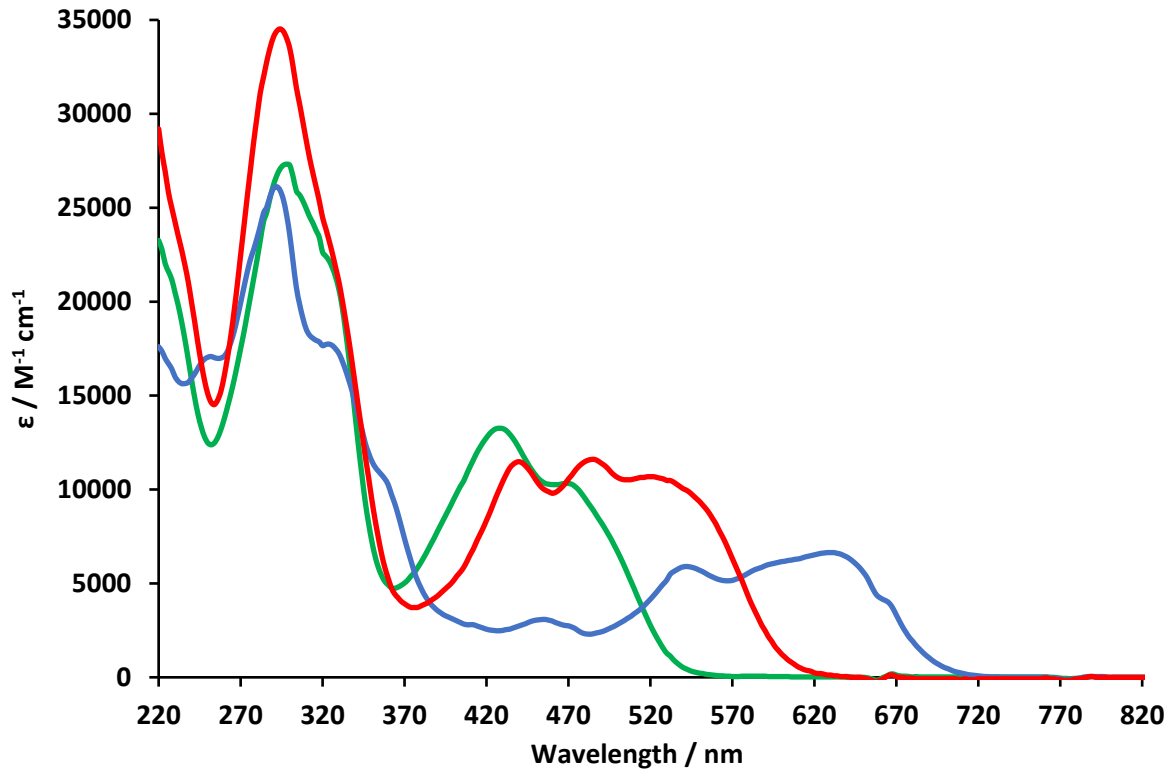

*Figure 3.11: The UV-Vis spectra of complexes **3** (red), **6** (green) and **7** (blue) in THF.*

The UV-Vis spectra of complex **3, 6** and **7** in THF are displayed in Figure 3.11 and the major transitions assigned in Figure 3.12. Due to the number of transitions the UV assignments were aided by TD-DFT (section 3.4.4.1). Complexes **3, 6** and **7** have a cis-Piv-π → Piv-π* transition at 296 nm, 294 nm and 292 nm respectively and a trans-Piv-π → Piv-π* transition at 326 nm. Complex **7** has a LMCT (pyridazine-π → Mo_2-δ*) at 364 nm but the LMCT for complexes **3** and **6** is unobserved as a result of the larger Mo_2-δ/pyridazine-π separation. The predominant Mo_2-δ → pyridazine-π* MLCT for complexes **3, 6** and **7** occur at 520 nm, 426 nm and 630 nm respectively. The MLCT of **6** is blue shifted in comparison to **3** as the pyridazine-π* orbital is much higher in energy, coupled with a slight decrease in the energy of the Mo_2-δ orbital. The MLCT of **7** is red shifted in comparison to **3** as a result of the lower pyridazine-π* orbital which results from the O for S substitution. The Mo_2-δ → Mo_2-δ* in complex **3** and **6** is obscured by the intense MLCT, Mo_2-δ → Mo_2-π*and Mo_2- π → Mo_2-δ* but occurs

at 454 nm in **7**. The Mo_2-δ → Mo_2-δ* transition can be observed in **7** as the transitions in the visible region are red shifted in comparison to **3** as a result of the decreased pyridazine-π*energy and the slight decrease in Mo_2-δ. The transitions in the visible region for **7** show a decrease in intensity as a result of the decreased conjugation between the metal and the ligand caused by the deviation away from being planar.

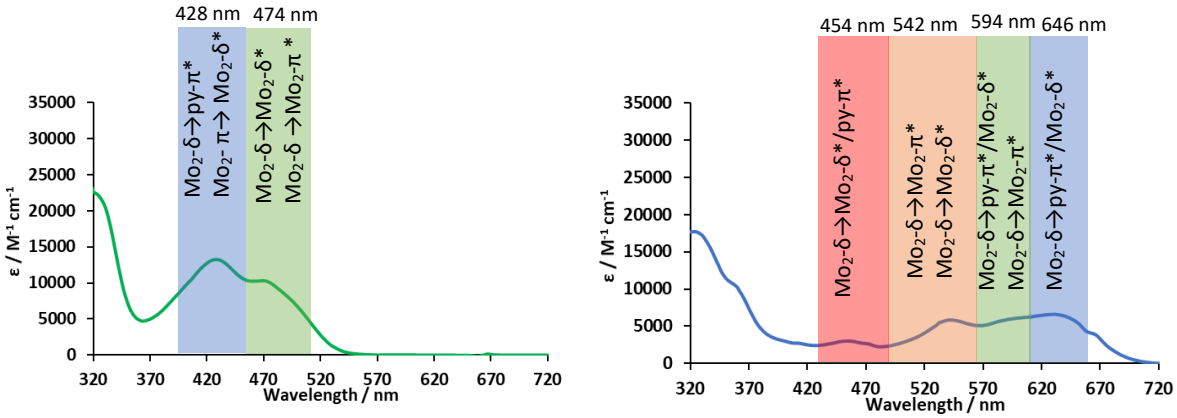

*Figure 3.12: The UV-Vis assignments for complexes **6** (left) and **7** (right).*

3.4.7 *Spectroelectrochemistry*

In order to understand the electronic properties of complexes **6** and **7** and their redox products, spectroelectrochemical studies have been carried out. The UV-Vis-NIR-IR spectra of complexes [**6**]^n and [**7**]^n (n= 0, 1, 2) were collected from in 0.1 M NBu_4PF_6 / THF solutions.

The UV-Vis-NIR-IR spectra of **6**, **6**$^+$ and **6**$^{2+}$ are displayed in Figure 3.13. The sequential formation of **6**$^+$ and **6**$^{2+}$ in the spectroelectrochemical studies is evidenced by the appearance of two separate isosbestic points in the **6** → **6**$^+$ and **6**$^+$ → **6**$^{2+}$ spectra at 19531 cm^{-1} (512 nm) and 19455 cm^{-1} (514 nm) respectively. Upon oxidation from **6** → **6**$^+$ several spectral changes occur in the UV-Vis NIR, the most prominent of which is the growth of a low intensity Gaussian band in the NIR at 3809 cm^{-1} (2625 nm). The magnified portion of the spectra shows the intervalence charge transfer (IVCT) transition, which can be well fitted using a single Gaussian curve which is typical for a class II compound.[23] The UV-Vis-

NIR spectrum of **6**$^{+}$ is in excellent agreement with the IR spectrum. This is further confirmed as upon oxidation to the doubly oxidised species the transition disappears. An in-depth discussion of the intervalence charge transfer band can be found in section 3.4.8 below.

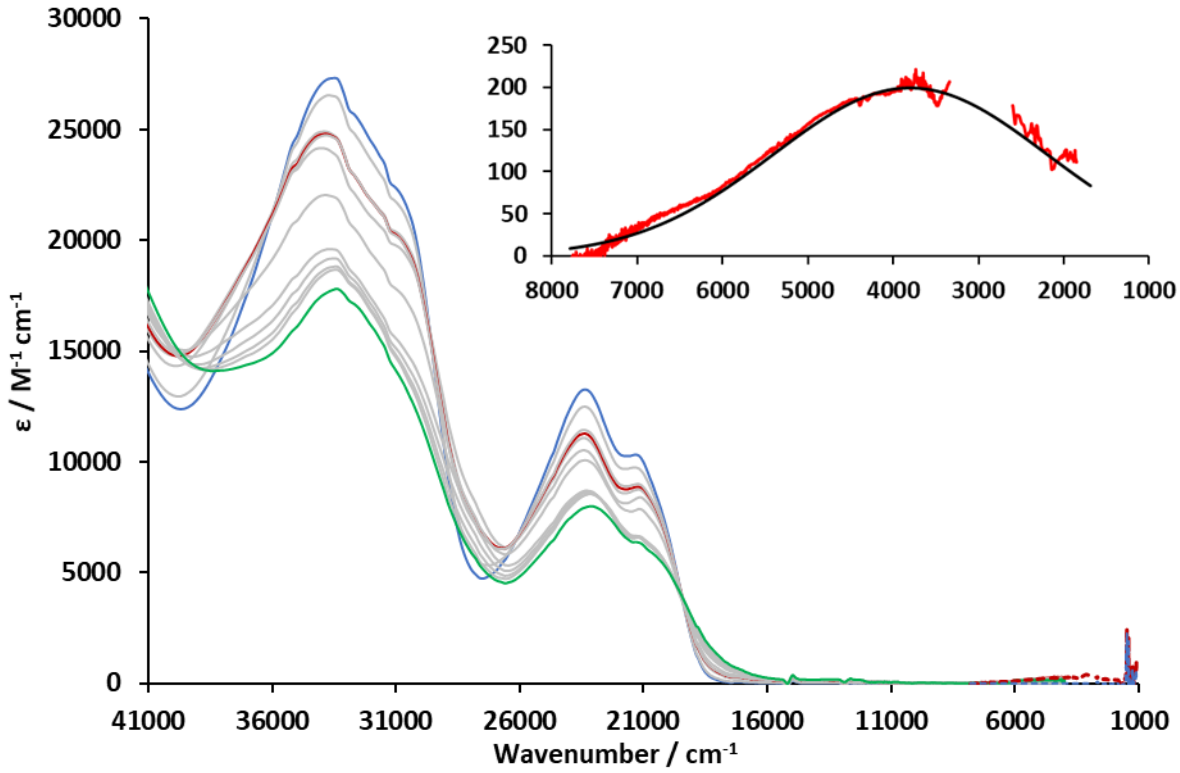

*Figure 3.13: The UV-Vis NIR SEC (solid line) and the IR SEC (Dashed line) of complex **6** in 0.1M NBu_4PF_6 /THF. **6** (blue), **6**$^{+}$ (red) and **6**$^{2+}$ (green). Top Right: A magnified portion of the IR spectra for **6**$^{+}$ showing the charge resonance transition (red), the Gaussian curves used to determine the integral (Black dashed lines), and the sum of the Gaussian curves (black solid line). The region around 3000 cm^{-1} is not shown due to strong THF CH vibrations.*

The MLCT (Mo_2-δ → pyridazine- π*) for **6** is observed at 23364 cm^{-1} (428 nm). Following the **6** → **6**$^{+}$ oxidation the MLCT decreases in intensity, red shifts to 23255 cm^{-1} (430 nm) and begins to broaden. The peak at 21097 cm^{-1} (474 nm) decreases in intensity and broadens but shows no observable change in energy, the broadening is expected to be due to the growth of a LMCT transition (pyridazine-π→Mo_2-δ). Following the **6**$^{+}$ → **6**$^{2+}$ oxidation the MLCT red shifts further to 22831 cm^{-1} (438 nm) and decreases in intensity. The peak at 21097 cm^{-1} (474 nm) red shifts to 20746 cm^{-1} (484 nm), decreases in energy and significantly broadens once again. The spectra regained its original features following the reduction back to the neutral species but at ca. 60 % intensity as a result of the quasi-reversible

second oxidation. As class II compounds show solvent dependence the spectroelectrochemistry was attempted in acetonitrile but the complex decomposed upon oxidation.

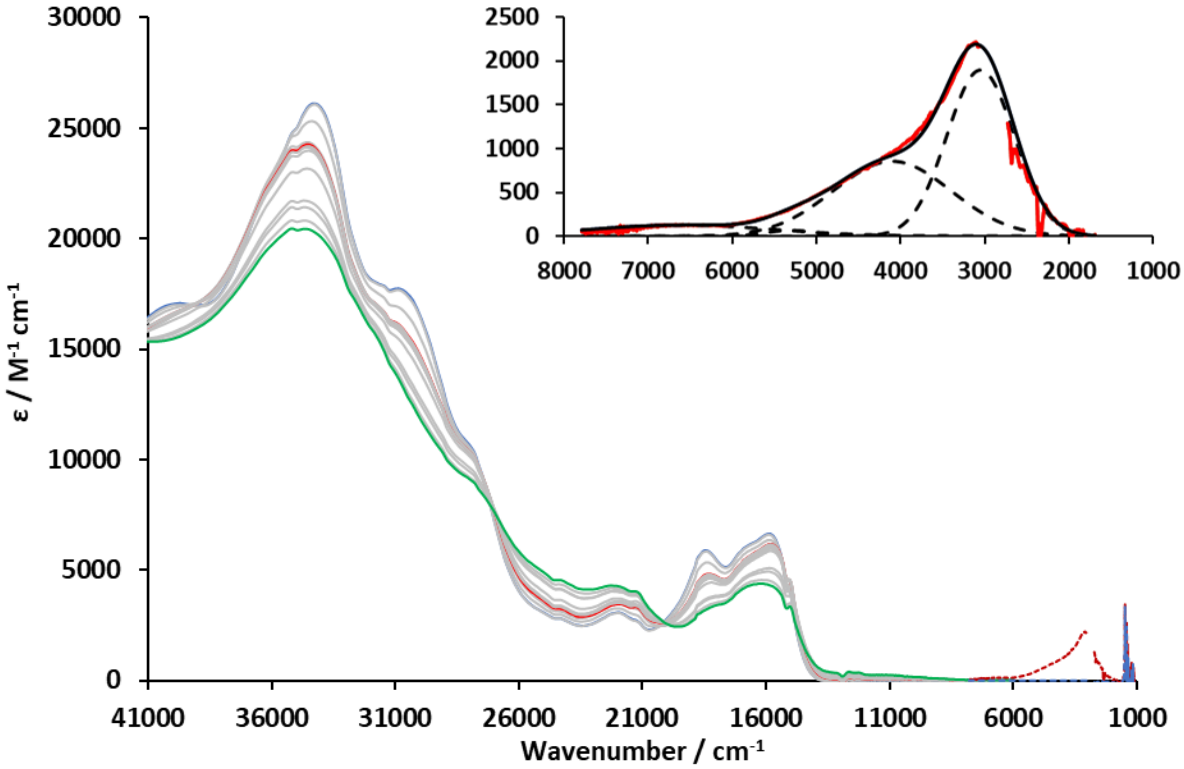

*Figure 3.14: The UV-Vis NIR SEC (solid line) and the IR SEC (Dashed line) of complex **7** in 0.1M NBu_4PF_6 /THF. **7** (blue), $\mathbf{7}^{+}$ (red) and $\mathbf{7}^{2+}$ (green). Top Right: A magnified portion of the IR spectra for $\mathbf{7}^{+}$ showing the charge resonance transition (red), the Gaussian curves used to determine the integral (Black dashed lines), and the sum of the Gaussian curves (black solid line). The region around 3000 cm^{-1} is not shown due to strong THF CH vibrations.*

The UV-Vis-NIR-IR spectra of **7**, $\mathbf{7}^{+}$ and $\mathbf{7}^{2+}$ are displayed in Figure 3.14. The sequential formation of $\mathbf{7}^{+}$ and $\mathbf{7}^{2+}$ in the spectroelectrochemical studies is evidenced by the appearance of two separate isosbestic points in the **7** → $\mathbf{7}^{+}$ and $\mathbf{7}^{+}$ → $\mathbf{7}^{2+}$ spectra at 15385 cm^{-1} (650 nm) and 14451 cm^{-1} (691 nm). Upon oxidation from **7** → $\mathbf{7}^{+}$ several spectral changes occur in the UV-Vis NIR, the most prominent of which is the growth of a charge resonance band in the IR at 3136 cm^{-1} (3189 nm). The band is assigned as a charge resonance band associated with a class III system as it is relatively intense, non-Gaussian, exhibits significant low energy cut off, and disappears when the complex is doubly oxidised. The UV-SEC and IR sec are in excellent agreement for the charge resonance band but as the charge resonance

transition coincides with strong THF CH vibrations at 3000 cm^{-1}, the IR-SEC was repeated in d_8-THF to red shift the solvent absorptions. A comparison of the charge resonance band observed for **7**$^{+}$ in THF and d_8-THF is shown in Figure 3.15, and the spectra are similar to one another. An in-depth discussion of the charge resonance band can be found in section 3.4.8.

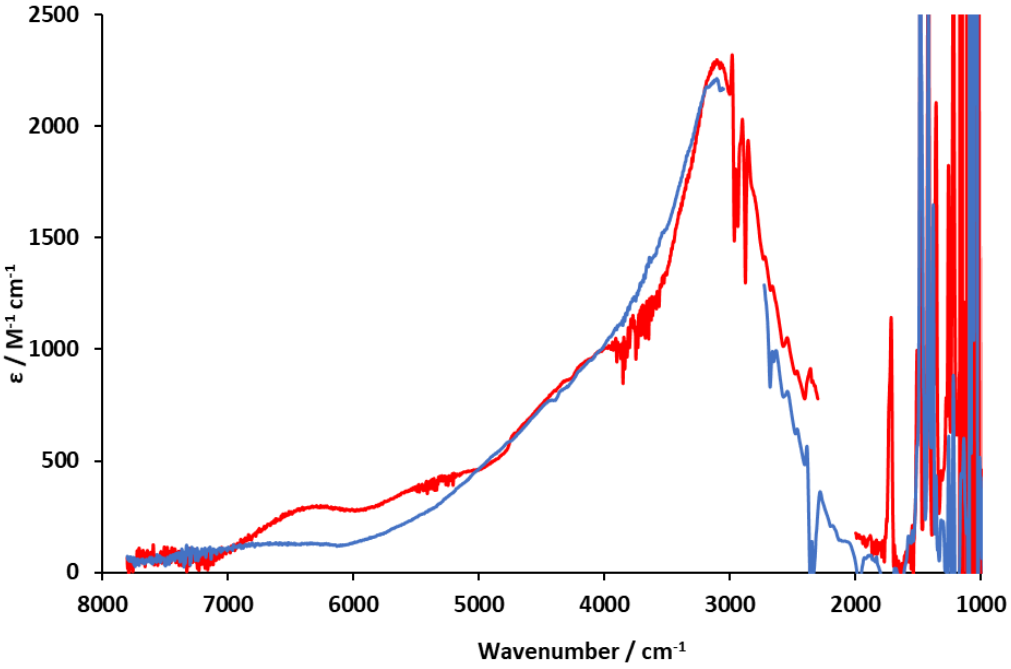

Figure 3.15: The IR spectra for ***7***$^{+}$ *showing the charge resonance transition in THF (blue) and* d_8*-THF (red).*

Upon oxidation (**7** → **7**$^{+}$) a minor decrease in intensity of the MLCT (Mo_2-δ → pyridazine- π*) transition is observed, the MLCT also blue shifts from 15480 cm^{-1} (646 nm) to 15923 cm^{-1} (628 nm). The Mo2-δ → Mo2-δ*/pyridazine-π* transition at 22026 cm^{-1} (454 nm) decrease in intensity but do not change in energy. The LMCT (pyridazine- π → Mo_2-δ*) transition at 16835 cm^{-1} (594 nm) increases in intensity but does not change in energy. As the SOMO is evenly situated between the pyridazine-π (HOMO-8) and π* (LUMO) in **7'** both an MLCT (Mo_2-δ → pyridazine- π*) and LMCT (pyridazine- π → Mo_2-δ) are observed in the radical cations. The transition at 18450 cm^{-1} (542 nm) decreases in intensity with no observable change in the energy of the transition. Following the **7**$^{+}$ → **7**$^{2+}$ oxidation the MLCT decreases

in intensity and blue shifts to 16025 cm^{-1} (624 nm), whereas the LMCT at 16835 cm^{-1} (594 nm) continues to decrease in intensity but shows no change in the energy of the transition. The transition at 18450 cm^{-1} (542 nm) shows a further decrease in intensity. The spectra regained its original features following the reduction back to the neutral species, but considerable bleaching was observed.

3.4.8 *Calculation of the cross-coupling matrix parameter (H_{ab})*

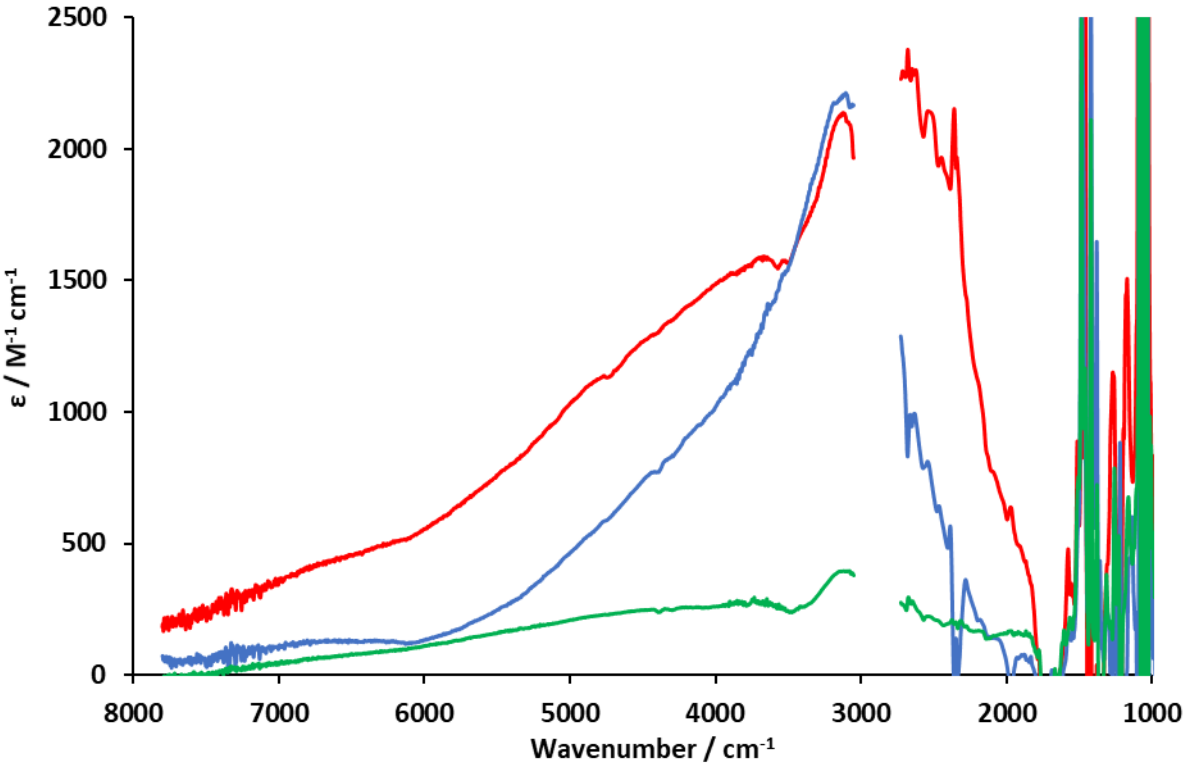

*Figure 3.16: The overlayed charge resonance transitions of **3**⁺ (red), **6**⁺ (green) and **7**⁺ (blue). The region around 3000 cm^{-1} is not shown due to strong THF CH vibrations.*

The charge resonance bands for **3**⁺, **6**⁺ and **7**⁺ are compared in Figure 3.16. Complex **3**⁺ and **7**⁺ are both classified as being class III as the charge resonance bands are relatively intense, non-Gaussian with significant low energy cut off. Complex **6**⁺ is classified as being class II, as the band has low intensity and Gaussian in shape. The peak maxima (ν_{max}) for the transitions are 2780 cm^{-1} 3809 cm^{-1} and 3136 cm^{-1} for **3**⁺, **6**⁺ and **7**⁺ respectively. The predicted peak width at half height ($\Delta\nu_{1/2}$°), predicts the peak width for a Gaussian transition centred at the ν_{max} of the experimental peak. For complex **6**⁺ the

experimental peak width at half height ($\Delta\nu_{1/2}$) calculated from the high energy side was 3866 cm^{-1} which was greater than the calculated $\Delta\nu_{1/2}°$ of 2966 cm^{-1}. Complex $\mathbf{7}^{+}$ has an experimental $\Delta\nu_{1/2}$ of 1534 cm^{-1} and a calculated $\Delta\nu_{1/2}°$ of 2691 cm^{-1}, the smaller observed band width is a result of the increased low energy cut off with lesser degree of vibronic progression than observed in complex $\mathbf{3}^{+}$, this decrease in vibronic progression could indicate an increase in the through space ET component for $\mathbf{7}^{+}$. The bandwidth is also coupled to the extent of the electronic coupling, a decreased bandwidth is consistent with an increase of the electronic coupling parameter (H_{ab}).[23,24]

Table 3.6: Summary of the NIR absorptions observed for $\mathbf{3}^{+}$, $\mathbf{6}^{+}$ and $\mathbf{7}^{+}$.

Complex	ν_{max} / cm^{-1}	ε_{max} / M^{-1} cm^{-1}	H_{ab} / cm^{-1}	$\Delta\nu_{1/2}$ / cm^{-1}	$\Delta\nu_{1/2}°$ / cm^{-1}
$\mathbf{3}^{+}$	2780	2311	1390	4114	2534
$\mathbf{6}^{+}$	3809	199	638	3866	2966
$\mathbf{7}^{+}$	3136	2181	1568	1534	2691

The H_{ab} of a class II compound is calculated using Equation 3.2.1 (see section 1.3.2.1).[23,24] The ν_{max}, ε_{max} and $\Delta\nu_{1/2}$ can all be experimentally determined using the IVCT transition but the effective ET distance is difficult to determine experimentally as a result of delocalisation onto the bridging ligand.[21,25] Although the dimetal separation in complex $\mathbf{6}^{+}$ is ~0.06 Å greater than for $\mathbf{3}^{+}$, the actual electron transfer distance can only be determined by Stark spectroscopy. Therefore, the calculated r_{ab} of 1.713 Å for **3** will be used for the determination of H_{ab} resulting in an upper estimate for the H_{ab}. The estimated H_{ab} for complex $\mathbf{6}^{+}$ was 638 cm^{-1} around half the H_{ab} calculated for **3** despite the complexes employing nearly identical ligand architectures (Table 3.6). The addition of the phenyl ring results in a decrease in electronic coupling, this can be explained by looking at the through space $Mo_2\cdots Mo_2$ separation in the neutral and the mixed valent states and comparing them to **1 – 5.** The calculated internuclear separation for **6** is 3.645 Å which is marginally longer than the calculated separation of **3**

which is 3.635 Å (Table 3.2). Upon oxidation complexes **1 – 5** show a decrease in the through space $Mo_2 \cdots Mo_2$ separation which is expected to increase the H_{ab} as well as the thermodynamic stability of the mixed valence state. Conversely upon oxidation of **6** the through space $Mo_2 \cdots Mo_2$ separation increases to 3.667 Å which is ~0.06 Å more than **3**$^+$, the addition of the phenyl ring is expected to have added rigidity to the ligand backbone preventing the redox centres from moving closer together.[26] This results in a decrease in the through space ET component, resulting in a decrease in the H_{ab} and the complex being assigned as class II.

$$H_{ab} = \frac{2.06 \times 10^{-2} (\upsilon_{max}\, \varepsilon_{max}\, \Delta\upsilon_{1/2})^{1/2}}{r_{ab}} \qquad (3.2.1)$$

$$H_{ab} = \frac{1}{2}\upsilon_{max} \qquad (3.2.2)$$

Equation 3.2: Calculation of the electronic coupling parameter (H_{ab}) for (1) a class II compound and (2) a class III compound.

As complex **7**$^+$ is class III Equation 3.2.2 can be used to determine the H_{ab}, which was found to be 1688 cm^{-1}. The increased H_{ab} of **7**$^+$ when compared to complex **3**$^+$ is consistent with changing the chelating atom from O to S commonly seen throughout literature.[5,11,27] Liu *et al.* have shown that in the complex $[Mo_2(DAniF)_3]_2(\mu_2\text{-}E_2CCE_2)$ where E is O or S, that changing the bridging ligand from [OO-OO] to [SO-SO] results in an increase in H_{ab} from 2376 cm^{-1} to 2726 cm^{-1} although this study only takes into account the through bond ET component.[5] The O/S substitution results in **7**$^+$ being more strongly coupled than **3**$^+$ and this a result of an increase in both the through bond and through space ET transfer components. The DFT shows that the two redox centres are more strongly coupled than **3** with a larger HOMO/HOMO-1 separation with the pyridazine-π and π* being closer in energy to the non-degenerate Mo_2-δ orbitals indicating better through bond coupling. Equally, the calculated through space $Mo_2 \cdots Mo_2$ separation is 3.353 Å which decreases to 3.348 Å upon oxidation and is ~0.27 Å less

than $\mathbf{3}^+$. The large decrease in the through space separation is expected to have increased the through space ET component.

3.4.9 *Electron Paramagnetic Resonance Spectroscopy*

The MV complexes $\mathbf{3}^+$, $\mathbf{6}^+$ and $\mathbf{7}^+$ were prepared by *in-situ* chemical oxidation of the neutral complexes using one equivalent of silver hexafluorophosphate ($AgPF_6$) and immediately characterised using EPR spectroscopy at room temperature. The resulting EPR spectra and their simulations are displayed in Figure 3.17, and the g-factor and simulated hyperfine couplings are shown in Table 3.7. Molybdenum has two spin active isotopes ^{95}Mo and ^{97}Mo with I=5/2 with a combined natural abundance of 25 %, the remaining 75 % consists of isotopes with I=0. The experimental spectra all consist of a central peak at a g-factor of 1.93 – 1.94 typical of an electron based in an Mo_2-δ orbital. The central peak arises as a result of all the *I=0* isotopes and the satellite spectra arise from the ^{95,97}Mo isotopes with I=5/2.[28] The magnitude of the hyperfine couplings can indicate the extent of electron delocalisation, a hyperfine of ~2.8 mT indicates that the electron is evenly shared between two Mo atoms such as that observed for $[Mo_2(Piv)_4]^+$ or in the class II compound $[Mo_2(Piv)_3]_2(\mu_2$-1,4-tetrafluoroterePhthalate$)^+$.[29] The magnitude of the hyperfine halves to ~1.4 mT when electron is evenly shared between four Mo atoms, like those observed for the class III compound $[(Mo_2(Piv)_3)_2(\mu_2$-oxalate$)]^+$.[30]

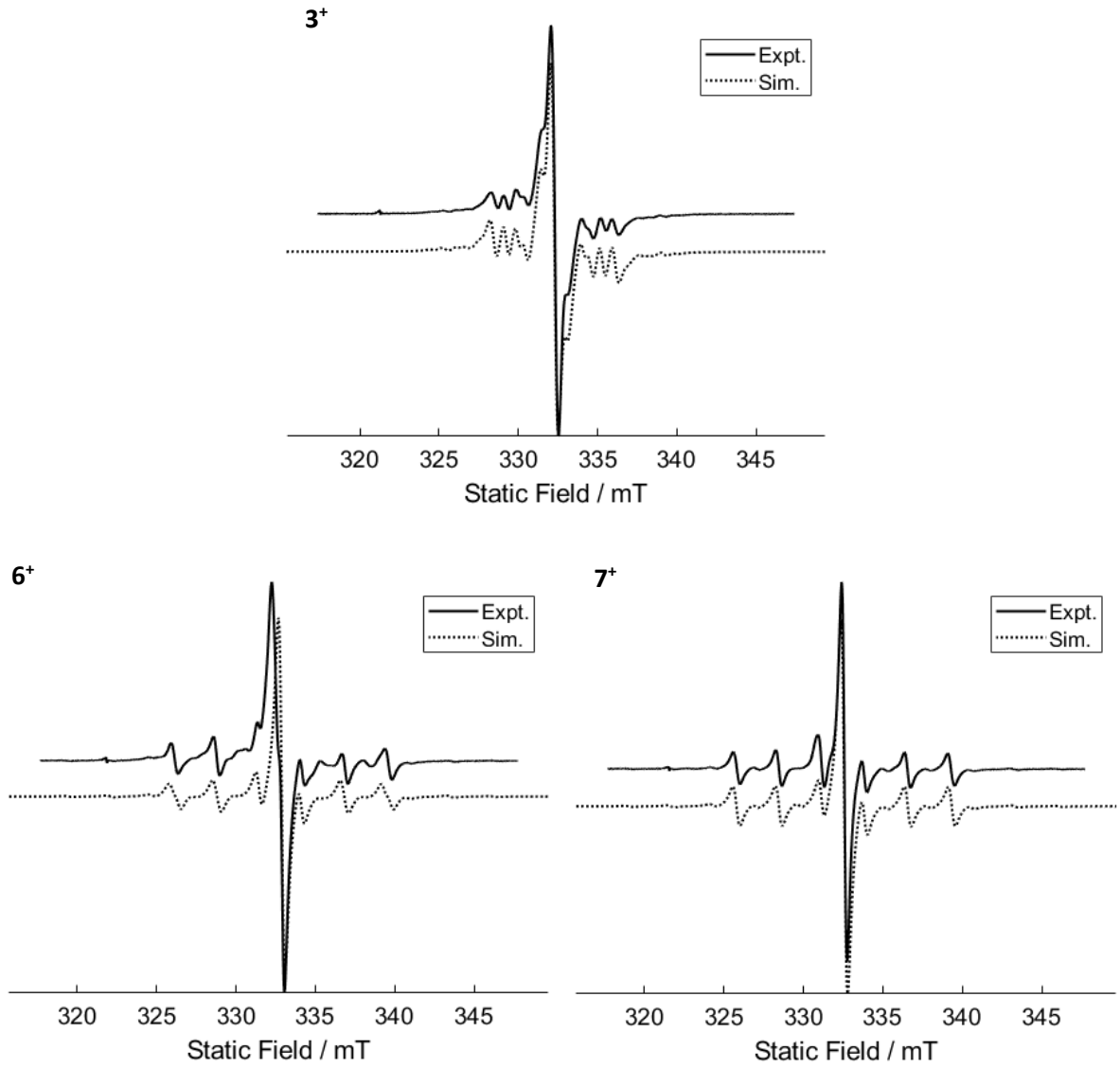

*Figure 3.17: Experimental (solid) and simulated (dashed) X-band Epr spectra of **3**$^{+}$, **6**$^{+}$ and **7**$^{+}$ in THF. The abnormality at 321 mT is a quartz impurity.*

Table 3.7: Summary of the EPR spectra data obtained from the simulated EPR spectra.

Compound	g-factor	A_{Iso} (1) / mT	A_{Iso} (2) / mT
3^{+}	1.933	1.447	1.161
6^{+}	1.932	2.641	2.489
7^{+}	1.933	2.588	-

The EPR spectrum of complex **6**$^{+}$ is shown in Figure 3.17, it displays a central peak at a g-factor of 1.932 with two sets of hyperfine couplings, which arise from the different coordination environments on the Mo resulting in the polarisation of the bond as discussed in chapter 2.[29] The hyperfine splitting can be well simulated using two equally weighted (A_{iso}(1)= 1Mo, A_{iso}(2)= 1Mo) independent hyperfine couplings of 2.641 mT and 2.489 mT, indicating the electron is localised on one dimolybdenum redox centre which is in agreement with the spectroelectrochemical assignment as class II (Figure 3.18). The hyperfine couplings A_{Iso} (1) and A_{Iso} (2) are similar in magnitude indicating the dimolybdenum bond is less polarised in **6**$^{+}$ than in **3**$^{+}$.

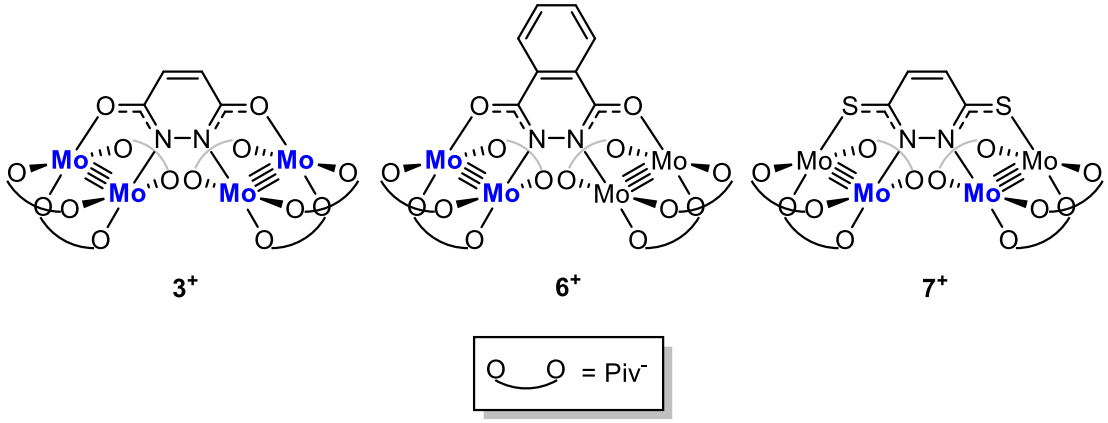

*Figure 3.18: Highlighting the electron delocalisation (blue) of **3**$^{+}$, **6**$^{+}$ and **7**$^{+}$.*

The EPR spectrum of **7**$^{+}$ is shown in Figure 3.17, it displays a central peak at a g-factor of 1.933 with one set of hyperfine coupling. The spectra can be well simulated using one hyperfine coupling of 2.588 mT (A_{iso}(1)= 2Mo). Complex **3**$^{+}$ and **7**$^{+}$ are both class III but display distinctly different EPR spectra, with complex **7**$^{+}$ exhibiting a spectrum more like complex **6**$^{+}$. The spectroelectrochemistry shows that the complex is class III but the magnitude of the hyperfine coupling indicates that the electron is delocalised across two molybdenum atoms and despite the differences in coordination environments only a single hyperfine is observed. The electron is therefore delocalised between both Mo_2 redox units, but the quadruple bond must be fully polarised, this is further confirmed by the presence of only a single hyperfine coupling. The electron is transferred between the two-molybdenum atoms

coordinated to the nitrogen's (Mo-N) in the pyridazine with the molybdenum atoms coordinated to the sulphur (Mo-S) remaining uninvolved (Figure 3.18). The Mulliken spin density confirms polarisation of the dimolybdenum quadruple bond with the spin densities calculated to be 0.17 and 0.32 for Mo-S and Mo-N respectively. The Mulliken spin densities indicate polarisation of the Mo-Mo bond but not to the degree observed experimentally. The polarisation could be a result of the 'bent' nature of the ligand, where a considerable contraction of the Mo-N bond is observed. This is the first example of a class III complex containing dimetal redox centres where the bond is polarised to such an extent that it results in only one half of the MM bond being involved in ET.

3.5 Conclusions

Three dimolybdenum dimers $[Mo_2(Piv)_3]_2(\mu_2\text{-Dop})$, $[Mo_2(Piv)_3]_2(\mu_2\text{-Phthal})$ and $[Mo_2(Piv)_3]_2(\mu_2\text{-Pdt})$ have been synthesised by stirring the deprotonated ligand with $[Mo_2(Piv)_3(MeCN)_2][BF_4]$ and characterised by ^1H NMR spectroscopy. All complexes displayed complicated spectra UV-Vis spectra with mixture of transitions in the visible region. The spectra were rationalised by DFT and shown to have transitions arising from transitions such as Mo_2-δ → Mo_2-π*, Mo_2-δ → pyridazine-π* and Mo_2-π → Mo_2-δ*. The electrochemistry shows that $[Mo_2(Piv)_3]_2(\mu_2\text{-Pdt})$ (ΔE_{pc} = 0.517 V) shows greater thermodynamic stabilisation of the MV state than $Mo_2(Piv)_3]_2(\mu_2\text{-Dop})$ (ΔE_{pc} = 0.444 V), whereas, $[Mo_2(Piv)_3]_2(\mu_2\text{-Phthal})$ (ΔE_{pc} = 0.366 V) shows a decrease in the thermodynamic stability. All complexes are believed to have a significant degree of through space coupling, as the calculated through space $Mo_2\cdots Mo_2$ separation is the longest in $[Mo_2(Piv)_3]_2(\mu_2\text{-Phthal})$ and the shortest in $[Mo_2(Piv)_3]_2(\mu_2\text{-Pdt})$ which could significantly impact the degree of coupling between the redox centres. The UV-Vis-NIR-IR spectra of the MV complexes show $[Mo_2(Piv)_3]_2(\mu_2\text{-Dop})^+$ and $[Mo_2(Piv)_3]_2(\mu_2\text{-Pdt})^+$ are fully delocalised (Class III) whereas, $[Mo_2(Piv)_3]_2(\mu_2\text{-Phthal})$ shows localisation of the electron (Class II). The EPR spectra of $[Mo_2(Piv)_3]_2(\mu_2\text{-Phthal})^+$ and $[Mo_2(Piv)_3]_2(\mu_2\text{-Dop})^+$ show the complexes are localised and delocalised respectively. Whereas, at first the EPR spectrum for the complex $[Mo_2(Piv)_3]_2(\mu_2\text{-Pdt})^+$ appears to show localisation, it in fact shows that the electron is evenly shared between two molybdenum atoms from different redox units. This is a remarkable example of electron localisation in a fully delocalised system and is believed to be one of the first examples. Electron transfer is typically described as either localised or delocalised between two redox centres, but this chapter shows that there is unequal distribution of the electron between the redox centres providing an example of how electronic coupling can be further tuned. This fundamental study therefore provides valuable insights into ET, rectification and will be important in the design on functional materials.

3.6 Experimental

See chapter 8 for the methods and materials section.

3.6.1 *Synthesis of 3,6-Pyridazinedithiol (H_2Pdt).*

3,6-dichloropyradazine (7.500 g, 0.05 mol) and sodium hydrogen sulphide monohydrate (18.630 g, 0.25 mol) were added to a Schlenk tube and suspended in a 2:1 mixture of methanol and water (120 mL). The suspension was heated at reflux for 15 hours at which point the solution was acidified using hydrochloric acid (1 M, ca. 80 mL) until no more yellow precipitate formed. The suspension was cooled to room temperature, followed by cooling to -18 °C overnight. The yellow precipitate was isolated by filtration and washed with cold methanol (3 x 30 mL) followed by diethyl ether (3 x 100 mL) to afford the product as a bright yellow solid. Yield 3.67 g (48 %) ^{1}H NMR (400 MHz, DMSO-d_6) δ 14.84 (s, 2H), 7.54 (s, 2H).

3.6.2 *Synthesis of $[Mo_2(Piv)_3]_2(\mu_2$-Phthal) (6)*

$Mo_2(Piv)_4$ (0.728 g, 1.22 mmol) and $[Mo_2(Piv)_2(MeCN)_6][BF_4]_2$ (1.000 g, 1.22 mmol) were added to a Schlenk flask and dissolved in a mixture of dichloromethane (20 mL) and MeCN (10 mL), the red solution was refluxed for 17 hours and cooled to room temperature. H_2Phthal (0.198 g, 1.22 mmol) and NaOMe (0.132 g, 2.45 mmol) were suspended in MeOH (20 mL) and stirred at room temperature for 17 hours to yield a colourless solution, which was then added dropwise to the $[Mo_2(Piv)_3]^+$. This resulted in an immediate colour change to dark orange, and the resulting solution was stirred for a further 20 hours. The solvents were removed under reduced pressure and the products extracted into a mixture of hexane and dichloromethane (10 ml, 1:1) and purified by column chromatography (eluent dichloromethane /hexane (50:50 (v/v)) → dichloromethane collecting the first orange band. The solvent was removed under reduced pressure and washed with hexane (3 x 10 ml) and dried to afford **6** as an orange solid. Yield 0.210 g (16 %) ^{1}H NMR (400 MHz, DMSO-d_6) δ 8.39 (dd, J = 6.1, 3.3 Hz, 2H), 7.82 (dd, J = 6.0, 3.4 Hz, 2H), 1.29 (s, 36H), 1.29 (s, 18H). MALDI-TOF-MS calcd. monoisotopic MW for

$Mo_4C_{38}H_{58}O_{14}N_2$, 1150.7, found *m/z* 1150.3 (M+). Elemental analysis Calcd. For $Mo_4C_{38}H_{58}O_{14}N_2$, C, 39.66; H, 5.08; N, 2.43; Found C, 39.68; H, 5.27; N, 2.31.

3.6.3 *Synthesis of $[Mo_2(Piv)_3]_2(\mu_2$-Pdt) (7)*

$Mo_2(Piv)_4$ (0.519 g, 0.87mmol) and $[Mo_2(Piv)_2(MeCN)_6][BF_4]_2$ (0.710 g, 0.87 mmol) were added to a Schlenk flask and dissolved in a mixture of dichloromethane (20 mL) and MeCN (10 mL), the red solution was refluxed for 17 hours and cooled to room temperature. H_2PDT (0.166 g, 0.87 mmol) and NaOMe (0.095 g, 1.75 mmol) were suspended in MeOH (20 mL) and stirred at room temperature for 17 hours to yield a colourless solution, which was then added dropwise to the $[Mo_2(Piv)_3]^+$. This resulted in an immediate colour change to dark green, and the resulting solution was stirred for a further 20 hours. The solvents were removed under reduced pressure and the products extracted into a mixture of hexane and dichloromethane (10 ml, 1:1) and purified by column chromatography (eluent dichloromethane /hexane (50:50 (v/v)) → dichloromethane/hexane (80:20 (v/v)) collecting the first blue band. The solvent was removed under reduced pressure and washed with hexane (3 x 10 ml) and dried to afford **6** as an dark blue solid. Yield 0.134 g (14 %) ^{1}H NMR (400 MHz, DMSO-d_6) δ 7.21 (s, 2H), 1.33 (s, 18H), 1.31 (s, 36H). MALDI-TOF-MS calcd. monoisotopic MW for $Mo_4C_{34}H_{56}O_{12}N_2S_2$, 1132.8, found *m/z* 1132.2 (M+). Elemental analysis Calcd. For $Mo_4C_{34}H_{56}O_{12}N_2S_2$, C, 36.05; H, 4.98; N, 2.47; Found C, 36.17; H, 5.13; N, 2.29.

3.7 References

1 M. H. Chisholm, F. Feil, C. M. Hadad and N. J. Patmore, *J. Am. Chem. Soc.*, 2005, **51**, 18150–18158.

2 J. Hicks, S. P. Ring and N. J. Patmore, *Dalt. Trans.*, 2012, **41**, 6641.

3 Y. Yang Wu, M. Meng, G. Yi Wang, P. Feng and C. Y. Liu, *Chem. Commun.*, 2017, **53**, 3030–3033.

4 F. A. Cotton, Z. Li, C. Y. Liu and C. A. Murillo, *Inorg. Chem.*, 2007, **46**, 7840–7847.

5 Y. N. Tan, T. Cheng, M. Meng, Y. Y. Zhang, C. Y. Liu, M. F. Sun, Y. Zheng and P. J. Low, *J. Phys. Chem. C*, 2017, **121**, 27860–27873.

6 R. H. Cayton, M. H. Chisholm, J. C. Huffman and E. B. Lobkovsky, *J. Am. Chem. Soc.*, 1991, **113**, 8709.

7 J. Hübscher, T. Gruber, W. Seichter, J. Kortus and E. Weber, *J. Mol. Struct.*, 2015, **1091**, 88–97.

8 F. A. Cotton, L. M. Daniels, E. A. Hillard and C. A. Murillo, *Inorg. Chem.*, 2002, **41**, 2466–2470.

9 J. M. Casas, R. H. Cayton and M. H. Chisholm, *Inorg. Chem.*, 1991, **30**, 358–360.

10 S. Mallick, T. Cheng, L. Chen, M. Meng, Y. Y. Zhang and C. Y. Liu, *Dalt. Trans.*, 2017, **46**, 5711–5723.

11 X. Xiao, C. Y. Liu, Q. He, M. J. Han, M. Meng, H. Lei and X. Lu, *Inorg. Chem.*, 2013, **52**, 12624–12633.

12 M. H. Chisholm and N. J. Patmore, *J. Chem. Soc. Dalt. Trans.*, 2006, 3164–3169.

13 D. E. Richardson and H. Taube, *Inorg. Chem.*, 1981, **20**, 1278–1285.

14 C. E. B. Evans, M. L. Naklicki, A. R. Rezvani, C. A. White, V. V. Kondratiev and R. J. Crutchley, *J. Am. Chem. Soc.*, 1998, **120**, 13096–13103.

15 R. J. Crutchley, in *Advances in Inorganic Chemistry*, 1994, pp. 273–325.

16 C. Lapinte, *J. Organomet. Chem.*, 2008, **693**, 793–801.

17 B. S. Dolinar and J. F. Berry, *Dalt. Trans.*, 2014, **43**, 6165–6176.

18 C. Lin, J. D. Protasiewicz, E. T. Smith and T. Ren, *Inorg. Chem.*, 1996, **35**, 6422–6428.

19 M. T. Kang, M. Meng, Y. N. Tan, T. Cheng and C. Y. Liu, *Chem. - A Eur. J.*, 2016, **22**, 3115–3126.

20 M. J. Han, C. Y. Llu and P. F. Tian, *Inorg. Chem.*, 2009, **48**, 6347–6349.

21 G. Y. Zhu, M. Meng, Y. N. Tan, X. Xiao and C. Y. Liu, *Inorg. Chem.*, 2016, **55**, 6315–6322.

22 D. D. Méndez-Hernández, P. Tarakeshwar, D. Gust, T. A. Moore, A. L. Moore and V. Mujica, *J. Mol. Model.*, 2013, **19**, 2845–2848.

23 D. M. D'Alessandro and F. R. Keene, *Chem. Soc. Rev.*, 2006, **35**, 424–440.

24 B. S. Brunschwig, C. Creutz and N. Sutin, *Chem. Soc. Rev.*, 2002, **31**, 168–184.

25 D. M. D'Alessandro, P. H. Dinolfo, J. T. Hupp, P. C. Junk and F. R. Keene, *Eur. J. Inorg. Chem.*, 2006, 772–783.

26 S. Puhl, T. Steenbock, C. Herrmann and J. Heck, *Angew. Chemie - Int. Ed.*, 2020, **59**, 2407–2413.

27 X. Xiao, M. Meng, H. Lei and C. Y. Liu, *J. Phys. Chem. C*, 2014, **118**, 8308–8315.

28 M. H. Chisholm, *Philos. Trans. R. Soc. A Math. Phys. Eng. Sci.*, 2008, **366**, 101–112.

29 M. H. Chisholm, *Coord. Chem. Rev.*, 2013, **257**, 1576–1583.

30 M. H. Chisholm and N. J. Patmore, *Acc. Chem. Res.*, 2007, **40**, 19–27.

The influence of bridging ligand topology on electron delocalisation in mixed valence complexes

4.1 Abstract

A series of dimolybdenum dimers of formula $[Mo_2(Piv)_3]_2(\mu_2$-bridge) (where Piv = trimethylacetate. bridge = pyrazine-2,3-diol (**8**), 2,3-dihydroquinoxaline (**9**) and 2,3-Pyridazinedithiol (**10**)) have been synthesised and characterised by ^{1}H NMR spectroscopy. The stability of the mixed valent (MV) state generated following a one electron oxidation has been probed by cyclic voltammetry, with the compounds displaying ΔE_{pc} of 0.477 V in **8**, 0.429 V in **9** and 0.550 V in **10.** The UV-Vis-NIR spectra of $\mathbf{8}^+$ and $\mathbf{9}^+$ exhibit a relatively intense charge resonance band in the NIR region with low energy cut off, consistent with full delocalisation of the electron between the dimetal units (Class III). Complex $\mathbf{10}^+$ exhibits a relatively intense symmetric charge resonance band in the NIR, the compound has been assigned as class IV. The complexes have a cross coupling matrix parameter (H_{ab}) of 2043 cm^{-1} for $\mathbf{8}^+$, 2036 cm^{-1} for $\mathbf{9}^+$ and 2223 cm^{-1} for $\mathbf{10}^+$. Electron paramagnetic resonance spectroscopy of the MV species indicate the electron predominantly resides in a Mo_2-δ orbital with a g-factor of 1.93-1.94. Complexes $\mathbf{8}^+$, $\mathbf{9}^+$ and $\mathbf{10}^+$ have two hyperfine couplings of between 1.09 mT and 1.45 mT indicating the electron is fully delocalised over all four Mo atoms.

4.2 Influence of bridging topology on electron transfer

In chapter 2 the introduction of asymmetry to the bridge by the addition of electron donating and withdrawing groups was discussed; the complexes were expected to have substantial stabilisation resulting from through space coupling. In chapter 3 the effect of internuclear separation in through space coupled dimolybdenum MV complexes was explored. In both chapters the electronic stabilisation observed for these complexes was expected to have a significant through space contribution. Structural isomerism can lead to large changes in the internuclear separation, and this chapter explores the effect this has on the stabilisation of the mixed valent state.

The study of redox-active moieties linked by conjugated π systems has received much attention for many decades due in a large part to the mixed-valence (MV) complexes that can be generated following one-electron redox processes.[1,2] The majority of studies have explored linear systems, largely of $[L_xM_A]$−bridge−$[M_BL_x]$ architecture where the redox groups are often metallic in nature.[3–6] Typically, these bridges incorporate a substituted *p*-phenylene moiety due to its conjugated π system and its high functionality. The substitution pattern of the phenylene moiety has been shown to facilitate electron transfer (ET) in the case of *ortho* and *para* substitutions or impede ET like *meta* substituted phenylene.[7,8]

Lapinte *et al.* have reported two complexes with the formula, $[(\eta^2\text{-dppe})(\eta^5\text{-}C_5Me_5)Fe–C{\equiv}C–]_2(C_6H_4)$ (Figure 4.1), one complex employs a *para* substituted phenylene bridge, while the other employs a *meta* substituted phenylene bridge.[9–11]

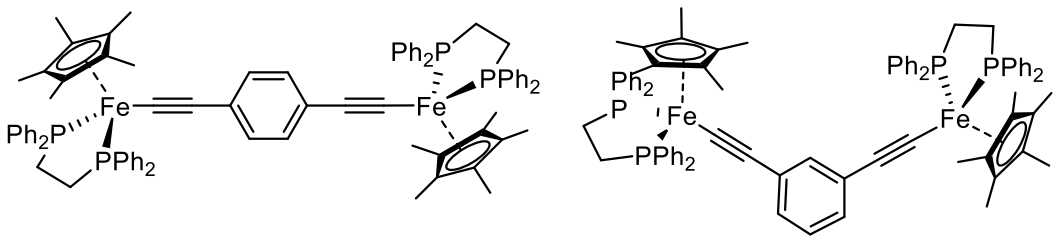

Figure 4.1: The $[(\eta^2\text{-dppe})(\eta^5\text{-}C_5Me_5)Fe–C{\equiv}C–]_2(C_6H_4)$ complexes reported by Lapinte et al.

The thermodynamic stability of the MV state was probed electrochemically, both complexes exhibited two one electron oxidation events corresponding to the sequential removal of electrons from the Fe^{II} centres. The larger the difference between the two half wave potentials ($\Delta E_{1/2}$) between the two oxidative events, the greater the thermodynamic stability of the MV state, the magnitude of which can judiciously be used to assess the degree of electronic coupling. The reported $\Delta E_{1/2}$ values are 0.26 V and 0.13 V for the *para* and *meta* substituted derivatives respectively. Despite the *meta* derivative having a Fe···Fe separation of 10.2 Å, which is shorter than the *para* derivative (11.6 Å), it showed a considerable decrease in the thermodynamic stability of the MV state. Absorption spectra of the MV complexes showed a charge resonance band (class III) for the *para* derivative and an intervalence charge transfer band (class II) for the *meta* derivative. Analysis of the charge resonance bands showed that the *para* and *meta* derivatives had cross-coupling matrix parameters (H_{ab}) of 1008 cm^{-1} and 161 cm^{-1} respectively.[12,13] The complexes were analysed by scanning tunnelling microscopy (STM) to determine whether the *meta* substituted complex exhibited through space coupling. For the *para* substituted complex STM analysis confirmed the class III assignment, the analysis of the *meta* substituted complex confirmed the class II assignment but showed no sign of through space coupling. The authors conclude that through bond electron transfer occurs in both cases, and despite the extended distance observed for the *para* substituted complex it showed significantly greater coupling, reinforcing that the topology of the ligand is essential to tuning the degree of electronic coupling.

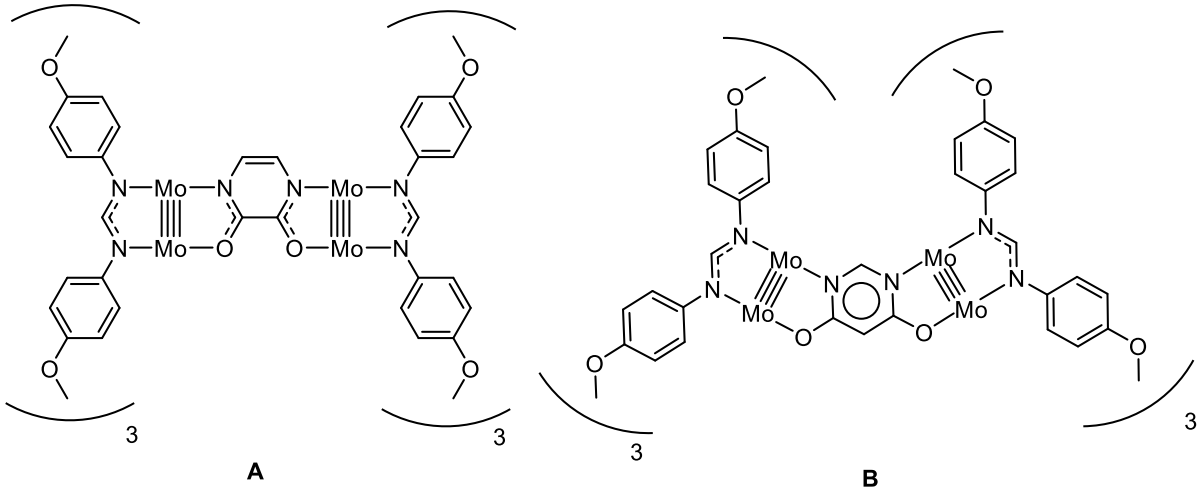

Figure 4.2: The Cyclic Polyamidato bridged [Mo2(DAniF)3]2(μ2-L) complexes reported by Cotton et al. where the bridges are2,3-dioxy-1,4-pyrazinate (A) or 4,6-dioxypyrimidinate (B).

Structural isomerism of the bridge and how it effects dimolybdenum dimers is less well explored. Cotton *et al.* reported two complexes with the structure $[Mo_2(DAniF)_3]_2(\mu_2\text{-L})$ (Where DAniF = N,N′-di-*p*-anisylformamidinate) the bridging ligand was either 2,3-dioxy-1,4-pyrazinate (**A**) or 4,6-dioxypyrimidinate (**B**) (Figure 4.2).[14] The stability of the MV state was probed by cyclic voltammetry, complex **A** had a $\Delta E_{1/2}$ of 0.258 V and complex **B** had a $\Delta E_{1/2}$ of 0.187 V. Complex **B** is expected to have a considerable degree of coulombic interaction as a result of the decreased $Mo_2\cdots Mo_2$ separation, which is expected to increase the $\Delta E_{1/2}$ observed for **B**. The authors describe the bridge in complex **A** as having a *meta* substitution of the nitrogen's and the bridge in **B** as having a *para* substitution of the nitrogen atoms. It is believed that as *meta* substituted nitrogen's in complex **B** decreases the number of possible resonance structures which affects the energetics and symmetry of the compound resulting in a decreased thermodynamic stability of the MV state. As a result of the bulky DAniF ligand, the compound containing the *meta* substituted bridge could not be synthesised.

4.3 Aims

The effect of substituted phenylene bridges has been well studied for monometallic redox centres but the effect of ligand topology on dimolybdenum complexes remains relatively unexplored. Given the dramatic effect that changing the ligand topology has on monometallic species a variety of structural isomers of the bridges employed in chapter 3 will be employed as the bridging ligands in this chapter. These ligands have a 2,3-dihydroxy or 2,3-dithiopyridazine core (Figure 4.3) which will allow for electron transfer to occur across a linear bridge and are unexpected to facilitate through space electron transfer as a result of the increased $Mo_2 \cdots Mo_2$ separation.

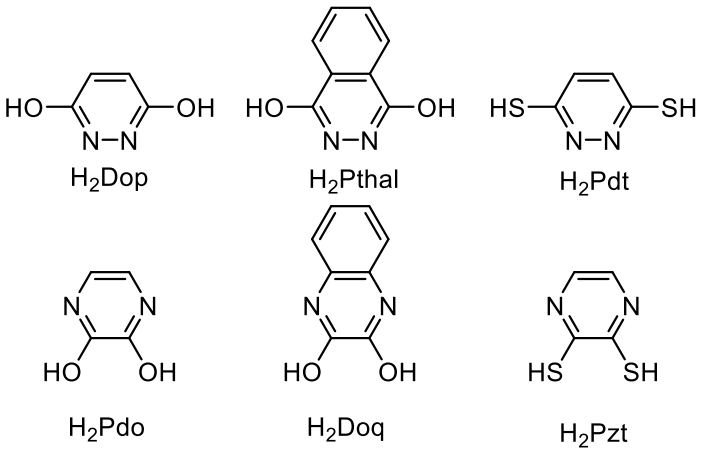

Figure 4.3:(Top) The bridging ligands employed in chapter 3 (Bottom) The bridging ligands targeted for chapter 4.

Electrochemical and spectroelectrochemical studies will be used to probe electron delocalisation between the dimetal units in the MV state. Based on previous studies, differences in the electronic coupling would be evidenced by changes in the $\Delta E_{1/2}$ values obtained by cyclic voltammetry and the cross-coupling matrix, H_{ab}, obtained by the analysis of the IVCT transition in the NIR region. The delocalisation of the electron will be probed using EPR spectroscopy and theoretical calculations. This series of compounds will provide a rare opportunity to probe the effect of bridging ligand topology on dimolybdenum dimers and will also allow for comparisons to be drawn regarding the effect the through space component has on the complexes reported in chapter 3.

4.4 Results and discussion

4.4.1 *Synthesis*

2,3-dihydroquinoxaline (H_2Doq) was prepared according to a literature procedure by the condensation reaction between oxalic acid and 1,2-diaminobenzene (Scheme 4.1).[15] 2,3-Pyridazinedithiol (H_2Pzt) was synthesised through a nucleophilic aromatic substitution reaction, by refluxing 1,4-dichloropyradazine with sodium hydrogen sulphide in a 2:1 MeOH: H_2O mixture following a literature preparation (Scheme 4.1).[16]

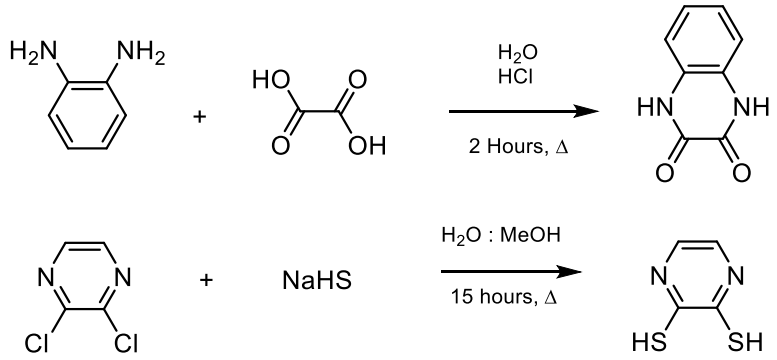

Scheme 4.1: The syntheitc route to 2,3-dihydroquinoxaline (H_2Doq) and 2,3-Pyridazinedithiol (H_2Pzt)

H_2Pzt was deprotonated in a methanolic solution of sodium methoxide, but pyrazine-2,3-diol (H_2Pdo) and H_2Doq could not be deprotonated in the same manner due to the insolubility of the acid and sodium salt in methanol. Therefore, H_2Doq was deprotonated with *n*-butyllithium in THF and H_2Pdo was deprotonated using tetrabutylammonium hydroxide in methanol. $[Mo_2(Piv)_3]_2(\mu_2$-Pdo) (**8**), and $[Mo_2(Piv)_3]_2(\mu_2$-Pzt) (**10**) were synthesised by stirring the red monocationic intermediate $[Mo_2(Piv)_3(MeCN)_2][BF_4]$ with $(NBu_4)_2$Pdo and Na_2Pzt. $[Mo_2(Piv)_3]_2(\mu_2$-Doq) (**9**) was prepared in a similar fashion by stirring the monocationic intermediate $[Mo_2(Piv)_3(MeCN)_2][BF_4]$ with Li_2Doq as reported in literature.[17] The reaction resulted in an immediate colour change (**8** = red, **9** = orange and **10** = green) and the reaction was stirred for a further 17 hours to ensure completion (Scheme 4.2). The solvent was removed *in vacuo,* and the ^{1}H NMR spectra indicated several impurities. The products were purified using air sensitive column chromatography to isolate **8** as an orange solid (22 %), **9** as

an orange solid (18 %) and **10** as a dark green solid (41 %). The modest yields reflect the multistep reaction which generates numerous by-products as well as the difficulty in purifying the complexes. Complexes **8 - 10** are soluble in THF and DMSO and were found to be analytically pure by elemental analysis. The complexes have been characterised by ^{1}H NMR spectroscopy and MALDI-TOF mass spectrometry. Despite numerous attempts to crystallise complexes **8 – 10** for X-ray diffraction, suitable crystals could not be obtained, although the dimetal units are all expected to be co-planar with one another.

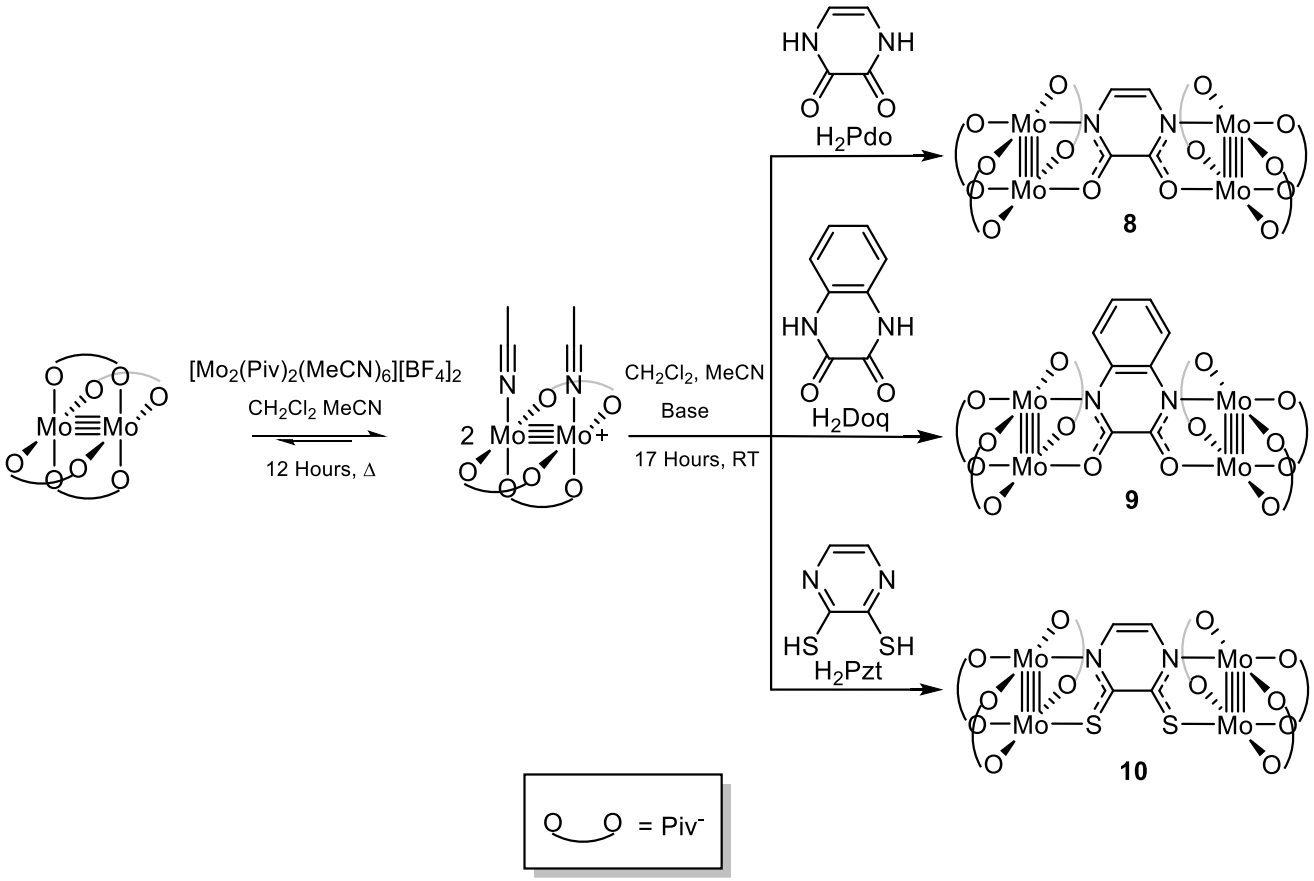

*Scheme 4.2: Synthesis of $[Mo_2(Piv)_3]_2(\mu_2$-Pdo) (**8**), $[Mo_2(Piv)_3]_2$ (μ_2-Doq) (**9**) and $[Mo_2(Piv)_3]_2(\mu_2$-Pzt) (**10**).*

4.4.2 *^{1}H NMR spectroscopy*

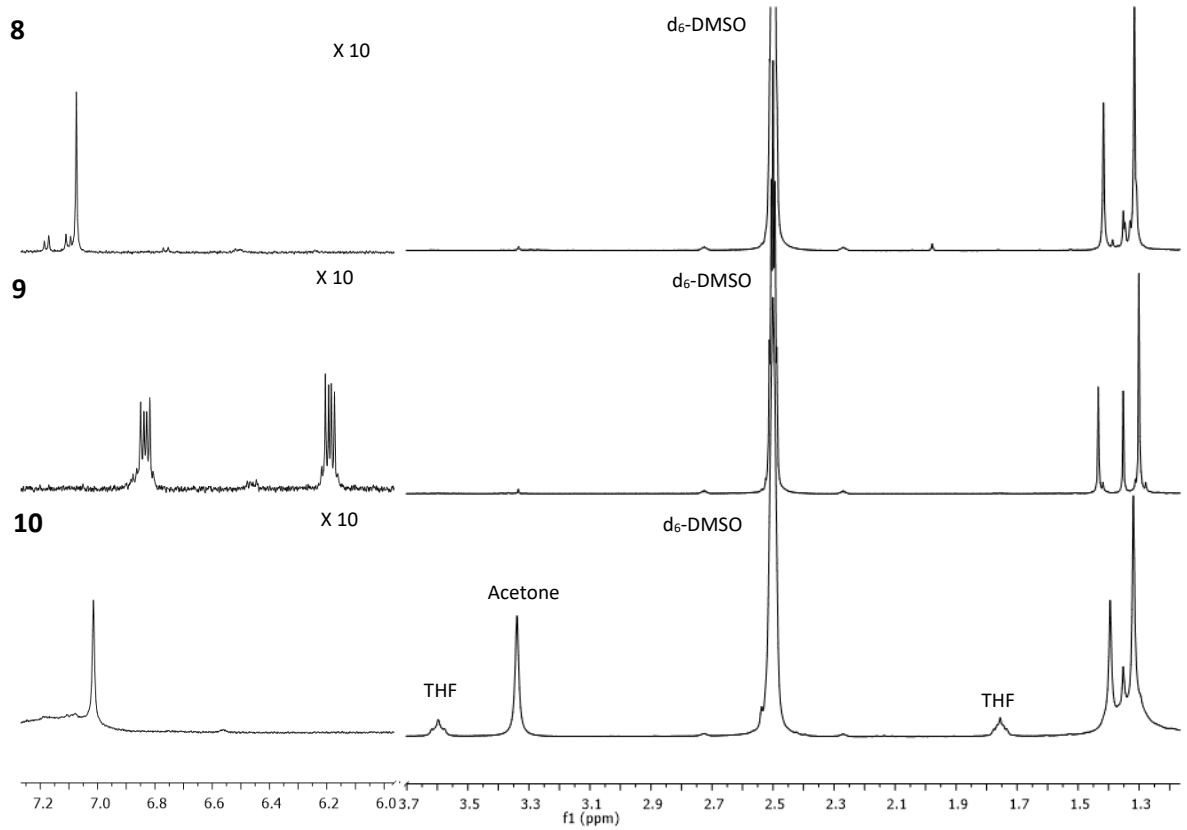

*Figure 4.4: ^{1}H NMR spectra of complexes **8 – 10** in d_6-DMSO Left: A magnified portion of the aromatic region showing bridging ligand resonances.*

The ^{1}H NMR spectra of H_2Pdo and H_2Doq are consistent with literature.[15,16] The ^{1}H NMR spectra for complexes **8 – 10** in d_6-DMSO are shown in Figure 4.4. Complex **8** has a 2:1 Piv integration pattern at 1.31 and 1.28 ppm that is expected for a monosubstituted dimolybdenum complex. The Pdo^{2-} ligand has two protons on the backbone, which are observed as a singlet at 7.54 ppm indicating that the ligand is bound to two equivalent dimolybdenum redox centres. The spectrum of **9** a known complex matches literature with two singlets at 1.43 and 1.30 ppm in a 1:2 ratio typical for a monosubstituted dimolybdenum complex.[17] The bridge resonances are observed as two doublet of doublets (J = 6.1, 3.4 Hz) at 6.83 and 6.19 ppm.[18] The ^{1}H NMR spectrum of **10** exhibits the expected 2:1 Piv resonances at 1.32 and 1.40 ppm and a singlet at 7.02 ppm corresponding to the Pzt backbone. All complexes have an impurity at 1.36 ppm and 1.11 ppm which are assigned as $Mo_2(Piv)_4$ and free pivalic acid respectively. These impurities are a result of facile ligand scrambling in the presence of DMSO

commonly observed for dimolybdenum complexes containing carboxylate ligands.[18,19] The impurities are not observed in the electrochemistry which is performed in THF, nor are they observed in the EA. Complex **10** has acetone in the sample which originates from an improperly dried NMR tube. Prior to submission for elemental analysis all complexes were dried under high vacuum for 48 hours.

4.4.3 *Theoretical calculations*

Theoretical calculations have been employed to help rationalise the observed spectroscopic behaviour of complexes **8, 9** and **10** and were carried out by Dr Nathan Patmore and Dr Anthony Meijer (University of Sheffield). DFT calculations were performed on model complexes (**8', 9'** and **10'**), in which the pivalate ligands have been replaced by formate groups to reduce computational time. The calculated frontier molecular orbital energy level diagram for **8', 9'** and **10'** is shown in Figure 4.5.

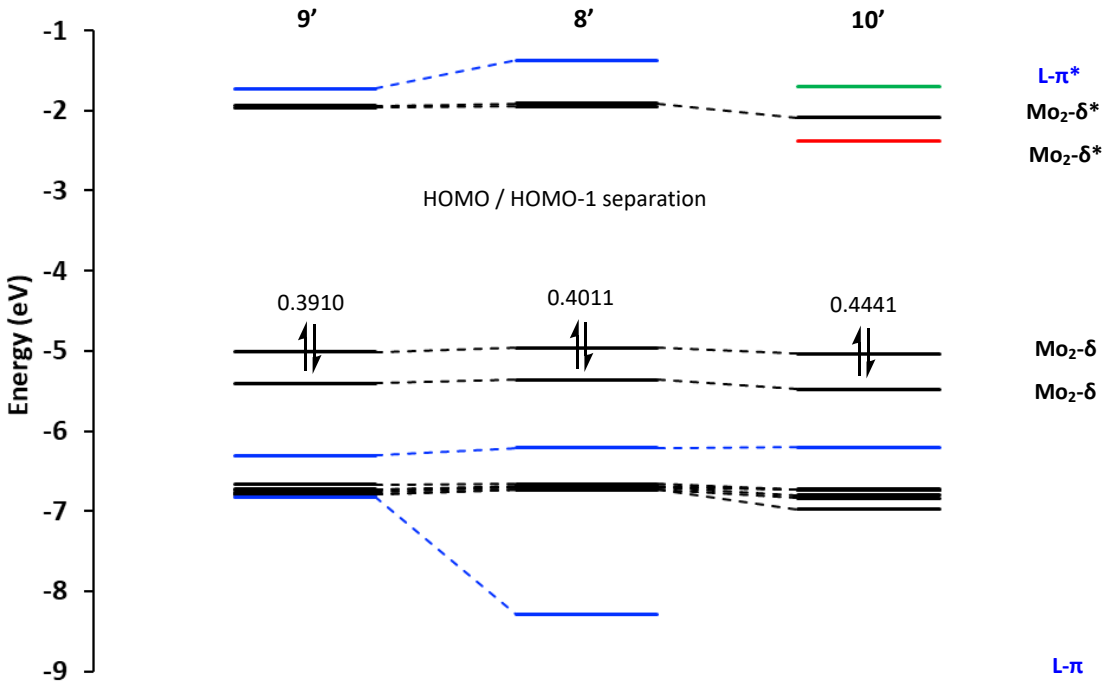

*Figure 4.5: The calculated frontier orbital energy level diagrams of model compounds **8', 9'** and **10'**.*

For all three complexes the HOMO and HOMO-1 are both Mo_2-δ orbitals, the orbitals are non-degenerate as the HOMO results from the in-phase combination of the Mo_2-δ orbitals with the pyrazine-π orbital, whereas, the HOMO-1 is obtained from the out-of-phase combination of the Mo_2-

δ and the pyrazine-π* orbital.[20] The HOMO/HOMO-1 separation is indicative of the extent of electronic coupling between the two redox centres.

The HOMO/HOMO-1 separations for complexes **8', 9'** and **10'** are 0.4011 eV,0.3910 eV and 0.4441 eV respectively, in all cases the HOMO/HOMO-1 separations are greater than the non-linear derivatives (**3', 6'** and **7'**) and are therefore expected to show an increase in coupling. Complex **10'** has the greatest HOMO/HOMO-1 separation and is expected to show stronger coupling than **8'** and **9'.** The decrease in the energy of the HOMO between **8'** and **10'** is a result of the decreased π donation from the sulphur 3p orbital compared to that of the oxygen 2p orbital.[21] For complexes **8'** and **9'** the LUMO and LUMO+1 are the Mo_2-δ* orbitals and LUMO+2 is the pyrazine-π* orbital. Whereas, Complex **10'** shows significant mixing between the pyrazine-π* and Mo_2-δ* orbitals as shown in Figure 4.6, resulting in the LUMO being assigned as the Mo_2-δ*/pyrazine-π* and the LUMO+2 being assigned as the pyrazine-π*/Mo_2-δ*. The pyrazine-π orbital with the correct symmetry to facilitate ET is the HOMO-10 in **8'** and the HOMO-9 in **9'** but remained unidentified in complex **10'**. The mechanism of stabilisation of the MV state for complexes **8'** and **10'** is expected to be from both the electron hopping and hole hopping mechanisms. However, for **9'** the mechanism of stabilisation is expected to only result from the hole hopping mechanism as the Mo_2-δ/pyrazine-π separation (1.81 eV) is significantly smaller than the Mo_2-δ/pyrazine-π* (3.29 eV) separation.

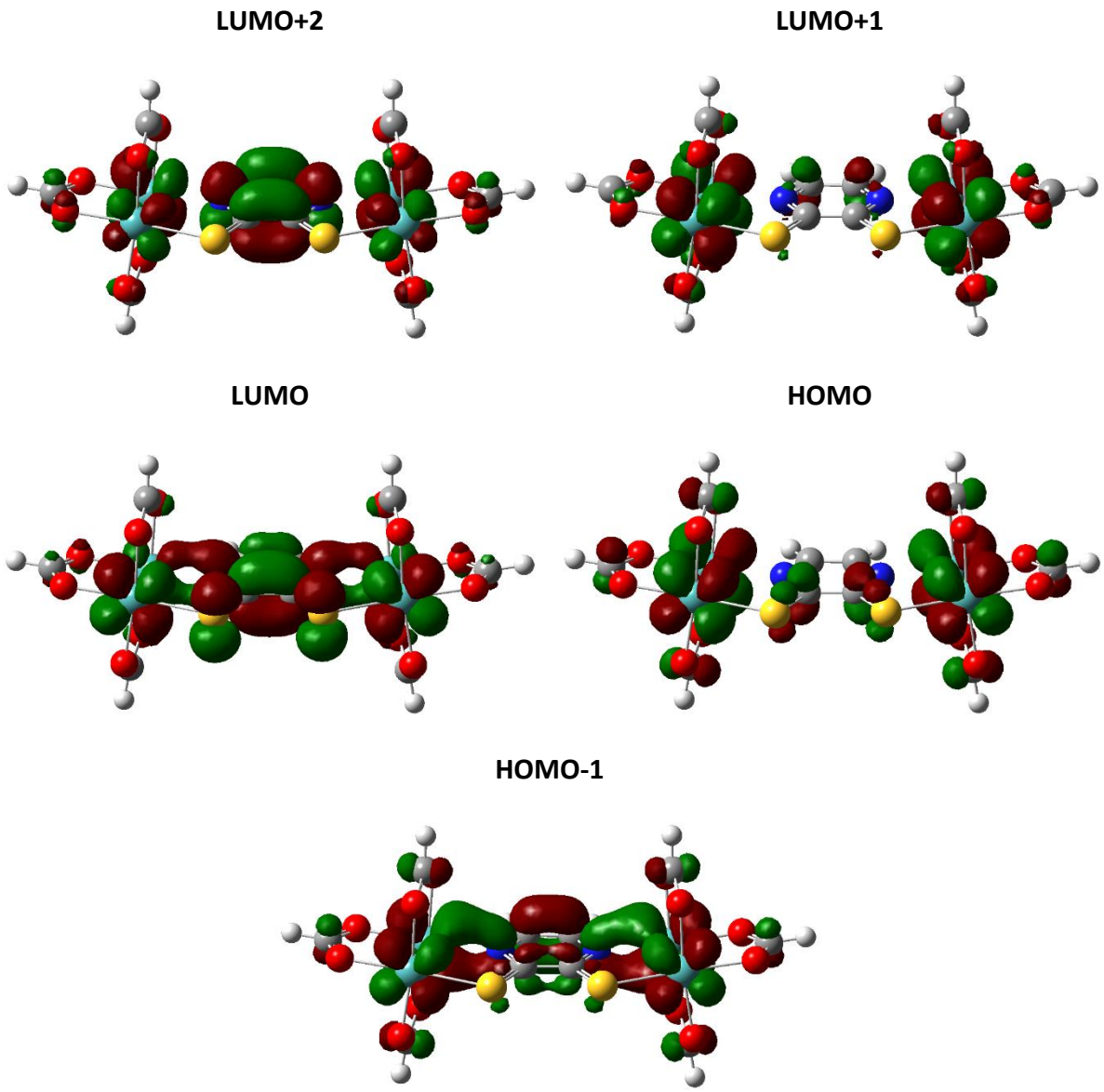

*Figure 4.6: Gausview plots (0.03 isosurface value) of selected orbitals for **10'**.*

4.4.3.1 Calculated absorption spectra

The optical transitions for **8', 9'** and **10'** were calculated in THF using time dependent DFT (TD-DFT), with the calculated transition energies summarised in Table 4.1, Table 4.2 and Table 4.3 respectively. The experimental spectra (*vide infra*) and calculated spectra are in good agreement in both energy and intensity. The calculated spectra predict the transitions at a slightly higher energy as a result of changing the ancillary ligands from Piv to formate groups, which decreases the energy of the HOMO and increases the energy of any transitions occurring from the Mo_2-δ orbitals. The spectra for **8'** has

three very intense transitions at 341 nm, 414 nm and 432 nm which arise due to the pyrazine-π → Mo_2-δ* LMCT, Mo_2-δ → pyrazine-π* MLCT and Mo_2-δ → Mo_2-π*transition respectively. The spectra also have several low intensity transitions consisting of Mo_2-δ → Mo_2-δ*and Mo_2-π → Mo_2-δ* transitions.

*Table 4.1: Calculated transitions for **8'** (f > 0.005)in THF, transitions are assigned on their most significant character.*

Energy / eV	λ_{max} / nm	*f*	Transition	Assignment
2.381	520	0.0413	HOMO → LUMO+1	Mo_2-δ → Mo_2-δ*
2.864	432	0.0231	HOMO-1 → LUMO+1	Mo_2-δ → Mo_2-δ*
2.865	432	0.1246	HOMO-1 → LUMO	Mo_2-δ → Mo_2-π*
2.994	414	0.3019	HOMO → LUMO+2	Mo_2-δ → pyrazine-π*
3.189	388	0.0121	HOMO-4 → LUMO	Mo_2-π → Mo_2-δ*
3.417	362	0.0116	HOMO-1 → LUMO+2	Mo_2-δ → pyrazine-π*
3.630	341	0.3845	HOMO-2 → LUMO	pyrazine-π → Mo_2-δ*

The most prominent transitions for complex **9'** are the Mo_2-δ → pyrazine-π* MLCT at 458 nm, the Mo_2-δ → Mo_2-π* at 443 nm and the pyrazine-π → Mo_2-δ*LMCT at 394 nm. The complex has low intensity transitions consisting of the Mo_2-δ → Mo_2-δ*and pyrazine-π → Mo_2-δ* transitions.

*Table 4.2: Calculated transitions for **9'** (f > 0.005) in THF, transitions are assigned on their most significant character.*

Energy / eV	λ_{max} / nm	*f*	Transition	Assignment
2.392	518	0.0122	HOMO → LUMO+1	Mo_2-δ → Mo_2-δ*
2.705	458	0.2541	HOMO → LUMO+2	Mo_2-δ → pyrazine-π*
2.794	443	0.1533	HOMO → LUMO+4	Mo_2-δ → Mo_2-π*
2.892	428	0.0165	HOMO-1 → LUMO	Mo_2-δ → Mo_2-δ*
3.142	394	0.0374	HOMO-1 → LUMO+2	Mo_2-δ → Pyrazine-π*
3.712	334	0.2164	HOMO-2 → LUMO	Pyrazine-π → Mo_2-δ*
3.778	328	0.0453	HOMO-2 → LUMO+1	Pyrazine-π → Mo_2-δ*

Complex **10'** shows a large degree of orbital mixing, like that observed for **7'**, and the most prominent transition is the pyrazine-π → Mo_2-δ* LMCT at 356 nm. The complex contains other strong transitions at 591 nm, 458 nm and 457 nm which corresponds to the Mo_2-δ → Mo_2-δ*/pyrazine-π* and Mo_2-δ → pyrazine-π*/Mo_2-δ* transitions.

*Table 4.3: Calculated transitions for **10'** (f > 0.005)in THF, transitions are assigned on their most significant character.*

Energy / eV	λ_{max} / nm	*f*	Transition	Assignment
2.098	591	0.1476	HOMO→LUMO	Mo_2-δ → Mo_2-δ*/pyrazine-π*
2.654	467	0.0327	HOMO→LUMO+3	Mo_2-δ → Mo_2-π*
2.703	458	0.1499	HOMO→LUMO+2	Mo_2-δ → pyrazine-π* /Mo_2-δ*, Mo_2-δ → Mo_2-π*
2.711	457	0.1823	HOMO→LUMO+2	Mo_2-δ → pyrazine-π*/Mo_2-δ*, Mo_2-δ → Mo_2-π*
3.228	384	0.0158	HOMO-1→LUMO+2	Mo_2-δ → pyrazine-π*/Mo_2-δ*
3.372	367	0.0298	HOMO-2→LUMO	pyrazine-π → Mo_2-δ*/pyrazine-π*
3.474	356	0.2560	HOMO-2→LUMO+1	pyrazine-π → Mo_2-δ*

4.4.4 *Electrochemistry*

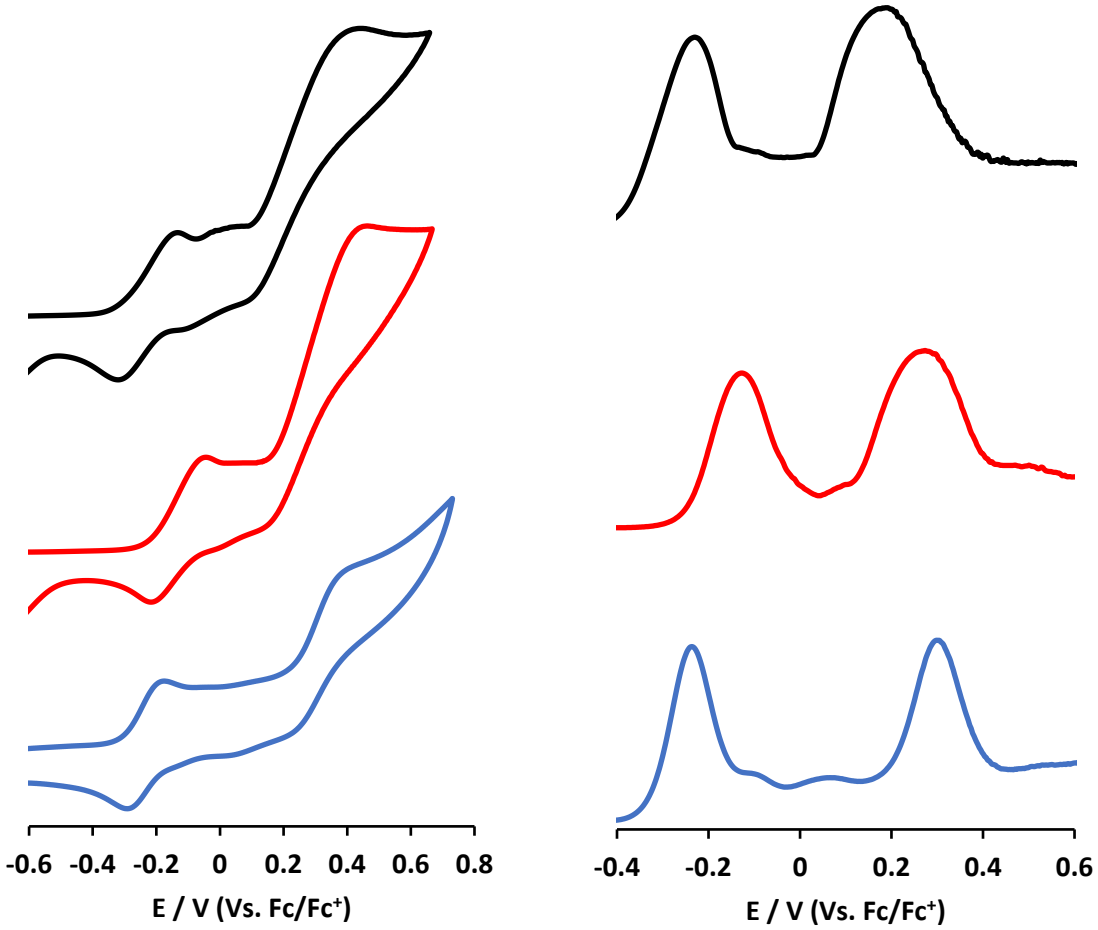

*Figure 4.7: CV (left, 100 mVs^{-1}) and DPV (right, 10 mVs^{-1}) of complexes **8** (black), **9** (red) and **10** (blue) in 0.1 M NBu_4PF_6/ THF solution at a concentration of 5 mM, and referenced against the Fc/Fc^+ couple (0.00 V).*

The cyclic voltammograms and differential pulse voltammograms of **8**, **9** and **10** in 0.1 M NBu_4PF_6 / THF are displayed in Figure 4.7, and the data summarised in Table 4.4. All complexes show two successive one electron oxidations corresponding to the removal of electrons from the Mo_2-δ orbitals. As the complexes have a quasi-reversible second oxidation the $E_{1/2}(2)$ could not be determined and instead the potentials are reported as the cathodic peak potentials (E_{pc}), which in turn were used to estimate the values of $\Delta E_{1/2}$. As the K_c can only be strictly determined for reversible redox processes, the discussion will revolve around the ΔE_{pc}, although the K_c is included in Table 4.4 for comparison.[22]

*Table 4.4: Cyclic voltammetry data for complexes **8, 9** and **10** in 0.1 M NBu_4PF_6 / THF solution at a concentration of 5 mM, and referenced against the Fc/Fc^+ couple (0.00 V). Cyclic voltammetry data for complexes **3**, **6** and **7** is included for comparison.*

Complex	$E_{1/2}(1)$ / V	$E_{pc}(1)$ / V	$E_{pc}(2)$ / V	ΔE_{pc} / V	K_c (x 10^6)
8	-0.268	-0.230	0.247	0.477	115
9	-0.141	-0.135	0.294	0.429	17.9
10	-0.249	-0.232	0.318	0.550	1990
3	-0.165	-0.133	0.311	0.444	321
6	-0.114	-0.041	0.325	0.366	1.54
7	-0.011	0.021	0.538	0.517	550

The calculated $Mo_2 \cdots Mo_2$ separation for complexes **8 – 10** are given in Table 4.5. These values range between 7.916 Å and 6.871 Å and are too great to facilitate through space electron coupling.[23] Therefore, unlike the nonlinear derivatives (**3, 6** and **7**) the linear derivatives (**8 – 10**) are expected to have a negligible through space electron transfer component stabilising the MV state.

*Table 4.5: The calculated through space $Mo_2 \cdots Mo_2$ separation for complexes **8 – 10.***

Complex	$Mo_2 \cdots Mo_2$ / Å	$Mo_2^{0.5+} \cdots Mo_2^{0.5+}$ / Å
8'	6.912	6.836
9'	6.871	6.792
10'	7.916	7.828
3'	3.635	3.613
6'	3.645	3.667
7'	3.353	3.348

The first oxidation potentials for **8**, **9** and **10** are $E_{1/2}$ (1) = -0.268 V, -0.141 V and -0.249 V respectively. These are cathodically shifted compared to their nonlinear derivatives **3** (-0.165 V), **6** (-0.114 V) and **7** (-0.011 V). The oxidation potentials match the trends shown in the DFT where the absolute energy of the HOMO of linear bridges **8** (-4.963 eV)**, 9** (-5.012 eV) and **10** (-4.963 eV) are higher in energy than their nonlinear counterparts **3** (-5.040 eV), **6** (-5.050 eV) and **7** (-5.040 eV) and are therefore more easily oxidised.[24] This is believed to be a result of increased mixing of the Mo_2-δ and the pyrazine-π orbitals increasing the absolute energy of the Mo_2-δ. Complex **9** has a decreased electron density on the dimolybdenum core compared to **8** as a result of π back bonding into the extended π system of the ligand and is therefore more difficult to oxidise.[25,26] Despite the increased basicity of the ligand when changing the donor atom from O to S, the oxidation potentials of **8** and **10** show little variation unlike that commonly observed in literature.[21,27–34]

The ΔE_{pc} for **8**, **9** and **10** are 0.477 V, 0.429 V and 0.550 V respectively, the magnitude of the ΔE_{pc} values for all complexes show considerable thermodynamic stabilisation of the MV state, and are indicative of class III compounds.[17,35,36] The ΔE_{pc} for **3**, **6** and **7** are 0.444 V, 0.366 V and 0.517 V, both the linear and nonlinear derivatives follow the same trend with the sulfonated bridges (**7** and **10**) having the greatest thermodynamic stability of the MV state and the bridge containing the phenyl group having the weakest stabilisation (**6** and **9**). This is in agreement with the HOMO/HOMO-1 separation determined by DFT, where the **10** had the largest separation and **9** had the smallest for the linear

bridges and **7** had the largest separation and **6** had the smallest for the nonlinear bridges. The decreased coupling observed for complex **6** is a result of the increased distances between the redox centres as discussed in chapter 3. Whereas, the decreased thermodynamic stabilisation observed for **9** is believed to be a result of only the hole hopping mechanism being thermodynamically accessible resulting in a decrease in stabilisation (*vide infra*). The increased thermodynamic stability of the sulfonated bridges is a result of the increased overlap provided by the sulphurs diffuse p-orbitals which is commonly observed in literature.[21,27–34] The linear derivatives show an increased thermodynamic stability when compared to the nonlinear derivatives which is believed to be a result of increased mixing of the Mo_2-δ and the pyrazine-π orbitals increasing the absolute energy of the Mo_2-δ. Cotton *et al.* have shown that the use of structural isomers for the bridge can have a pronounced effect on the thermodynamic stabilisation of the MV state by using the complex $[Mo_2(DAniF)_3]_2(\mu_2$-Bridge) (DAniF = *N,N'*-di(*p*-anisyl)-formamidinate) where the bridge is either 4,6-dioxypyrimidinate or 2,3-dioxypyrazinate.[14] When the bridge was 4,6-dioxypyrimidinate the $\Delta E_{1/2}$ was 0.187 V and when the bridge was changed to 2,3-dioxypyrazinate the $\Delta E_{1/2}$ increased to 0.258 V. The increase in the $\Delta E_{1/2}$ was attributed to the *ortho* arrangement of the 2,3-dioxypyrazinate compared to the *meta* arrangement of 4,6-dioxypyrimidinate. It should be noted that they believe the electronic coupling of the complex containing the 4,6-dioxypyrimidinate bridge contained considerable electrostatic and through space coupling. The difference in the $\Delta E_{1/2}$ between $[Mo_2(DAniF)_3]_2(\mu_2$-2,3-dioxypyrazinate) and **8** arise as a result of changing the ancillary ligands which is well documented in literature.[37,38] As both the linear and nonlinear derivatives have a *meta* and *para* arrangement respectively it becomes apparent that the relative orientation of the donor atoms on the ring also play an important role in facilitating through bond electron transfer.

4.4.5 *UV-Vis Absorption spectroscopy*

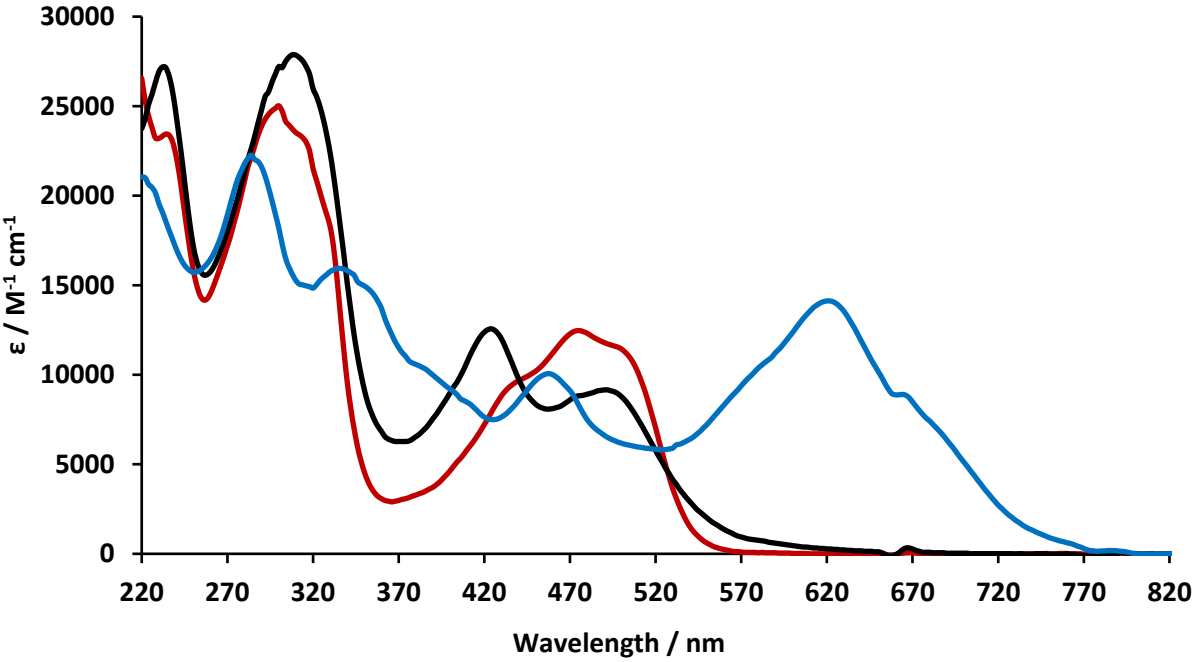

*Figure 4.8:The UV-Vis spectra of **8** (black), **9** (red) and **10** (blue) in THF.*

The UV-Vis spectra of complexes **8 - 10** in THF are displayed in Figure 4.8 and the major transitions assigned in Figure 4.9. Due the number of transitions and the degree of orbital hybridisation the UV assignments were aided by TD-DFT. The UV spectrum of **9** is consistent with literature.[18] All complexes have a cis-Piv- π → Piv-π* transition between 320-300 nm, but due to a strong pyrazine-π → Mo_2-δ* transitions at ~330 nm, neither the pyrazine-π → Mo_2-δ* nor the trans-Piv- π → Piv-π* transitions can be assigned. The predominant Mo_2-δ → pyrazine-π* MLCT for complexes **8, 9** and **10** occur at 430 nm, 438 nm and 461 nm respectively. The MLCT for complexes **8** and **10** are blue shifted in comparison to **3** and **7** as a result of the increased pyrazine-π* energy. Whereas, the MLCT for complex **9** is redshifted in comparison to **6**, as a result of the increased orbital overlap between the metal and the ligand raising the energy of the Mo_2-δ and lowering the energy of the pyrazine-π*. The lowest energy transition observed for complex **10** occurs at 632 nm and arises from the Mo_2-δ → Mo_2-δ*/ pyrazine-π* mixed transition. The Mo_2-δ → Mo_2-δ* transitions are low in intensity and obscured by more intense transitions in complex **8** and **9**. The Mo_2-δ → Mo_2-π* transitions are observed at 494 nm and

484 nm for complexes **8** and **9**, the Mo_2-δ → Mo_2-π* for complex **10** is overlaid with the MLCT. The transitions for complex **10** are more intense than complex **7**, as complex **10** is coplanar it therefore has increased conjugation between the metal and the ligand.

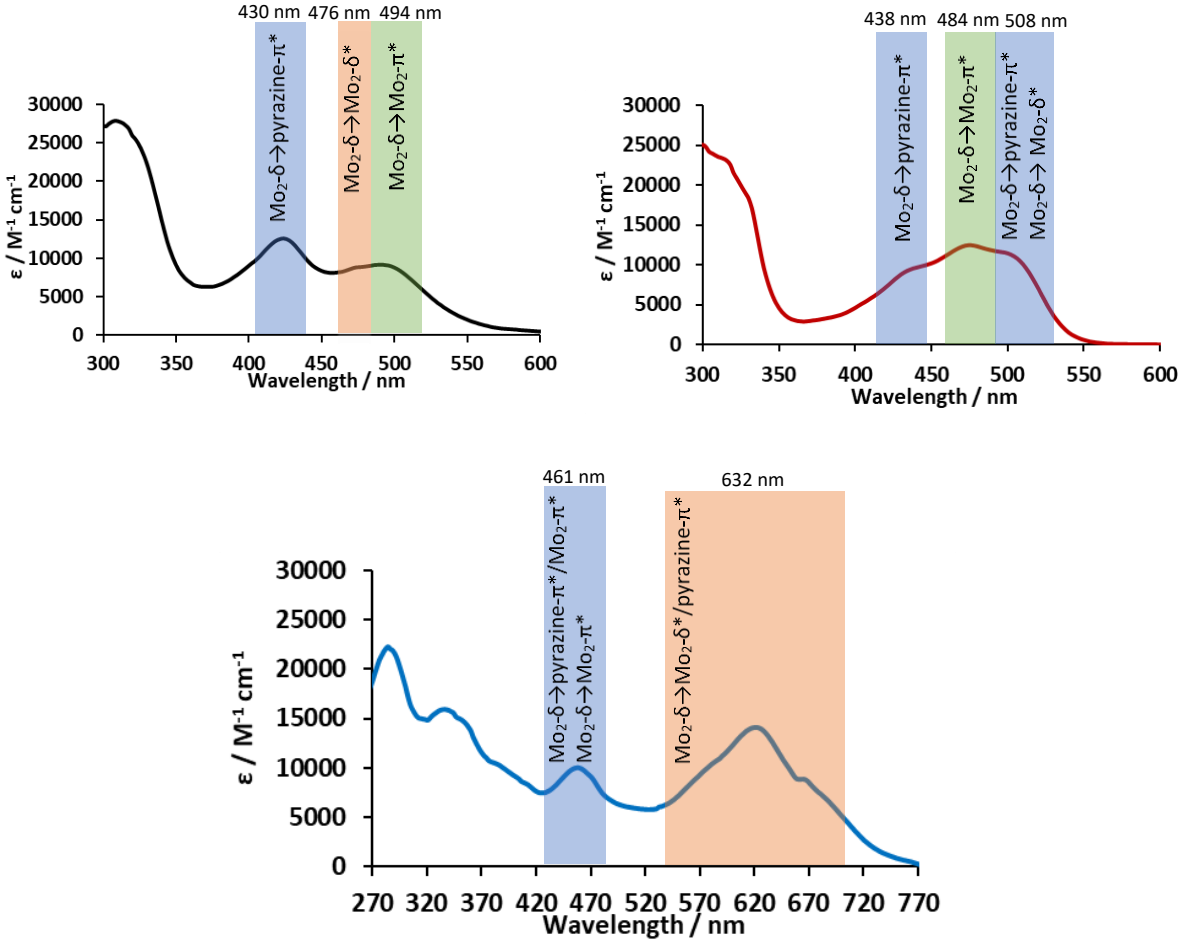

*Figure 4.9: The UV-Vis assignments for complexes **8** (top left), **9** (top right) and **10** (bottom).*

4.4.6 *Spectroelectrochemistry*

In order to quantify the cross-coupling matrix parameter (H_{ab}) of complexes **8, 9** and **10** and their redox products, spectroelectrochemical studies have been carried out. The UV-Vis-NIR-IR spectra of complexes [**8- 10**]^n (n= 0, 1, 2) were collected from 1 mM solutions in 0.1 M NBu_4PF_6/THF for the UV-Vis-NIR region, and in the IR from 10 mM solutions in 0.1 M NBu_4PF_6/THF.

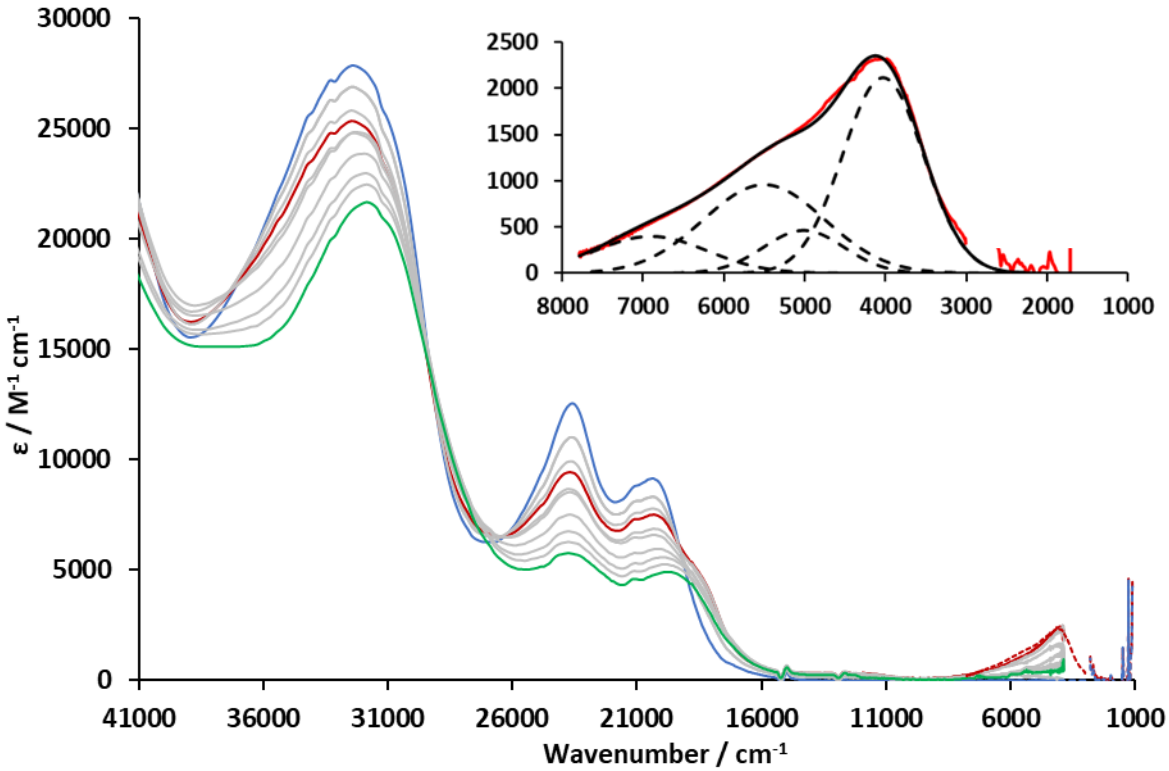

*Figure 4.10: The UV-Vis NIR SEC (solid line) and the IR SEC (Dashed line) of complex **8** in 0.1M NBu_4PF_6 /THF. **8** (blue), **8**$^{+}$ (red) and **8**$^{2+}$ (green). Top Right: A magnified portion of the IR spectra for **8**$^{+}$ showing the charge resonance transition (red), the Gaussian curves used to determine the integral (Black dashed lines), and the sum of the Gaussian curves (black solid line). The region around 3000 cm^{-1} is not shown due to strong THF CH vibrations.*

The UV-Vis-NIR-IR spectra of **8**, **8**$^{+}$ and **8**$^{2+}$ are displayed in Figure 4.10. The sequential formation of **8**$^{+}$ and **8**$^{2+}$ in the spectroelectrochemical studies is evidenced by the appearance of two separate isosbestic points in the **8** → **8**$^{+}$ and **8**$^{+}$ → **8**$^{2+}$ spectra at 19455 cm^{-1} (514 nm) and 18587 cm^{-1} (538 nm) respectively. Upon oxidation from **8** → **8**$^{+}$ several spectral changes occur in the UV-Vis NIR, the most prominent of which is the growth charge resonance band in the NIR at 4086 cm^{-1} (2447 nm). The band is assigned as a charge resonance band as it is relatively intense, non-Gaussian, exhibits significant low energy cut off and disappears when the complex is doubly oxidised. The UV-SEC and IR-SEC are in excellent agreement for the charge resonance band. The MLCT for **8** is observed at 23256 cm^{-1} (430 nm) following the **8** → **8**$^{+}$ oxidation the MLCT decreases in intensity but shows no change in energy. The LMCT (pyrazine-π → Mo_2-δ*) at 20242cm^{-1} (494 nm) decreases in intensity and red shifts to 20000 cm^{-1} (500 nm). A new peak grows in at 18382 cm^{-1} (544 nm) and can be observed as a shoulder on the

LMCT transition, this has been assigned as a second LMCT transition (pyrazine-π → Mo_2-δ) consistent with the hole hopping mechanism. As the MLCT is still present the electron hopping mechanism also occurs indicating that the MV complex is stabilised by both formalisms and ET can occur through both the pyrazine-π and π* orbitals. Following the $\mathbf{8}^{+} \rightarrow \mathbf{8}^{2+}$ oxidation the two LMCT transitions (pyrazine-π → Mo_2-δ and pyrazine-π → Mo_2-δ*) both decrease in intensity with the peaks becoming a single indistinguishable peak at 19685 cm^{-1} (508 nm). The MLCT further decreases in intensity but shows no change in energy. The spectra regained its original features following the reduction back to the neutral species but had bleached to ca. 70 % of the original concentration.

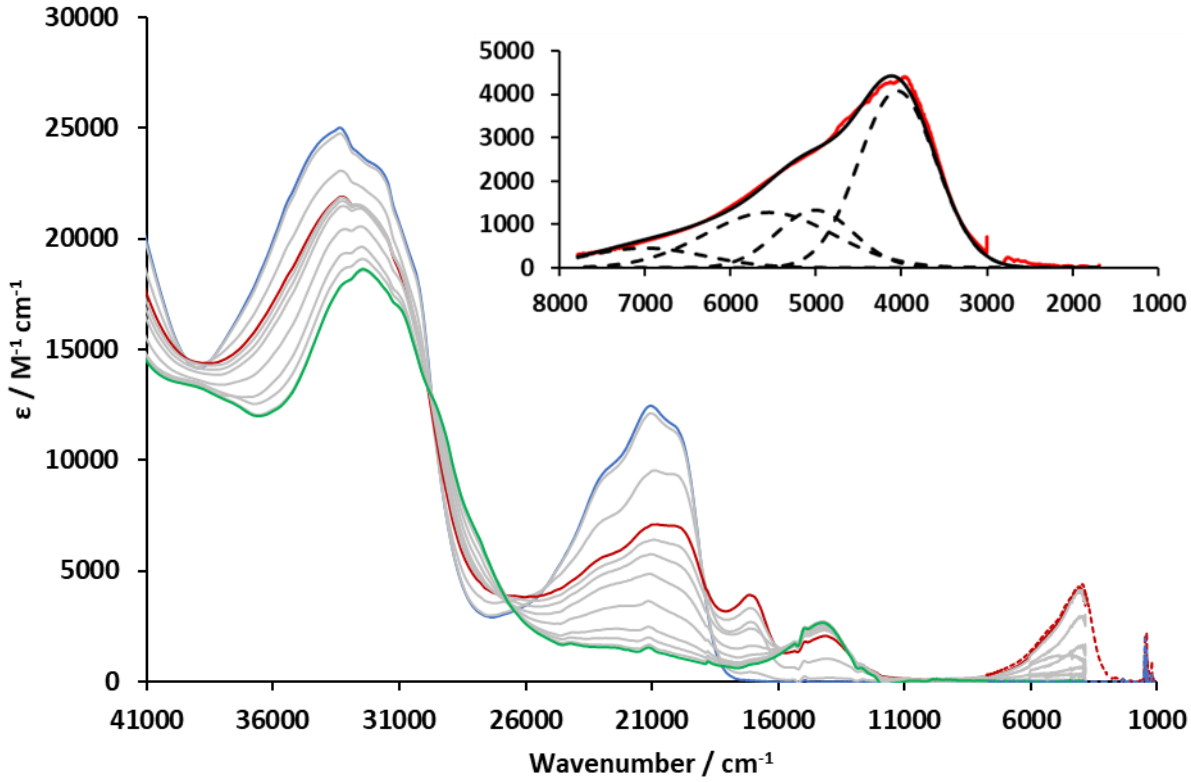

*Figure 4.11: The UV-Vis NIR SEC (solid line) and the IR SEC (Dashed line) of complex **9** in 0.1M NBu_4PF_6 /THF. **9** (blue), $\mathbf{9}^{+}$ (red) and $\mathbf{9}^{2+}$ (green). Top Right: A magnified portion of the IR spectra for $\mathbf{9}^{+}$ showing the charge resonance transition (red), the Gaussian curves used to determine the integral (Black dashed lines), and the sum of the Gaussian curves (black solid line). The region around 3000 cm^{-1} is not shown due to strong THF CH vibrations.*

The UV-Vis-NIR-IR spectra of **9**, $\mathbf{9}^{+}$ and $\mathbf{9}^{2+}$ are displayed in Figure 4.11. The sequential formation of $\mathbf{9}^{+}$ and $\mathbf{9}^{2+}$ in the spectroelectrochemical studies is evidenced by the appearance of two separate

isosbestic points in the **9** → **9**$^{+}$ and **9**$^{+}$ → **9**$^{2+}$ spectra at 18939cm^{-1} (528 nm) and 15923 cm^{-1} (628 nm) respectively. Upon oxidation from **9** → **9**$^{+}$ several spectral changes occur in the UV-Vis NIR, the most prominent of which is the growth charge resonance band in the NIR at 4072 cm^{-1} (2456 nm). The band is assigned as a charge resonance band as it is relatively intense, non-Gaussian, exhibits significant low energy cut off and disappears when the complex is doubly oxidised. The UV-SEC and IR-SEC are in excellent agreement for the charge resonance band. The MLCT for **9** is observed at 20661 cm^{-1} (484 nm) following the **9** → **9**$^{+}$ oxidation the MLCT decreases in intensity but shows no change in energy. The transitions at 22831 cm^{-1} (438 nm) and 19685 cm^{-1} (508 nm) decrease in intensity and show no change in the energy of the transitions. A new peak grows in at 17123 cm^{-1} (584 nm) which is relatively intense, this new transition has been provisionally assigned as a second charge resonance band (Mo_2-π → Mo_2-δ) a discussion of which can be found below. A second less intense peak grows in at 13888 cm^{-1} (720 nm) which is assigned as an LMCT (pyrazine-π → Mo_2-δ) which is consistent with the DFT as the HOMO/pyrazine-π* separation is 1.815 eV whereas the HOMO/pyrazine-π separation is 3.284 eV. Following the **9**$^{+}$ → **9**$^{2+}$ oxidation the peaks in the visible region (22831 cm^{-1} (438 nm), 20661 cm^{-1} (484 nm) and 19685 cm^{-1} (508 nm)) and the peak at 17123 cm^{-1} (584 nm) disappear entirely. The LMCT (pyrazine-π → Mo_2-δ) grows in intensity but does not change in energy. The spectra regained its original features following the reduction back to the neutral species, but the compound had bleached to around ca. 80 % of the original concentration.

The transition at 17123 cm^{-1} (584 nm) in the spectrum of **9**$^{+}$ is believed to arise from the Mo_2-π → Mo_2-δ excitation. The transition could either be an interconfigurational (IC) transition where the Mo_2-π → Mo_2-δ transition occurs on the same redox centre or a second charge resonance transition where the Mo_2-π → Mo_2-δ excitation occurs between redox centres (Figure 4.12).[39] If the transition were an IC transition, a similar feature would be expected in the MV spectrum of $Mo_2(Piv)_3(HDoq)$.[40] As the transition is unobserved in the MV spectrum of $Mo_2(Piv)_3(HDoq)$, the transition is provisionally assigned as a second charge resonance transition. The reason this transition arises in complex **9**$^{+}$ and

is unobserved in other complexes remains unanswered. This is believed to be one of the only examples of a covalent dimolybdenum complex containing two separate charge resonance transitions.

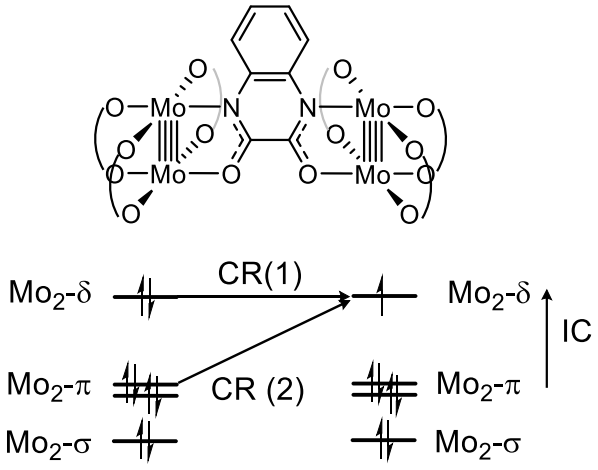

Figure 4.12: A schematic highlighting the charge resonance transitions (CR) and the interconfigurtaional (IC) transition.

The UV-Vis-NIR-IR spectra of **10**, **10**$^{+}$ and **10**$^{2+}$ are displayed in Figure 4.13. The sequential formation of **10**$^{+}$ and **10**$^{2+}$ in the spectroelectrochemical studies is evidenced by the appearance of two separate isosbestic points in the **10** → **10**$^{+}$ and **10**$^{+}$ → **10**$^{2+}$ spectra at 14205 cm^{-1} (704 nm) and 13966 cm^{-1} (716 nm) respectively. Upon oxidation from **10** → **10**$^{+}$ several spectral changes occur in the UV-Vis NIR, the most prominent of which is the growth of a relatively intense symmetric band in the NIR at 4446 cm^{-1} (2249 nm). The band is assigned as a charge resonance band as it is relatively intense and symmetric akin to the class IV transitions reported by Lear *et al.* like a class III charge resonance band, the transition disappears when the complex is doubly oxidised.[41] The charge resonance band will be discussed in detail in section 4.4.7. The UV-SEC and IR-SEC are in excellent agreement for the charge resonance band. In **10** the MLCT (Mo_2-δ → pyrazine-π*/Mo_2-δ*) appears at 21692 cm^{-1} (461 nm) following the **10** → **10**$^{+}$ oxidation the MLCT decreases in intensity but does not change in energy. The peak at 16129 cm^{-1} (620 nm, Mo_2-δ → Mo_2-δ*/pyrazine-π*) redshifts to 15873 cm^{-1} (630 nm) broadens and shows a small decrease in intensity. The peak at 29412 cm^{-1} (340 nm, Pyrazine-π → Mo_2-δ*) decreases in intensity. A new transition begins to grow in at ~26000 cm^{-1} which is believed to be a new

LMCT transition (Pyrazine-π → Mo_2-δ) consistent with a hole hopping mechanism. Following the **10**$^{+}$ → **10**$^{2+}$ oxidation the MLCT transition decreases in intensity and is no longer identifiable. The Mo_2-δ →Mo_2-δ/pyrazine-π* transition at 15873 cm^{-1} (630 nm) decreases in intensity and redshifts to 15674 cm^{-1} (638 nm) but does not show any signs of further broadening. The Pyrazine-π → Mo_2-δ* transition at 29412 cm^{-1} (340 nm) decreases in intensity and becomes indistinguishable from the spectrum. The new LMCT transition (Pyrazine-π → Mo_2-δ) is centred at 25773 cm^{-1} and has decreased in intensity. The spectra regained its original features following the reduction back to the neutral species, but the compound had bleached to around 60 % of the original concentration.

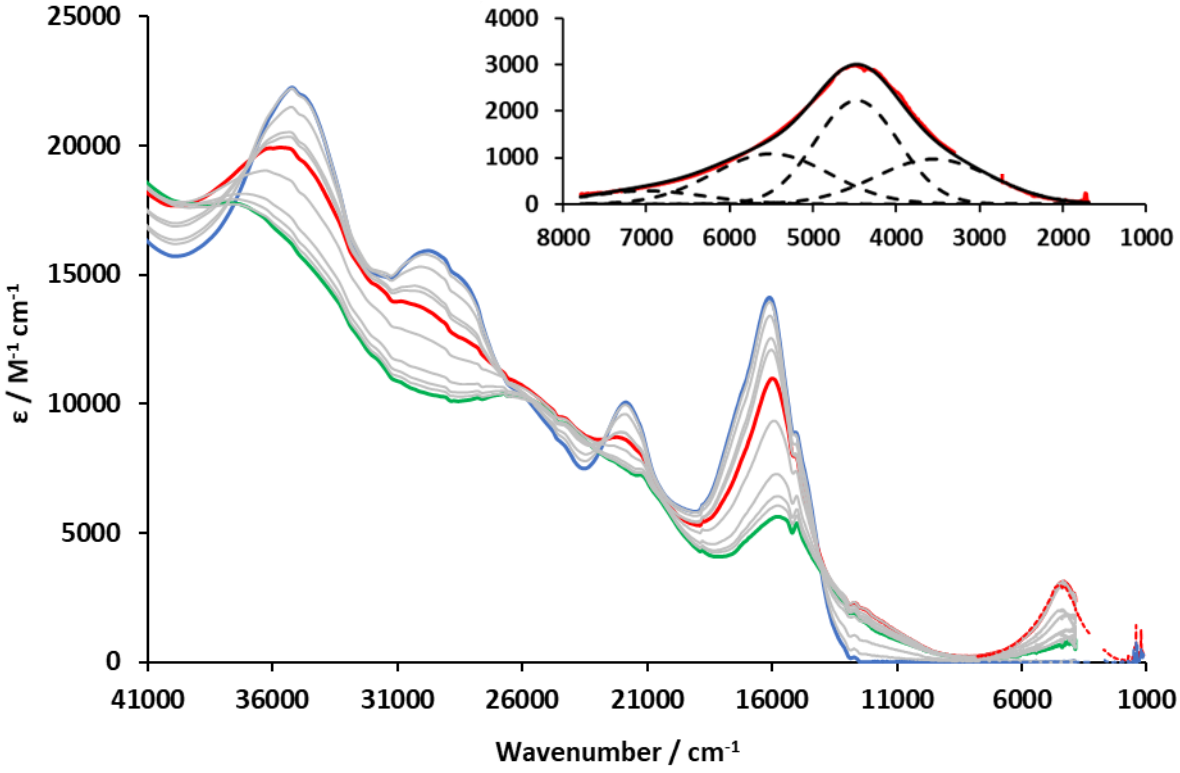

*Figure 4.13: The UV-Vis NIR SEC (solid line) and the IR SEC (Dashed line) of complex **10** in 0.1M NBu_4PF_6 /THF. **10** (blue), **10**$^{+}$ (red) and **10**$^{2+}$ (green). Top Right: A magnified portion of the IR spectra for **10**$^{+}$ showing the charge resonance transition (red), the Gaussian curves used to determine the integral (Black dashed lines), and the sum of the Gaussian curves (black solid line). The region around 3000 cm^{-1} is not shown due to strong THF CH vibrations.*

4.4.7 *Calculation of the cross-coupling matrix parameter (H_{ab})*

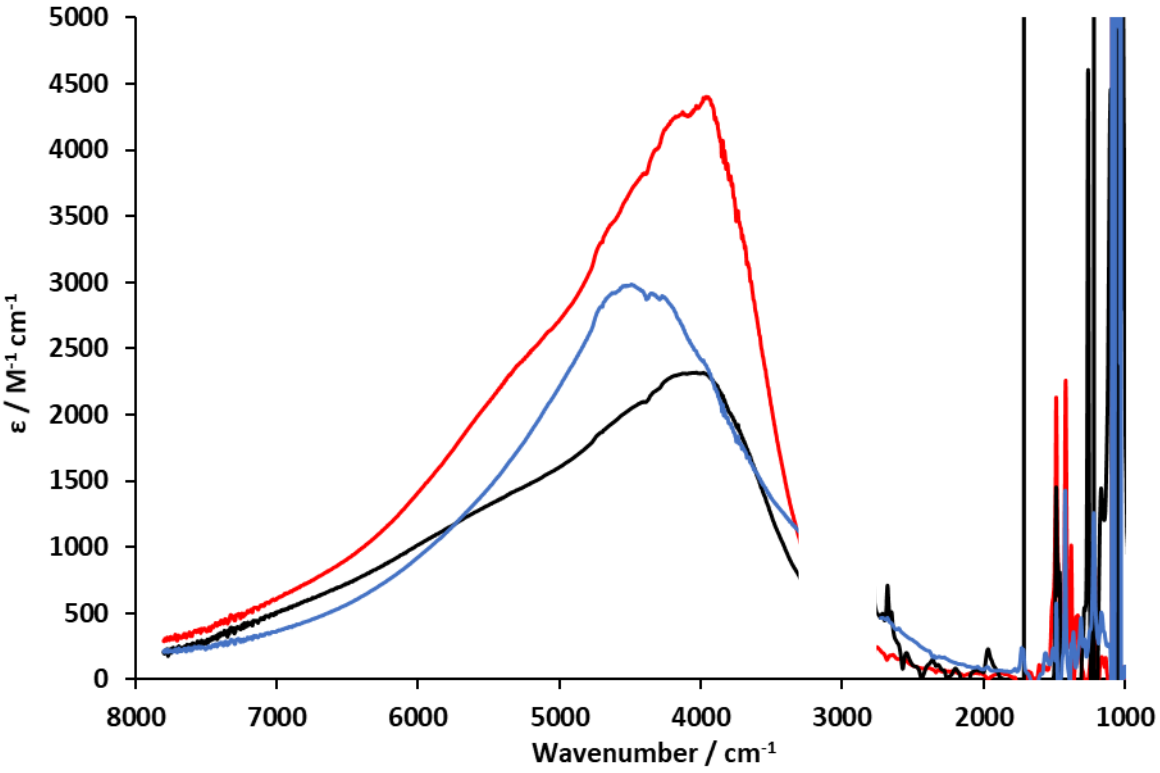

*Figure 4.14: The overlayed charge resonance transitions of **8**$^+$ (black), **9**$^+$ (red) and **10**$^+$ (blue). The spectrum around 3000 cm^{-1} is not shown due to strong THF CH vibrations.*

The charge resonance bands of **8**$^+$ **- 10**$^+$ are displayed in Figure 4.14, the charge resonance bands for complexes **8**$^+$ and **9**$^+$ are classified as being class III as they are relatively intense, non-Gaussian with significant low energy cut off. Class III complexes experience low energy cut off of the charge resonance band at $2H_{ab}$.[40,42]

Whereas, the charge resonance band for complex **10**$^+$ becomes sharper and more symmetric, which is in disagreement with the two-state model where more strongly coupled systems should experience a progressively narrower non-Gaussian band with an increased degree of low energy cut off. The variation in band profile compared to the profile predicted by the two-state model indicates that **10**$^+$ has gone past the description for a classical class III complex. **10**$^+$ has been tentatively assigned as a class IV compound where the observed charge resonance band becomes more symmetric with

increased coupling due to change in character from vibronic to entirely electronic as described by Lear *et al.*[41] Similarly, Liu *et al.* describe these complexes as molecular radicals where the electronic nature of the complex should be determined on the entirety of the molecule as opposed from the coupling of constituent diabatic states as shown in Figure 4.15. The relatively flat potential energy surfaces calculated for the two-state model for very strongly coupled systems does not account for the symmetric charge resonance band. Liu *et al.* predicted that the symmetric band was a result of both the ground state and excited state being equal in shape, unlike in a class III compound where the excited state typically has a parabolic curve.[29] Class IV compounds were first reported in 2009 and very few examples have been reported in the literature since, providing a new example of a class IV system is imperative to fully understand the pronounced effect of very strongly coupled systems and how they differ from strongly coupled systems.[43]

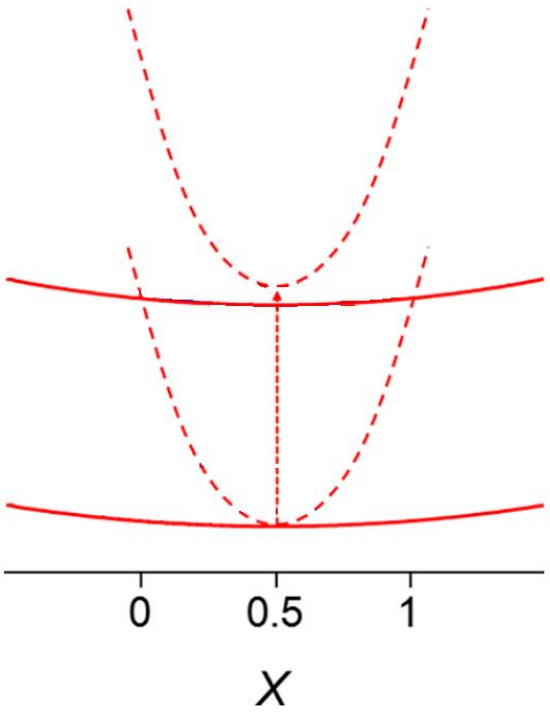

Figure 4.15: The potential energy surfaces for a class III compound (solid) and a class IV compound(dashed). Reprinted with permission from reference. Copyright (2013) American Chemical Society.[29]

The H_{ab} of strongly coupled systems (Class III and Class IV) is calculated using Equation 4.1 (Section 1.3.1). The H_{ab} were determined to be 2043 cm^{-1}, 2036 cm^{-1} and 2223 cm^{-1} for **8**$^+$, **9**$^+$ and **10**$^+$ respectively (Table 4.6). This is in agreement with the findings of the DFT, where complex **9** has the smallest HOMO/HOMO-1 separation and **10** has the largest. The increased H_{ab} of **10**$^+$ when compared to complex **8**$^+$ is consistent with changing the chelating atom from O to S commonly seen throughout literature.[29,31,44] Whereas the marginal decrease in the H_{ab} of **9**$^+$ when compared to **8**$^+$ can be attributed to the addition of the phenyl ring, resulting in the pyrazine-π* becoming much higher in energy compared to the HOMO preventing the hole hopping mechanism as seen by the loss of the MLCT in the SEC.

$$H_{ab} = \frac{1}{2} v_{max}$$

Equation 4.1: Calculation of the electronic coupling parameter (H_{ab}) for a strongly coupled (class III and class IV) compound.

These complexes can be readily compared to [$(Mo_2(Piv)_3)_2(\mu_2$-oxalate)] an analogous complex with a similar r_{ab}, a H_{ab} of 2000 cm^{-1} and a HOMO/HOMO-1 separation of 0.63 eV.[6] Complex **8** has a greater H_{ab} despite the similarities but a much smaller HOMO/HOMO-1 separation 0.4011 eV indicating that [$(Mo_2(Piv)_3)_2(\mu_2$-oxalate)] should be more strongly coupled than **8.** The use of an aromatic ring with a donor atom contained within the ring prevents the free rotation of the C-C bond increasing the orbital overlap as the redox centres and the ligand all remain coplanar. [$(Mo_2(Piv)_3)_2(\mu_2$-oxalate)] can undergo free rotation around the oxalate C-C bond where the barrier to rotation is very low at between 3.0 and 4.4 kcal mol^{-1}, resulting in a decrease in orbital overlap and therefore decreasing the H_{ab}.[41,6]

*Table 4.6: Summary of the NIR absorptions observed for **8**$^+$, **9**$^+$ and **10**$^+$ with complexes **3**$^+$, **6**$^+$ and **7**$^+$ included for comparison.*

Complex	ν_{max} /cm^{-1}	ε_{max} / M^{-1} cm^{-1}	H_{ab} / cm^{-1}	$\Delta\nu_{1/2}$ [a] / cm^{-1}	$\Delta\nu_{1/2}$ ° / cm^{-1}
8$^+$	4086	2338	2043	3338	3072
9$^+$	4072	4408	2036	2710	3066
10$^+$	4446	3007	2223	1884	1932
3$^+$	2780	2311	1390	4114	2534
6$^+$	3809	199	638	3866	2966
7$^+$	3136	2181	1668	1534	2691

[a] Calculated from the high energy side of the transition

The linear and nonlinear complexes follow the same trend with the sulfonated bridges (**7**$^+$ and **10**$^+$) being the most strongly coupled and the bridge containing the phenyl group having the weakest coupling (**6**$^+$ and **9**$^+$). The linear complexes (**8**$^+$, **9**$^+$ and **10**$^+$) have a substantially greater H_{ab} than their nonlinear counterparts (**3**$^+$, **6**$^+$ and **7**$^+$) despite having negligible through space coupling. It has been commonly observed that *ortho* and *para* substituted benzene rings have a substantially lower energy barriers to through bond electron transfer than their *meta* substituted derivatives.[9] As a result it is believed that the nonlinear derivatives have a higher energy barrier to through bond electron transfer than their linear counterparts decreasing the H_{ab}. This is in agreement with the observations for **6** and **9**, as both MV states are primarily governed by the through bond component, complex **6** is weakly coupled whereas complex **9** is strongly coupled as a result of the changes in the barrier to electron transfer. It should be noted that despite the large decrease in the H_{ab} observed for the nonlinear derivatives they only show a marginal decrease in their thermodynamic stability as indicated by the $\Delta E_{1/2}$. This shows that there is substantial thermodynamic stabilisation of the MV state by coulombic interactions in the nonlinear derivatives.

4.4.8 *Electron Paramagnetic Resonance Spectroscopy*

For the EPR experiments, the MV complexes **8**$^{+}$ **- 10**$^{+}$ were prepared by the *in-situ* chemical oxidation of the neutral complexes by the addition of one equivalent of silver hexafluorophosphate ($AgPF_6$) in THF and the resulting solutions immediately characterised by electron paramagnetic resonance spectroscopy at room temperature. Immediate measuring of the MV ion is imperative due to degradation which arises from facile ligand scrambling which was observed as new features appearing in the spectra during prolonged experiments.[45] The spectra and their simulations are shown in Figure 4.16 and the g factor and simulated hyperfine couplings shown in Table 4.7.

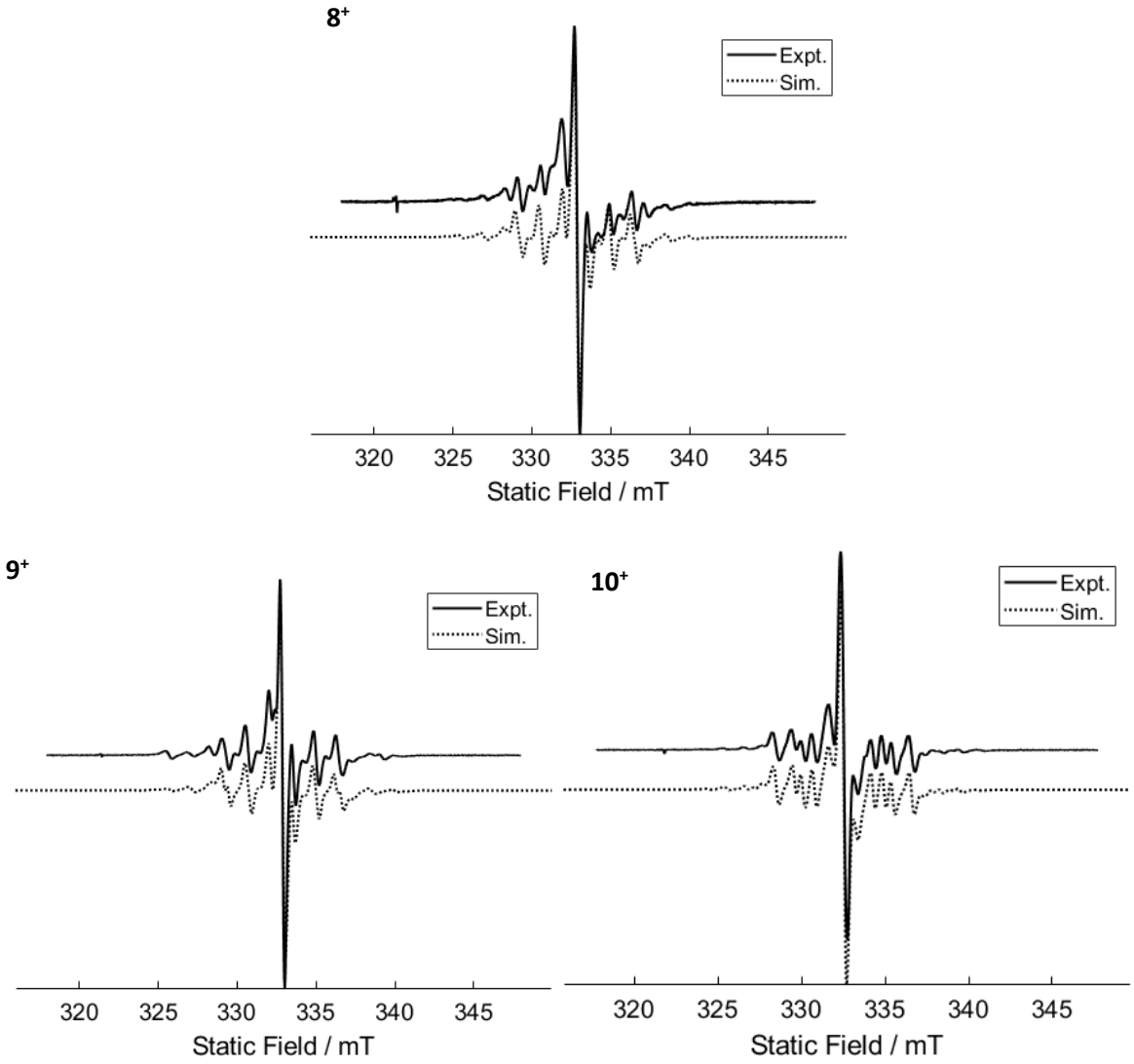

*Figure 4.16: Experimental (solid) and simulated (dashed) X-band EPR spectra of **8**$^{+}$, **9**$^{+}$ and **10**$^{+}$ in THF. The abnormality at 321 mT is a quartz impurity.*

The EPR spectra of dimolybdenum species has one central peak (*I=0*, 75% abundance) at a *g*-factor of between 1.93 – 1.94, the hyperfine couplings (^{95}Mo and ^{97}Mo with *I*=5/2, 25 % abundance) are observed as a sextet surrounding the central peak.[46] The magnitude of the hyperfine couplings can indicate the extent of electron delocalisation, a hyperfine of ~2.8 mT indicates that the electron is localised, whereas when the hyperfine coupling halves to ~1.4 mT the electron is delocalised between redox centres.[20,47]

*Table 4.7: Summary of the EPR spectra data obtained from the simulated EPR spectra for complexes **3**$^{+}$ and **6**$^{+}$ - **10**$^{+}$.*

Compound	g-factor	A_{Iso} (1) / mT	A_{Iso} (2) / mT
8^{+}	1.930	1.451	1.348
9^{+}	1.932	1.436	1.297
10^{+}	1.932	1.550	1.122
3^{+}	1.933	1.447	1.161
6^{+}	1.932	2.641	2.489
7^{+}	1.933	2.588	-

The EPR spectrum of complex **8**$^{+}$ is shown in Figure 4.16, it displays a central peak at a g-factor of 1.930 with two sets of hyperfine couplings, which arise from the different coordination environments of the Mo resulting in the polarisation of the bond as discussed in chapter 2.[47] The hyperfine couplings can be well simulated using two equally weighted (A_{iso}(1)= 2Mo, A_{iso}(2)= 2Mo) independent hyperfine couplings of 1.451 mT and 1.348 mT, indicating the electron is delocalised across the entire system on the EPR timescale (~10^{-9} s) which is in agreement with the class III spectroelectrochemical assignment. Compound **8**$^{+}$ has a less polarised bond than in its nonlinear derivative **3**$^{+}$, it is believed that the large polarisation observed for complex **3**$^{+}$ is a result of the through space component of the electron transfer drawing electron density to the central two molybdenum's in the nonlinear derivatives.

The EPR spectrum of complex **9**$^{+}$ is shown in Figure 4.16, it displays a central peak at a g-factor of 1.932 with two sets of hyperfine couplings. The hyperfine couplings can be well simulated using two equally weighted (A_{iso}(1)= 2Mo, A_{iso}(2)= 2Mo) independent hyperfine couplings of 1.436 mT and 1.297 mT, indicating the electron is delocalised across the entire system on the EPR timescale (~10^{-9} s) which is in agreement with the class III spectroelectrochemical assignment. Compound **9**$^{+}$ is class III and has two hyperfine couplings of ~1.2 mT which reflect this, but the nonlinear derivative **6**$^{+}$ is class II and has hyperfine couplings of ~2.4 mT. There is no discernible difference in the polarisation of the dimolybdenum bonds between **9**$^{+}$ and **6**$^{+}$ as the electron transfer mechanism occurs primarily through bond in both cases.

The EPR spectrum of complex **10**$^{+}$ is shown in Figure 4.16, it displays a central peak at a g-factor of 1.930 with two sets of hyperfine couplings. The hyperfine couplings can be well simulated using two equally weighted (A_{iso}(1)= 2Mo, A_{iso}(2)= 2Mo) independent hyperfine couplings of 1.451 mT and 1.348 mT, indicating the electron is delocalised across the entire system on the EPR timescale (~10^{-9} s). **10**$^{+}$ has been assigned as being class IV as a result of the symmetric charge resonance band, but as the electron is still delocalised across four molybdenums no change in the EPR spectra between a class III and class IV compound should be observed. Despite both compounds **10**$^{+}$ and **7**$^{+}$ being fully delocalised the spectra differ substantially as a result of the polarisation of the dimolybdenum bond. **7**$^{+}$ has a fully polarised bond where two of the molybdenum's remain uninvolved in ET despite being delocalised. Whereas the molybdenum bond in **10**$^{+}$ shows greater polarisation than **8**$^{+}$ as a result of changing the chelating atom from O to S but not to the degree observed in **7**$^{+}$. It is believed that the large polarisation observed for complex **7**$^{+}$ is a result of the through space component of the electron transfer drawing electron density to the central two molybdenum's in the nonlinear derivatives.

4.5 Conclusions

By the substitution of the labile acetonitrile ligands in $[Mo_2(Piv)_3(MeCN)_2][BF_4]$, three complexes were synthesised $[Mo_2(Piv)_3]_2(\mu_2\text{-Pdo})$ (**8**), $[Mo_2(Piv)_3]_2(\mu_2\text{-Doq})$ (**9**) and $[Mo_2(Piv)_3]_2(\mu_2\text{-Pzt})$ (**10**). The electrochemical data indicates all complexes have strong thermodynamic stabilisation of the MV state. Surprisingly, the complexes **8 – 10** exhibit greater thermodynamic stabilisation of the MV state compared to the nonlinear derivatives despite having negligible through space interactions. In all cases the magnitude of the $\Delta E_{1/2}$ is indicative of strongly coupled systems.

The UV-Vis-NIR spectra for the MV complexes **8** and **9** show a relatively intense non-Gaussian transition with varying degrees of low energy cut off consistent with full delocalisation (class III) of the electron. The UV-Vis spectra of $\mathbf{9}^+$ exhibits a transition in the visible region which has been assigned as a second charge resonance transition, which is believed to be one of the only examples of a dimolybdenum dimer having two charge resonance transitions. The UV-Vis-NIR spectra for the MV complex **10** exhibits a relatively intense symmetric band in the NIR consistent with extremely strong coupling between the dimolybdenum redox centres (Class IV) and is one of very few systems which exhibit class IV behaviour. The EPR spectra are consistent with full delocalisation of the MV state and in all cases the bonds are less polarised than their nonlinear counterparts indicating substantial through space electron transfer in the nonlinear derivatives. This study demonstrates that ligand topology has a pronounced effect on the stabilisation of dimolybdenum complexes. It has shown that despite the increased $Mo_2\cdots Mo_2$ separation greater electronic coupling was observed in the linear derivatives despite having negligible through space coupling. This reinforces that through bond electron transfer is more efficient than through space electron transfer.

4.6 Experimental

See chapter 8 for the methods and materials section.

4.6.1 *Synthesis of $[Mo_2(Piv)_3]_2(\mu_2$-Pdo) (8)*

$Mo_2(Piv)_4$ (0.728 g, 1.22 mmol) and $[Mo_2(Piv)_2(MeCN)_6][BF_4]_2$ (1.000 g, 1.22 mmol) were added to a Schlenk flask and dissolved in a mixture of dichloromethane (20 mL) and MeCN (10 mL), the red solution was refluxed for 17 hours and cooled to room temperature. Pyrazine-2,3-diol (0.136 g, 1.22 mmol) was suspended in MeOH (20 mL) and tetrabutylammonium hydroxide (2.45 mL. 2.45 mmol, 1.0 M) was added, the resulting suspension was stirred at room temperature for 17 hours to yield a colourless solution, which was then added dropwise to the $[Mo_2(Piv)_3]^+$. This resulted in an immediate colour change to a dark red. The resulting solution was stirred for a further 20 hours. The solvents were removed under reduced pressure and the products extracted into a mixture of hexane and dichloromethane (10 ml, 1:1) and purified by column chromatography (eluent dichloromethane /hexane (50:50 (v/v)) → dichloromethane → THF/ dichloromethane (2:98 (v/v)) collecting the first orange band. The solvent was removed under reduced pressure and washed with hexane (3 x 10 ml) and dried to afford **8** as a dark orange solid. Yield 0.295 g (22 %) ^{1}H NMR (400 MHz, DMSO-d_6) δ 7.54 (s, 2H), 1.31 (s, 36H), 1.28 (s, 18H). MALDI-TOF-MS calcd. monoisotopic MW for $Mo_4C_{34}H_{56}O_{14}N_2$, 1100.6, found *m/z* 1100.4 (M+). Elemental analysis Calcd. For $Mo_4C_{34}H_{56}O_{14}N_2$, C, 37.10; H, 5.13; N, 2.55; Found C, 37.15; H, 5.44; N, 2.28.

4.6.2 *Synthesis of $[Mo_2(Piv)_3]_2(\mu_2$-Doq) (9)*

$Mo_2(Piv)_4$ (0.728 g, 1.22 mmol) and $[Mo_2(Piv)_2(MeCN)_6][BF_4]_2$ (1.000 g, 1.22 mmol) were added to a Schlenk flask and dissolved in a mixture of dichloromethane (20 mL) and MeCN (10 mL), the red solution was refluxed for 17 hours and cooled to room temperature. 2,3-dihydroquinoxaline (0.198 g, 1.22 mmol) was suspended in THF (20 mL) and cooled to -78 ℃ to this suspension n-Butyl lithium (1.53 mL, 2.44 mmol, 1.6 M) was added dropwise. The suspension was warmed to room temperature, stirred for 17 hours to yield a colourless solution. The deprotonated ligand was added dropwise to the

$[Mo_2(Piv)_3]^+$ solution which resulted in an immediate colour change to a dark orange, the solution was stirred for a further 20 hours. The solvents were removed under reduced pressure and the products extracted into a mixture of hexane and dichloromethane (10 ml, 1:1) and purified by column chromatography (eluent dichloromethane/hexane (50:50 (v/v)) → dichloromethane → THF/ dichloromethane (2:98 (v/v)) collecting the second orange band. The solvent was removed under reduced pressure and washed with hexane (3 x 10 ml) and dried to afford **9** as a dark orange solid. Yield 0.264 g (18 %) ^{1}H NMR (400 MHz, DMSO-d_6) δ 6.83 (dd, J = 6.2, 3.4 Hz, 2H), 6.19 (dd, J = 6.1, 3.4 Hz, 2H), 1.43 (s, 18H), 1.30 (s, 36H). MALDI-TOF-MS calcd. monoisotopic MW for $Mo_4C_{38}H_{58}O_{14}N_2$, 1150.7, found *m/z* 1150.5 (M+). Elemental Anal. Calcd. For $Mo_4C_{38}H_{58}O_{14}N_2$, C, 39.66; H, 5.08; N, 2.43; Found C, 39.91; H, 5.44; N, 2.50.

4.6.3 *Synthesis of $[Mo_2(Piv)_3]_2(\mu_2$-Pzt) (10)*

$Mo_2(Piv)_4$ (0.728 g, 1.22 mmol) and $[Mo_2(Piv)_2(MeCN)_6][BF_4]_2$ (1.000 g, 1.22 mmol) were added to a Schlenk flask and dissolved in a mixture of dichloromethane (20 mL) and MeCN (10 mL), the red solution was refluxed for 17 hours and cooled to room temperature. 2,3-Pyridazinedithiol (0.176 g, 1.22 mmol) and NaOMe (0.132 g, 2.45 mmol) were suspended in MeOH (20 mL) and stirred at room temperature for 17 hours to yield a colourless solution, this solution was then added dropwise to the $[Mo_2(Piv)_3]^+$. This resulted in an immediate colour change to a dark green, the resulting solution was stirred for a further 20 hours. The solvents were removed under reduced pressure and the products extracted into a mixture of hexane and dichloromethane (10 ml, 1:1) and purified by column chromatography (eluent dichloromethane/hexane (50:50 (v/v)) → dichloromethane → dichloromethane/THF (5:95 (v/v)) collecting the first green band. The solvent was removed under reduced pressure and washed with hexane (3 x 10 ml) and dried to afford **10** as a dark green solid. Yield 0.573 g (41 %) ^{1}H NMR (400 MHz, DMSO-d_6) δ 7.02 (s, 2H), 1.40 (s, 18H), 1.32 (s, 36H). MALDI-TOF-MS calcd. monoisotopic MW for $Mo_4C_{34}H_{56}O_{12}N_2S_2$, 1132.8, found *m/z* 1132.3 (M+). Anal. Calcd. For $Mo_4C_{34}H_{56}O_{12}N_2S_2$, C, 36.05; H, 4.98; N, 2.47; Found C, 36.32; H, 4.54; N, 2.68.

4.7 References

1 A. Stebler, J. H. Ammeter, U. Furholz and A. Ludil, *Inorg. Chem.*, 1984, **23**, 2764–2767.

2 R. J. Crutchley, in *Advances in Inorganic Chemistry*, 1994, pp. 273–325.

3 J. W. Seyler, W. Weng, Y. Zhou and J. A. Gladysz, *Organometallics*, 1993, **12**, 3802–3804.

4 M. Brady, W. Weng, Y. Zhou, J. W. Seyler, A. J. Amoroso, A. M. Arif, M. Böhme, G. Frenking and J. A. Gladysz, *J. Am. Chem. Soc.*, 1997, **119**, 775–788.

5 F. Coat, M. A. Guillevic, L. Toupet, F. Paul and C. Lapinte, *Organometallics*, 1997, **16**, 5988–5998.

6 B. E. Bursten, M. H. Chisholm, R. J. H. Clark, S. Firth, C. M. Hadad, A. M. Macintosh, P. J. Wilson, P. M. Woodward and J. M. Zaleski, *J. Am. Chem. Soc.*, 2002, **124**, 3050–3063.

7 C. Rovira, D. Ruiz-Molina, O. Elsner, J. Vidal-Gancedo, J. Bonvoisin, J. P. Launay and J. Veciana, *Chem. - A Eur. J.*, 2001, **7**, 240–250.

8 A. Heckmann and C. Lambert, *Angew. Chemie - Int. Ed.*, 2012, **51**, 326–392.

9 C. Lapinte, I. Ledoux, S. Brasselet, J. Zyss and C. Lapinte, *Organometallics*, 2000, **19**, 5235–5237.

10 C. Lapinte, *J. Organomet. Chem.*, 2008, **693**, 793–801.

11 T. Weyland, K. Costuas, L. Toupet and C. Lapinte, *Organometallics*, 2000, **19**, 4228–4239.

12 N. Le Narvor and C. Lapinte, *Organometallics*, 1995, **14**, 634–639.

13 R. C. Quardokus, Y. Lu, N. A. Wasio, C. S. Lent, F. Justaud, C. Lapinte and S. A. Kandel, *J. Am. Chem. Soc.*, 2012, **134**, 1710–1714.

14 F. A. Cotton, J. P. Donahue, C. A. Murillo, L. M. Pérez and R. Yu, *J. Am. Chem. Soc.*, 2003, **125**, 8900–8910.

15 W. Cho, H. Cho, C. S. Lee, B. Y. Lee, B. Moon and J. Kang, *Organometallics*, 2014, **33**, 1617–1622.

16 S. R. Kennedy, M. N. Kozar, H. P. Yennawar and B. J. Lear, *Polyhedron*, 2016, **103**, 100–104.

17 R. H. Cayton, M. H. Chisholm, J. C. Huffman and E. B. Lobkovsky, *J. Am. Chem. Soc.*, 1991, **113**, 8709.

18 R. H. Cayton, M. H. Chisholm, J. C. Huffman and E. B. Lobkovsky, *J. Am. Chem. Soc.*, 1991, **113**, 8709–8724.

19 J. M. Casas, R. H. Cayton and M. H. Chisholm, *Inorg. Chem.*, 1991, **30**, 358–360.

20 M. H. Chisholm and N. J. Patmore, *Acc. Chem. Res.*, 2007, **40**, 19–27.

21 M. H. Chisholm and N. J. Patmore, *J. Chem. Soc. Dalt. Trans.*, 2006, 3164–3169.

22 D. E. Richardson and H. Taube, *Inorg. Chem.*, 1981, **20**, 1278–1285.

23 B. Ding, C. Hua, C. J. Kepert and D. M. D'Alessandro, *Chem. Sci.*, 2019, **10**, 1392–1400.

24 D. D. Méndez-Hernández, P. Tarakeshwar, D. Gust, T. A. Moore, A. L. Moore and V. Mujica, *J. Mol. Model.*, 2013, **19**, 2845–2848.

25 B. S. Dolinar and J. F. Berry, *Dalt. Trans.*, 2014, **43**, 6165–6176.

26 C. Lin, J. D. Protasiewicz, E. T. Smith and T. Ren, *Inorg. Chem.*, 1996, **35**, 6422–6428.

27 J. Hicks, S. P. Ring and N. J. Patmore, *Dalt. Trans.*, 2012, **41**, 6641.

28 F. A. Cotton, Z. Li, C. Y. Liu and C. A. Murillo, *Inorg. Chem.*, 2007, **46**, 7840–7847.

29 Y. N. Tan, T. Cheng, M. Meng, Y. Y. Zhang, C. Y. Liu, M. F. Sun, Y. Zheng and P. J. Low, *J. Phys. Chem. C*, 2017, **121**, 27860–27873.

30 S. Mallick, T. Cheng, L. Chen, M. Meng, Y. Y. Zhang and C. Y. Liu, *Dalt. Trans.*, 2017, **46**, 5711–5723.

31 X. Xiao, C. Y. Liu, Q. He, M. J. Han, M. Meng, H. Lei and X. Lu, *Inorg. Chem.*, 2013, **52**, 12624–12633.

32 M. T. Kang, M. Meng, Y. N. Tan, T. Cheng and C. Y. Liu, *Chem. - A Eur. J.*, 2016, **22**, 3115–3126.

33 M. J. Han, C. Y. Llu and P. F. Tian, *Inorg. Chem.*, 2009, **48**, 6347–6349.

34 G. Y. Zhu, M. Meng, Y. N. Tan, X. Xiao and C. Y. Liu, *Inorg. Chem.*, 2016, **55**, 6315–6322.

35 M. H. Chisholm and N. J. Patmore, *Molecular Metal-Metal Bonds: Compounds, Synthesis, Properties*, Wiley, 1st edn., 2015.

36 M. H. Chisholm, B. J. Lear, A. Moscatelli and L. A. Peteanu, *Inorg. Chem.*, 2010, **49**, 3706–3713.

37 S. Byungho and H. M. Goff, *Inorganica Chim. Acta*, 1994, **226**, 231–235.

38 G. Giuffrida and S. Campagna, *Coord. Chem. Rev.*, 1994, **135**–**136**, 517–531.

39 K. D. Demadis, C. M. Hartshorn and T. J. Meyer, *Chem. Rev.*, 2001, **101**, 2655–2685.

40 D. M. D'Alessandro and F. R. Keene, *Chem. Soc. Rev.*, 2006, **35**, 424–440.

41 B. J. Lear and M. H. Chisholm, *Inorg. Chem.*, 2009, **48**, 10954–10971.

42 B. S. Brunschwig, C. Creutz and N. Sutin, *Chem. Soc. Rev.*, 2002, **31**, 168–184.

43 J. P. Launay, *Eur. J. Inorg. Chem.*, 2020, **2020**, 329–341.

44 X. Xiao, M. Meng, H. Lei and C. Y. Liu, *J. Phys. Chem. C*, 2014, **118**, 8308–8315.

45 M. H. Chisholm and A. M. Macintosh, *J. Chem. Soc., Dalt. Trans.*, 1999, 1205–1208.

46 M. H. Chisholm, *Philos. Trans. R. Soc. A Math. Phys. Eng. Sci.*, 2008, **366**, 101–112.

47 M. H. Chisholm, *Coord. Chem. Rev.*, 2013, **257**, 1576–1583.

Ancillary ligand effects on charge transport in hydrogen bonded dimers of dimers

5.1 Abstract

A series of paddlewheel complexes of the form $Mo_2(O_2CR)_3(HDop)$ (where O_2CR =2,4,6-triisopropylbenzoate (**11**, TiPB) or trimethylacetate (**14**) and H_2Dop = 3,6-dihydroxypyridazine) and *trans*-$Mo_2(TiPB)_2(O_2CL)(HDop)$ (where O_2CL = chloroacetic acid (**12**) or phenylpropiolic acid (**13**)) have been synthesised and characterised by ^1H NMR spectroscopy, UV-Vis spectroscopy and DFT calculations. They have been found to form self complementary hydrogen bonded dimers in noncoordinating solvents. The stability of the mixed valent (MV) state generated following a one electron oxidation has been probed by cyclic voltammetry, with the compounds displaying $\Delta E_{1/2}$ of 0.157 V in **11**, 0.103 V in **13** and 0.119 V in **14**. The spectroelectrochemical measurements do not display a intervalence charge resonance band and the electron paramagnetic resonance spectroscopy of the MV species indicate the electron is localised on the EPR timescale indicating that the electron transfer process in these complexes likely occurs via the underexplored mechanism of proton-coupled mixed valency. We observe that varying the ancillary ligand has a pronounced effect on both the redox potential of the complex and the stability of the mixed valence state, although these two factors do not appear to be related**.**

5.2 Proton coupled mixed valency

Chapters 2, 3 and 4 have focused on mixed valence (MV) systems containing covalently bound bridging ligands, but, in recent years MV compounds where stabilization occurs over a self-complimentary hydrogen bond have also been reported. Stabilisation of the MV state over a hydrogen bond can occur by three main mechanisms: if there is sufficient overlap between the donor and acceptor orbitals electron transfer (ET) can occur.[1,2] The stabilisation mechanism can also occur by proton transfer[3] or by a mechanism that is related to the proton coordinate in the self-complimentary hydrogen bond called proton coupled mixed valency (PCMV).[4–6]

The stability of the MV state for all mechanisms can be probed electrochemically by examining the magnitude of the separation between the two-half wave redox potentials ($\Delta E_{1/2}$). When electronic coupling (overlap of the donor-bridge-acceptor orbitals) stabilises the MV state an intervalence charge transfer (IVCT) band would also be observed in the absorption spectra of the MV species, and the electronic coupling matrix (H_{ab}) can be calculated in the same manner as for covalent systems.[7] The rate of electron transfer can be determined by IR coalescence if the rate of electron transfer exceeds 10^{-10} s.[8] Proton transfer and PCMV mechanisms would not exhibit an IVCT transition in the MV absorption spectra as they do not involve direct orbital overlap between the donor and acceptor redox centres. The rate constant for proton transfer and PCMV is likely to be much slower, but perhaps could be measured by NMR line broadening as achieved for proton coupled electron transfer (PCET).[9,10] For example the rate of PCET in $[Fe(H_2bim)_3]^{2+}$ + $[Fe(H_2bim)_2(Hbim)]^{2+}$ (H_2bim = 2,2'-biimidazoline) was found to be 5.8 x M^{-1} s^{-1}, which is between the electrochemical and EPR timescales.[9]

Patmore *et al.* have previously reported the complexes $[Mo_2(TiPB)_3(HDON)]_2$ and $[Mo_2(TiPB)_3(HDop)]_2$ (where TiPB = 2,4,6-triisopropylbenzoate, HDON = 2,7-dihdroxy-1,8-napthyridine and HDop = 3,6-dihydroxypyridazine). The complexes were shown to form self-complementary hydrogen bonds in solution (Figure 5.1), and electrochemical analysis indicated thermodynamic stabilisation of the mixed valent state. The absorption spectra of the MV complexes did not exhibit a IVCT transition in the NIR

and the stabilisation mechanism is believed to be PCMV.[4–6] The rates of electron transfer in this system are currently unknown but analysis has shown that it lays between the NMR (10^{-5} s) and the EPR timescales (10^{-10} s).

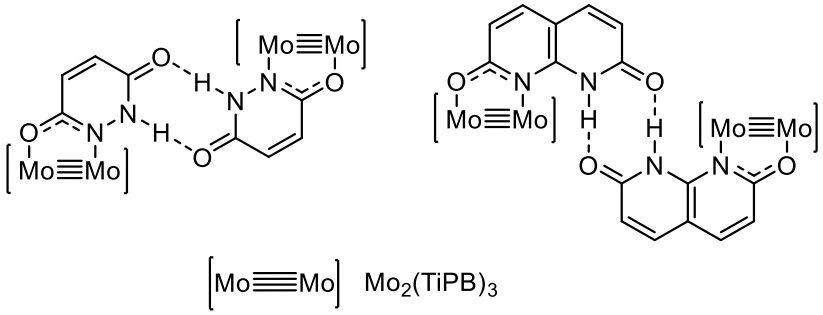

Figure 5.1 The structures of the [Mo(TiPB)$_3$Bridge]$_2$ (where TiPB is triisopropyl benzoate, (Right) H_2DON is 2,7-dihdroxy-1,8-napthyridine and (Left) H_2 DOP = 3,6-dihydroxypyridazine.

The PCMV mechanism is described as a "dipole induced electron self-exchange mechanism", with the most insightful explanation being provided by DFT modelling. The DFT showed that partial proton transfer from the donor complex to the acceptor complex occurs, which generates a dipole resulting in electron transfer (Figure 5.2).

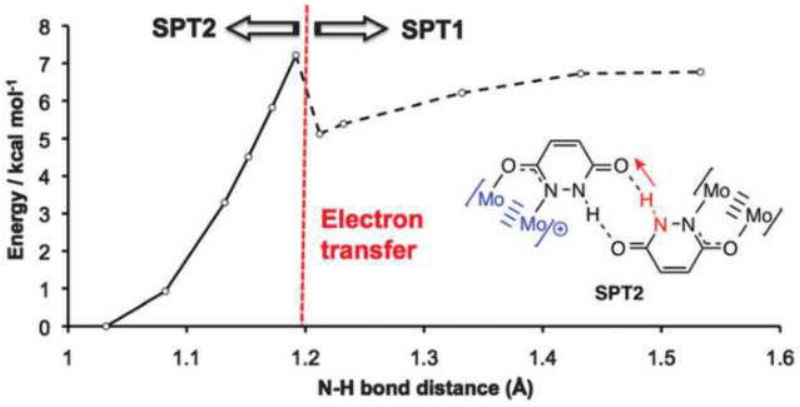

Figure 5.2: the DFT modelling of proton transfer from the donor towards the acceptor resulting in the generation of a dipole which induces electron transfer. Figure Reproduced by permission of The Royal Society of Chemistry.[6]

5.3 Aims

It is commonly observed in covalent MV systems that electronic modification of the ancillary ligand can have a large impact on the thermodynamic stability of the MV state.[11] Although changing the ancillary is known to affect both the absolute energy of the Mo_2-δ and therefore the oxidation potential and degree of coupling between the two redox centres.[12,13] In the PCMV mechanism the ET event is governed by the proton coordinate, therefore variation in the ancillary ligands should have a negligible effect on the method of stabilisation due to the remote nature of the ancillary ligands if the PCMV mechanism is correct. Using the model complex $Mo_2(TiPB)_3HDop$ the *trans* ancillary ligand will be substituted and the effect of the ancillary ligand on the PCMV mechanism will be probed.

Electronic coupling between the dimetal units will be evaluated through electrochemical and spectroelectrochemical studies. Based on previous studies, differences in the electronic coupling would be evidenced by changes in the $\Delta E_{1/2}$ values obtained by cyclic voltammetry and an evaluation of spectral coalescence in the spectrochemical studies.

5.4 Results and discussion

5.4.1 *Synthesis*

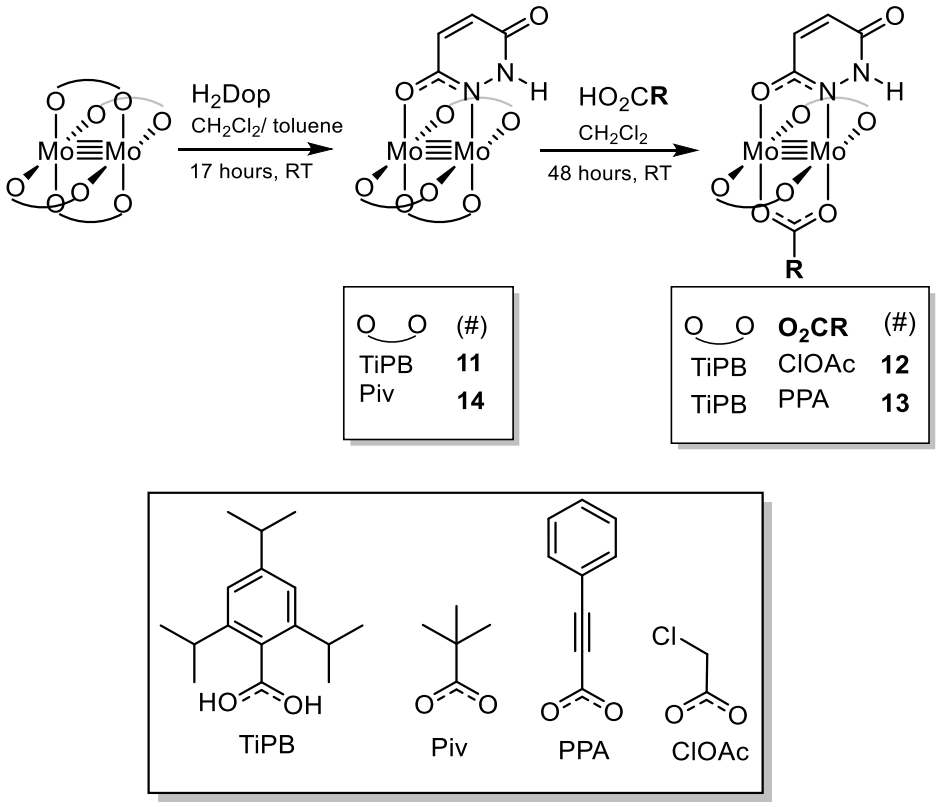

*Scheme 5.1: Synthesis of $Mo_2(TiPB)_3(HDop)$ (**11**), $Mo_2(TiPB)_2(HDop)(ClOAc)$ (**12**), $Mo_2(TiPB)_2(HDop)(PPA)$ (**13**) and $Mo_2(Piv)_3(HDop)$ (**14**).*

$Mo_2(TiPB)_3(HDop)$ (**11,** TiPB = 2,4,6-triisopropylbenzoate, H_2Dop = 3,6-Dihydroxypyridazine) was prepared according to literature by reacting stoichiometric amounts of H_2Dop with the homoleptic precursor $Mo_2(TiPB)_4$ (Scheme 5.1).[4] $Mo_2(TiPB)_2(HDop)(ClOAc)$ (**12,** ClOAc = chloroacetate) and $Mo_2(TiPB)_2(HDop)(PPA)$ (**13**, PPA = phenylpropiolate) were synthesised by stirring **11** with HClOAc and HPPA in CH_2Cl_2. Over the course of 48 hours a red precipitate formed and was isolated by centrifugation and purified by washing the precipitate with CH_2Cl_2 to yield **12** as a red solid (91 %) and **13** as red solid (74 %). The synthesis of **12** and **13** is highly regiospecific with only the trans isomer being formed. This is believed to be a result of steric interactions as proposed for other $Mo_2(O_2CR)_2(O_2CR')_2$ complexes.[14] $Mo_2(Piv)_3HDop$ (**14**) is an analogous complex to **11** and can be

prepared by stirring $Mo_2(Piv)_4$, H_2Dop and triethylamine in CH_2Cl_2. The solvent was removed *in vacuo* and the red solid was washed with hexane to yield **14** as a red solid (80 %). The addition of base to the synthesis of **14** decreases reaction time but the reaction proceeds with or without base. All the complexes are soluble in DMSO and THF but only complexes **11, 13** and **14** are soluble in CH_2Cl_2. All complexes were found to be pure by elemental analysis. The complexes have been characterised by ^{1}H NMR spectroscopy and MALDI-TOF mass spectrometry. Despite numerous attempts crystals suitable for X-ray diffraction of complexes **11 – 14** could not be obtained.

5.4.2 *^{1}H NMR spectroscopy*

The ^{1}H NMR spectra for complexes **11** and **14** in $CDCl_3$ and the ^{1}H NMR spectra for complexes **12** and **13** in d_6-DMSO are shown in Figure 5.3. The spectra of **12** and **13** are conducted in DMSO as the complexes are insoluble in $CDCl_3$. The ^{1}H NMR spectrum of **11** is consistent with the literature.[4] Complex **12** has a number of TiPB environments with the Ar-C***H***(CH_3) protons are observed as two overlaid septets at 2.90 ppm, the Ar-CH(C***H***$_3$) protons are observed as a series of overlaid doublets at 1.21 ppm and the Ar-***H*** protons are observed as a singlet at 7.09 ppm. ClOAc has two protons which are observed as a singlet at 4.94 ppm. The HDop ligand has three resonances; two doublets at 6.80 ppm and 7.59 ppm which correspond to the HDop backbone and a singlet at 10.61 ppm which corresponds to the NH. The ^{1}H NMR spectrum of **13** has two TiPB ligands with the Ar-C***H***(CH_3) protons observed at 2.91 ppm, the Ar-CH(C***H***$_3$) protons are observed at 1.22 ppm and the Ar-***H*** protons are observed at 7.10 ppm. The PPA ligand resonances occur at 7.59 ppm and 7.76 ppm but the resonance at 7.76 ppm is overlaid with a HDop backbone proton. The second HDop backbone is observed at 6.87 ppm and the NH is observed at 10.68 ppm. The ^{1}H NMR spectrum of **14** has the expected 2:1 Piv resonances at 1.38 ppm and 1.50 ppm, the HDop backbone is observed at 6.62 ppm and 7.38 ppm with the NH observed at 11.30 ppm.

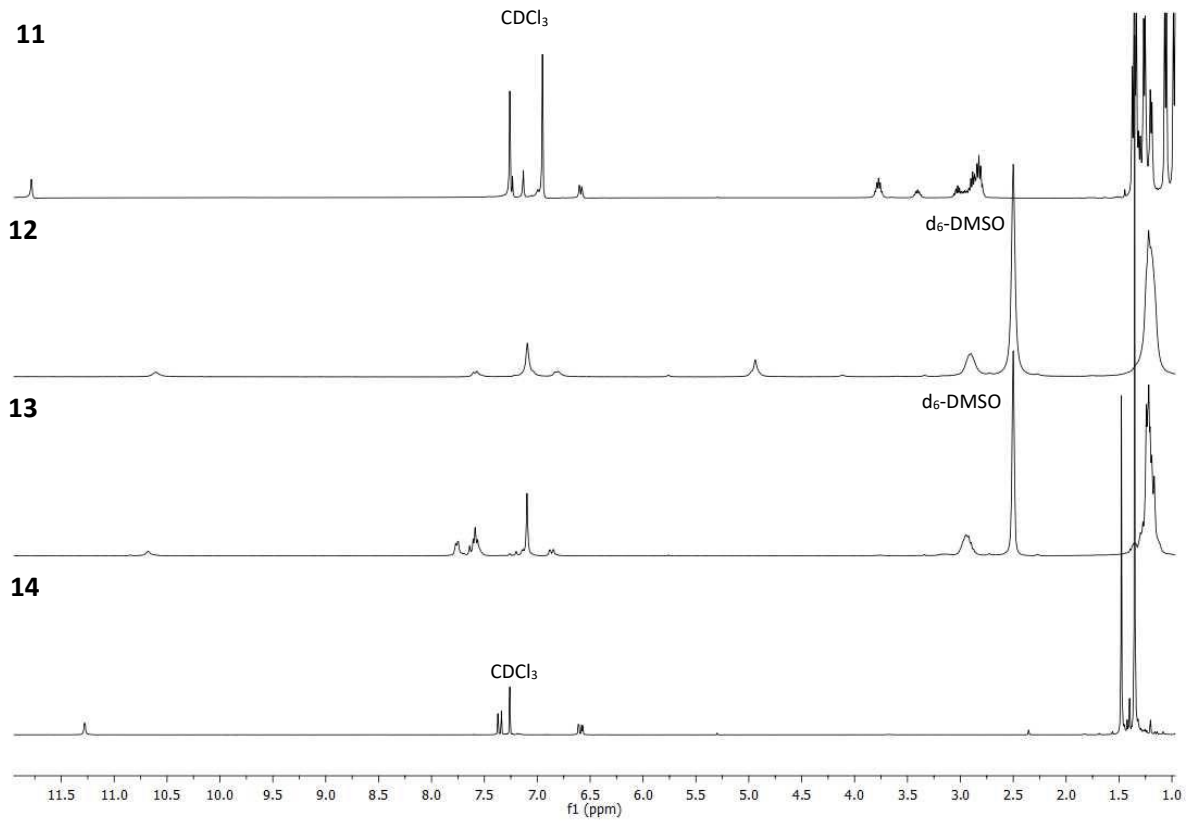

*Figure 5.3: ^{1}H NMR of $Mo_2(TiPB)_3HDop$ (**11**) and $Mo_2(Piv)_3HDop$ (**14**) in $CDCl_3$ and the ^{1}H NMR of $Mo_2(TiPB)_2(HDop)ClOAc$ (**12**) and $Mo_2(TiPB)_2(HDop)PPA$ (**13**) in d_6-DMSO.*

5.4.3 *IR-spectroscopy*

The IR spectra of complexes **11 – 14** are shown in Figure 5.4. The expected *C=O* symmetric and asymmetric lactam stretches occur at 1560 cm^{-1} and 1650 cm^{-1} for all complexes. All complexes also have a weak absorption at 3200 cm^{-1} corresponding to the *N-H* stretch. There is no evidence of the -OH tautomer in either the ^{1}H NMR spectra or in the IR spectra for any of the complexes which is an agreement with the findings of Patmore *et al.*[4] The asymmetric stretches of the ancillary carboxylates for all complexes are observed at 1360 and 1480 cm^{-1}. The alkyne IR handle for complex **13** can be observed as a sharp medium intensity band at 2215 cm^{-1}.

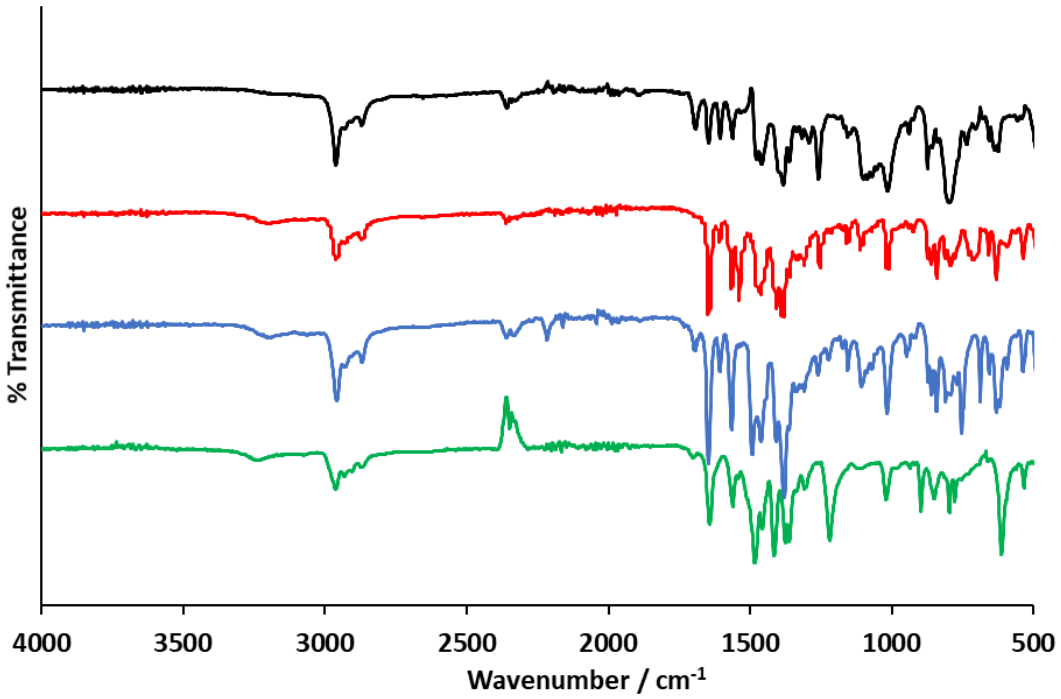

*Figure 5.4: The IR spectra of complexes of complexes **11** (black), **12** (red), **13** (blue) and **14** (green) in the solid state.*

5.4.4 *Diffusion ordered spectroscopy*

The HDop ligand in complex **11** forms self-complementary hydrogen bonds generating a hydrogen bonded dimer of dimers with a high association constant in non-coordinating solvents such as CH_2Cl_2 and $CHCl_3$ (Figure 5.1).[4] The addition of coordinating solvents such as THF and DMSO to solutions of [**11**]$_2$ results in the formation of the monomeric paddlewheel complex. The change in hydrodynamic volume between the dimer and the monomer can be observed by diffusion ordered spectroscopy (DOSY). Complex **11**, **13** and **14** were dissolved in $CDCl_3$ (0.5 mL) and their DOSY spectra collected and a diffusion coefficient obtained. To the same sample DMSO (50 µL) was then added and the spectra were reacquired, and the results are shown in Table 5.1.

*Table 5.1: DOSY data for complexes **11, 13** and **14**.*

Compound	Solvent	Average Diffusion Coefficient (x 10^{-10}) (m^2s^{-1})	Hydrodynamic Radius (Å)[a]	Hydrodynamic Volume ($Å^3$)[b]
$[11]_2$	$CDCl_3$	5.70	9.27	3340
11	$CDCl_3$ + d_6-DMSO	7.60	6.95	1410
$[13]_2$	$CDCl_3$	4.38	9.29	3450
13	$CDCl_3$ + d_6-DMSO	5.42	7.50	1766
$[14]_2$	$CDCl_3$	4.77	8.51	2582
14	$CDCl_3$ + d_6-DMSO	6.35	6.39	1096

[a] calculated using the Stokes-Einstein equation (5.1.1) [b] calculated using the volume of a sphere (5.1.2)

The hydrodynamic radius was determined from average diffusion coefficient using the Stokes-Einstein equation (Equation 5.1.1), where r is the hydrodynamic radius (Å), k_b is the Boltzmann constant (1.3806 x 10^{-23} $m^2Kgs^{-2}K^{-1}$), T is the absolute temperature (K), η is the viscosity of the solvent (5.37 x 10^{-4} $Kgm^{-1}s^{-1}$ for $CDCl_3$)[15], D is the diffusion coefficient (m^2s^{-1}) and V is the volume of a sphere ($Å^3$). The viscosity of the solution was assumed to remain the same following the addition of DMSO as the volume added would not be enough to significantly affect the viscosity. The hydrodynamic volume was then calculated using Equation 5.1.2 assuming the complexes are spherical.

$$r = \frac{k_b T}{6\eta\pi D} \quad \textbf{(1)}$$

$$V = \frac{4}{3}\pi r^3 \quad \textbf{(2)}$$

Equation 5.1: (1) The Stokes-Einstein equation and (2) the formula to calculate the volume of a sphere.

For complex **11** the volume of the dimer was found to be 3340 $Å^3$ which decreases to 1410 $Å^3$ upon the addition of DMSO which is consistent with dimer being split into two monomeric units as reported in literature.[4] The hydrodynamic volume of complex **13** and **14** both halve upon the addition of DMSO consistent with the complexes dimerising in non-coordinating solvents like previously reported. Due to the insolubility of complex **12** in $CDCl_3$ the DOSY spectra could not be obtained.

5.4.5 *Theoretical calculations*

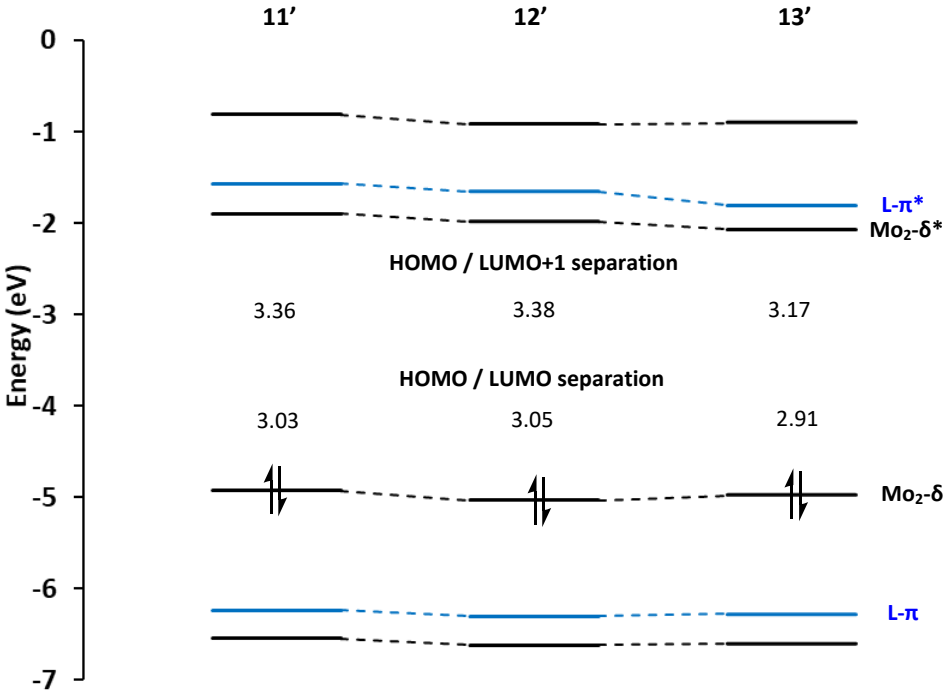

*Figure 5.5: The calculated frontier orbital energy level diagrams of model compounds **11', 12'** and **13'**.*

Theoretical calculations have been carried out by Dr Nathan Patmore and Dr Anthony Meijer (University of Sheffield). DFT calculations were performed on model complexes (**11', 12'** and **13'**), in which the TiPB ligands have been replaced by formate groups to reduce computational time. The calculated frontier molecular orbital energy level diagram for **11', 12'** and **13'** is shown in Figure 5.5.

For all three model complexes, the HOMO is the Mo_2-δ and the LUMO is the Mo_2-δ*. The addition of the electron withdrawing group in **12'** lowers the energy of the HOMO relative to **11'**. The LUMO+1 for **11'** and **12'** is the HDop-π* but the for **13'** the LUMO+1 extends to incorporate both the HDop-π* and the PPA-π*, the extended π systems results in a decrease in energy of both the HDop-π* and Mo_2-δ. The addition of the Cl group decreases the energy of the Mo_2-δ, Mo_2-δ* and HDop-π* but very little variation of the HOMO/LUMO and HOMO/LUMO+1 is observed between **11'** and **12**' unlike that observed between **11'** and **13**'.

5.4.6 *Electrochemistry*

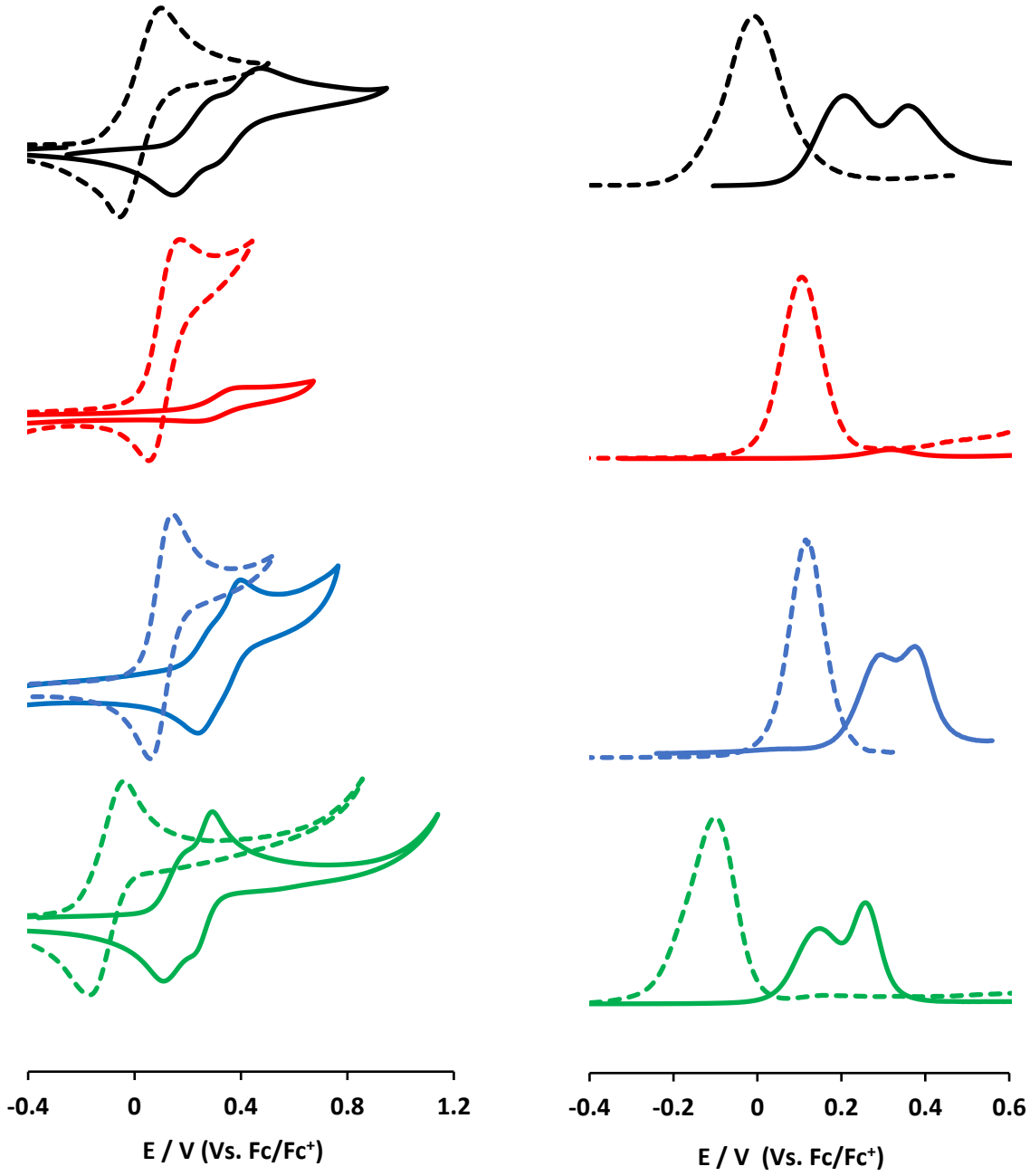

*Figure 5.6: CV (left, 100 mVs^{-1}) and DPV (right, 10 mVs^{-1}) of complexes **11** (black), **12** (red), **13** (blue) and **14** (green) in 0.1 M NBu_4PF_6/ CH_2Cl_2 (solid) and CH_2Cl_2 + 0.5 mL of DMSO (dashed) solutions at a concentration of 5 mM, and referenced against the Fc/Fc^+ couple (0.00 V).*

The cyclic voltammograms and differential pulse voltammograms of **11 , 12, 13** and **14** in 0.1 M NBu_4PF_6 / CH_2Cl_2 (solid) and CH_2Cl_2 + 0.5 mL of DMSO (dashed) solutions are displayed in Figure 5.6, and the data summarised in Table 5.2. Complexes [**11**]$_2$, [**13**]$_2$ and [**14**]$_2$ show two reversible successive one electron oxidations corresponding to the removal of electrons from the Mo_2-δ orbitals in CH_2Cl_2. Upon the addition of a coordinating solvent, in this case DMSO only a single peak is observed as the communication between the redox centres is disrupted, the addition of DMSO solubilises complex **12** which is insoluble in CH_2Cl_2.

*Table 5.2: Cyclic voltammetry data for complexes **11, 12, 13** and **14** in 0.1 M NBu_4PF_6 / CH_2Cl_2 and THF solutions at a concentration of 5 mM, and referenced against the Fc/Fc^+ couple (0.00 V).*

Compound	Solvent	$E_{1/2}$ (1) / V	$E_{1/2}$ (2) / V	$\Delta E_{1/2}$ / V	K_c
[11]$_2$	Dichloromethane	0.209	0.369	0.157	451
11	THF	0.006	-	-	-
12	THF	0.057	-	-	-
[13]$_2$	Dichloromethane	0.269	0.372	0.103	55
13	THF	0.049	-	-	-
[14]$_2$	Dichloromethane	0.139	0.257	0.119	103
14	THF	-0.115	-	-	-

The first oxidation potentials for **11, 12**, **13** and **14** in THF are $E_{1/2}$(1) = 0.006 V, 0.057 V, 0.049 V and -0.115 V respectively, the redox potential of **11** is consistent with literature.[4] Complex **12** and **13** are more difficult to oxidise than **11** which is in agreement with the lower absolute energy of the Mo_2-δ orbitals determined by DFT as a result of the electron withdrawing nature of the ClOAc and PPA ligands.[16] Complex **14** is more easily oxidised than **11** as Piv is a better donor than TiPB. The first oxidation potentials of the dimeric complexes **[11]$_2$, [13]$_2$** and **[14]$_2$** in CH_2Cl_2 follow the same trend found in THF. The $\Delta E_{1/2}$ for **[11]$_2$, [13]$_2$** and **[14]$_2$** are 0.157 V, 0.103 V and 0.119 V respectively, this equates to values of K_c between 55 (**[13]$_2$**) and 451 (**[11]$_2$**). The addition of the electron withdrawing ancillary ligand PPA resulted in a decrease in the thermodynamic stability of the mixed valence state compared to **[11]$_2$**. Changing the ancillary ligands from TiPB to Piv also results in a decrease in the stability of the MV state. In a previous study by Patmore *et al.* on the complexes $[Mo_2(TiPB)_3HDON]_2$

and $[Mo_2(TiPB)_2(HDON)(ClOAc)]_2$ (where H_2DON = 2,7-dihydroxy-1,8-naphthyridine) changing the ancillary ligand was shown to have minimal effect on the stability of the MV state with $[Mo_2(TiPB)_3HDon]_2$ and $[Mo_2(TiPB)_2(HDon)(ClOAc)]_2$ having $\Delta E_{1/2}$ of 0.140 V and 0.131 V respectively.[5] In this study, the variation of a single ancillary ligand has been shown to change the electronic properties of the dimetal core, and with the correct tuning it may be possible to increase the stability of the mixed valent state.

5.4.7 *UV-Vis absorption spectroscopy*

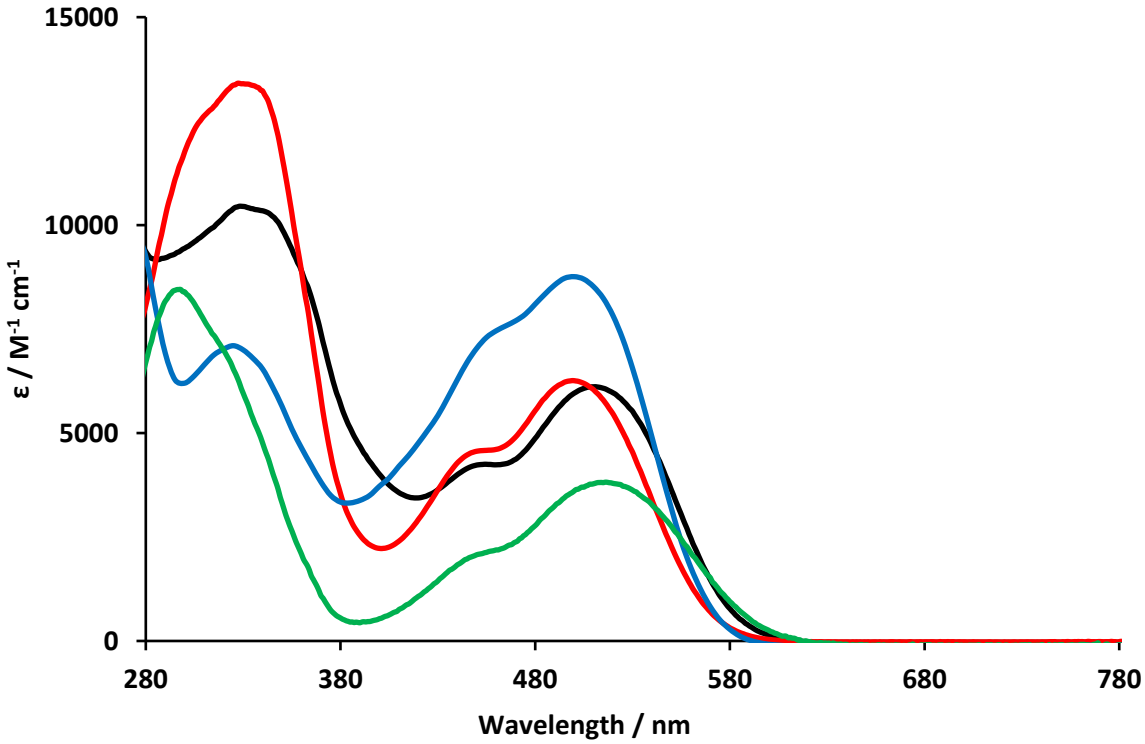

*Figure 5.7: The UV-Vis spectra of **11** (black), **12** (red), **13** (blue) and **14** (green) in DMSO.*

The UV-Vis spectra of complexes **11 - 14** in DMSO are displayed in Figure 5.7 and the major transitions assigned in Table 5.3. The spectra were conducted in DMSO to ensure complete dissolution of the complexes. The most prominent transition in the spectra is the Mo_2-δ → HDop-π* transition which occurs at 511 nm, 500 nm, 500 nm and 517 nm for complexes **11, 12, 13** and **14** respectively. The Mo_2-δ → HDop-π* transition of **12** and **13** is blue shifted compared to **11** as a result of the electron-

withdrawing nature of the ClH_2CCO_2 and PPA ligands stabilising the Mo_2-δ. The intensity of the Mo_2-δ → HDop-π* transition is consistent between **11** and **12** but the transition is more intense for **13** as a result of the PPA-π* mixing with the HDop- π*. The Mo_2-δ → HDop-π* transition for **14** is red shifted in comparison to **11** as the Piv ligand is more electron donating than the TiPB ligand. The next transition at ~450 nm is the HDop-π→ HDop-π* which shows little variation between all complexes.

*Table 5.3: The UV-Vis data for **11** (black), **12** (red), **13** (blue) and **14** (green) in DMSO.*

Compound	HDop-π → HDop-π* λ / nm (ε / M^{-1} cm^{-1})	Mo_2-δ → HDop-π* λ / nm (ε / M^{-1} cm^{-1})
11	450 (4250)	511 (6100)
12	450 (4550)	500 (6250)
13	460 (7450)	500 (8800)
14	450 (2050)	517 (3800)

5.4.8 *Spectroelectrochemistry*

In covalent mixed valence systems the degree of coupling can be determined by evaluating the charge resonance band in the NIR region of the absorption spectrum.[17] Complex **11** was shown to be stabilised by proton coupled mixed valency (PCMV), as a result a charge resonance band is not observed as there is insufficient overlap between the donor and the acceptor orbitals, the stabilisation of the MV state is instead governed by the proton co-ordinate. In order to determine if the complex **[13]$_2$** and **[14]$_2$** are stabilised by the PCMV mechanism spectroelectrochemical studies have been carried out. The UV-Vis-NIR spectra of complex [**13**]$_2^n$ (n= 0, 1, 2) were collected in CH_2Cl_2 following sequential additions of 0.5 equivalents of $AgPF_6$ as in-situ SEC measurements resulted in the precipitation of the complex. The UV-Vis-NIR spectra of complex [**14**]$_2^n$ (n= 0, 1, 2) were collected from 1 mM CH_2Cl_2 solutions in 0.1 M NBu_4PF_6 for the UV-Vis-NIR region, and in the IR from 10 mM CH_2Cl_2 solutions following sequential additions of 0.5 equivalents of $AgPF_6$.

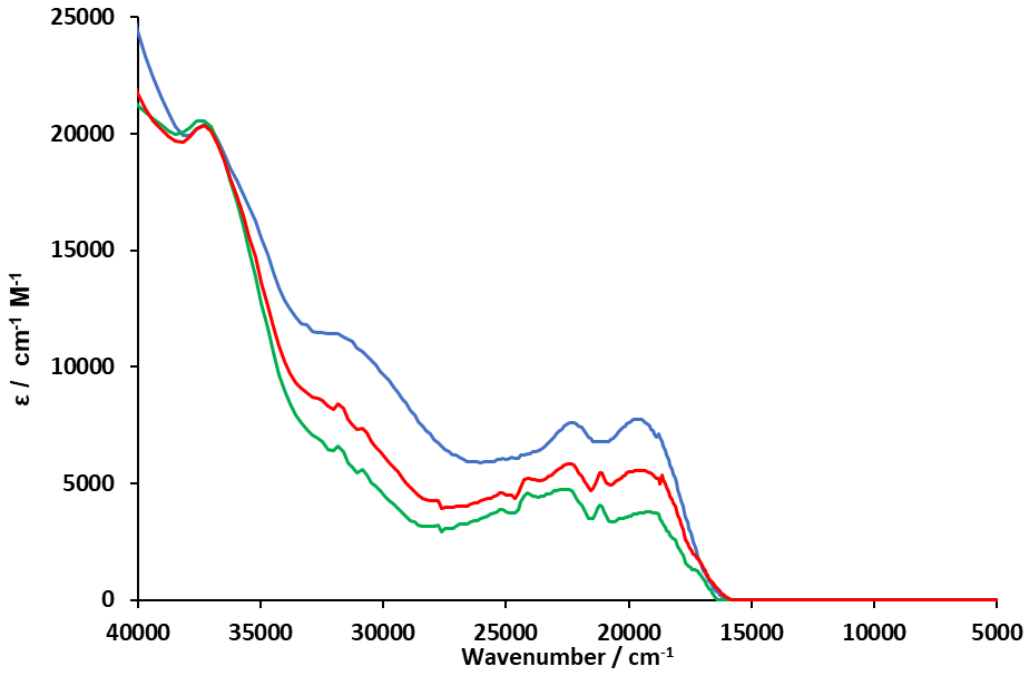

*Figure 5.8: The UV-Vis NIR SEC (solid line) of complex [**13**]$_2$(blue), [**13**]$_2^+PF_6$ (red) and [**13**]$_2^{2+}$ $2PF_6$ (green) in CH_2Cl_2.*

The UV-Vis-NIR spectra of **[13]$_2$**, **[13]$_2^+$** and **[13]$_2^{2+}$** are displayed in Figure 5.8. Following the **[13]$_2$** → **[13]$_2^+$** oxidation there is no sign of a transition in the NIR consistent with the criteria for PCMV. The MLCT for **[13]$_2$** is observed at 19531 cm^{-1} (512 nm) following the **[13]$_2$** → **[13]$_2^+$** oxidation the MLCT decreases in intensity but shows no change in energy. The HDop-π → HDop-π* at 22321 cm^{-1} (448 nm) transition decreases in energy but doesn't change in energy. Following the **[13]$_2^+$** → **[13]$_2^{2+}$** both the MLCT and HDop-π → HDop-π* decrease in energy but show no change in the energy of the transition.

The groups of Kubiak and Lui have successfully used the coalescence of vibrational bands to estimate ET rates in the MV species, although this was only possible as ET was faster than the vibrational timescale (10^{10} s^{-1}) in their systems.[18–20] The rate of ET for complex **[11]$_2^+$** was too slow to be observed on the IR timescale, consistent with the PCMV mechanism. The SEC-IR of **[13]$_2$** was run by Dr Luke Wilkinson at -30 °C in 0.1 M NBu_4PF_6 / CH_2Cl_2 and the spectra displayed in Figure 5.9. The C=O lactam

stretches (Figure 5.9) and the PPA alkyne stretch (Figure 5.10) are good IR handles for spectroelectrochemical measurements.

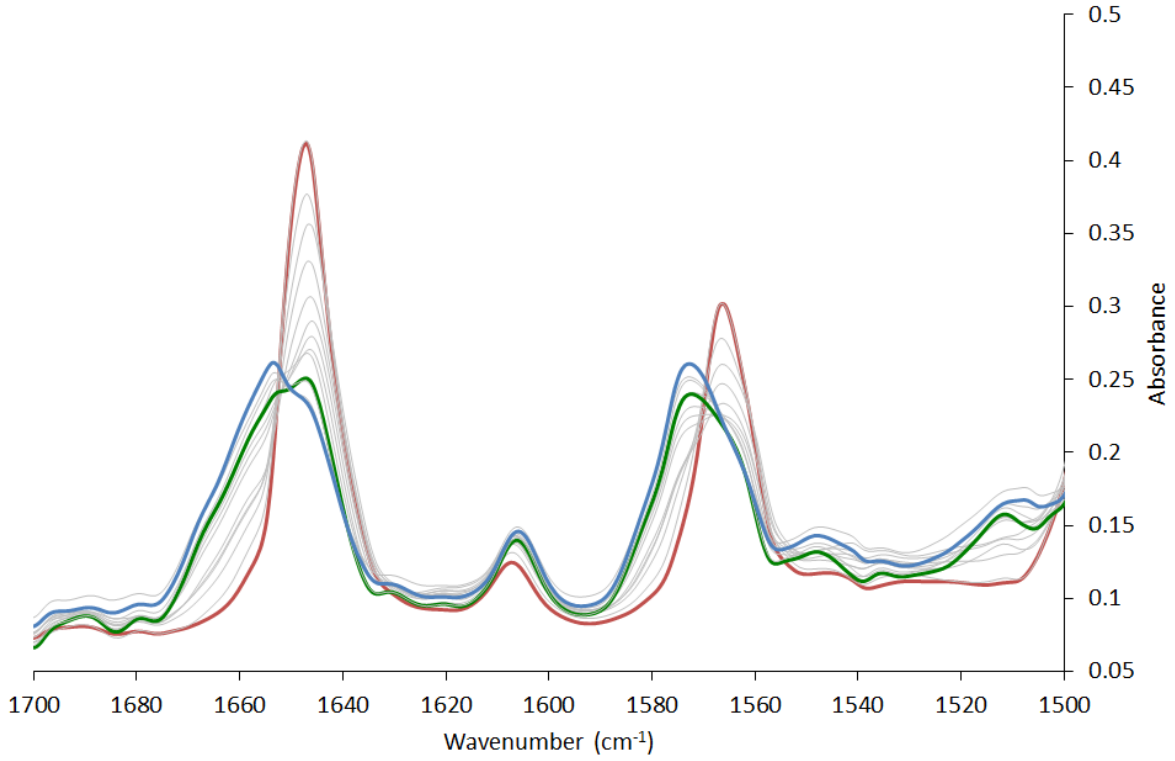

Figure 5.9: IR SEC spectra of ***[13]$_2$*** *taken at -30 °C in with 0.1 M $TBAPF_6/CH_2Cl_2$. Spectroelectrochemical transition from* ***[13]$_2$*** *(red) to* ***[13]$_2^+$*** *(green) and* ***part way towards [3]$_2^{2+}$*** *(blue).*

The IR C=O lactam stretch blueshifts from 1647 cm^{-1} in **[13]$_2$** to 1657 cm^{-1} in **[13]$_2^{2+}$**, accompanied by band broadening. The blue shift of the IR stretch has been attributed to reduced Mo_2–δ → ligand–π* back bonding following the oxidation.[6] The C=O lactam stretch in **[13]$_2^+$** is a superposition of the **[13]$_2$** and **[13]$_2^{2+}$** transitions and shows no peak coalescence indicating the rate of ET is slower than the IR timescale consistent with the PCMV mechanism. The same trend is observed for the stretch at ~ 1570 cm^{-1} and the resonance at ~1610 cm^{-1} is a ring breathing resonance.[6] The IR alkyne stretch of **[13]$_2$,** **[13]$_2^+$** and **[13]$_2^{2+}$** are displayed in Figure 5.10. The alkyne stretch of redshifts from 2217 cm^{-1} in **[13]$_2$** to 2210 cm^{-1} in **[13]$_2^{2+}$**. The alkyne stretch in **[13]$_2^+$** is a superposition of both the **[13]$_2$** and **[13]$_2^{2+}$** and once again shows no peak coalescence. Interestingly, the alkyne stretch increases in intensity going

from **[13]$_2$** to **[13]$_2^+$** and finally **[13]$_2^{2+}$**, this is believed to arise as a result of the increasing dipole in the complex following the sequential oxidations.

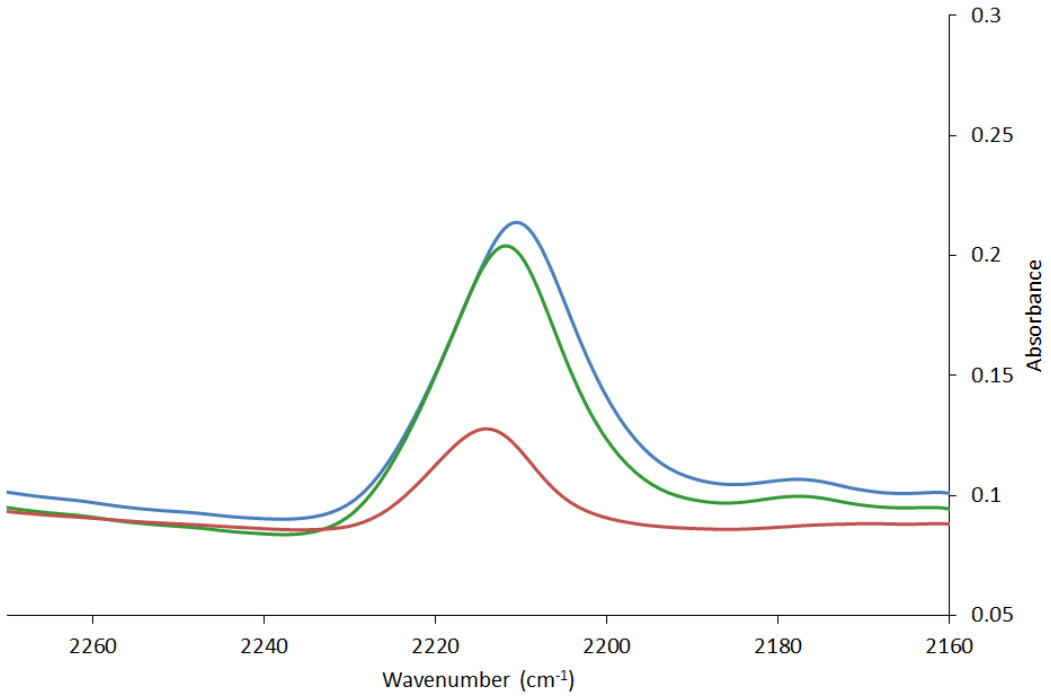

*Figure 5.10: IR SEC spectra of **[13]$_2$** taken at -30 °C in with 0.1 M TBAPF$_6$/CH$_2$Cl$_2$. Spectroelectrochemical transition from **[13]$_2$** (red) to **[13]$_2^+$** (green) and **part way towards [13]$_2^{2+}$** (blue).*

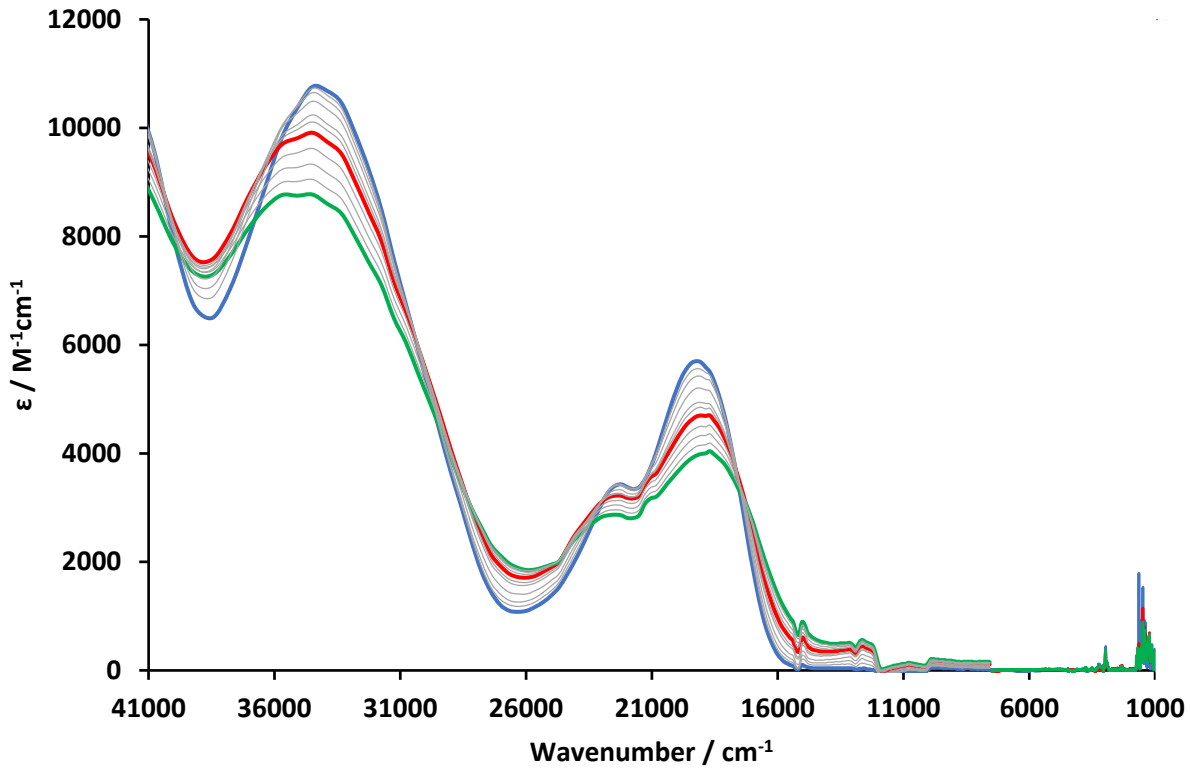

Figure 5.11: The UV-Vis NIR SEC and the IR SEC of complex ***[14]$_2$*** *in 0.1M NBu_4PF_6 /THF.* ***[14]$_2$*** *(blue),* ***[14]$_2^+$*** *(red) and* ***[14]$_2^{2+}$*** *(green).*

The UV-Vis-NIR-IR spectra of **[14]$_2$**, **[14]$_2^+$** and **[14]$_2^{2+}$** are displayed in Figure 5.11. The sequential formation of **[14]$_2^+$** and **[14]$_2^{2+}$** in the spectroelectrochemical studies is evidenced by the appearance of two separate isosbestic points in the **[14]$_2$** → **[14]$_2^+$** and **[14]$_2^+$** → **[14]$_2^{2+}$** spectra at 17699cm^{-1} (565 nm) and 17241 cm^{-1} (580 nm) respectively. Following the **[14]$_2$** → **[14]$_2^+$** oxidation there is no sign of a transition in the NIR. The MLCT for **[14]$_2$** is observed at 19047 cm^{-1} (525 nm) following the **[14]$_2$** → **[14]$_2^+$** oxidation the MLCT decreases in intensity, broadens and redshifts to 18867 cm^{-1} (530 nm). The broadening is likely the result of the appearance of a HDop-π →Mo_2-δ LMCT. The HDop-π → HDop-π* at 22471 cm^{-1} (445 nm) transition decreases in intensity, broadens and blue shifts to 22727 cm^{-1} (440 nm). Following the **[14]$_2^+$** → **[14]$_2^{2+}$** the MLCT transition further decreases in intensity, broadens and redshifts to 18518 cm^{-1} (540 nm). The HDop-π → HDop-π* transition continues to decrease in intensity, broaden and further blue shifts to 22988 cm^{-1} (435 nm). The spectra regained its original features following the reduction back to the neutral species but at ca. 90 % intensity.

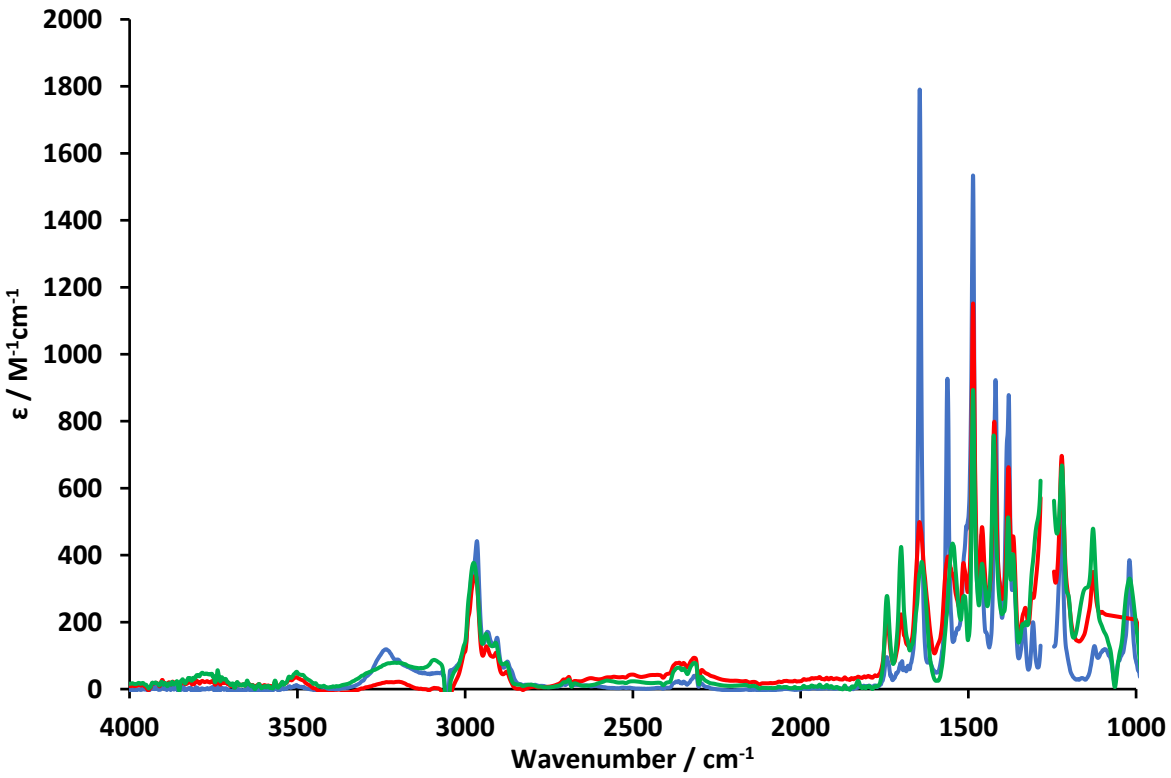

Figure 5.12:The IR spectra of ***[14]$_2$*** *(red) to* ***[14]$_2^+$PF$_6$*** *(green) and* ***[14]$_2^{2+}$2PF$_6$*** *(blue) in CH_2Cl_2 the region around 1200 cm^{-1}has been removed as a result of strong solvent absorbances.*

The SEC-IR of **[14]$_2$**, **[14]$_2^+$** and **[14]$_2^{2+}$** in CH_2Cl_2 are displayed in Figure 5.12. The MV and the doubly oxidised species were generated by the sequential reaction with stoichiometric equivalents of $AgPF_6$. The C=O and N-H stretches of the lactam bridging ligands are employed as handles for the SEC measurements. The N-H stretch for **[14]$_2$** appears as a broad band at 3235 cm^{-1} following the oxidation to the MV species and the doubly oxidised species the band broadens making a comparison difficult. A magnified portion of the spectra containing the C=O lactam stretch is shown in Figure 5.13. The IR C=O lactam stretch redshifts from 1562 cm^{-1} in **[14]$_2$** to 1546 cm^{-1} in **[14]$_2^{2+}$**, accompanied by band broadening. The C=O lactam stretch in **[14]$_2^+$** is a superposition of the **[14]$_2$** and **[14]$_2^{2+}$** transitions and shows no peak coalescence indicating the rate of ET is slower than the IR timescale consistent with the PCMV mechanism.

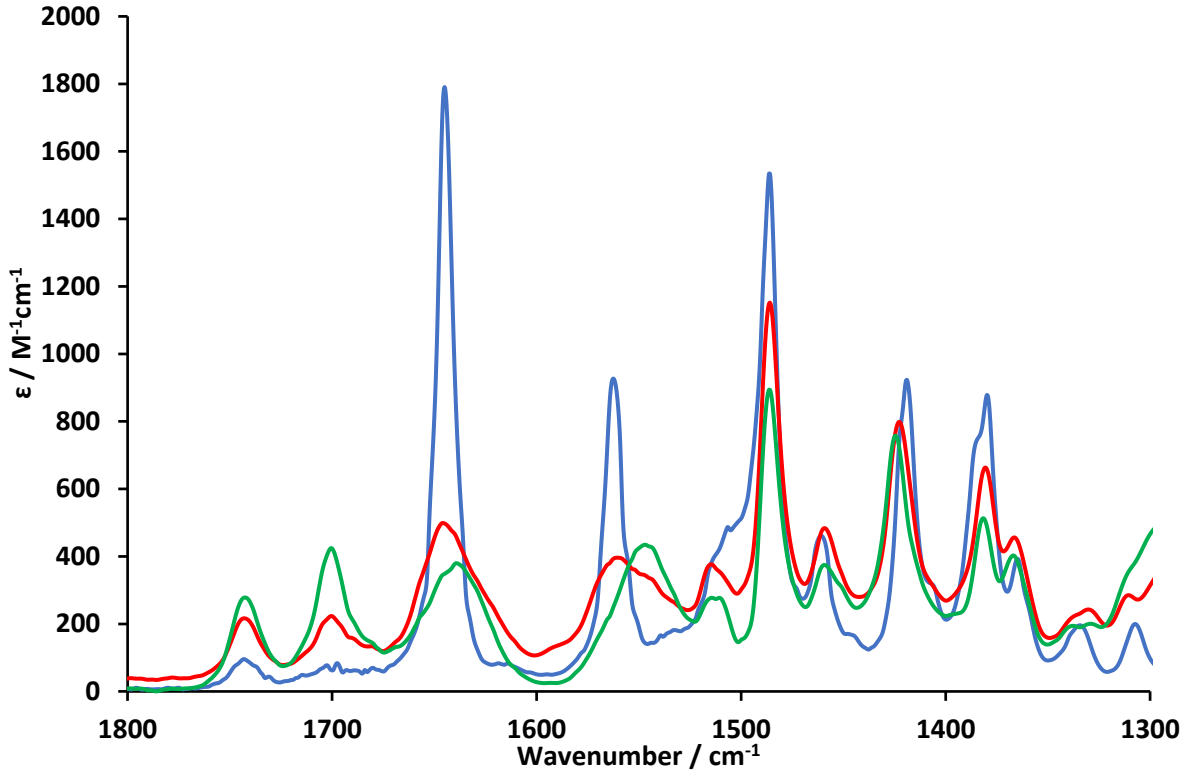

Figure 5.13: The IR spectra of the carbonyl region of complexes ***[14]$_2$*** *(red) to* ***[14]$_2^+$PF$_6$*** *(green) and* ***[12]$_2^{2+}$2PF$_6$*** *(blue) in CH_2Cl_2.*

5.4.9 *EPR*

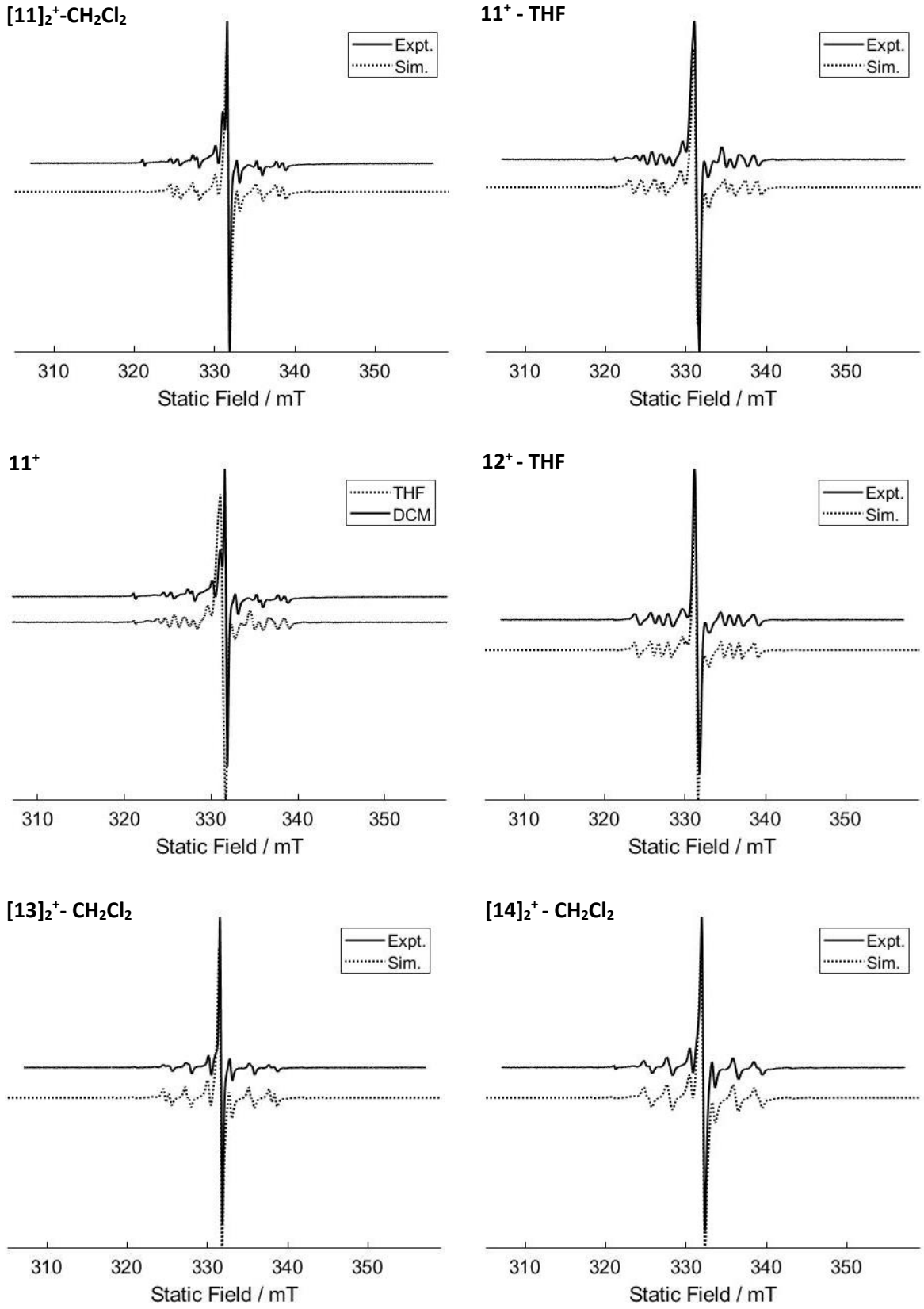

*Figure 5.14: Experimental (solid) and simulated (dashed) X-band Epr spectra of **11⁺, 12⁺, 13⁺** and **14⁺**. The abnormality at 321 mT is a quartz impurity.*

For the EPR experiments, the MV complexes **11^+ - 14^+** were prepared by the *in-situ* chemical oxidation of the neutral complexes by the addition of one equivalent of silver hexafluorophosphate ($AgPF_6$) in either CH_2Cl_2 or THF and the resulting solutions immediately characterised by electron paramagnetic resonance spectroscopy at room temperature.[21] The spectra and their simulations are shown in Figure 5.14 and the g factor and simulated hyperfine couplings reported in Figure 5.4.

*Table 5.4: Summary of the EPR spectra data obtained from the simulated EPR spectra for complexes **11^+ - 14^+**.*

Compound	Solvent	g-factor	A_{Iso} (1) / mT	A_{Iso} (2) / mT
$[11]_2^+$ [a]	CH_2Cl_2	1.936	2.360	2.680
$[11]_2^+$ [b]	CH_2Cl_2	1.939	3.28	2.53
11^+	THF	1.939	2.470	3.037
12^+	THF	1.938	2.099	2.850
$[13]_2^+$	CH_2Cl_2	1.937	2.399	2.648
$[14]_2^+$	CH_2Cl_2	1.934	2.529	2.729

[a] The hyperfine couplings determined in this study [b]The hyperfine couplings reported by Patmore *et al.*[6]

The EPR spectra of dimolybdenum species has one central peak (*I=0*, 75% abundance) at a *g*-factor of between 1.93 – 1.94, the hyperfine couplings (^{95}Mo and ^{97}Mo with *I*=5/2, 25 % abundance) are observed as a sextet surrounding the central peak.[12] The magnitude of the hyperfine couplings can indicate the extent of electron delocalisation, a hyperfine of ~2.8 mT indicates that the electron is localised, whereas when the hyperfine coupling halves to ~1.4 mT the electron is delocalised between redox centres.[22,23] For a complex stabilised by the PCMV mechanism the hyperfine couplings are expected to be ~2.8 mT as the rate of ET is believed to be slower than the EPR timescale.

The EPR spectrum of $[\mathbf{11}]_2^+$ in CH_2Cl_2 differs from the spectrum previously reported by Patmore *et al.* The reason for the discrepancies is twofold, firstly, the signal to noise ratio was improved allowing for the hyperfines to be more easily identified. Secondly, the hyperfine couplings reported by Patmore were estimated from the spectrum, whereas in this study the use of simulation software allowed for a more accurate determination of the hyperfine couplings.[5] The Spectra were also recorded in THF and independent hyperfine couplings of 2.470 mT and 3.037 mT were found. The axial coordination of THF results in an increase in the observed hyperfine couplings when compared to the spectra run in CH_2Cl_2.

The EPR spectrum of complex $\mathbf{12}^+$ has two independent hyperfine couplings of 2.099 mT and 2.850 mT. The bond is more polarised than $\mathbf{11}^+$ due to the addition of the electron withdrawing group exacerbating the polarisation of the dimolybdenum bond which is discussed in-depth in chapter 2.

The EPR spectra of complexes $\mathbf{13}^+$ and $\mathbf{14}^+$ in CH_2Cl_2 displays a central peak at a g-factor of 1.937 and 1.934 each with two sets of hyperfine couplings respectively. The hyperfine couplings of $\mathbf{13}^+$ are 2.399 mT and 2.648 mT, and the hyperfine couplings of $\mathbf{14}^+$ are 2.529mT and 2.729 mT. The magnitude of the hyperfine couplings in both cases indicate the electron is localised on the EPR timescale (~10^{-9} s) which is consistent with the PCMV mechanism. As electron transfer rates for stabilisation mechanisms that are dependent on the proton co-ordinate are typically slower than the EPR timescale.[9]

5.5 Conclusions

A series of paddlewheel complexes of the form $Mo_2(O_2CR)_3$(HDop) (where O_2CR =2,4,6-triisopropylbenzoate (**11**, TiPB) or trimethylacetate (**14**)) and *trans*-$Mo_2(TiPB)_2(O_2CL)$(HDop) (where O_2CL = chloroacetic acid (**12**) or phenylpropiolic acid (**13**)) have been synthesised. The complexes **11, 13** and **14** were shown to form self-complementary hydrogen bonded dimers in CH_2Cl_2, whereas, complex **12** was insoluble in non-coordinating solvents. Complexes **11, 13** and **14** all showed thermodynamic stabilisation of the MV state following a one electron oxidation in CH_2Cl_2. Changing the ancillary ligands resulted in complexes $\mathbf{[13]_2^+}$ and $\mathbf{[14]_2^+}$ being less thermodynamically stable in comparison to $\mathbf{[11]_2^+}$. The MV state is believed to be stabilised by a dipole induced electron transfer mechanism and should, therefore, be related to the $Mo_2^{4+/5+}$ redox potentials. However, as the redox potential of $\mathbf{[11]_2^+}$ lies in between that of $\mathbf{[13]_2^+}$ and $\mathbf{[14]_2^+}$, it is apparent that the PCMV mechanism has further nuances in the stabilisation of the MV state. These nuances could revolve around the steric interaction of the redox centres, the pKa of the bridging ligand and the and the interaction between the metal and bridge orbitals. There are hundreds of covalently bridged model MV complexes and consequently ancillary ligand effects are well understood in covalent systems. Whereas, there are comparably few examples of hydrogen bonded MV complexes. This work presents the second systematic study on the effect the ancillary ligand has in hydrogen bonded MV species. Clearly, further work is needed to understand the effect of the ancillary ligand has on these species.

5.6 Experimental

See chapter 8 for the methods and materials section. Complex **14** was synthesised in tandem with Rachel Stocks, a final year project I was supervising.

5.6.1 *Synthesis of $Mo_2(TiPB)_2(HDop)(ClH_2CCO_2)$ (12)*

$Mo_2(TiPB)_3(HDop)$ (0.216 g, 0.20 mmol) and finely ground ClH_2CCO_2H (0.028 g, 0.30 mmol) were added to a Schlenk tube and dissolved in CH_2Cl_2 (30 mL). The reaction was stirred at room temperature for 48 hours, over which time the colour of the solution changed from purple to red. The solvent was reduced *in vacuo* to ca. 5 mL resulting in the formation of a bright red solid. The red precipitate was isolated by centrifugation and the mother liquor was decanted off. The resulting solid was washed with CH_2Cl_2 (5 mL) and isolated by centrifugation, before drying *in vacu*o to yield the product. Yield 0.162 g (91 %) as a red solid. ^{1}H NMR (400 MHz, DMSO–d_6): δ_H 10.63 (s, 1H), 7.59 (d, J = 9.8 Hz, 1H), 7.09 (s, 4H), 6.82 (d, J = 9.6 Hz, 1H), 4.94 (s, 2H), 2.91 (m, 6H), 1.26 – 1.12 (m, 36H). ^{13}C NMR (100 MHz, DMSO–d_6): δ_C 182.7, 176.3, 163.4, 157.6, 153.1, 149.1, 144.6, 135.7, 128.9, 42.2, 34.2, 32.5, 24.4. MALDI-TOF-MS calcd. monoisotopic MW for $C_{38}H_{51}ClMo_2N_2O_8$, 891.10, found m/z 891.4, (M^+). Elemental Analysis calcd. for $C_{38}H_{51}ClMo_2N_2O_8$, C, 51.21; H, 5.77; N, 3.14; Found C, 51.13; H, 5.71; N, 3.05.

5.6.2 *Synthesis of $Mo_2(TiPB)_2(HDop)(PPA)$ (13)*

$Mo_2(TiPB)_3(HDop)$ (0.198 g, 0.18 mmol) and HPPA (0.027 g, 0.18 mmol) were added to a Schlenk tube and dissolved in CH_2Cl_2 (30 mL). The reaction was stirred at room temperature for 48 hours, over which time the colour of the solution changed from purple to red. The solvent was removed *in vacuo*, and hexane (10 mL) added. A red precipitate was isolated by centrifugation and the mother liquor decanted. The resulting solid was washed with hexane (10 mL) and the product was isolated by centrifugation, the mother liquor decanted and evacuated to dryness to yield the product. Yield 0.126 g (74 %) as a red solid. ^{1}H NMR (400 MHz, DMSO–d_6): δ_H 10.73 (s, 1H), 7.81 – 7.68 (m, 2H), 7.66 – 7.51 (m, 4H), 6.87 (d, J = 10.1 Hz, 1H), 2.90 (m, 6H), 1.25 – 1.16 (m, 36H). ^{13}C NMR (100 MHz, DMSO–d_6): δ_C

181.1, 171.5, 162.9, 159.2, 157.2, 149.5, 145.1, 144.5, 143.9, 133.1, 131.3, 128.7, 120.8, 119.3, 82.6, 82.2, 34.2, 32.3, 24.4 MALDI-TOF-MS calcd. monoisotopic MW for $C_{45}H_{54}Mo_2N_2O_8$, 946.20, found m/z 946.3, (M^+). Elemental Analysis calcd. for $C_{45}H_{54}Mo_2N_2O_8$, C, 57.33; H, 5.77; N, 2.97; Found C, 57.45; H, 5.89; N, 2.64.

5.6.3 *Synthesis of $Mo_2(Piv)_3(HDop)$ (14)*

$Mo_2(Piv)_4$ (0.208 g, 0.35 mmol) and H_2Dop (0.039 mg, 0.35 mmol) were added to a Schlenk tube and dissolved in toluene (15 mL), immediately followed by the addition of NEt_3 (47 µL, 0.35 mmol). The resulting solution was stirred at room temperature for 24 hours over which time the solution changed from yellow to red. The solvent was removed *in vacuo* and replaced with hexane (10 mL) to afford a colourless solution and a red precipitate. The precipitate was isolated by centrifugation and the mother liquor decanted. The resulting solid was washed with hexane (10 mL) and the product was isolated by centrifugation and dried *in vacuo* to yield 0.161 g (80 %) of a red solid. ^{1}H NMR (400 MHz, $CDCl_3$): δ_H 11.28 (d, J = 2.7 Hz, 1H), 7.35 (d, J = 9.8 Hz, 1H), 6.59 (d, J = 9.0 Hz, 1H), 1.48 (s, 9H), 1.35 (s, 18H). ^{13}C NMR (100 MHz, $CDCl_3$): δ_C 191.5, 190.5, 162.5, 159.4, 128.7, 128.1, 126.4, 40.8, 28.6, 26.9 MALDI-TOF-MS calcd. monoisotopic MW for $C_{19}H_{30}Mo_2N_2O_8$, 606.96, found m/z 606.4, (M^+). Elemental Analysis calcd. for $C_{19}H_{30}Mo_2N_2O_8$, C, 37.63; H, 4.99; N, 4.62; Found C, 37.81; H, 5.04; N, 4.56.

5.7 References

1 H. Sun, J. Steeb and A. E. Kaifer, *J. Am. Chem. Soc.*, 2006, **128**, 2820–2821.

2 G. Canzi, J. C. Goeltz, J. S. Henderson, R. E. Park, C. Maruggi and C. P. Kubiak, *J. Am. Chem. Soc.*, 2014, **136**, 1710–1713.

3 M. Tadokoro, T. Inoue, S. Tamaki, K. Fujii, K. Isogai, H. Nakazawa, S. Takeda, K. Isobe, N. Koga, A. Ichimura and K. Nakasuji, *Angew. Chemie - Int. Ed.*, 2007, **46**, 5938–5942.

4 L. A. Wilkinson, L. McNeill, A. J. H. M. Meijer and N. J. Patmore, *J. Am. Chem. Soc.*, 2013, **135**, 1723–1726.

5 L. A. Wilkinson, L. McNeill, P. A. Scattergood and N. J. Patmore, *Inorg. Chem.*, 2013, **52**, 9683–9691.

6 L. A. Wilkinson, K. B. Vincent, A. J. H. M. Meijer and N. J. Patmore, *Chem. Commun.*, 2016, **52**, 100–103.

7 B. S. Brunschwig, C. Creutz and N. Sutin, *Chem. Soc. Rev.*, 2002, **31**, 168–184.

8 T. Ito, N. Imai, T. Yamaguchi, T. Hamaguchi, C. H. Londergan and C. P. Kubiak, *Angew. Chemie - Int. Ed.*, 2004, **43**, 1376–1381.

9 J. M. Mayer, *Annu. Rev. Phys. Chem.*, 2004, **55**, 363–390.

10 M. H. V. Huynh and T. J. Meyer, *Chem. Rev.*, 2007, **107**, 5004–5064.

11 T. Cheng, M. Meng, H. Lei and C. Y. Liu, *Inorg. Chem.*, 2014, **53**, 9213–9221.

12 M. H. Chisholm, *Philos. Trans. R. Soc. A Math. Phys. Eng. Sci.*, 2008, **366**, 101–112.

13 T. Ren, *Chem. Rev.*, 2008, **108**, 4185–4207.

14 B. S. Dolinar and J. F. Berry, *Dalt. Trans.*, 2014, **43**, 6165–6176.

15 A. M. Crabtree and J. F. O'Brien, *J. Chem. Eng. Data*, 1991, **36**, 140–142.

16 D. D. Méndez-Hernández, P. Tarakeshwar, D. Gust, T. A. Moore, A. L. Moore and V. Mujica, *J. Mol. Model.*, 2013, **19**, 2845–2848.

17 D. M. D'Alessandro and F. R. Keene, *Chem. Soc. Rev.*, 2006, **35**, 424–440.

18 J. C. Goeltz and C. P. Kubiak, *J. Am. Chem. Soc.*, 2010, **132**, 17390–17392.

19 T. Cheng, D. X. Shen, M. Meng, S. Mallick, L. Cao, N. J. Patmore, H. L. Zhang, S. F. Zou, H. W. Chen, Y. Qin, Y. Y. Wu and C. Y. Liu, *Nat. Commun.*, 2019, **10**, 1–10.

20 M. B. Robin and P. Day, *Adv. Inorg. Chem. Radiochem.*, 1968, **10**, 247–422.

21 M. H. Chisholm and A. M. Macintosh, *J. Chem. Soc., Dalt. Trans.,* 1999, 1205–1208.

22 M. H. Chisholm and N. J. Patmore, *Acc. Chem. Res.*, 2007, **40**, 19–27.

23 M. H. Chisholm, *Coord. Chem. Rev.*, 2013, **257**, 1576–1583.

Attempts at decreasing the effective electron transfer distance in hydrogen bonded dimolybdenum dimers

6.1 Abstract

With an aim to decrease the internuclear separation between hydrogen bonded dimetal units, and therefore increase the stability of the MV radicals formed upon oxidation, a series of dimetal imidazole complexes of the form $Mo_2(TiPB)_3(HL)$ (TiPB = 2,4,6-triisopropylbenzoate) where HL = mercaptoimidazole (**15**), mercaptobenzimidazole (**16**), hydroxybenzimidazole (**17**) and complexes of the form $Mo_2(Piv)_3(HL)$ (Piv = trimethylacetate) where HL = mercaptoimidazole (**18**), mercaptobenzimidazole (**19**) and hydroxybenzimidazole (**20**) were synthesised. These complexes have been studied by ^1H NMR spectroscopy, UV-Vis spectroscopy, cyclic voltammetry and X-ray diffraction. Surprisingly, the UV-Vis spectra do not show evidence of strong coupling between the imidazole-π and Mo_2-δ orbitals, with no Mo_2-δ → imidazole-π* MLCT observed in the visible region. Electrochemical analyses of the complexes show a single oxidation in CH_2Cl_2 and the magnitude of the $E_{1/2}$ indicates that the imidazole ligands act as π-donors. The oxidation potentials do not explain the surprising air sensitivity found for these complexes. This is the first systematic study of dimolybdenum imidazole complexes.

6.2 The effect of internuclear separation on the degree of electronic coupling

In chapter 5 the effect the modulation of the highest occupied molecular orbital (HOMO) had on the stabilisation of the mixed valent state over a self-complimentary hydrogen bond was explored. In this chapter, ligands that could potentially decrease the internuclear separation in hydrogen bonded mixed valence complexes were investigated.

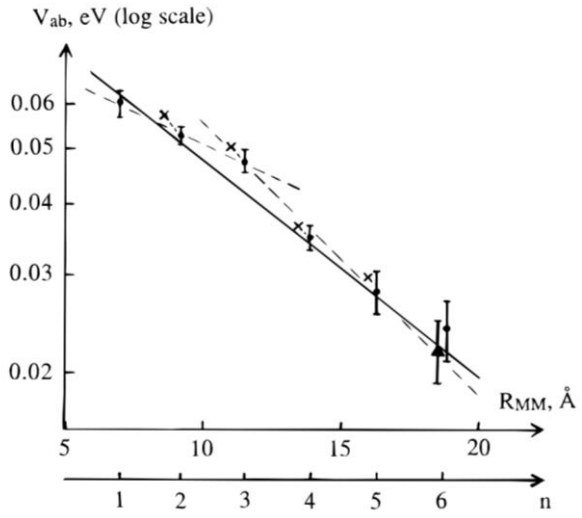

Figure 6.1: A plot of Log(V_{ab}) Vs. r_{ab} for Fc-[CH=CH]$_n$Fc (where n = 1-6) showing the exponential relationship of electronic coupling with distance. Reprinted with permission from the American Chemical Society.[1]

In covalent mixed valence (MV) systems the degree of electronic coupling has been shown to be dependent on the effective internuclear separation (r_{ab}) between the two redox centres.[2,3] Sprangler *et al.* used model diferrocenylpolyenes with the general formula Fc-[CH=CH]$_n$-Fc (where n = 1-6) were synthesised to explore the effect increasing the r_{ab} had on the thermodynamic stabilisation of the MV state and the degree of electronic coupling.[1] The thermodynamic stabilisation of the MV state was probed using cyclic voltammetry, if the complexes have a thermodynamically stable MV state then two sequential one electron oxidations should be observed. The magnitude of the separation between the half wave potentials ($\Delta E_{1/2}$) is a measure of the thermodynamic stabilisation of the mixed valent state. The reported $\Delta E_{1/2}$ were 0.170 V, 0.129 V and 0.100 V where n was 1, 2 and 3 respectively. When n was 3 - 6 only a single two electron oxidation was observed. The UV-Vis NIR spectra of the complexes

all exhibit an intervalence charge transfer (IVCT) band in the NIR, in all cases the complexes exhibit localisation (class II) of the electron on one redox centre. The measured electronic coupling parameter ($V_{ab} = H_{ab}$) was determined to be 495 cm^{-1}, 430 cm^{-1}, 390 cm^{-1}, 290 cm^{-1}, 230 cm^{-1}, 195 cm^{-1} and 177 cm^{-1} when n = 1, 2, 3, 4, 5 and 6 respectively. A plot of the Ln(v_{ab}) Vs. r_{ab} (Figure 6.1) gives a linear relationship that shows the degree of electronic coupling decreases exponentially with distance. The gradient of the slope is the decay coefficient which in this case is 0.087 $Å^{-1}$ corresponding to the electronic coefficient decreasing by a factor of 2 for every 8 Å.[4]

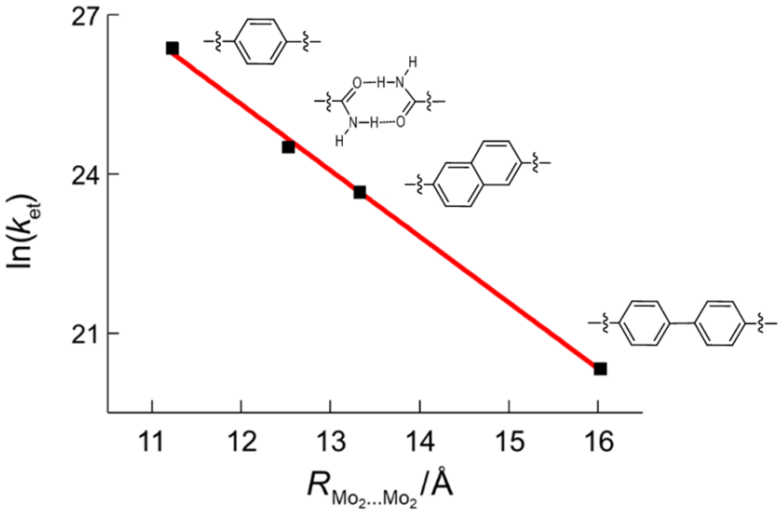

Figure 6.2: A plot of ln(k_{et}) Vs. R_{MM} (Å) for $Mo_2(DAniF)_3$-bridge- $Mo_2(DAniF)_3$ showing the exponential relationship between k_{et} and r_{mm}.

Liu *et al.* have reported a number of dimolybdenum dimers with the general formula $Mo_2(DAniF)_3$-Bridge-$Mo_2(DAniF)_3$ (DAniF= N,N′-di(*p*-anisyl)formamidinate) where the bridges consists of either terephthalate, 2,6-naphthalenedicarboxylate and biphenyl-4,4′-dicarboxylate.[5–7] The stability of the MV state was probed electrochemically and the $\Delta E_{1/2}$ decreased with the increasing bridge length as expected. All complexes exhibited an IVCT transition in the NIR with H_{ab} values of 589 cm^{-1}, 390 cm^{-1} and 245 cm^{-1} when the bridges were terephthalate, 2,6-naphthalenedicarboxylate and biphenyl-4,4′-dicarboxylate respectively. The rate of electron transfer (k_{et}) was determined by the coalescence of IR vibrational bands of the MV state. When ln(k_{et}) was plotted against the electron transfer distance a

linear relationship is observed as expected (Figure 6.2). Liu *et al.* reports the complex $Mo_2(DAniF)_3$-oxamate which was shown to dimerise in non-coordinating solutions and to exhibit thermodynamic stabilisation of the MV state with a reported $\Delta E_{1/2}$ of 0.138 V. The MV complex exhibited an IVCT transition in the NIR and had a H_{ab} of 172 cm^{-1}. The k_{et} was determined by the coalescence of IR bands and found to be 3 x 10^{10} s^{-1}, the plot of ln(k_{et}) *vs.* r_{ab} was found to be consistent with the trend observed for the covalent complexes. As the complex followed the same trend ET over a hydrogen bond can occur equally as well as π conjugated bridges.

In an attempt to synthesise the complex $[(Mo_2(Piv)_3]_2(\mu_2$-IMT) (IMT= 2-imidazolinethione) Chisholm *et al.* isolated the complex $Mo_2(Piv)_3$(HIMT) instead (Figure 6.1).[8] It was believed that $[(Mo_2(Piv)_3]_2(\mu_2$-IMT) would have a very short internuclear separation and would therefore have strong electronic coupling. Despite not achieving the desired goal, the complex represents one of the first dimolybdenum complex containing an imidazole ligand.

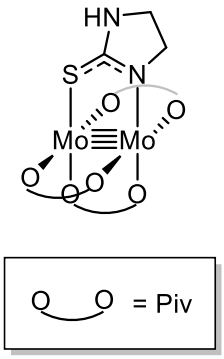

Figure 6.3: The $Mo_2(Piv)_3$(HIMT) complex isolated by Chisholm et al.

6.3 Aims

In covalent mixed valent systems, the effect of the electron transfer distance is well documented and understood, but the effect of electron transfer distance on the stabilisation of the MV state over a hydrogen bond has yet to be explored.

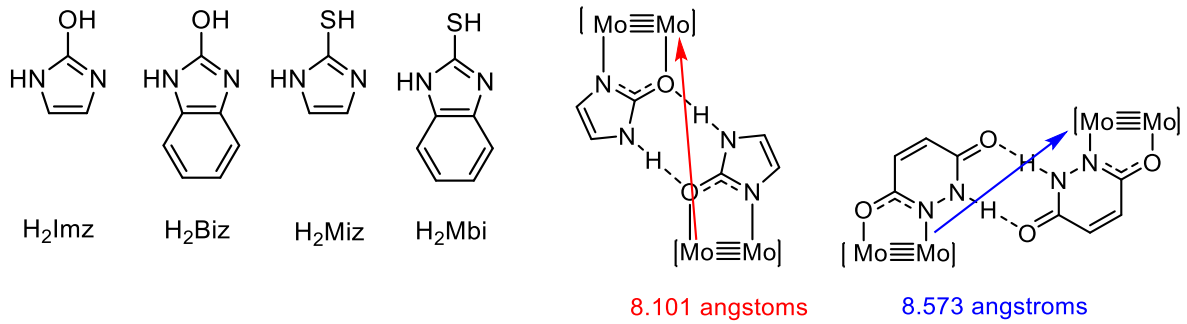

Figure 6.4: The bridging ligands targeted in the chapter 6 and a schematic showing the decrease in $Mo_2\cdots Mo_2$ separation afforded by the imidazole ligands.

The targeted bridges are shown in Figure 6.4. The ligands employ N and O or S atoms to coordinate to the dimolybdenum core. The imidazoles are calculated to have a $Mo_2\cdots Mo_2$ separation of 8.101 Å which is less than 8.573 Å calculated for $Mo_2(O_2CR)_3$(HDop). The decrease in separation is expected to increase the degree of electronic coupling. The use of the mercapto derivatives is also expected to increase the degree of electronic coupling, similarly to that observed in covalent dimolybdenum MV complexes, this is also of interest as the use of sulphur in MV complexes stabilised over a hydrogen bond remains unexplored. To determine whether the complexes dimerise in solution DOSY spectroscopy will be performed. Electrochemical analysis will then be used to determine whether the complexes show thermodynamic stabilisation of the mixed valence state, which will be evidenced by two sequential one electron oxidations. If the complexes exhibit have a thermodynamically stable MV state, spectroelectochemical measurements will be taken to determine the method and degree of stabilisation. This study will allow for the systematic study of dimolybdenum imidazole complexes which remains relatively unexplored, as well as probing for new ligands which can form suitable self-complimentary hydrogen bonds that can facilitate the formation of a MV complex.

6.4 Results and discussion

6.4.1 Synthesis

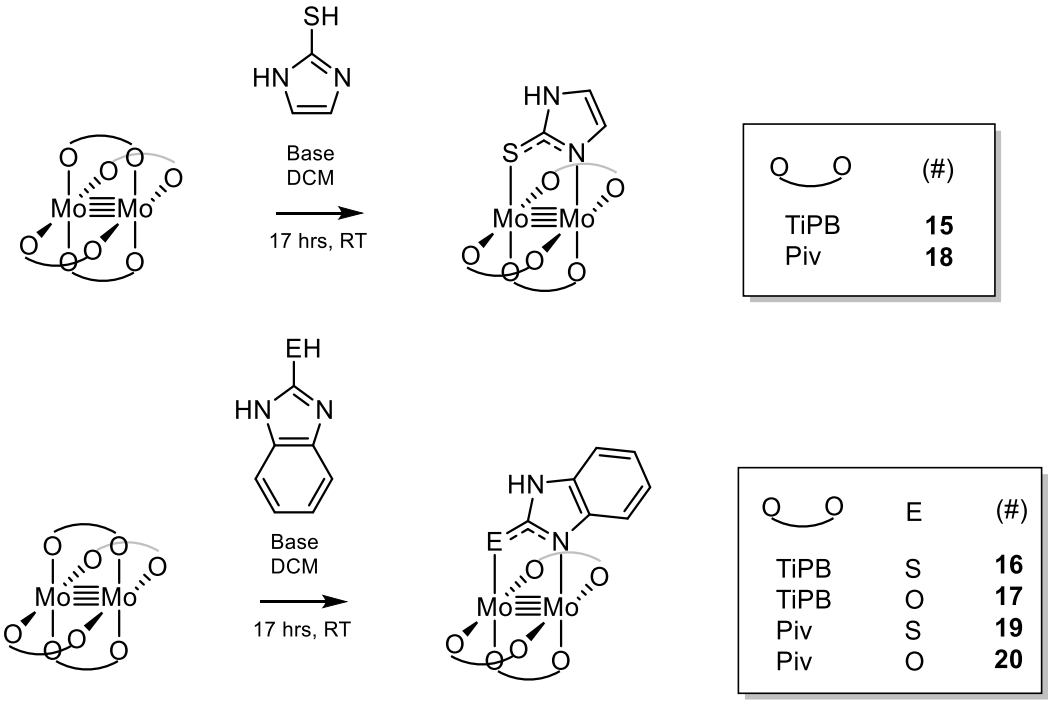

*Scheme 6.1: Synthesis of $Mo_2(TiPB)_3(HMiz)$ (**15**), $Mo_2(TiPB)_3(HMbi)$ (**16**), $Mo_2(TiPB)_3(HBiz)$ (**17**) $Mo_2(Piv)_3(HMiz)$ (**18**), $Mo_2(Piv)_3(HMbi)$ (**19**) and $[Mo_2(Piv)_3(HBiz)$(**20**).*

The commercially available ligands 2-mercaptoimidazole (H_2Miz) and 2-mercaptobenzimidazole (H_2Mbi) were deprotonated using triethylamine in CH_2Cl_2. Whereas, 2-hydroxybenzimidazole was deprotonated using tetrabutylammonium hydroxide in CH_2Cl_2, as the triethylammonium salt of 2-hydroxybenzimidazole was insoluble in CH_2Cl_2. $Mo_2(TiPB)_{3(}HMiz)$ (**15**), $Mo_2(TiPB)_3(HMbi)$ (**16**), $Mo_2(TiPB)_3(HBiz)$ (**17**) $Mo_2(Piv)_3(HMiz)$ (**18**), $Mo_2(Piv)_3(HMbi)$ (**19**) and $Mo_2(Piv)_3(HBiz)$ (**20**), were prepared by stirring the homoleptic complexes $Mo_2(O_2CR)_4$ (Where O_2CR is TiPB or Piv) with the deprotonated ligand (Scheme 6.1). The reactions went brown after 17 hours and the solvent removed *in vacuo.* The ^1H NMR spectra of the crude product indicated a mix of *trans*-$Mo_2(O_2CR)_2(imidazole)_2$, unreacted $Mo_2(O_2CR)_4$, unidentified decomposition products and the desired product. These complexes were extremely air sensitive and are suspected of being light sensitive in solution and the solid state. Exposure to air in either the solid state or in solution resulted in an immediate change in

colour from yellow to brown. When the reactions were repeated in the absence of light the resulting solution is bright yellow, although contains the same impurities with less of the unidentified decomposition product. The desired products were purified using air sensitive column chromatography to isolate the complexes as yellow solids with moderate to low yields ranging from 39 % for **16** to 9 % for **18**. The complexes (**15 – 20**) all exhibit excellent solubility in common organic solvents. Prolonged dissolution results in ligand scrambling typical of dimolybdenum carboxylate complexes.[9–11]

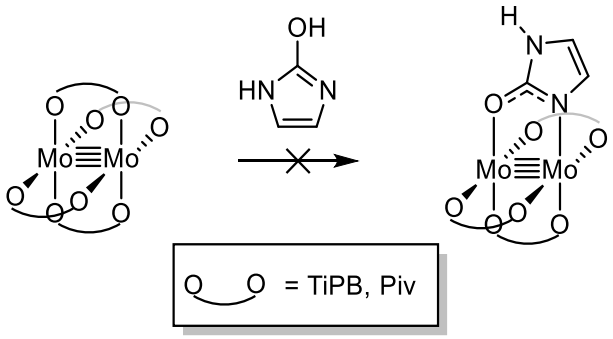

Scheme 6.2:Attempted synthesis of $Mo_2(O_2CR)_3(HImz)$

Complexes containing 2-hydroxyimidazole could not be isolated, despite varying the solvent (DCM, THF, toluene, DMSO, DMF), temperature (reflux), base (eg. NEt_3, K^tBuO and NaMeO), reaction time (17 hours – 2 weeks) and the use of monocationic complex $[Mo_2(Piv)_3(MeCN)_2][BF_4]$ as a starting material; in all cases the ^1H NMR of the resulting solids showed no sign of a reaction (Scheme 6.2). This was believed to be due to the insolubility of the proligand, even in polar solvents such as DMF and DMSO. Although complexes containing 2-mercaptoimidazole[12–15] and 2-mercaptobenzimidazole[16–18] are relatively well known, complexes containing 2-hydroxybenzimidazole and 2-hydroxyimidazole ligands remain unreported in literature to the best of the authors knowledge.

Complexes **15 – 20** have all been characterised by ^1H NMR spectroscopy and the crystal structures for complex **15, 17** and **18** were obtained. Due to the extreme air sensitivity of the complexes, adequate elemental analysis was only obtained for complexes **15** and **18**.

6.4.2 X-ray crystallography

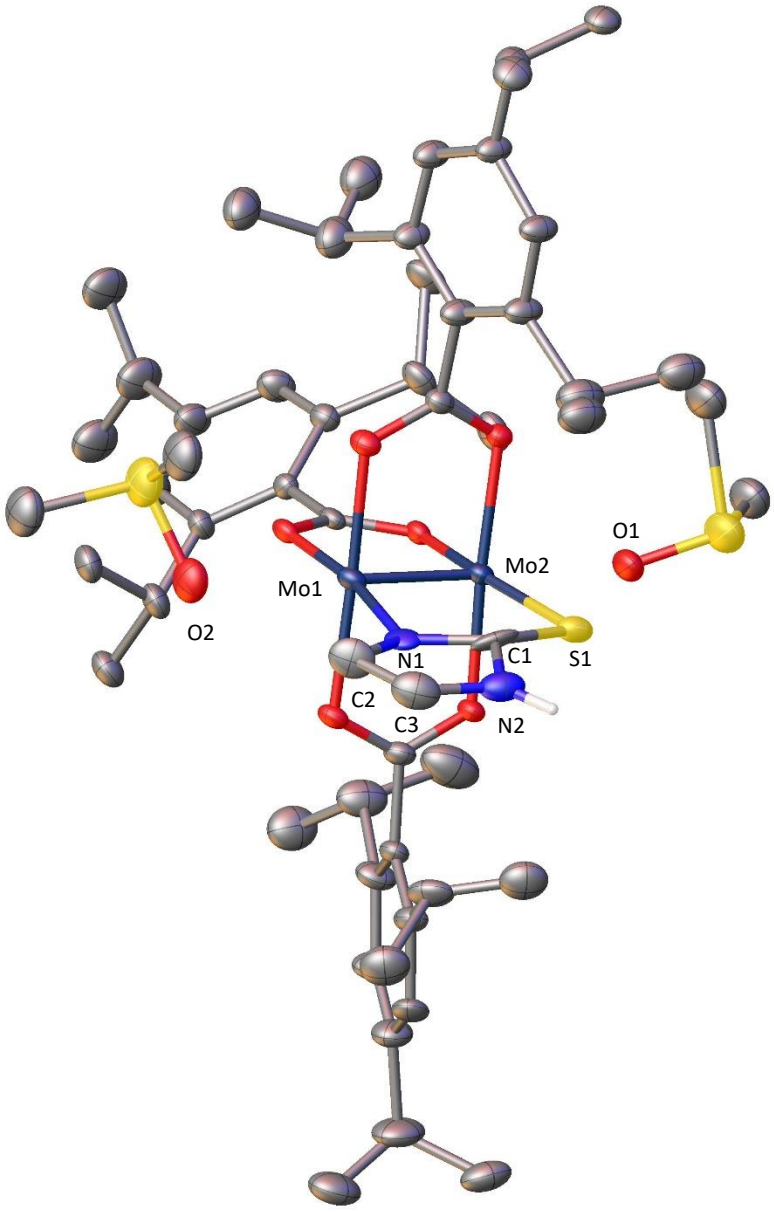

*Figure 6.5: Solid-state structure $Mo_2(TiPB)_3(HMiz)(DMSO)_3$ (**15**) as determined by single-crystal XRD. Anisotropic displacement parameters are shown at 30 % probability. All hydrogen atoms with the exception of the bridging hydrogen are omitted for clarity. Selected bond lengths (Å) and angles (°): Mo1-Mo2 = 2.1172(9), Mo1-S1 = 2.420(8), Mo2-N1 = 2.21(3), C1-S1 = 1.69(4), C1-N1 = 1.37(5), Mo1-O2 = 2.758(6), Mo2-O1 = 2.504(6), C2-C3 =1.34(3), N1-C2= 1.37(3), N2-C3 = 1.37(3), Mo1-S1-C1 =99.8(8), Mo2-N1-C1 = 117(2) and N1-C1-S1 = 126.4(15).*

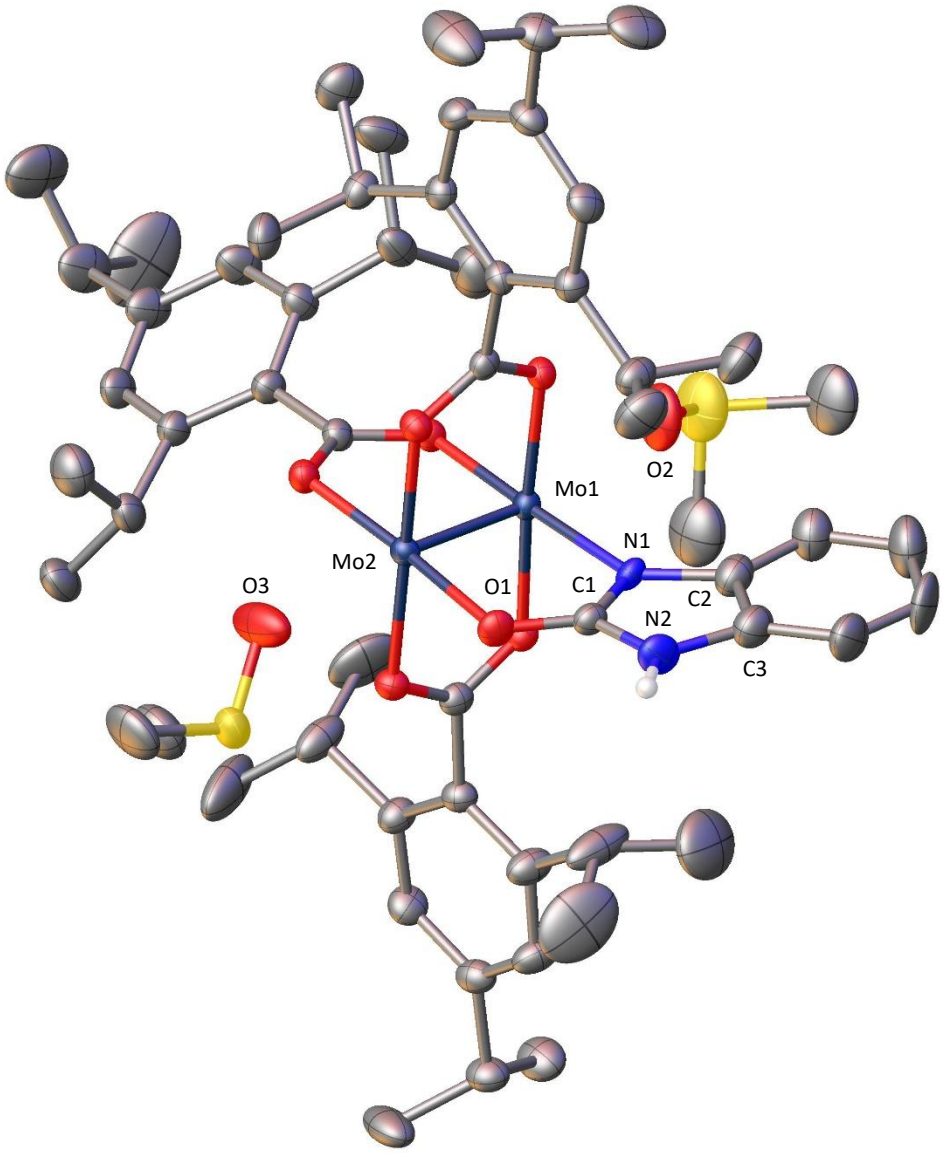

*Figure 6.6: Solid-state structure $Mo_2(TiPB)_3(HBiz)(DMSO)_3$ (**17**) as determined by single-crystal XRD. Anisotropic displacement parameters are shown at 50 % probability. All hydrogen atoms with the exception of the bridging hydrogen are omitted for clarity. Selected bond lengths (Å) and angles (°): Mo1-Mo2 = 2.1090(3), Mo1-O1 = 2.135(2), Mo2-N1 = 2.154(2), C1-O1 = 1.284(3), C1-N1 = 1.327(4), Mo1-O2 = 2.505(3), Mo2-O3 = 2.586(3), C2-C3 =1.407(5), N1-C2= 1.411(4), N2-C3 = 1.416(5), Mo1-O1-C1 =114.76(18), Mo2-N1-C1 = 115.05(18) and N1-C1-O1 = 124.5(3).*

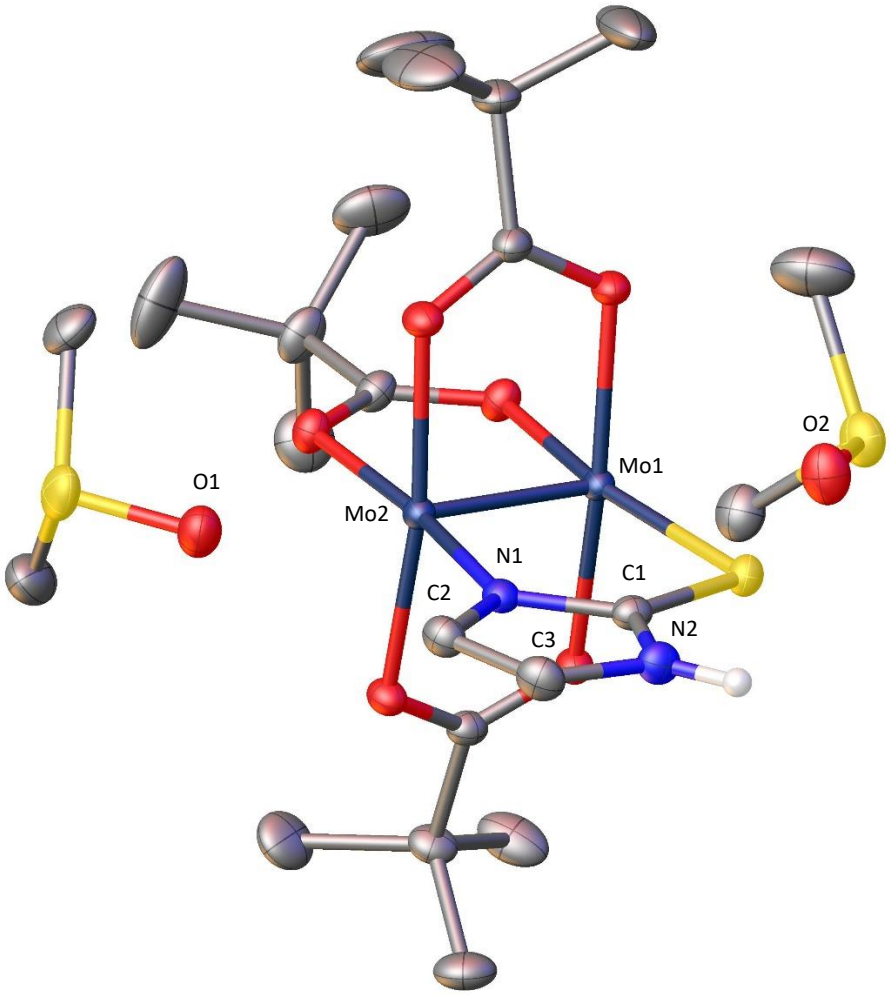

*Figure 6.7: Solid-state structure $Mo_2(Piv)_3(HMiz)(DMSO)_3$ (**18**) as determined by single-crystal XRD. Anisotropic displacement parameters are shown at 50 % probability. All hydrogen atoms with the exception of the bridging hydrogen are omitted for clarity. Selected bond lengths (Å) and angles (°): Mo1-Mo2 = 2.1138(3), Mo1-S1 = 2.4783(6), Mo2-N1 = 2.150(2), C1-S1 = 1.715(2), C1-N1 = 1.347(2), Mo1-O2 = 2.620(2), Mo2-O1 = 2.587(3), C2-C3 =1.357 (3), N1-C2= 1.384(2), N2-C3 = 1.378(2), Mo1-S1-C1 =100.28(6), Mo2-N1-C1 = 120.83(10) and N1-C1-S1 = 124.41(12).*

Single crystals of **15**$(DMSO)_3$, **17**$(DMSO)_3$ and **18**$(DMSO)_3$ were grown by the slow diffusion of degassed water into DMSO solutions of **15, 17** and **18** at room temperature in an NMR tube. The structures were determined by single X-ray diffraction, and are shown in Figure 6.5, Figure 6.6 and Figure 6.7, selected bond lengths are given in Table 6.1, the cell parameters and refinement results are given in the experimental chapter (8).

For complexes **15** and **17**, the solvent was removed from the NMR tube and the crystals scraped out in air and immediately coated in degassed water. A crystal was then chosen and mounted onto the goniometer head as quickly as possible and data acquired. For a very brief portion of time the crystals were exposed to air resulting in degradation of the crystal quality, which is believed to be the reason why the final R-factor was 0.1154 and 0.0607 for complexes **15** and **17**. Following this method complex **18** had a final R-factor of 0.0886, but by changing the way these crystals were isolated resulted in a new structure being determined with a final R-factor 0.0382 demonstrating the extreme air sensitivity of these complexes. This newly developed method involved using a syringe to remove the crystals in the mother liquor from the NMR tubes, these were then placed in a receptacle under an inert atmosphere to mount the desired crystal minimising the exposure to air.

The unit cell of complexes **15**$(DMSO)_3$ and **17**$(DMSO)_3$ were found to be monoclinic and the structures were solved in the $P2_1/c$ and $P2_1/n$ space groups respectively. The unit cell of complex **18**$(DMSO)_3$ was found to be triclinic and solved in the space group P-1. Complex **15** was found to be disordered with the isopropyl groups and the axial DMSO molecules disordered over two positions. In addition, the structure contained disorder in the position of the mercaptoimidazole which was disordered over two positions with occupancies of 0.558(9) and a 0.442(9).

*Table 6.1: bond lengths (Å) for complex **15**(DMSO)$_3$, **17**(DMSO)$_3$ and **18**(DMSO)$_3$*

Bond	**15**(DMSO)$_3$	**17**(DMSO)$_3$	**18**(DMSO)$_3$
Mo-Mo	Mo1-Mo2 2.1172(9)	Mo1-Mo2 2.1090(3)	Mo1-Mo2 2.1138(3)
Mo-E	Mo1-S1 2.420(8)	Mo1-O1 2.135(2)	Mo1-S1 2.4783(6)
Mo-N	Mo2-N1 2.21(3)	Mo2-N1 2.154(2)	Mo2-N1 2.150(2)
Mo-L$_{ax}$	Mo1-O2 2.758(6)	Mo1-O2 2.505(3)	Mo1-O2 2.620(2)
	Mo2-O1 2.504(6)	Mo2-O3 2.586(3)	Mo2-O1 2.587(3)

The structures show the expected paddlewheel arrangement of the ligands around the dimetal core and are bound to three carboxylate ligands and an imidazole ligand in the expected ECN (E = O or S) coordination mode. All complexes have two axially coordinated DMSO which show preferential coordination of one DMSO molecule. The differences in axial coordination is less pronounced in **18** than that observed in complexes **15** and **17** indicating steric hinderance has a role in the axial coordination of DMSO as TiPB is more sterically hindering than Piv. A third DMSO molecule (omitted) is hydrogen bonded to the NH of the bridging ligand. The MoMo bond lengths for complexes **15, 17** and **18** are 2.1172(9) Å, 2.1090(3) Å and 2.1138(3) Å respectively. The observed bond lengths are typical for dimolybdenum paddlewheel complexes but changing the ancillary ligand from TiPB (**15**) to Piv (**18**) results in a significant decrease in the dimolybdenum bond length.[8,19] The bond length for **17** is significantly shorter than both **15** and **18**, this decrease in MoMo bond length results from the O for S substitution, as the C1-O1 (1.284(3) Å) bond in **17**(DMSO)$_3$ is shorter than the C1-S1 (1.69(4) Å) bond in **15**(DMSO)$_3$ the MoMo bond contracts. To the authors knowledge there have been no structural studies of transition metal complexes containing the hydroxybenzimidazole ligand despite the mercaptobenzimidazole containing complexes being well studied.

6.4.3 ^{1}H NMR spectroscopy

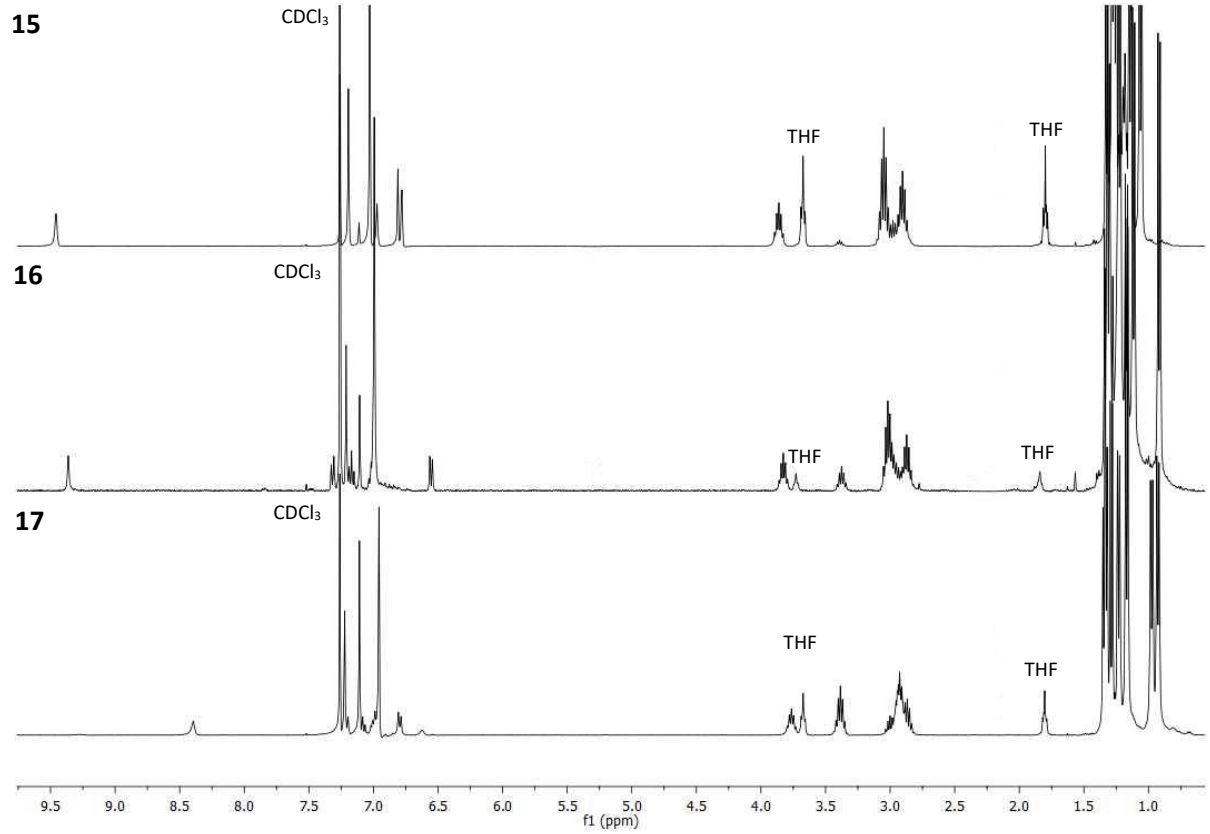

*Figure 6.8: ^{1}H NMR spectra of complexes **15** - **17** in $CDCl_3$.*

The ^{1}H NMR spectra of complexes **15** - **17** in $CDCl_3$ are shown in Figure 6.8. The NMR samples were immediately run following their preparation. Complexes **15, 16** and **17** have diagnostic TiPB resonances with a 2:1 intensity ratio, a result of the complex containing two cis-TiPB ligands and one trans-TiPB ligand. The chemical shifts of the TiPB protons are similar across the series and will only be discussed briefly. The TiPB Ar-CH(C***H***$_3$)$_2$ resonances are observed as doublets at a chemical shift of 0.75-1.5 ppm with an integration pattern of 24: 12: 12 :6. The TiPB Ar-C***H***$(CH_3)_2$ peaks have an integration pattern of 4: 2: 2: 1 and are observed as septets at a chemical shift of between 2.75 and 3.75 ppm. The TiPB Ar-***H*** resonances are observed as singlets with an integration pattern of 2: 1 between 7.0 and 7.2 ppm.

The mercaptoimidazole (**15** and **16**) N-***H*** proton chemical shifts occur at 9.62 ppm and 9.36 ppm respectively, whereas, the hydroxyimidazole N-***H*** proton in **17** is shifted upfield to 8.31 ppm. The bridging ligand backbone for complex **15** is observed as two doublets at 6.81 ppm and 6.68 ppm. Complexes **16** and **17** have two doublets and two triplets between 7.3-6.5 ppm which correspond to the phenyl protons on the aromatic backbone of the mercaptobenzimidazole and hydroxybenzimidazole ligands respectively.

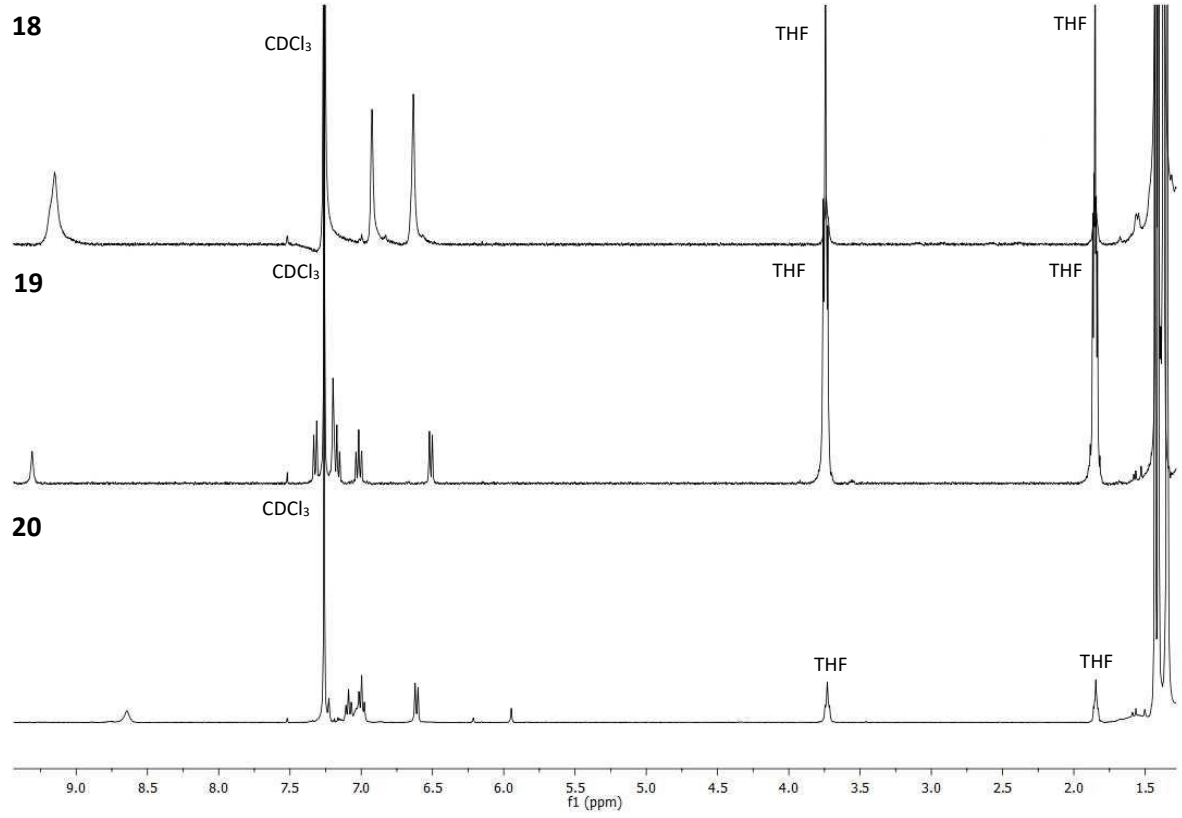

*Figure 6.9: ^{1}H NMR spectra of complexes **18** - **20** in $CDCl_3$.*

The ^{1}H NMR spectra of complexes **18** - **20** in $CDCl_3$ are shown in Figure 6.9. All complexes exhibit two singlets in a 2:1 ratio between 1.43 ppm and 1.37 ppm corresponding to the pivalate ancillary ligands. The mercaptoimidazole (**18** and **19**) N-***H*** proton chemical shifts occur at 10.03 ppm and 10.05 ppm respectively, whereas, the N-***H*** proton in **17** is shifted upfield to 8.64 ppm. The bridging ligand backbone for complex **18** is observed as two doublets at 6.93 and 6.63 ppm. Complexes **19** and **20** have two doublets and two triplets between 7.32 - 6.55 ppm which correspond to the phenyl protons

on the aromatic backbone of the mercaptobenzimidazole and hydroxybenzimidazole ligands respectively. The coordinated THF can be removed by placing the compounds under high vacuum for 48 hours, this was performed prior to electrochemical analysis, diffusion ordered spectroscopy and the submission of the elemental analysis.

*Table 6.2: ^{1}H NMR N-H chemical shifts of complexes **15-20** in $CDCl_3$ and in DMSO-d_6*

Compound	$CDCl_3$ / ppm	DMSO-d_6 / ppm
15	9.62	12.65
16	9.36	12.89
17	8.39	11.19
18	10.03	12.07
19	10.05	12.66
20	8.64	11.56

The ^{1}H NMR spectra above were conducted in $CDCl_3$, a non-coordinating solvent which can facilitate the formation of self-complimentary hydrogen bonds. If the complexes were forming self-complimentary hydrogen bonded dimers, then the addition of DMSO would disrupt the hydrogen bond and a shift in the NH peak could be observed in the ^{1}H NMR spectrum. The NH chemical shifts for complexes **15 – 20** in both $CDCl_3$ and DMSO-d_6 are reported in Table 6.2. In all the cases the NH peak is shifted downfield in DMSO. The change in chemical shift is consistent with a change in environment but it is not possible to conclude whether the complex forms a dimer in solution as the crystal structure of **17** shows that DMSO hydrogen bonds to the NH proton in the solid state and could also account for the large chemical shift. To determine if the complexes form dimers in solution diffusion ordered spectroscopy was conducted.

6.4.4 Diffusion ordered spectroscopy

Complex **15 – 20** were dissolved in $CDCl_3$ (0.5 mL) and their DOSY spectra collected and a diffusion coefficient obtained. To the same sample DMSO-d_6 (50 µL) was carefully added and the spectra were reacquired, and the results are shown in Table 6.3.

*Table 6.3: DOSY data for complexes **15-20**.*

Complex	Solvent	Average Diffusion constant (x 10^{-10}) (m^2s^{-1})	Hydrodynamic radius (Å)	Hydrodynamic volume ($Å^3$)
15	$CDCl_3$	5.49	7.39	1694
	$CDCl_3$ + d_6-DMSO	3.99	10.18	4427
16	$CDCl_3$	5.59	7.26	1603
	$CDCl_3$ + d_6-DMSO	3.10	13.09	9399
17	$CDCl_3$	5.30	7.65	1879
	$CDCl_3$ + d_6-DMSO	3.28	12.35	7908
18	$CDCl_3$	8.12	5.00	523
	$CDCl_3$ + d_6-DMSO	4.69	8.64	2710
19	$CDCl_3$	7.76	5.23	601
	$CDCl_3$ + d_6-DMSO	4.78	8.49	2565
20	$CDCl_3$	7.16	5.67	765
	$CDCl_3$ + d_6-DMSO	5.26	7.72	1932

The hydrodynamic radius was determined from average diffusion coefficient using the Stokes-Einstein equation and the hydrodynamic volume was then calculated using assuming the complexes are spherical. A discussion of the Stokes-Einstein equation can be found in chapter 5. Complexes **15 – 17** have a hydrodynamic volume of between 1603 $Å^3$(**16**) – 1879 $Å^3$ (**17**) in $CDCl_3$ which is equivalent to the monomer of **11** (1410 $Å^3$),[20] indicating these complexes are very likely monomeric in non-co-ordinating solvents. Following the addition of DMSO the hydrodynamic volume of complexes **15 – 17** increases to between 4427 $Å^3$ (**15**) and 9399 $Å^3$ (**16**). Complex **18 – 20** have a hydrodynamic volume of between 523 $Å^3$(**18**) - 765 $Å^3$ (**20**), the hydrodynamic volume is consistent with the monomer of complex **14** (1096 $Å^3$) indicating these complexes are likely monomeric. Addition of DMSO resulted in

an increase in the hydrodynamic volume to 2710 Å^3, 2565 Å^3 and 1932 Å^3 for **18**, **19** and **20** respectively. All complexes have hydrodynamic volumes that are indicative of being monomeric in noncoordinating solvents.

Upon the addition of DMSO-d_6 the hydrodynamic volume surprisingly increases for all complexes. The crystal structures of complexes **15, 17** and **18** show that each complex forms a DMSO adduct with two axially coordinated DMSO, and one DMSO hydrogen bonded to the NH of the imidazole but the formation of the DMSO adduct does not explain the substantial increase in volume observed. One possible explanation for this is that the addition of DMSO could cause aggregation of the complex in solution resulting in the larger than expected volume increase.[21] However, further work would be needed in order to understand the observed increase in concentration. To explore this concentration effects of the analyte can be probed and the volume of DMSO added could also be probed.

6.4.5 Electrochemistry

The cyclic voltammograms and differential pulse voltammograms for complexes **15** – **20** in 0.1 M NBu_4PF_6 / CH_2Cl_2 solutions are shown in Figure 6.10 for the $Mo_2(TiPB)_3$(imdazole) complexes and Figure 6.11 for the $Mo_2(Piv)_3$imdazole complexes and the data is summarised in Table 6.4. All complexes show a reversible one electron oxidation processes corresponding to the removal of an electron from the Mo_2-δ orbital. Kubiak *et al.* report a number of hydrogen bonded triruthenium oxo clusters that are monomeric and only dimerise following a one electron reduction, it is therefore possible that the complexes may dimerise following a one electron oxidation.[22–24]

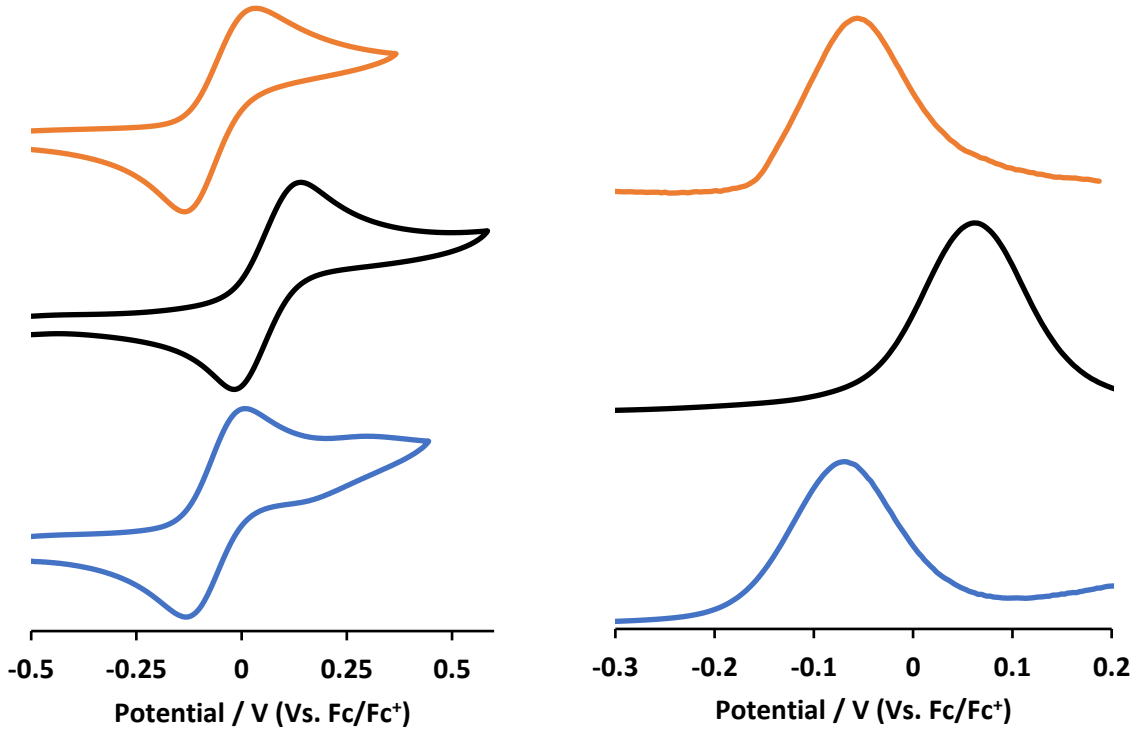

*Figure 6.10: CV (left, 100 mVs^{-1}) and DPV (right, 10 mVs^{-1}) of complexes **15** (orange), **16** (black) and **17** (blue) in 0.1 M NBu_4PF_6/ CH_2Cl_2 at a concentration of 5 mM and referenced against the Fc/Fc^+ couple (0.00 V).*

The complexes show no signs of dimerising in solution and the electrochemistry definitively show the complexes do not stabilise a MV state. The oxidation potentials of complexes **15**, **16** and **17** in CH_2Cl_2 are -0.055 V, 0.058V and -0.060 V respectively, complex **15** and **17** are cathodically shifted and complex **16** is anodically shifted when compared to the homoleptic start material $Mo_2(TiPB)_4$ (0.08 V).[25] Mercaptoimidazole and mercaptobenzimidazole ligands decrease electron density on the dimolybdenum core making them more difficult to oxidise. As mercaptoimidazole is a more donating ligand than mercaptobenzimidazole, complex **15** is more anodically shifted than **16**.[13,17,26–29] Complex **17** is cathodically shifted compared to complex **16** which is consistent with the O for S substitution of the donor atom commonly observed in literature.[5]

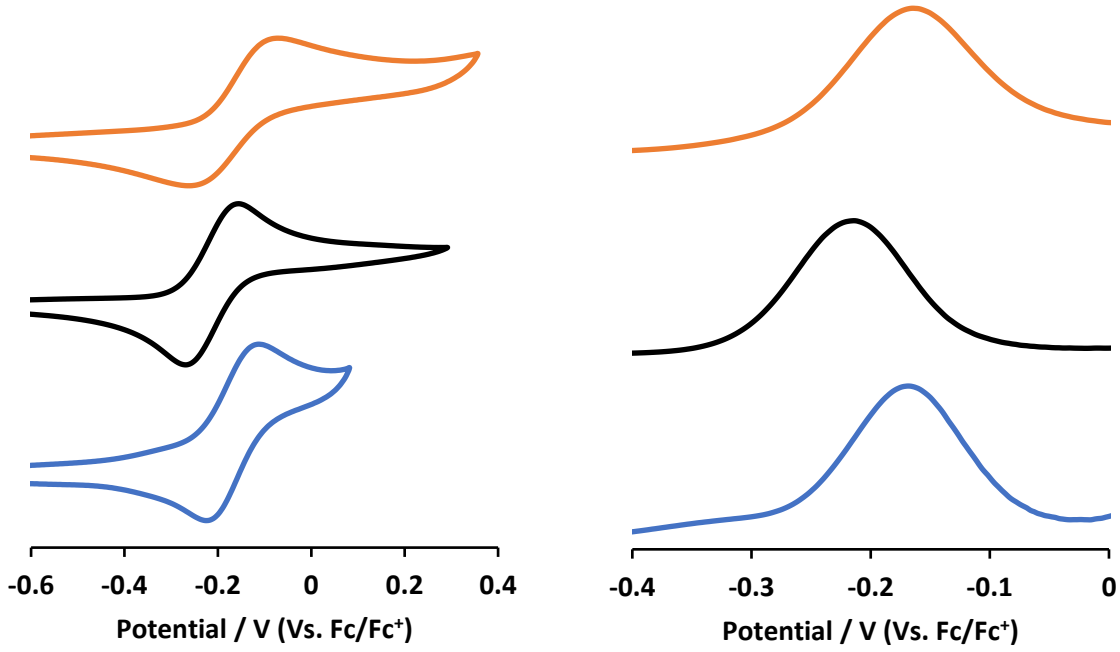

*Figure 6.11: CV (left, 100 mVs^{-1}) and DPV (right, 10 mVs^{-1}) of complexes **18** (orange), **19** (black) and **20** (blue) in 0.1 M NBu_4PF_6/ CH_2Cl_2 at a concentration of 5 mM and referenced against the Fc/Fc^+ couple (0.00 V).*

*Table 6.4: Cyclic voltammetry data for complexes **15 – 20** in 0.1 M NBu_4PF_6 / CH_2Cl_2 at a concentration of 5 mM and referenced against the Fc/Fc^+ couple (0.00 V).*

Complex	$E_{1/2}$ / V	ΔE_p / V	ΔE_p Fc / V
15	-0.055	0.140	0.080
16	0.058	0.130	0.095
17	-0.060	0.130	0.085
18	-0.165	0.165	0.130
19	-0.213	0.110	0.070
20	-0.167	0.100	0.080

The oxidation potentials of complexes **18**, **19** and **20** in CH_2Cl_2 are -0.165 V, -0.213V and -0.167 V respectively, all complexes are cathodically shifted when compared to the homoleptic start material $Mo_2(Piv)_4$ (-0.04 V).[30] The $Mo_2(Piv)_3$(imidazole) oxidation potentials are cathodically shifted when compared to $Mo_2(TiPB)_3$(imidazole). Complex **18** and **20** follow the same trend found *vide supra.* Complex **19** is cathodically shifted compared to **20,** this shift is not typical for the O for S substitution, and the exact reason for the shift remains unknown.

The oxidation potential reported for the complexes do not explain the observed air sensitivity, complex **19** has the most negative oxidation potential and is the easiest to oxidise, but complex **5** (-0.213 V) has a comparable first oxidation potential but it does not exhibit the air sensitivity observed in complexes **15 – 20**.

6.4.6 UV-Vis Absorption spectroscopy

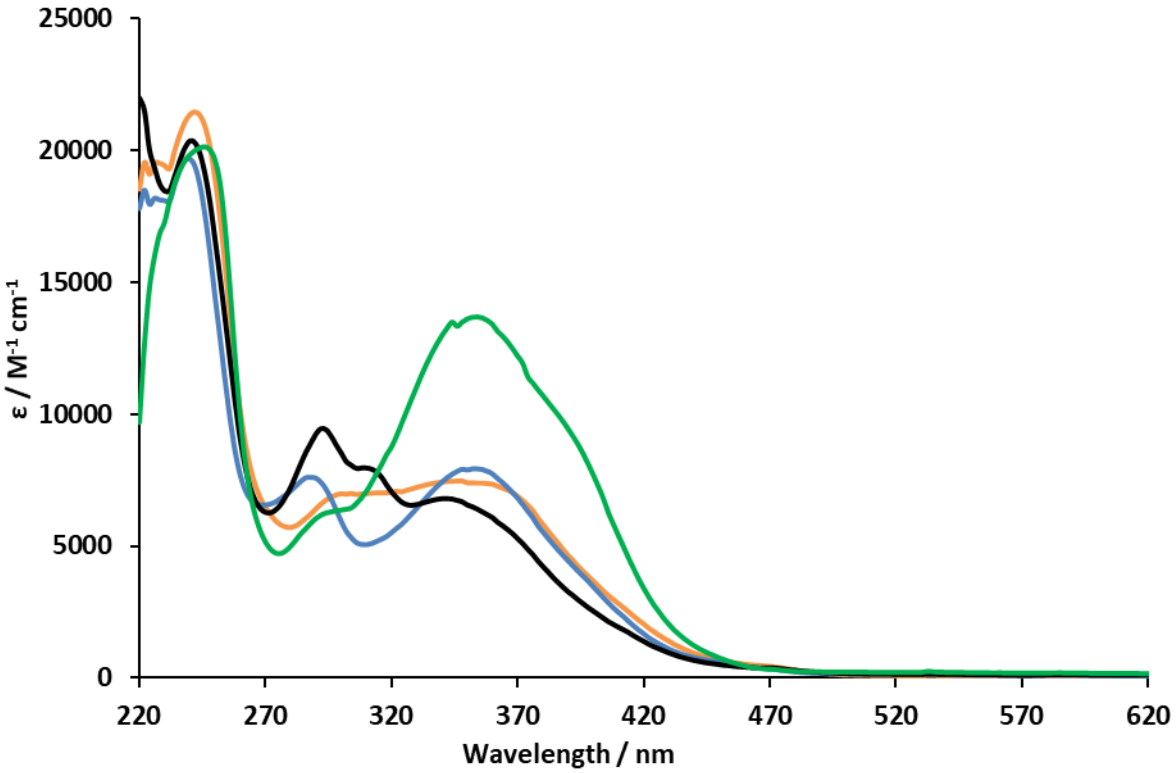

*Figure 6.12: UV-Vis absorption spectra for complexes **15** (orange), **16** (black), **17** (blue) and $Mo_2(TiPB)_4$ (green) in CH_2Cl_2.*

The UV-Vis absorption spectra for complexes **15 – 18** and $Mo_2(TiPB)_4$ in CH_2Cl_2 are displayed in Figure 6.12 with the data summarised in Table 6.5. For each of the species the high energy transitions between 230 – 250 nm are the TiPB-π → TiPB-π* transition consistent with literature.[31,32] The broad transitions centred at ~360 nm are attributed to the Mo_2-δ → TiPB-π* MLCT transition. [25,33] The Mo_2-δ → Mo_2-δ* transitions are low in intensity and occur at 470 nm, 459 nm and 469 nm for complexes **15**, **16** and **17** respectively. The electron donating nature of the imidazole ligands increases the energy

of the Mo_2-δ and Mo_2-δ* orbital energies but an overall decrease in the Mo_2-δ/ Mo_2-δ* separation is observed.[17] Compared to $Mo_2(TiPB)_4$ the imidazole complexes show a decrease in the Mo_2-δ/ Mo_2-δ* separation and a redshift of the Mo_2-δ → Mo_2-δ* transition. The Mo_2-δ → Mo_2-δ* transition is masked by the intense MLCT in $Mo_2(TiPB)_4$.[25,33] As the HMbi ligand is the least electron donating imidazole in this study the Mo_2-δ → Mo_2-δ* transition is the least redshifted.

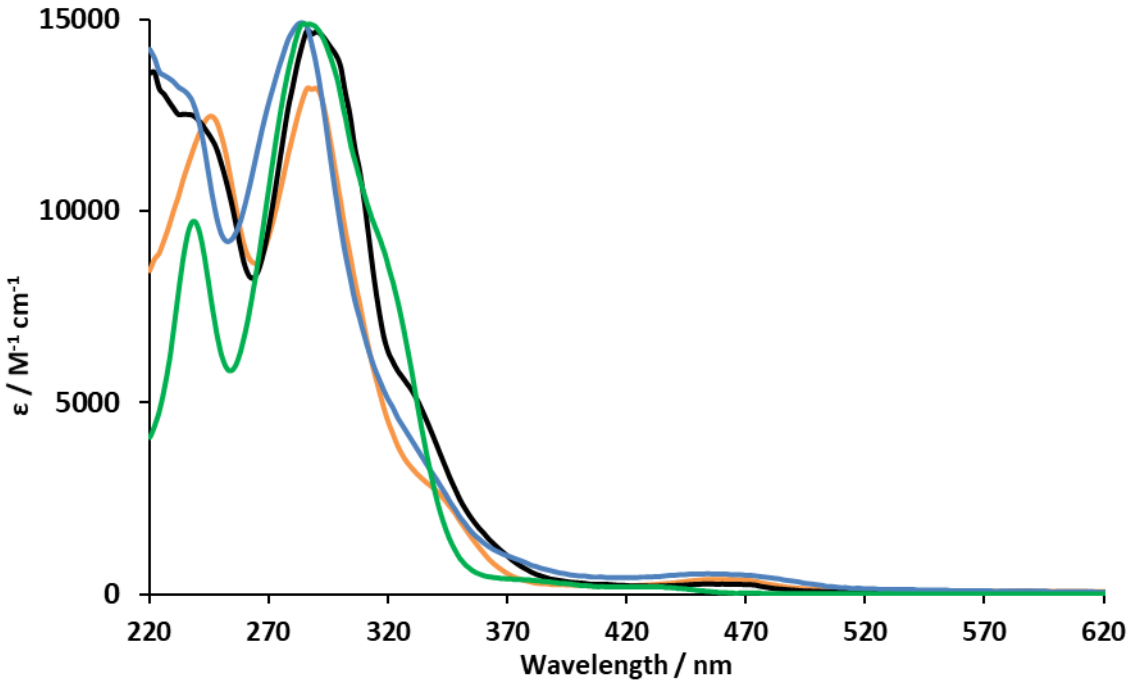

*Figure 6.13: UV-Vis absorption spectra for complexes **18** (orange), **19** (black), **20** (blue) and $Mo_2(Piv)_4$ (green) in CH_2Cl_2.*

The UV-Vis absorption spectra from complexes **18 – 20** and $Mo_2(Piv)_4$ in CH_2Cl_2 are shown in Figure 6.13 and summarised in Table 6.5. The low energy, low intensity transitions centred at 460 nm, 448 nm and 461 nm for **18, 19** and **20** and at 435 nm for $Mo_2(Piv)_4$ are the Mo_2-δ → Mo_2-δ* transition.[26] These transitions are redshifted when compared to $Mo_2(Piv)_4$ as the ligands are electron donating as discussed *vide supra*. The highest energy transitions at ~240 nm is the Piv-π → Piv-π* transitions.[26]

Complexes **15 – 20** do not display a ligand to metal charge transfer band nor do they display a metal to ligand charge transfer in the UV-Vis spectra. As these features aren't present the imidazole-π and π* are likely too high in energy relative to the Mo_2-δ orbital to facilitate electron transfer.

*Table 6.5: UV-Vis absorption data for complexes **15 – 20,** $Mo_2(Piv)_4$ and $Mo_2(TiPB)_4$ in CH_2Cl_2*

Compound	Piv/TiPB-π→π* λ / nm (ε / M^{-1} cm^{-1})	Mo_2-δ → TiPB-π* λ / nm (ε / M^{-1} cm^{-1})	Mo_2-δ→ Mo_2-δ* λ / nm (ε / M^{-1} cm^{-1})
$Mo_2(TiPB)_4$	242 (19990)	354 (13500)	-
15	242 (21130)	364 (7280)	470 (460)
16	240 (20306)	344 (6800)	459 (400)
17	240 (19680)	352 (7930)	469 (387)
$Mo_2(Piv)_4$	239 (9728)	-	435 (160)
18	246 (12470)	-	460 (380)
19	236 (12520)	-	448 (270)
20	236 (12862)	-	461 (539)

6.5 Conclusions

This chapter presents the first systematic of dimolybdenum complexes employing pendant imidazole ligands. These complexes take the form of $Mo_2(TiPB)_3(HL)$ where HL = mercaptoimidazole (**15**), mercaptobenzimidazole (**16**), hydroxybenzimidazole (**17**) and $Mo_2(Piv)_3HL$ where HL = mercaptoimidazole (**18**), mercaptobenzimidazole (**19**) and hydroxybenzimidazole (**20**). The crystal structures show the complexes bind in the expected ECN coordination mode. The crystal structure of **17** is the first reported coordination complex containing the hydroxybenzimidazole ligand which is surprising as the ligand is relatively simple and the analogous mercaptobenzimidazole complexes are comparatively well reported. Surprisingly, the absorption spectra show no observable Mo_2-δ → imidazole-π* MLCT in the visible region, indicating there is very little coupling between the imidazole and Mo_2-δ orbitals. DOSY spectroscopy indicates that the complexes do not form "dimer of dimers" in non-coordinating solvents. The complexes all exhibit a one electron oxidation between -0.213 V and 0.058 V, the electrochemistry indicates the complexes do not stabilise the MV state. Although these complexes do not from self-complimentary hydrogen bonds, they have been shown to hydrogen bond to DMSO in both the solid and solution states and could be used to hydrogen bond to different bridging ligands allowing for the study of asymmetric MV across hydrogen bonds.

6.6 Experimental

See chapter 8 for the methods and materials section.

6.6.1 Synthesis of $Mo_2(TiPB)_3(HMiz)$ (15)

In the absence of light a suspension of $Mo_2(TiPB)_4$ (1.000 g, 0.85 mmol) and 2-Mercaptoimidazole (0.085 g, 0.85 mmol) in dichloromethane (40 mL) was treated with triethylamine (116 µL, 0.84 mmol) and stirred at room temperature for 17 hours during which time the solution became darker in colour. The solvent was removed *in vacuo* and the crude product extracted into mixture a of hexane and dichloromethane (10 ml, 1:1) and purified by column chromatography using gradient elution (eluent dichloromethane /hexane (50:50 (v/v)) → dichloromethane /hexane (80:20 (v/v))) collecting the second of three close running yellow bands. The solvent was removed *in vacuo* to isolate **15** as a yellow solid. Yield 0.262 g (30 %) ^{1}H NMR (400 MHz, $CDCl_3$) δ 9.62 (s, 1H), 7.19 (s, 2H), 7.03 (s, 4H), 6.81 (d, *J* = 7.7 Hz, 1H), 6.68 (d, *J* = 7.7 Hz, 1H), 3.84 (m, 6.6 Hz, 2H), 3.04 (m, 6.5 Hz, 5H), 2.91 (m, *J* = 6.9 Hz, 2H), 1.32 (d, *J* = 6.9 Hz, 6H), 1.26 (d, *J* = 6.9 Hz, 24H), 1.13 (d, *J* = 6.8 Hz, 12H), 1.07 (d, *J* = 6.8 Hz, 12H). (400 MHz, DMSO-d_6) δ 12.25 (s, 1H), 7.23 (s, 2H), 7.05 (d, *J* = 7.7 Hz, 1H), 7.02 (s, 4H), 6.71 (d, *J* = 7.7 Hz, 1H), 4.06 – 3.89 (m, 6.6 Hz, 2H), 3.11 (m, 6.6 Hz, 4H), 2.98 (m7.6 Hz, 1H), 2.93 – 2.82 (m, 6.6 Hz, 2H), 1.28 (d, 6.8 Hz, 18H), 1.19 (d, 6.8 Hz, 12H), 1.10 (d, *J* = 6.8 Hz, 12H), 0.98 (d, *J* = 6.8 Hz, 12H). Elemental analysis Calcd. For $C_{55}H_{74}Mo_2N_2O_6S$, C, 59.29; H, 7.02; N, 2.71; Found C, 59.06; H, 7.24; N, 2.56.

6.6.2 Synthesis of $Mo_2(TiPB)_3(HMbi)$ (16)

In the absence of light a suspension of $Mo_2(TiPB)_4$ (1.000 g, 0.85 mmol) and 2-Mercaptobenzimidazole (0.127 g, 0.85 mmol) in dichloromethane (40 mL) was treated with triethylamine (116 µL, 0.84 mmol) and stirred at room temperature for 17 hours during which time the solution became darker in colour. The solvent was removed *in vacuo* and the crude product extracted into mixture a of hexane and dichloromethane (10 ml, 1:1) and purified by column chromatography using gradient elution (eluent dichloromethane /hexane (50:50 (v/v)) → dichloromethane /hexane (90:10 (v/v))) collecting the second of three close running yellow bands. The solvent was removed *in vacuo* to isolate **16** as a yellow

solid. Yield 0.364 g (39 %) ^{1}H NMR (400 MHz, $CDCl_3$) δ 9.36 (s, 1H), 7.32 (d, *J* = 7.9 Hz, 1H), 7.21 (s, 2H), 7.17 (t, *J* = 7.7 Hz, 1H), 7.06 – 7.01 (m, 1H), 6.99 (s, 4H), 6.55 (d, *J* = 8.1 Hz, 1H), 3.83 (m, *J* = 7.0 Hz, 2H), 3.38 (m, *J* = 6.5 Hz, 1H), 3.00 (m, *J* = 6.5 Hz, 4H), 2.87 (m, *J* = 6.6 Hz, 2H), 1.23 (d, *J* = 6.8 Hz, 24H), 1.17 (d, *J* = 6.7 Hz, 6H), 1.11 (d, *J* = 6.8 Hz, 12H), 0.92 (d, *J* = 6.8 Hz, 12H). (400 MHz, DMSO-d_6) δ 12.89 (s, 1H), 7.36 (d, *J* = 7.8 Hz, 1H), 7.30 (s, 2H), 7.19 (s, 1H), 7.10 (t, *J* = 5.1 Hz, 1H), 7.06 (s, 4H), 6.91 (t, *J* = 7.8 Hz, 1H), 3.93 (m, *J* = 6.5 Hz, 2H), 3.54 (m, *J* = 6.7 Hz, 1H), 3.12 (m, *J* = 6.6 Hz, 4H), 2.94 (m, *J* = 6.6 Hz, 2H), 1.36 (t, *J* = 6.4 Hz, 18H), 1.25 (d, *J* = 6.7 Hz, 12H), 1.12 (d, *J* = 6.8 Hz, 12H), 0.88 (d, *J* = 6.7 Hz, 12H).). Elemental analysis Calcd. For $C_{55}H_{74}Mo_2N_2O_6S$, C, 60.99; H, 6.89; N, 2.59; Found C, 46.36; H, 7.30; N, 1.77.

6.6.3 Synthesis of $Mo_2(TiPB)_3(HBiz)$ (17)

In the absence of light a suspension of $Mo_2(TiPB)_4$ (1.000 g, 0.85 mmol) and 2-hydroxybenzimidazole (0.112 g, 0.85 mmol) in dichloromethane (40 mL) was treated with tetrabutylammonium hydroxide in methanol (0.84 mL, 1.0 M, 0.84 mmol) and stirred at room temperature for 17 hours during which time the solution became darker in colour. The solvent was removed *in vacuo* and the crude product extracted into mixture a of hexane and dichloromethane (10 ml, 1:1) and purified by column chromatography using gradient elution (eluent dichloromethane /hexane (50:50 (v/v)) → dichloromethane /hexane (75:25 (v/v))) collecting the second of three close running yellow bands. The solvent was removed *in vacuo* to isolate **17** as a yellow solid. Yield 0.152 g (17 %) ^{1}H NMR (400 MHz, $CDCl_3$) δ 8.39 (s, 1H), 7.22 (s, 2H), 7.20 (m, 1H), 7.11 (s, 4H), 7.07 (m, 1H), 7.00 (m, 1H), 6.80 (d, *J* = 7.7 Hz, 1H), 3.76 (m, *J* = 6.5 Hz, 2H), 3.38 (m, *J* = 6.7 Hz, 2H), 3.01 (m, *J* = 6.5 Hz, 1H), 2.86 (m, *J* = 6.9 Hz, 4H), 1.23 (d, *J* = 6.9 Hz, 6H), 1.17 (d, *J* = 6.7 Hz, 24H), 0.98 (d, *J* = 6.8 Hz, 12H), 0.93 (d, *J* = 6.7 Hz, 12H). (400 MHz, DMSO-d_6) δ 11.19 (s, 1H), 7.54 (m, 1H), 7.15 (m, 1H), 7.01 (s, 2H), 6.94 (m, 1H), 6.87 (s, 4H), 6.81 (d, *J* = 7.0 Hz, 1H), 3.71 (m, 2H), 3.63 (s, 2H), 3.43 (m, *J* = 6.2 Hz, 1H), 2.79 (m, *J* = 14.1, 7.0 Hz, 4H), 1.14 (d, *J* = 6.9 Hz, 18H), 1.09 (d, *J* = 6.6 Hz, 12H), 0.98 (d, *J* = 6.5 Hz, 12H), 0.86 (d, *J* = 5.9 Hz, 12H). Elemental analysis Calcd. For $C_{55}H_{74}Mo_2N_2O_7$, C, 61.91; H, 6.99; N, 2.63; Found C, 55.99; H, 7.51; N, 2.21.

6.6.4 Synthesis of $Mo_2(Piv)_3(HMiz)$ (18)

In the absence of light $Mo_2(Piv)_4$ (1.000 g, 1.68 mmol) and 2-Mercaptoimidazole (0.168 g, 1.68 mmol) were suspended in dichloromethane (40 mL) to which triethylamine was then added (234 µL, 1.68 mmol). The resulting solution was stirred for 17 hours at room temperature. The solvent was removed under reduced pressure and the crude product extracted into a mixture of hexane and dichloromethane (10 ml, 1:1) and purified by column chromatography using gradient elution (eluent dichloromethane /hexane (50:50 (v/v)) → dichloromethane → THF/ dichloromethane (2:98 (v/v)) collecting the second yellow band. The solvent was removed under reduced pressure and dried to afford **18** as a yellow solid. Yield 0.176 g (15 %) ^{1}H NMR (400 MHz, $CDCl_3$) δ 10.03 (s, 1H), 6.93 (d, *J* = 7.7 Hz, 1H), 6.63 (d, *J* = 7.7 Hz, 1H), 1.40 (s, 18H), 1.39 (s, 9H). (400 MHz, DMSO-d_6) δ 12.07 (s, 1H), 6.97 (d, *J* = 7.7 Hz, 1H), 6.58 (d, *J* = 7.7 Hz, 1H), 1.35 (s, 9H), 1.32 (s, 18H). Elemental analysis Calcd. For $C_{18}H_{30}Mo_2N_2O_6S$, C, 36.37; H, 5.09; N, 4.71; Found C, 36.40; H, 5.15; N, 4.49.

6.6.5 Synthesis of $Mo_2(Piv)_3(HMbi)$ (19)

In the absence of light $Mo_2(Piv)_4$ (1.000 g, 1.68 mmol) and 2-Mercaptobenzimidazole (0.252 g, 1.68 mmol) were suspended in dichloromethane (40 mL) to which triethylamine was then added (234 µL, 1.68 mmol). The resulting solution was stirred for 17 hours at room temperature. The solvent was removed under reduced pressure and the crude product extracted into a mixture of hexane and dichloromethane (10 ml, 1:1) and purified by column chromatography using gradient elution (eluent dichloromethane /hexane (50:50 (v/v)) → dichloromethane → THF/ dichloromethane (1:99 (v/v)) collecting the second yellow band. The solvent was removed under reduced pressure and dried to afford **19** as a yellow solid. Yield 0.098 g (9 %) ^{1}H NMR (400 MHz, $CDCl_3$) δ 10.05 (s, 1H), 7.32 (d, *J* = 7.9 Hz, 1H), 7.20 (t, *J* = 7.4 Hz, 1H), 7.01 (t, *J* = 7.4 Hz, 1H), 6.55 (d, *J* = 8.2 Hz, 1H), 1.42 (s, 9H), 1.37 (s, 18H). (400 MHz, DMSO-d_6) δ 12.66 (s, 1H), 7.25 (d, *J* = 7.8 Hz, 1H), 7.05 (dt, *J* = 8.1, 3.1 Hz, 1H), 6.92 (d, *J* = 7.6 Hz, 1H), 6.88 – 6.80 (m, 1H), 1.38 (s, 9H), 1.31 (s, 18H). Elemental analysis. Calcd. For $C_{22}H_{32}Mo_2N_2O_6S$, C, 41.00; H, 5.00; N, 4.35; Found C, 41.35; H, 5.28; N, 4.19.

6.6.6 Synthesis of $Mo_2(Piv)_3(HBiz)$ (20)

In the absence of light $Mo_2(Piv)_4$ (1.000 g, 1.68 mmol) and 2-hydroxybenimidazole (0.168 g, 1.68 mmol) were suspended in dichloromethane (40 mL) to which tetrabutylammonium hydroxide was then added (1.68 mL, 1.0 M, 1.68 mmol). The resulting solution was stirred for 17 hours at room temperature. The solvent was removed under reduced pressure and the crude product extracted into a mixture of hexane and dichloromethane (10 ml, 1:1) and purified by column chromatography using gradient elution (eluent dichloromethane /hexane (50:50 (v/v)) → dichloromethane → THF/ dichloromethane (2:98 (v/v)) collecting the second yellow band. The solvent was removed under reduced pressure and dried to afford **20** as a yellow solid. Yield 0.185 g (18 %) ^{1}H NMR (400 MHz, $CDCl_3$) δ 8.64 (s, 1H), 7.23 (d, *J* = 7.6 Hz, 1H), 7.09 (t, *J* = 7.6 Hz, 1H), 7.00 (t, *J* = 7.6 Hz, 1H), 6.61 (d, *J* = 7.7 Hz, 1H), 1.43 (s, 9H), 1.41 (s, 18H). (400 MHz, DMSO-d_6) δ 11.56 (s, 1H), 7.17 (d, *J* = 7.7 Hz, 1H), 6.98 – 6.85 (m, 3H), 1.39 (s, 9H), 1.30 (s, 18H).

6.7 References

1 A. C. Ribou, J. P. Launay, M. L. Sachtleben, H. Li and C. W. Spangler, *Inorg. Chem.*, 1996, **35**, 3735–3740.

2 M. B. Robin and P. Day, *Adv. Inorg. Chem. Radiochem.*, 1968, **10**, 247–422.

3 N. S. Hush, *Electrochim. Acta*, 1968, **13**, 1005–1023.

4 J. R. Reimers and N. S. Hush, *Inorg. Chem.*, 1990, **29**, 3686–3697.

5 X. Xiao, M. Meng, H. Lei and C. Y. Liu, *J. Phys. Chem. C*, 2014, **118**, 8308–8315.

6 G. Y. Zhu, M. Meng, Y. N. Tan, X. Xiao and C. Y. Liu, *Inorg. Chem.*, 2016, **55**, 6315–6322.

7 T. Cheng, D. X. Shen, M. Meng, S. Mallick, L. Cao, N. J. Patmore, H. L. Zhang, S. F. Zou, H. W. Chen, Y. Qin, Y. Y. Wu and C. Y. Liu, *Nat. Commun.*, 2019, **10**, 1–10.

8 R. H. Cayton, M. H. Chisholm, E. F. Putilina and K. Folting, *Polyhedron*, 1993, **12**, 2627–2633.

9 H. Chen and F. A. Cotton, *Polyhedron*, 1995, **14**, 2221–2224.

10 M. H. Chisholm and A. M. Macintosh, *J. Chem. Soc., Dalt. Trans.*, 1999, 1205–1208.

11 F. Basolo and R. G. Pearson, *Mechanisms of Inorganic reactions*, Wiley, New York, 1967.

12 K. Pang, J. S. Figueroa, I. A. Tonks, W. Sattler and G. Parkin, *Inorganica Chim. Acta*, 2009, **362**, 4609–4615.

13 J. Jolley, W. I. Cross, R. G. Pritchard, C. A. McAuliffe and K. B. Nolan, *Inorganica Chim. Acta*, 2001, **315**, 36–43.

14 T. S. Lobana, A. K. Sandhu, R. K. Mahajan, G. Hundal, S. K. Gupta, R. J. Butcher and A. Castineiras, *Polyhedron*, 2017, **127**, 25–35.

15 N. A. Sanina, E. V. Kniazkina, R. A. Manzhos, N. S. Emel'Yanova, A. G. Krivenko and S. M. Aldoshin, *Inorganica Chim. Acta*, 2016, **449**, 61–68.

16 S. C. Chen, R. M. Yu, Z. G. Zhao, S. M. Chen, Q. S. Zhang, X. Y. Wu, F. Wang and C. Z. Lu, *Cryst. Growth Des.*, 2010, **10**, 1155–1160.

17 A. Al-Harbi, Y. Rong and G. Parkin, *Dalt. Trans.*, 2013, **42**, 11117–11127.

18 S. De Han, X. H. Miao, S. J. Liu and X. H. Bu, *Dalt. Trans.*, 2015, **44**, 560–567.

19 F. A. Cotton, L. M. Daniels, E. A. Hillard and C. A. Murillo, *Inorg. Chem.*, 2002, **41**, 2466–2470.

20 L. A. Wilkinson, L. McNeill, A. J. H. M. Meijer and N. J. Patmore, *J. Am. Chem. Soc.*, 2013, **135**, 1723–1726.

21 R. Ferrazza, B. Rossi and G. Guella, *J. Phys. Chem. B*, 2014, **118**, 7147–7155.

22 J. C. Goeltz and C. P. Kubiak, *J. Am. Chem. Soc.*, 2010, **132**, 17390–17392.

23 G. Canzi, J. C. Goeltz, J. S. Henderson, R. E. Park, C. Maruggi and C. P. Kubiak, *J. Am. Chem. Soc.*, 2014, **136**, 1710–1713.

24 T. M. Porter, G. P. Heim and C. P. Kubiak, *J. Am. Chem. Soc.*, 2018, **140**, 12756–12759.

25 B. G. Alberding, M. H. Chisholm, Y. Chou, J. C. Gallucci, Y. Ghosh, T. L. Gustafson, N. J. Patmore, C. R. Reed, C. Turro and M. Sheep, *Inorg. Chem.*, 2009, **48**, 4394–4399.

26 R. H. Cayton, M. H. Chisholm, J. C. Huffman and E. B. Lobkovsky, *J. Am. Chem. Soc.*, 1991, **113**, 8709.

27 C. Lin, J. D. Protasiewicz, E. T. Smith and T. Ren, *Inorg. Chem.*, 1996, **35**, 6422–6428.

28 B. S. Dolinar and J. F. Berry, *Dalt. Trans.*, 2014, **43**, 6165–6176.

29 C. Ma and A. F. Hill, *Dalt. Trans.*, 2019, **48**, 1976–1992.

30 R. H. Cayton, M. H. Chisholm, J. C. Huffman and E. B. Lobkovsky, *J. Am. Chem. Soc.*, 1991, **113**, 8709–8724.

31 L. A. Wilkinson, L. McNeill, P. A. Scattergood and N. J. Patmore, *Inorg. Chem.*, 2013, **52**, 9683–

9691.

32 F. A. Cotton, L. M. Daniels, E. A. Hillard and C. A. Murillo, *Inorg. Chem.*, 2002, **41**, 1639–1644.

33 S. E. Brown-Xu, M. H. Chisholm, C. B. Durr, T. L. Gustafson and T. F. Spilker, *J. Am. Chem. Soc.*, 2014, **136**, 11428–11435.

Thesis overview and concluding remarks

The study of mixed valency using model MV complexes is fundamental in understanding more complex MV systems like those found in nature, as well as using the research to investigate and develop future technologies such as molecular electronics and biomimetics. Chapter one focused on the study of MV complexes and how dimoybdneum paddlewheel complexes are ideal redox centres to study electron transfer. Electron transfer across covalent (chapter 2 – 4) and hydrogen bonded (chapter 5 and 6) interfaces has been rigorously examined.

This thesis reports the synthesis of seventeen novel dimolybdenum complexes. The clean isolation of these complexes relied heavily upon air sensitive column chromatography, a technique which was refined by trial and error within the group. To the authors knowledge chromatography has not been employed in the purification of dimolybdenum paddlewheel complexes previously. The use of column chromatography to purify dimolybdenum complexes is of note as it can potentially facilitate the isolation of previous un-isolatable or difficult to isolate complexes. The complexes were all structurally characterised by ^{1}H NMR spectroscopy, IR spectroscopy and where possible XRD. The thermodynamic stability of the MV state was determined electrochemically. The degree of electronic coupling was determined by using UV-Vis-NIR and IR spectroelectrochemistry and the electron delocalisation probed using EPR and DFT. With the aid of Dr Chris Wedge the EPR spectra could be simulated providing a further insight into localisation of an electron within the redox active unit as well as between the redox units. The DFT conducted by Professor Anthony Meijer and Dr Nathan Patmore helped rationalise the complicated absorption spectra, as well as providing further insights into the mechanism of stabilisation.

In chapter 2 the synthesis of two symmetric and three asymmetric dimolybdenum dimers of the general formula of $[Mo_2(Piv)_3]_2(\mu_2$-R,R'Dop) was described. The complexes have a significant degree of through space electron transfer, evidenced by minimal changes in the spectral shape and energy of the charge resonance transitions in the UV-Vis-IR spectra of the MV complexes despite variations in

the electron donor/acceptor groups. The number of studies on strongly coupled asymmetric systems is limited and challenges remain in understanding these systems. The complexes reported provide the first studies on asymmetric MV complexes stabilised by through space electron transfer. This study has applications in the fundamental understanding of both through space electron transfer and asymmetric MV, the knowledge of which can be extended to the design of molecular electronics but more specifically molecular rectifiers.

Electron transfer is typically described as either localised or delocalised between two redox centres, but chapter 3 shows that there can unequal distribution of the electron between redox centres, providing an example of how electronic coupling can be further tuned. The chapter described the synthesis of three dimolybdenum dimers $[Mo_2(Piv)_3]_2(\mu_2\text{-Dop})$, $[Mo_2(Piv)_3]_2(\mu_2\text{-Pthal})$ and $[Mo_2(Piv)_3]_2(\mu_2\text{-Pdt})$. Structural changes to the bridging ligand changed the through space $Mo_2\cdots Mo_2$ separation. The degree of electronic coupling and the degree of localisation of the systems has been related to the $Mo_2\cdots Mo_2$ separation. EPR analysis of $[Mo_2(Piv)_3]_2(\mu_2\text{-Pdt})^+$ shows that the electron is evenly shared between two molybdenum atoms from different redox units. This is a remarkable example of electron localisation in a fully delocalised system and is believed to be one of the first examples.

This study employed structural isomers of the bridging ligands in chapter 3, the findings demonstrate that ligand topology has a pronounced effect on the stabilisation of dimolybdenum complexes. The chapter reports the synthesis and analysis of the complexes $[Mo_2(Piv)_3]_2(\mu_2\text{-Pdo})$, $[Mo_2(Piv)_3]_2(\mu_2\text{-Doq})$ and $[Mo_2(Piv)_3]_2(\mu_2\text{-Pzt})$. In all cases these complexes exhibit greater electronic coupling compared to the complexes reported in chapter 3, despite the increased $Mo_2\cdots Mo_2$ separation and negligible through space coupling in the linear derivatives. This reinforces that through bond electron transfer is more efficient than through space electron transfer. Surprisingly, $[Mo_2(Piv)_3]_2(\mu_2\text{-Pzt})$ was found to be class IV, this is one of very few complexes to be assigned as such. As there are very few examples of class IV compounds, $[Mo_2(Piv)_3]_2(\mu_2\text{-Pzt})$ provides an insight into the extremes of electronic coupling.

The effect of changing the ancillary ligand in covalent systems has been well documented, but to date only one systematic study on the effects ancillary ligands have on MV complexes stabilised over hydrogen bonds has been reported. Complexes of the form $Mo_2(TiPB)_2(O_2CL)(HDop)$ were synthesised. The UV-Vis-NIR spectroelectrochemistry confirmed these complexes were stabilised by PCMV mechanisms, which is evidenced by the absence of an IVCT transition. Chapter 5 is the second systematic study of the effect of the ancillary ligand on the MV complexes stabilised over hydrogen bonds.

Chapter 6 presents the first systematic study of dimolybdenum complexes employing pendant imidazole ligands. These complexes take the form of $Mo_2(O_2CR)_3(Imidazole)$ and were used in an attempt to study new systems that can stabilise the MV state over a self-complimentary hydrogen bond. Although these complexes do not from self-complimentary hydrogen bonds or stabilise the MV state, they have been shown to hydrogen bond to DMSO in both the solid and solution states and could be used to hydrogen bond to different bridging ligands allowing for the study of asymmetric MV across hydrogen bonds.

The examples reported above reinforce that dimolybdenum redox centres are incredibly versatile both synthetically and spectroscopically with a number of techniques being employed to probe the electronic coupling in the MV state. Overall, this work has produced some interesting results which have an impact on a broad number of fields such as molecular electronics and biomimetics, as well as providing an insight into electronic coupling.

Experimental techniques and sample analysis

8.1 Experimental techniques

8.1.1 *Physical methods*

All reactions unless stated otherwise were carried out under an inert atmosphere using standard Schlenk line and glovebox techniques. Special precautions were taken to exclude light from both the reaction and purification of complexes **15 – 20**. Centrifugation was carried out using a Hettich Rotanta 460 centrifuge fitted with a 6 Schlenk rotor; all centrifugations were carried out at 1500 RPM for fifteen minutes.

8.1.2 *Air sensitive column chromatography*

Air sensitive column chromatography was conducted using a standard Schlenk filtration apparatus as shown in Figure 8.1, following adapted Schlenk line filtration techniques. The silica used was supplied by Sigma Aldrich with a particle size of 40 – 63 μM and dried in the filter stick under vacuum for twelve hours prior to running the column. The general column procedure is as follows, a 50:50 mix of CH_2Cl_2 and hexane was used to pack the column and 5 mL – 10 mL of the solvent mixture was used to load the column with 100 mg to 2 g of crude material. The 50:50 mix of CH_2Cl_2 and hexane was used to elute the first yellow band, which is the starting material $Mo_2(Piv)_4$ or $Mo_2(TiPB)_4$. The polarity of the solvent is increased in 10 % CH_2Cl_2 steps until the next band begins to separate on the column. The second band was eluted as a coloured solution and was generally found to be the product. This band was typically collected in three Schlenk flasks (300 ml capacity), and the solvent immediately removed *in vacuo*. The composition of each band was determined by ^1H NMR spectroscopy, before combining the clean fractions. On some occasion the product did not elute in CH_2Cl_2 solvent, the polarity of the eluent was once again increased by increments of 1 % THF in CH_2Cl_2 until the product was eluted.

Figure 8.1: Air sensitive column chromatography apparatus.

8.1.3 *Materials*

Reaction solvents were dried over CaH_2 and distilled under argon using a vertical still head apparatus and stored over molecular sieves in a Youngs tap flask. Methanol was dried over magnesium methoxide and distilled and stored as above. Dimethylsulfoxide and dimethylsulfoxide-d_6 were stirred over CaH_2 and then distilled under reduced pressure and stored over molecular sieves. CD_2Cl_2 and $CDCl_3$ were dried over CaH_2 and distilled under reduced pressure using short path distillation apparatus. Tetrahydrofuran-d_8 was dried over a potassium mirror and distilled using a short path apparatus under reduced pressure. Triethylamine, water and tetrabutylammonium hydroxide in methanol (1 M) were sparged with nitrogen for ca. 45 mins prior to use. The compounds: $Mo_2(TiPB)_4$,[1] $Mo_2(TiPB)_3HDop$,[2] $[Mo_2(Piv)_2(MeCN)_6][BF_4]_2$,[3] 2,3-dihydroxyquinoxaline[4] and 2,3-pyrazinedithiol[5] were prepared according to literature procedures. All other compounds were purchased from commercial sources and used without any further purification.

8.2 Analytical techniques

8.2.1 *NMR spectroscopy*

Air sensitive NMR samples were prepared in the glovebox under an argon atmosphere. The samples were prepared in a standard NMR tube fitted with an NMR tube cap and further sealed using parafilm. All spectra were recorded on one of the following spectrometers: a Bruker AV(III) 400 MHz, Bruker Fourier 300 MHz, Bruker Avance Neo 600 MHz or a Bruker AV1 500 MHz. Chemical shifts are referenced against the protio impurity solvent resonances ($CDCl_3$ ^{1}H 7.26 ^{13}C 77.0, dimethylsulfoxide-d_6 ^{1}H 2.50, ^{13}C 39.52, THF-d_8 ^{1}H 1.72 and 3.58 ^{13}C 37.21 and 25.31). DOSY experiments were performed in non-coordinating solvents (0.5 mL) at ca. 5 mM concentration on a Bruker AV(III) 400 MHz spectrometer using the DOSY automation process. The sample was then doped with 50 µL of DMSO and the process repeated. The diffusion coefficient (D) was determined by using Topspin to analyse the data. The hydrodynamic radii (r) were calculated using the Stokes-Einstein equation: $r = (kT/6\pi\eta D)$ where k is the Boltzmann constant, T is the temperature in Kelvin, η is the solvent viscosity. The radii were then used to approximate the hydrodynamic volume assuming a spherical system using $V = 4/3(\pi r^3)$.

8.2.2 *Absorption spectroscopy*

UV-Vis spectra were obtained on a Shimadzu UV 3600+ spectrometer at a concentration of 1 mM in a Rotaflow modified quartz cuvette (0.1 cm pathlength).

8.2.3 *IR spectroscopy*

ATR-IR spectra were recorded in the solid state using a Thermo Scientific Nicolet 380 spectrometer equipped with a diamond press.

8.2.4 *Cyclic Voltammetry*

Electrochemical measurements (cyclic voltammetry (CV) and differential pulse voltammetry (DPV)) for all complexes were collected at a range of scan rates for CV (100 – 500 mVs^{-1}) and at 10 mVs^{-1} for DPV, using a Palm Instruments EmStat2 potentiostat employing a platinum disc working electrode, a

platinum wire counter electrode, and a platinum wire pseudo-reference electrode. The voltammograms were obtained in 0.1 M NBu_4PF_6 / THF or CH_2Cl_2 solutions at a concentration of 5 mM. After each experiment a small amount of ferrocene or decamethylferrocene ($E_{1/2}$ vs. ferrocene -0.47 V)[6] was added as an internal reference.

8.2.5 *EPR Spectroscopy*

Electron paramagnetic resonance spectroscopy experiments were performed at 8.99 GHz (X-band) on a Jeol JES FA-100 spectrometer using a cylindrical cavity (TE011) with quartz insert at room temperature in both CH_2Cl_2 and THF (5 mM). The radical cations were generated in-situ by the dissolving the complex in a solution of $AgPF_6$ in THF or CH_2Cl_2 (0.9 eqv. for covalent systems and 0.45 eqv. for hydrogen bonded systems) in the glovebox, the spectra were then obtained immediately following sample preparation. EPR spectra simulations were conducted using the EasySpin package in MatLab.[7]

8.2.6 *UV-Vis-NIR spectroelectrochemistry*

Spectroelectrochemical measurements were conducted in a custom-made quartz cell with a pathlength of 0.05 cm. Spectra were obtained from 0.1 M NBu_4PF_6 / THF or CH_2Cl_2 solutions at a concentration of 1 mM. The cell contained a standard three electrode setup consisting of a flattened platinum wire working electrode, a platinum wire pseudo reference electrode and a coiled platinum wire as the counter electrode. The spectral measurements were recorded on a Shimadzu UV 3600+.

8.2.7 *IR spectroelectrochemistry*

Spectroelectrochemical measurements were conducted in a commercial liquid sample cell from Specac (product number GS20900) which has a pathlength of 0.002 cm. Spectra were obtained from 0.1 M NBu_4PF_6 / THF or CH_2Cl_2 solutions at a concentration of 10 mM.. The cell contained a standard three electrode setup consisting of a rhodium working electrode, a silver pseudo reference electrode and rhodium counter electrode. The spectral measurements were recorded on a JASCO 4100 FT-IR.

8.2.8 *Mass spectrometry*

Matrix assisted laser desorption ionisation time-of-flight spectrometry (MALDI-TOF) data was collected on a Bruker Reflex III mass spectrometer operated in linear, positive ion mode with an N_2 laser. The laser was used at the threshold required to produce a signal. The matrix used for each experiment was dithranol and this was integrated into the analyte by dissolving a mixture of dithranol and analyte into dried CH_2Cl_2.

8.2.9 *DFT*

Molecular structure calculations were performed using density functional theory as implemented in the Gaussian 09 software package. The B3LYP functional and the 6-31G* basis set were used for H, C, O, N, and S atoms,[8] along with the SDD energy consistent pseudopotentials for molybdenum.[9] All geometry optimizations were performed without symmetry constraints in a THF solvent cavity using the polarizable continuum model, as implemented in Gaussian 09.[10] The geometries were confirmed to be a minimum on the potential energy surface by frequency analysis.

8.2.10 *XRD*

Single crystal x-ray diffraction data was collected at 150(2) K on a Bruker Apex Duo diffractometer using a graphite monochromated Cu (Kα) radiation source and cold stream of N_2 gas. Crystals were mounted onto a X µm MiTeGen nylon loop using sparged water. The crystallographic refinement data for all complexes is given in Figure 8.1.

	$[Mo_2(Piv)_3]_2(\mu_2\text{-}Me_2Dop)(DMSO)_3$ (**5**)	$[Mo_2(Piv)_3]_2(\mu_2\text{-}Pdt)(DMSO)_2$ (**7**)	$Mo_2(TiPB)_3(Hmiz)(DMSO)_3$ (**15**)	$Mo_2(TiPB)_3(HBiz)(DMSO)_3$ (**17**)	$Mo_2(Piv)_3(HMiz)(DMSO)_3$ (**18**)
Empirical formula	$C_{42}H_{78}Mo_4N_2O_{17}S_3$	$C_{38}H_{68}Mo_4N_2O_{14}S_4$	$C_{57}H_{90}Mo_2N_2O_9S_4$	$C_{61}H_{92}Mo_2N_2O_{10}S_3$	$C_{24}H_{48}Mo_2N_2O_9S_4$
Formula weight	1363.00	1288.94	1267.42	1301.42	828.76
Temperature/K	150(2)	150(2)	150(2)	150(2)	150(2)
Crystal system	triclinic	triclinic	monoclinic	monoclinic	triclinic
Space group	P-1	P-1	$P2_1/c$	$P2_1/n$	P-1

Unit cell dimensions	a = 11.000(5) Å;
	α = 73.48(2)
	b = 14.635(7) Å;
	β =82.621(18)
	c = 19.685(8) Å;
	γ =79.01(3)
		a = 10.1056(9) Å;
		α = 75.150(4)
		b =15.0125(13) Å;
		β =89.899(4)
		c = 18.9412(17) Å;
		γ =75.229(4) °
			a = 10.4496(4) Å;
			α = 90 °
			b = 16.0710(6) Å;
			β = 96.5580(10) °
			c = 39.2743(11) Å;
			γ = 90 °
				a = 10.7931(3) Å;
				α =90 °
				b = 21.7991(8) Å;
				β =100.2250(10) °
				c =28.8620(10) Å;
				γ = 90 °
					a = 9.8076(17) Å;
					α =89.639(9) °
					b = 11.946(2) Å;
					β =81.940(9) °
					c =15.305(3) Å;
					γ =87.834(9) °

Volume/$Å^3$	2973(2)	2679.6(4)	6552.4(4)	6682.8(4)	1774.2(5)
Z	2	2	4	4	2
$\rho_{calc}g/cm^3$	1.522	1.598	1.285	1.294	1.551
μ/mm^{-1}	0.990	1.127	0.560	0.522	0.988
F(000)	1392.0	1308.0	2664.0	2736.0	852.0
Radiation	MoKα (λ = 0.71073)	MoKα (λ = 0.71073)	MoKα (λ = 0.71073)	MoKα (λ = 0.71073)	MoKα (λ = 0.71073)
2Θ range for data collection/°	4.4 to 54.934	4.108 to 69.146	4.228 to 50.15	4.69 to 55.07	5.31 to 66.408
Index ranges	-14 ≤ h ≤ 14 -18 ≤ k ≤ 18 -25 ≤ l ≤ 25	-16 ≤ h ≤ 16 -23 ≤ k ≤ 23 -30 ≤ l ≤ 30	-10 ≤ h ≤ 12 -19 ≤ k ≤ 16 -45 ≤ l ≤ 46	-14 ≤ h ≤ 13 -28 ≤ k ≤ 28 -37 ≤ l ≤ 37	-15 ≤ h ≤ 15 -15 ≤ k ≤ 18 -23 ≤ l ≤ 23
Reflections collected	35301	63130	49457	121883	27487
Independent reflections	13448 [R_{int} = 0.0678, R_{sigma} = 0.0873]	63130 [R_{int} = ?, R_{sigma} = 0.1483]	11597 [R_{int} = 0.0483, R_{sigma} = 0.0434]	15317 [R_{int} = 0.1172, R_{sigma} = 0.0480]	13365 [R_{int} = 0.0264, R_{sigma} = 0.0381]
Data/restraints/parameters	13448/356/791	63130/0/561	11597/506/846	15317/123/778	13365/72/398
Goodness-of-fit on F^2	1.053	1.022	1.113	1.041	1.066
Final R indexes [I>=2σ (I)]	R_1 = 0.0802, wR_2 = 0.1936	R_1 = 0.0865, wR_2 = 0.1960	R_1 = 0.0902, wR_2 = 0.2293	R_1 = 0.0448, wR_2 = 0.1120	R_1 = 0.0285, wR_2 = 0.0626
Final R indexes [all data]	R_1 = 0.1322, wR_2 = 0.2384	R_1 = 0.1608, wR_2 = 0.2398	R_1 = 0.1154, wR_2 = 0.2468	R_1 = 0.0607, wR_2 = 0.1211	R_1 = 0.0382, wR_2 = 0.0690
Largest diff. peakhole /e $Å^{-3}$	3.60/-1.68	2.43/-2.08	1.16/-1.08	1.40/-1.01	0.84/-0.94

Table 8.1: Crystallographic data for $[Mo_2(Piv)_3]_2(\mu_2\text{-}Me_2Dop)(DMSO)_3$, $[Mo_2(Piv)_3]_2(\mu_2\text{-}Pdt)(DMSO)_2$, $Mo_2(TiPB)_3(Hmiz)(DMSO)_3$, $Mo_2(TiPB)_3(HBiz)(DMSO)_3$ and $Mo_2(Piv)_3(HMiz)(DMSO)_3$

8.3 References

1 F. A. Cotton, L. M. Daniels, E. A. Hillard and C. A. Murillo, *Inorg. Chem.*, 2002, **41**, 1639–1644.

2 L. A. Wilkinson, L. McNeill, P. A. Scattergood and N. J. Patmore, *Inorg. Chem.*, 2013, **52**, 9683–9691.

3 J. M. Casas, R. H. Cayton and M. H. Chisholm, *Inorg. Chem.*, 1991, **30**, 358–360.

4 W. Cho, H. Cho, C. S. Lee, B. Y. Lee, B. Moon and J. Kang, *Organometallics*, 2014, **33**, 1617–1622.

5 S. R. Kennedy, M. N. Kozar, H. P. Yennawar and B. J. Lear, *Polyhedron*, 2016, **103**, 100–104.

6 N. G. Connelly and W. E. Geiger, *Chem. Rev.*, 1996, **96**, 877–910.

7 S. Stoll and A. Schweiger, *J. Magn. Reson.*, 2006, **178**, 42–55.

8 A. D. Becke, *J. Chem. Phys.*, 1993, **98**, 5648–5652.

9 D. Andrae, U. Häußermann, M. Dolg, H. Stoll and H. Preuß, *Theor. Chim. Acta*, 1990, **77**, 123–141.

10 M. J. Frisch, G. W. Trucks, H. B. Schlegel, G. E. Scuseria, M. a. Robb, J. R. Cheeseman, G. Scalmani, V. Barone, G. a. Petersson, H. Nakatsuji, X. Li, M. Caricato, a. V. Marenich, J. Bloino, B. G. Janesko, R. Gomperts, B. Mennucci, H. P. Hratchian, J. V. Ortiz, a. F. Izmaylov, J. L. Sonnenberg, Williams, F. Ding, F. Lipparini, F. Egidi, J. Goings, B. Peng, a. Petrone, T. Henderson, D. Ranasinghe, V. G. Zakrzewski, J. Gao, N. Rega, G. Zheng, W. Liang, M. Hada, M. Ehara, K. Toyota, R. Fukuda, J. Hasegawa, M. Ishida, T. Nakajima, Y. Honda, O. Kitao, H. Nakai, T. Vreven, K. Throssell, J. a. Montgomery Jr., J. E. Peralta, F. Ogliaro, M. J. Bearpark, J. J. Heyd, E. N. Brothers, K. N. Kudin, V. N. Staroverov, T. a. Keith, R. Kobayashi, J. Normand, K. Raghavachari, a. P. Rendell, J. C. Burant, S. S. Iyengar, J. Tomasi, M. Cossi, J. M. Millam, M. Klene, C. Adamo, R. Cammi, J. W. Ochterski, R. L. Martin, K. Morokuma, O. Farkas, J. B. Foresman and D. J. Fox, .